

Eco-friendly applications of hot spring bacterial protein  
in terms of heavy metal (lead) decontamination and  
energy harvesting system

*A thesis submitted for the degree of Doctor of Philosophy (Science)*  
*of*  
*Jadavpur University*



*Under the supervision of*

**Prof. Brajadulal Chattopadhyay**

Department of Physics

Jadavpur University

*Submitted by*

**Chetana Ghosal**

Department of Physics

Jadavpur University

Kolkata 700032

India

*Dedicated to My Beloved Parents*



**JADAVPUR UNIVERSITY**  
**KOLKATA-700032, INDIA**

**CERTIFICATE FROM THE SUPERVISOR**

This is to certify that the thesis entitled “**Eco-friendly applications of hot spring bacterial protein in terms of heavy metal (lead) decontamination and energy harvesting system**” submitted by **Chetana Ghosal**, who got her name registered on **16.11.2016** for the award of Ph.D. (Science) degree at Jadavpur University, is absolutely upon her own work under the supervision of Prof. Brajadulal Chattopadhyay, Professor, Department of Physics, Jadavpur University and that neither this thesis nor any part of it has been submitted for either any degree/diploma or any other academic award anywhere before.

*B. Chattopadhyay 8/12/22*

Signature of the Supervisor with seal



**Dr. Brajadulal Chattopadhyay**  
Professor  
Department of Physics  
Jadavpur University  
Kolkata - 700 032

# **DECLARATION**

I do hereby declare that the work embodied in this thesis entitled **“Eco-friendly applications of hot spring bacterial protein in terms of heavy metal (lead) decontamination and energy harvesting system”** which is being submitted for the degree of Doctor of Philosophy (Science) has been carried out by me in the Biophysics Laboratory, Department of Physics, Jadavpur University, Kolkata. Neither the thesis nor any part thereof has been presented anywhere earlier for any degree/diploma or academic award whatsoever.

Date: 08/12/22

Kolkata, India

*Chetana Ghosal*  
Chetana Ghosal

# Acknowledgement

I want to start by saying how grateful I am to have many people in my life with their valuable knowledge, advice, assistance, and blessing and they deserve my heartfelt thanks for their great bits of help during my Ph.D. study. First and foremost, I would like to express my sincere gratitude to my supervisor, Prof. Brajadulal Chattopadhyay, for his visionary guidance, enduring support and encouragement, meticulous care and attention. Whenever I experienced any problem during research, his good word, kindness and assistance always help me to overcome the difficulties.

I would also like to express my sincere thankfulness and indebtedness to Dr. Dipankar Mondal for his invaluable advice and feedback on my research and giving me permission to access his laboratory and instruments and research technique.

I would like to express my deepest hearty gratitude to Dr. Sujoy Kumar Ghosh for his valuable advice, active assistance, guidance, generous help, encouragement, and brilliant criticism and providing invaluable direction during my Ph.D. program.

I am deeply obliged to Dr. Abiral Tamang for his suggestions and for always being willing to give his kind support and assistance whenever I approached him.

I would like to give my special thanks to Kritish Roy for his pleasant cooperation in terms of valuable suggestion, kind assistance in my research work.

For financial support during the execution of the research work, I would like to express my profound sense of gratitude to DST Women Scientist Scheme-A (WOS-A), Government of India. Their financial support helps me a lot to complete my work successfully.

Of course, I would like to thank my fellow lab mates in this lovely group: Saheli di, Atreyee di, Avishek, Swarnali, Anwasha, Somashree, Subiah. They have lent their helping hand in each step of my research. Luckily, I have such a great friend who gives me endless love, making me feel home-like warmth in this lovely lab.

I express my deepest gratitude to Sangita and Bidisha di for their heart-warming love, support and assistance that gives me mental peace during my PhD time span.

Now, I would like to express my lifetime gratitude to my parents: Shri Mrityunjoy Ghosal and Smt. Sabita Ghosal, my source of life and strength. I am truly blessed to have such wonderful parents. Everything I am today and everything I may become tomorrow, is all for the sacrifices our parents made for me. There are not enough words to express how grateful I am to them. They give me full support no matter what decision I make and always encourage me to follow my heart. Their unconditional love has been giving me courage to optimistically face any challenges in my life. I also send my love and thankfulness to my sisters: Pragati and Ekata for their love and support.

Date: 08/12/22

Place: Kolkata

Chetana Ghosal  
Signature of the Candidate

(Chetana Ghosal)

# Table of Contents

	Page Number
Acknowledgement . . . . .	i
List of Figures . . . . .	vi
List of tables . . . . .	xiii
List of Abbreviation. . . . .	xiv
List of Publications . . . . .	xvi
Conference Presentations: . . . . .	xvii
Preface. . . . .	xix
 Chapter 1	
Introduction . . . . .	1
1.1 Environmental Bacteria/Protein: . . . . .	3
1.2 Heavy metal contamination and removal process . . . . .	5
1.3 Nanoparticles and their applications: . . . . .	8
1.4 Renewable Energy Harvester: . . . . .	9
1.5 Nanogenerator: . . . . .	11
1.6 Piezoelectric nanogenerator: . . . . .	12
1.6.1 Working Principle: . . . . .	12
1.6.2 Theoretical background: . . . . .	14
1.6.3 Piezoelectric materials: . . . . .	15
1.7 Poly(vinylidene fluoride) (PVDF): . . . . .	16
 Chapter 2	
Review of Literature. . . . .	20
2.1 Bacteria . . . . .	21
2.1.1 Discovery of Thermophile . . . . .	22
2.1.2 Importance of thermophilic enzyme . . . . .	23
2.2 Heavy metals and its consequences on Environment . . . . .	25
2.3 Various Heavy metal removal technique . . . . .	27
2.4 Role of bacteria/protein in heavy metal removal: . . . . .	31
2.5 Role of bacterial/protein in nanotechnology . . . . .	34

2.6 Role of bacteria in energy harvesting .....	36
2.7 Nanogenerator .....	37
2.8 Piezoelectric Nanogenerator .....	38
2.8.1. ZnO nanowires-based PENG: .....	39
2.8.2 PZT-Based PENGs .....	44
2.8.3 Composite Materials-Based PENG.....	46
2.8.4 Bio-materials based PENGs.....	49
2.8.5 Disadvantage and solution .....	51
2.8.6 PVDF based PENGs: .....	52
2.8.7 Limitations: .....	55

## Chapter 3

Materials and Methods .....	59
3.1. Bacterial purified protein sample preparation.....	61
3.1.1. Study of BKH2 and MDH1 Bacterium.....	61
3.1.2. Isolation and purification of bacterial Protein.....	64
3.1.3 Purified Protein justification by Lowry Method .....	66
3.1.4 Sodium Dodecyl Sulfate-Polyacrylamide Gel Electrophoresis (SDS-PAGE) technique: ...	67
3.2 Lead contamination removal.....	68
3.2.1 lead removal from lead nitrate solution .....	68
3.2.2 Identification of lead oxide precipitate .....	69
3.2.3 Toxicity study of the supernatant on bacterial growth.....	69
3.2.4. Photo-Catalytic activity of lead oxide.....	70
3.2.5 Preparation of electrospun nano-fiber .....	70
3.3 Bio-organic film preparation and Bio-Piezoelectric Nanogenerator fabrication using bacterial protein .....	71
3.3.1 Materials and film preparation .....	71
3.3.2 In-vitro biocompatibility study .....	72
3.3.3 Nanogenerator fabrication.....	74
3.3.4 Nanogenerator performance study .....	75
3.4 Materials and its performance Characterization and instrumental description .....	75
3.4.1 UV-VIS Spectrophotometer.....	76
3.4.2 Field emission scanning electron microscopy (FE-SEM).....	76
3.4.3 Transmission Electron Microscopy (TEM) .....	77
3.4.4 X-ray diffraction (XRD) .....	78
3.4.5 ICP (Inductively Coupled Plasma) Spectroscopy .....	78



3.4.6 Fourier transform infrared spectroscopy (FT-IR) .....	79
3.4.7 Dielectric and ferroelectric characterizations.....	79
3.4.8 Piezoelectric characterizations .....	80

## Chapter 4

### Results and Discussions. . . . . 81

4.1 Removal of Lead Contamination through the Formation of Lead-Nanoplates by a Thermophilic Bacterial Protein.....	82
4.1.1 Protein purification and SDS-PAGE analysis.....	83
4.1.2 The Inductively Coupled Plasma (ICP) analysis of powder precipitate .....	84
4.1.3 Surface morphology studies.....	85
4.1.4 FTIR Spectrum analysis.....	85
4.1.5 XRD analysis: .....	87
4.1.6 Nontoxicity test of Supernatant.....	88
4.1.7 Dye degradation activity .....	89
4.1.8 Conclusion .....	90
4.1.9 Surface morphology study of electrospun nano-fiber:.....	90
4.2. Bio-Organic Piezoelectric Nanogenerator .....	92
4.2.1 Biocompatibility analysis of Protein-PVDF films and Bio-Organic nanogenerator.....	93
4.2.2 Surface Morphology of films .....	99
4.2.3 Stress-Strain analysis: .....	101
4.2.5 DSC analysis:.....	106
4.2.7 Energy harvesting performance .....	110
4.2.9 Theoretical Simulation.....	119
4.2.10 Self-Power Healthcare Monitoring .....	120
4.2.11 Conclusion .....	124

## Chapter 5

### Conclusion and Future Outlook. . . . . 125

5.1 General Conclusion of thesis: .....	126
5.2 Future work:.....	129

## Chapter 6

### References . . . . . 131

# List of Figures

<b>Figure</b>	<b>Title</b>	<b>Page No.</b>
<b>1.1</b>	Effective eco-friendly techniques for elimination and recovery of harmful heavy metal and another important element from wastewater. Reproduced with permission [46]. Copyright 2022, Elsevier.	<b>6</b>
<b>1.2</b>	An epitome of various applications of nanogenerators as energy source. Reproduced with permission [85] Copyright 2017, Elsevier.	<b>11</b>
<b>1.3</b>	Description of the working principle of piezoelectric nanogenerator with the enhance of the applied external stress.	<b>13</b>
<b>1.4</b>	Illustration of Various Piezoelectric Materials	<b>15</b>
<b>1.5</b>	Schematic diagram of crystalline phase of PVDF. Reproduced with permission [91]. Copyright 2018, MDPI.	<b>16</b>
<b>2.1</b>	Morphological images of different thermophilic bacteria (a) represent TEM image of rod-shaped BKH1 bacterium. Reproduced with permission [16]. Copyright 2010, Elsevier. (b) shows the formation of Silica nanoparticles in presence of BKH1 bacterium. Reproduced with permission [17]. Copyright 2015, Elsevier. (c) TEM image of BKH2 bacterium. Reproduced with permission [18]. Copyright 2015, RSC Advances. (d) FESEM image of thermophilic MDH1 bacterium. Reproduced with permission [19]. Copyright 2016, Scientific Research Publishing.	<b>24</b>
<b>2.2</b>	Schematic diagram of different types of bacterial interactions with heavy metals in toxic wastewater. Reproduced with permission [163]. Copyright 2021, Elsevier.	<b>32</b>
<b>2.3</b>	Lead resistant mechanisms in bacteria. Reproduced with permission [170]. Copyright 2013, Elsevier.	<b>34</b>
<b>2.4</b>	A proposed schematic diagram of biosynthesis of Ag-nanoparticles using Ag-resistant bacterium. Reproduced with permission [175]. Copyright 2014, Royal Society of Chemistry.	<b>35</b>

- 2.5** A comparative description of electromagnetic, electrostatic, piezoelectric and triboelectric effect in energy harvesting application. Reproduced with permission [85]. Copyright 2017, Elsevier. **38**
- 2.6** Piezoelectric nanogenerators based on ZnO nanowire arrays. (a-c) Experimental design for converting nanoscale mechanical energy into electrical energy by a vertical piezoelectric (PZ) ZnO NW. Reproduced with permission [185]. Copyright 2006, Science. (d) Fabrication technique of the multi-layered NGs and rational growth of ZnO NW and NTP arrays [186]. Copyright 2008, American Chemical Society. (e) fully rollable PENG consisting of 1D ZnO nanorods which grown epitaxially on a 2D graphene electrode. Reproduced with permission [198]. Copyright 2010, Wiley-VCM. (f, g) PENG made of a free cantilever beam with a flexible polymer substrate, vertical ZnO NW arrays textured films on top and bottom surfaces along with electrodes Reproduces with permission [199]. Copyright 2011, American Chemical Society. (h) Design of a laterally packaged piezoelectric fine wire (PFW) generator on a flexible substrate. Reproduced with permission [200]. Copyright 2009, Nature Publishing Group. (i-l) Piezoelectric Energy harvesting from the movement of human index finger using an SWG representing by the I-V characteristic of the SWG. [187]. Copyright 2009, American Chemical Society. **41**
- 2.7** Flexible PENG based on ZnO nanowire arrays. (a-d) Structure and optical images of vertically integrated nanogenerator (VING) and multiple lateral-nanowire-array integrated nanogenerator (LING). Reproduced with permission [201]. Copyright 2010, Nature Publishing Group. Images (e-h) shows lateral ZnO nanowire array based flexible high output nanogenerator (HONG) by scalable sweeping printing method. Reproduced with permission [202]. Copyright 2010, American Chemical Society. (i-k) piezoelectric nanogenerator based on the conical shape of the as-grown ZnO nanowires, produced an output power which continuously drive a commercial small liquid crystal display (LCD). Reproduced with permission [203]. Copyright 2010, American Chemical Society. **43**
- 2.8** PZT based piezoelectric nanogenerator. (a-c) Schematic representation and optical microscopy image of crystalline PZT ribbons on a flexible PDMS substrate. Reproduced with permission [208]. Copyright 2012, American Chemical Society. (d-f) Represents the schematic diagram of wavy/buckled **44**

piezoelectric PZT ribbons and corresponding SEM images. Reproduced with permission [209]. Copyright 2011, American Chemical Society. (g, h) Fabrication process and optical image of a flexible PZT thin film-based PENG using the laser lift-off method, allowed more than 100 commercial blue LEDs to illuminate. Reproduced with permission [210]. Copyright 2014, Wiley-VCH. (i-k) fabrication process and SEM, optical image of a vertically aligned ultralong (PZT) nanofibers based high output PENG using electrospinning technique. Reproduced with permission [211]. Copyright 2013, American Chemical Society.

- 2.9** (a) BaTiO<sub>3</sub> thin films were deposited on a Pt/Ti/SiO<sub>2</sub>/(100) Si substrate to fabricate PENG using radio frequency magnetron sputtering. Reproduced with permission [219]. Copyright 2010, American Chemical Society. (b) a simple nanocomposite generator (NCG) was fabricated based on BaTiO<sub>3</sub> nanoparticles and graphitic carbons (i.e., carbon nanotubes and reduced graphene oxide). Reproduced with permission [220]. Copyright 2012, Wiley-VCH. (c) Lead-free NG based on Au/Cr-coated NaNbO<sub>3</sub> nanowire and poly(dimethyl siloxane) (PDMS) polymer composite polymer film. Reproduced with permission [221]. Copyright 2011, American Chemical Society. (d) A Hyper-Stretchable Elastic-Composite PENG based on PMN-PT particles and multiwalled carbon nanotubes (MWCNTs) in a silicone elastomer matrix and a very long Ag nanowires with outstanding energy harvesting performance. Reproduced with permission [222]. Copyright 2015, Wiley-VCM. (e) structure of piezoelectric single-crystal ZnSnO<sub>3</sub> nanocubes and PDMS polymer composite based hybrid piezoelectric nanogenerator. Reproduced with permission [223]. Copyright 2014, Wiley-VCM. **48**
- 2.10** (a, b) Schematic and optical diagram of Genetically modified bacterial viruses (M13 phages) based bio-piezoelectric device. Reproduced with permission [224]. Copyright 2012, Nature Publishing Group. (c) Schematic diagram of flexible PENG, fabricated using an anisotropic BaTiO<sub>3</sub> (BTO) nanocrystals and an M13 viral template by genetically programmed self-assembly process. Reproduced with permission [225]. Copyright 2013, American Chemical Society. (d) Describe the fabrication of bio-waste fish-scale based flexible bio-piezoelectric nanogenerator. Reproduced with permission [226]. Copyright 2016, American Institute of Physics. (e) Diagram of bio-piezoelectric nanogenerator using fish swim bladder as piezoelectric material. Reproduced **50**

with permission [227]. Copyright 2016, Elsevier.

- 2.11** (a) Schematic and SEM image of piezoelectric nanogenerator based on poly(vinylidene fluoride) (PVDF) nanofibers using near-field electrospinning (NFES) technique with electrical poling process. Reproduced with permission [228]. Copyright 2010, American Chemical Society. (b) Schematic diagram of nanoporous PVDF films using ZnO nanowire as template-based PENG exhibiting an efficient conversion of Sonic Wave driven mechanical oscillations to electricity. Reproduced with permission [229]. Copyright 2011, American Chemical Society. (c) Photograph and SEM image of free-standing sheets of highly aligned P(VDF-TrFe) nanofibers using electrospinning onto a fast-rotating collector. Reproduced with permission [230]. Copyright 2013, Nature Publishing Group. (d) Structure of sponge-like mesoporous PVDF thin film based piezoelectric nanogenerator. Reproduced with permission [232]. Copyright 2014, Wiley-VCM. **54**
- 2.12** Different phase transformation process of PVDF. **55**
- 2.13** (a), (b) represents digital photograph of Neat PVDF and Pt-NPs doped PVDF films, (b) digital photograph (left panel) represents good flexible feature of Pt-NPs doped PVDF film and FE-SEM image (right panel) of the film. Reproduced with permission [233]. Copyright 2014, The Royal Society of Chemistry. (c) Schematic diagram of fabrication of DNA assisted PVDF film based piezoelectric nanogenerator. Reproduced with permission [234]. Copyright 2015, American Chemical Society. (d) Schematic diagram of MOF-derived PVDF composite ferroelectret film-assisted mechanical energy harvester (MEH). Reproduced with permission [235]. Copyright 2020, American Chemical Society. **56**
- 4.1** (a) Protein purification curve (b) SDS-PAGE analysis of MDH1 bacterial protein **83**
- 4.2** (a)-(b) represents lead oxide nanoplates formation in powder form (c) ICP-OES analysis of powder precipitate shows existence of lead in the sample. **84**

<b>4.3</b>	(a) surface morphology from FESEM image shows nanoplate structure (b) elemental representation of lead oxide using EDX analysis (c) TEM image of nanoplates.	<b>85</b>
<b>4.4</b>	FTIR Spectrum of lead oxide nanoplates and inset image shows the enlarged view of the H-bond of nanoplates.	<b>86</b>
<b>4.5</b>	Crystalline structure analysis of lead oxide nanoplates using XRD	<b>87</b>
<b>4.6</b>	Non-toxic effect of supernatant on <i>E. coli</i> bacterial growth	<b>88</b>
<b>4.7</b>	Photocatalytic activity of lead oxide nanoplates on (a) MO; (b) BB and Percentage of dye degradation of (a) MO; (b) BB	<b>89</b>
<b>4.8</b>	(a) shows the digital photograph of electrospun Protein-PVDF nanofiber (b) FESEM image of porous protein-based nanofiber.	<b>91</b>
<b>4.9</b>	The BKH2 bacterial protein purification curve.	<b>91</b>
<b>4.10</b>	Biocompatibility tests: (a) Optical microscopy images showing growth of the <i>E. coli</i> bacterium over the surface of the PVDF-BP-0.25 bio-organic film and (b) Neat PVDF film. (c) Cell proliferation of the <i>E. coli</i> bacterium over the surface of PVDF-BP-0.25 and Neat PVDF films demonstrating the biocompatibility nature. (d) <i>E. coli</i> bacterial growth study from solid medium LB agar plate. (i) Digital images of LB agar plate along with PVDF-BP-0.25 film and (ii) Neat PVDF film. (iii) The immunofluorescence microscopy images of PVDF-BP-0.25 and (iv) Neat PVDF film. (v) The FE-SEM images of PVDF-BP-0.25 and (vi) Neat PVDF films. (e) Growth study of <i>E. coli</i> bacteria on the surface of the films collected from liquid LB media (i) FE-SEM image and (ii) immunofluorescence microscopy images of <i>E. coli</i> bacteria over the surface of PVDF-BP-0.25. (iii) The FE-SEM and (iv) immunofluorescence microscopy images of <i>E. coli</i> bacteria over the surface of Neat PVDF film. (f) (i) Digital images of LB agar plate along with PVDF-BP-0.25 film-based bio-organic nanogenerator, (ii) immunofluorescence microscopy image and (iii) FE-SEM images of <i>E. coli</i> bacteria over the surface of nanogenerator. (iv) Cell proliferation of the <i>E. coli</i> bacterium in liquid LB media in the presence of nanogenerator and without nanogenerator (control).	<b>94</b>
<b>4.11</b>	Cell viability study of films and device using MTT assay	<b>98</b>

- 4.12** (a) (i-iv) Surface morphology by FE-SEM representing the porous microstructure over the bio-organic films with different protein concentrations. The inset in (iv) shows the flexibility demonstration of the spongy film. (b) The cross-sectional FE-SEM images of (i) Neat PVDF, (ii) PVDF-BP-0.25, (iii) PVDF-BP-0.50 and (iv) PVDF-BP-1.0 films. The images representing the fact that with increasing BP content into PVDF the porosity was increased. **99**
- 4.13** Stress-strain curve of Neat PVDF and protein based PVDF films shows the softness of the films. **102**
- 4.14** (a) FT-IR spectra of the developed films. (b), (c), (d) represents Deconvolution of the FTIR spectra of bacterial protein incorporated PVDF films within the range  $930\text{ cm}^{-1}$  to  $780\text{ cm}^{-1}$ . (e) C–N double bond character in peptide bond due to resonating structure of amino acid. (f) Schematic representing the H-bonding interaction between the PVDF chain and resonating structure of peptide bonds followed by self-polarization of bio-organic material. (g) FT-IR spectra of the Neat PVDF and PVDF-BP films in the region of  $3500\text{--}3000\text{ cm}^{-1}$  showing broad peak, confirmed the broad intensified N-H stretching vibration in PVDF-BP films. (h) The FT-IR spectra in the frequency region of  $3075\text{--}2925\text{ cm}^{-1}$  representing frequency shifting of the CH<sub>2</sub> asymmetric ( $\nu_{\text{as}}$ ) and symmetric ( $\nu_{\text{s}}$ ) stretching vibration modes in PVDF-BP films. **103**
- 4.15** DSC thermograms under (a) heating cycle and (b) cooling cycle. **107**
- 4.16** Electrical properties of the Neat PVDF and the developed bio-organic films (a) Frequency dependent dielectric constant and (b) loss tangent (c) Electric field dependent polarization and (d) butterfly shaped piezoelectric strain hysteresis loops (e) The electrostrictive coefficients of the bio-organic PVDF-BP films and Neat PVDF film. **109**
- 4.17** The energy harvesting performance of the BONG. (a) Schematic of the designed BONG using the porous bio-organic film. (b) Generated open-circuit output voltage ( $V_{\text{oc}}$ ) and (c) short-circuit output current under 15 kPa pressure. (d) Pressure dependent output voltage in the range of 2–15 kPa pressure. (e) Voltage output within the pressure range of  $10\text{ Pa}^{-1}$  kPa pressure range under flat configuration and bending configuration of the device as shown schematically in the inset. (f) The voltage output from the device under repeated bending and releasing motions as schematically shown in the inset. (g) The voltage output from the nanogenerator under repeated twisting and releasing **111**

motion as shown schematically in the inset. (h) Output voltage and power variation across a range of load resistance of 5 k $\Omega$  – 10 M $\Omega$ . The inset shows operated 54 LEDs directly connected to BONG. (i) The charging performance of the commercial capacitors with the schematic of the used circuit in the inset. (j) The output power comparison of the BONG with the previously developed PENG and TENGs (k) The instantaneous output electrical energy per cycle from the BONG.

- 4.18** Finite element based theoretical simulation. (a) The applied stress distribution, **120**  
(b) the displacement distribution, (c) stress induced polarization distribution and  
(d) generated voltage distribution within the bio-organic films of different  
porosity as mentioned in the top portion.
- 4.19** Clinical applications of the BONG. (a) Schematic representing the healthcare **121**  
monitoring positions of a human body used in our study. (b) Radial artery pulse  
measurement under rest and running physical activities. (c) Carotid artery pulse  
measurement with (d) an enlarge signal of one cycle. (e) Thyroid artery pulse  
signal measurement. (f) Laryngeal prominence movement signals with (g) one  
cycle signal showing glottis open and closing response. (h) Repeated coughing  
action signals (upper panel) with STFT of one signal (lower panel). (i) Vocal  
cord vibration signal during speaking different words of ‘O’ , ‘N’ , ‘P’ , ‘D’ , ‘L’  
and (j) their 3-D STFT spectrogram.



## List of tables

<b>Table</b>	<b>Title</b>	<b>Page No.</b>
<b>2.1</b>	Some examples of conventional method of heavy metal removals.	<b>28</b>
<b>2.2</b>	The various bioremediation-based strategies regarding the removal of heavy metal pollutants from environment. Reproduced with permission [46]. Copyright 2022, Elsevier.	<b>29</b>
<b>4.1</b>	Mechano-sensitivity comparison of the BONG with the reported piezoelectric based pressure sensors.	<b>115</b>
<b>4.2</b>	The generated voltage, current and power output comparison of the BONG with previously developed piezoelectric nanogenerators. (NM: Not Mentioned)	<b>116</b>
<b>4.3</b>	A summary or comparison of device materials and capacitor charging performances of the BONG with the reported nanogenerators.	<b>117</b>
<b>4.4</b>	A comparison list of device materials, and energy conversion efficiency of the BONG with the reported nanogenerators.	<b>118</b>

# List of Abbreviation

$\mu$ W	microwatt
mW	milliwatt
GW	gigawatt
pC	Picocoulomb
$\mu$ F	microfarad
WHO	World health organization
DNA	Deoxyribonucleic acid
LB	Luria Broth
MTT	(3-(4,5-dimethylthiazol-2-yl)-2,5-diphenyltetrazolium bromide
BSA	Bovine serum albumin
SDS-PAGE	Sodium Dodecyl Sulfate-Polyacrylamide Gel Electrophoresis
MO	Methyl Orange
BB	Bromophenol Blue
IoT	Internet of Thing
EMGs	Electromagnetic generator
NG	Nanogenerator
PENG	Piezoelectric nanogenerators
TENG	Triboelectric nanogenerator
FTNG	Ferroelectretic nanogenerator
ZnO	Zinc oxide
NW	Nanowire
CNT	Carbon nanotube
PZT	Lead zirconate titanate
PVDF	Poly(vinylidene fluoride)
DMF	N, N-dimethyl formamide
PDMS	Polydimethylsiloxane
BP	bacterial protein

$V_{oc}$	Open-circuit voltage
$I_{sc}$	Short-circuit current
PVDFBP	Poly(vinylidene fluoride)-Bacterial Protein
BONG	Bio-Organic Nanogenerator
ICP-OES	Inductively Coupled Plasma Optical Emission Spectroscopy
FESEM	Field Emission Scanning Electron Microscopy
EDX	Energy Dispersive Spectrometer (EDX)
HRTEM	High-resolution transmission electron microscopy HRTEM
FTIR	Fourier Transform Infrared (FTIR) spectroscopy
XRD	X-ray diffraction (XRD)
DSC	Differential Scanning Calorimeter (DSC)
LED	light emitting diodes (LEDs)
LCD	LCD Liquid crystal display
$P_r$	Remnant polarization
$\epsilon_r$	Dielectric constant
$\tan \delta$	Loss tangent
P	Polarization
E	Electric field

# List of Publications

## Referred Journals:

1. **Ghosal, C.**, Ghosh, S.K., Roy, K., Chattopadhyay, B. and Mandal, D., 2022. Environmental bacteria engineered piezoelectric bio-organic energy harvester towards clinical applications. *Nano Energy*, 93, p.106843.
2. **Ghosal, C.**, Alam, N., Tamang, A. and Chattopadhyay, B., 2021. Removal of Lead Contamination through the Formation of Lead-Nanoplates by a Hot Spring Microbial Protein. *Advances in Microbiology*, 11(11), pp.681-693.
3. Show, S., **Ghosal, C.** and Chattopadhyay, B., 2016. Root Extracts (*Gymnadenia orchidis* Lindl) Facilitated Rapid Synthesis of Fluorescent Silver Nanoparticles (Ag-NPs) for Various Biological Applications. *Journal of Biomaterials and Nanobiotechnology*, 8(1), pp.109-124.
4. Show, S., Chattopadhyay, K., **Ghosal, C.**, Chattopadhyay, B., 2017. A Microbial Protein-Assisted Silica Ball Comprising of Silica Nanoparticles with Plausible Optical Properties for Multiple Applications. *SDRP Journal of Nanotechnology & Material Science*. 2(1), 1-8.

## Conference proceedings:

1. **Ghosal, C.**, Ghosh, S. K., Mandal, D., & Chattopadhyay, B. (2019, July). Protein promoted  $\beta$ -phase nucleation in poly (vinylidene fluoride) for energy harvesting applications. In *AIP Conference Proceedings* (Vol. 2115, No. 1, p. 030592). AIP Publishing LLC.

## Conference Presentations:

- Third International Conference on Nanomaterials: Synthesis, Characterization and Applications (ICN 2018). 11-12 May 2018, Mahatma Gandhi University, Kerala. Preparation And Characterization of Lead Oxide Nano-plates By Bio-template For Sustainable Development. Chetana Ghosal, Nurul Alam, Abiral Tamang, Brajadulal Chattopadhyay.
- 63<sup>rd</sup> DAE Solid State Physics Symposium. 18-22 December 2018, Haryana. Protein Promoted  $\beta$ -phase Nucleation in Poly (vinylidene fluoride) for Energy Harvesting Applications. Chetana Ghosal, Sujoy Kumar Ghosh, Dipankar Mandal, Brajadulal Chattopadhyay.
- National Conference on Recent Developments in Nanoscience and Nanotechnology. 29<sup>th</sup> -31<sup>st</sup> January 2019, Jadavpur University. PVDF/Protein composite for Energy Harvesting Applications Chetana Ghosal, Sujoy Kumar Ghosh, Dipankar Mandal, Brajadulal Chattopadhyay.
- India International Science Festival. 5-10 November 2019, Kolkata. Nucleation of Electro-active Phase in Bacterial Protein doped Poly(vinylidene fluoride) for Energy Harvesting Applications. Chetana Ghosal, Sujoy Kumar Ghosh, Dipankar Mandal, Brajadulal Chattopadhyay.
- National Seminar on New Directions in Physical Sciences. 25 February 2020. Jadavpur University, Kolkata.  $\beta$ -phase Nucleation in Bacterial Protein doped Poly (vinylidene fluoride) for Energy Harvesting Applications. Chetana Ghosal, Sujoy Kumar Ghosh, Dipankar Mandal, Brajadulal Chattopadhyay.
- One day Seminar on Recent Trend in Frontier Research in Physics. 6<sup>th</sup> March, 2018. Department of Physics, Jadavpur University, Kolkata.

- Introduction to Fractional Geometry and its Application in Condensed Matter Physics. 13-14<sup>th</sup> December, 2018. Condensed Matter Physics Research Center, Jadavpur University, Kolkata.
- National Seminar on Physics at Surfaces and Interfaces of Soft Materials (PSISM-2019). 26-27<sup>st</sup> September, 2019. Department of Physics. Jadavpur University, Kolkata.

# Preface

## **Eco-friendly applications of hot spring bacterial protein in terms of heavy metal (lead) decontamination and energy harvesting system**

Our planet has been suffering from extreme pollution for very long decades and becomes more dangerous to the life of all living objects on the planet. Nowadays, air, water, and soil pollution reached their maximum limit causing global warming, as a result, an increase in the average temperature of the earth. Maximum pollution originated from human irresponsible activities, lack of knowledge and proper implementation of modern Eco-friendly sustainable technologies. Heavy metals include lead, arsenic, mercury etc., the natural element of earth, listed one of the most pollutions causing entity to the environment because of its extreme exposure to the environment from different source like untreated industrial wastewater, unscientific anthropogenic activities like mining, different dyes, paints, pesticides etc. that seriously effect human health. Besides, the extreme use of fossil fuel not only creates high level of pollution but the world goes through major energy crisis. Therefore, to fight against environmental pollution, biomaterials based-technology such as environmental bacteria-based techniques acquire most valuable importance because of their biocompatible, eco-friendly feature and low cost in comparison with other physical/chemical process. Natural bacteria account for most of the biomass on earth, can be considered as living bio-factories, possesses unique ability to undergo evolutionary adaption in relatively short time spans and engineered the materials microstructure and properties. Furthermore, among the other bacteria, thermophilic bacteria receive more importance because of their extreme temperature tolerance feature which make them survive in extreme environmental condition.

Therefore, we proposed a new eco-friendly green approach to remove non-biodegradable, toxic heavy metal, lead from aqueous solution using thermophilic bacterial protein as bio-

template. The hot spring (at Metaldanga of temperature 42 °C) bacterial (named MDH1) protein was induced into the solution of lead compound (e.g., lead nitrate) whereas lead was precipitated as the form of lead oxide nanoplates as viewed by the electron microscope and analysed by inductively coupled plasma. The filtered supernatant doesn't exhibit any kind of toxic effect when applied into the growth of *E. coli* bacterium, implies lead free solution. And the as-formed lead oxide nanoplates were applied in dye (methyl orange and bromophenol blue) degradation activity. The process is clean and cost effective one which can be used not only for removal of lead contamination but also for removal of different dyes from environment.

We also demonstrate a concept and design principles of a biocompatible piezoelectric material with the assistance of thermophilic bacterial strain BKH2 collected from hot spring of Bakreshwar with temperature 65°C. The bacterial protein engineered the microstructure of organic polymer poly(vinylidene fluoride) (PVDF) in order to prepare the porous bio-organic films with increased biocompatibility, piezoelectric phase content and crystallinity. The porous microstructure significantly enhances the piezoelectric coefficient and piezoelectric figure of merit of the bio-organic film compared with non-porous pure PVDF. The designed porous bio-organic film based piezoelectric nanogenerator is capable to generate high output power and possesses favourable energy conversion efficiency which is further used for driving several commercial light emitting diodes (LEDs) and charge capacitors. The enhanced piezoelectric performance is attributed via porosity formation and validated through finite element method (FEM) based theoretical simulation. With the good biocompatibility and piezoelectric pressure sensitivity, the device was implemented towards clinical applications of real-time healthcare monitoring from subtle pulse pressure waveform detection to vibrotactile information collection. With its natural biocompatibility, easy to prepare formulation and superior energy harvesting performance, the bio-organic film offers



attractive prospects towards the development of effective, sustainable and autonomous electromechanical device for next generation self-powered biomedical devices.

Chapter 1

# Introduction

Mother Earth along with her all-living objects is moving towards the worst impairment because of human-made pollution disasters. Pollution, it may be air pollution, water, or soil pollution all causes extreme damage to the living environment. Maximum pollution originated from human irresponsible activities, lack of knowledge and proper implementation of modern Eco-friendly sustainable technologies. Heavy metals, natural element on earth but one of the main origins of our environmental pollution calamity. Our environment is polluted through heavy metal contamination in soil, water and agricultural food product which is one of the most noticeable states of concern for all living objects. Almost every health and environmental organization such as WHO, IARC and USEPA/IRIS showed their concern about heavy metal contamination and stated that heavy metals are conclusively cancer-causing agents and they can seriously affect organ deformation and destruction [1–4]. In the other hand, From the start of human civilization, energy is one of the most valuable sources of sustainability and improving our way of living. In the mid-17<sup>th</sup> century, first time coal was used as energy resource and a significant advancement in human lifestyle began which unlock the treasure of fossil fuels [5]. Then, in 18<sup>th</sup> and 19<sup>th</sup> century, fossil-fuel like oil, natural gas took place of huge energy generation and based on these fossil fuel industrial revolution was began which increase the standard of living of human generation. Next in 20<sup>th</sup> century the use of fossil-fuel increased extensively boundless with advancement in technology and exponential enhancement of energy consumption almost in every field. Many studies claimed that fossil fuels are the largest producer of greenhouse gas such as carbon dioxide which promotes global warming, a life-threatening effect on humans and also on all living organisms on earth [6]. Therefore, extreme fossil fuel burn imposed adverse effects on the environment concerning air pollution, water pollution, and ultimate climate change. On the other hand, these fossil fuels are limited, a concerning shortage will be seen in the near future and we are going to face an eventual deficiency of energy. In this circumstances, green

eco-friendly techniques are only option to save our environment and human life from the pollution disaster. Environmental Bacteria account for most biomass on earth, is one of the most favourable choices to control the pollution.

**1.1 Environmental Bacteria/Protein:** Bacteria is the first form of life originated on Earth about 4 billion years ago, belongs to prokaryotic microorganism family with shapes like spheres, rods, or spirals [7–8]. With a few micrometres in length, bacteria are ubiquitous i.e., present in most of its habitants such as water, soil, deep biosphere of Earth's crust, also in extreme environment as in radioactive waste and acidic hot spring. Millions of bacteria lives in human body most of them are non-pathogenic, having no toxic effect on human life and they are beneficial for immune system. Bacteria reproduced through binary fission and in laboratory they grown in solid and liquid media [9]. Some of these bacteria have an ability to survive in high temperature ranging from 45 °C to 122 °C, mostly found in various hot springs all over the world. These bacteria may be aerobic or anaerobic in nature. These thermophilic bacteria acquire good ability in biomineralization and degrade a variety of organic compounds used in waste processing and bioremediation [10–11]. These thermophilic bacteria acquire various protein which may be cellular or extra-cellular which plays an important role in assorted biological reaction. Therefore, to study the functionalities of the specific protein, bacteria are cultured in laboratory and developed specific knowledge and plausible application in different field such as nanotechnology, toxic heavy metal removal and in energy harvesting systems [12–14].

Proteins are large biomolecules that constitute with long polymer chains of amino acid residues. In organism, proteins accomplish various functions, such as helps in the replication of DNA, catalysis metabolic reaction, responding to stimuli and also creates cell structure besides, they are capable of transporting molecules from one location to another. Many

proteins denoted as enzymes that enhance biochemical reactions and are very important to metabolic process.

Thermophilic bacterial proteins access special ability that they are active at very high temperature i.e., not denatured in high temperature whereas other bacterial protein easily denatured at high temperature, makes them more favourable. Proteins contain linear polymer chain construct from series of twenty different L- $\alpha$ - amino acids having an amino group, a carboxyl group and a variable side chain, fold into unique 3D structure.

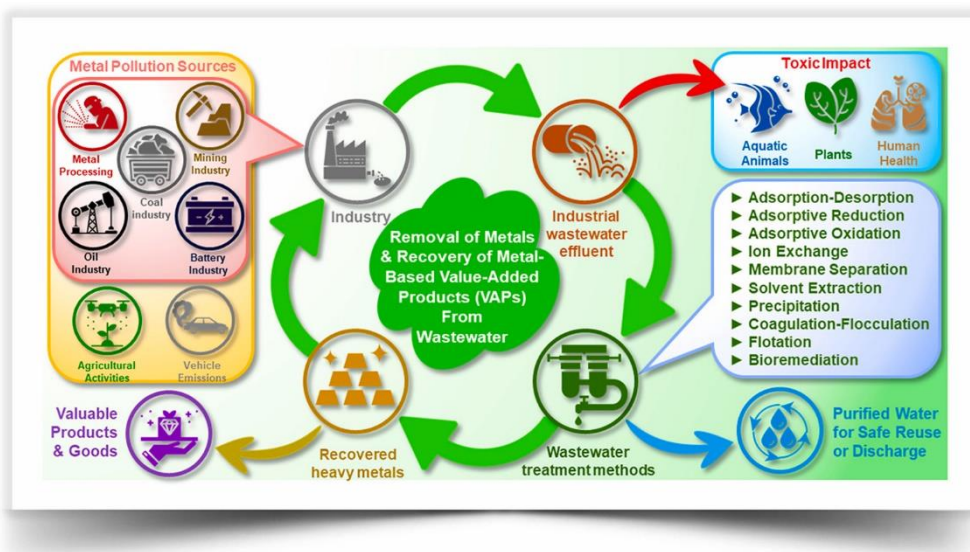
Thermostable proteins from hot spring bacteria are dominant biocatalysts for industrial and biotechnological grounds, because of their favourable performance at high temperatures whereas mesophilic bacterial protein would be entirely denatured. One of the classical examples relates to Taq DNA polymerase from *Thermus aquaticus*, isolated and purified from hot springs, that shaped the evolution of the PCR amplification technique plausible [15]. Now a days, PCR becomes the base of exclusive biomedical industries conducting rapid diagnosis of infectious disease. Furthermore, Biswas et al. (2010) reported a noble protein called bioremediase (UniProt Knowledgebase Accession No.: P86277), collected from a hot spring bacterium BKH1 (GenBank Accession No.: FJ177512), possess silica leaching activity, developed a new construction material when incorporated to the cement/cement–sand mixture that may be beneficial for self-healing concrete in future and also this bacterium has ability to the synthesis of silica nanoparticles (SiO<sub>2</sub>-NPs) [16–17]. From the same laboratory, another bacterial strain was reported named BKH2 collected from the same hot spring of Bakreshwar with self-healing and iron reducing properties of rod shaped, gram negative, anaerobic thermophilic strain grown at 65° C temperature like as BKH1 having impact in self-healing concrete technology [18]. Another thermophilic bacterial strain was identified from Metaldanga hot spring, MDH1 which grown at 42°C temperature possess good ability of gold nanoparticle formation [19].

**1.2 Heavy metal contamination and removal process:** Heavy metals describe as a class of metals contain an atomic density higher than 4000 kg/m<sup>3</sup> [20–21] which are toxic even at low metal ions concentrations [22–23]. The most commonly found heavy metals are lead, mercury, arsenic, bismuth, antimony, cadmium, titanium etc., are natural components of the earth's crust and cannot be degraded or destroyed. The individual sources of these heavy metal contaminations happen mainly due to the disposal of untreated or partially treated industrial wastewater and contaminated sewage from different industries and also, fuels used by ships along with heavy metal-containing pesticides, paints, dyes and fertilizers used in agricultural fields etc. [24–26]. In the other hand, lead-acid batteries, treated timber, electronic waste recycling yard and microplastic floating in water spreads heavy metal contamination in our environment [27–28]. Some recent heavy metal disaster occurred throughout the world including high level of lead contamination in drinking water which provided to the people of Flint, Michigan, US [29], Minamata disease, in Japan [30], Bento Rodrigues dam disaster happened in Brazil [31], occurrence of heavy metal in drinking water, in Hong Kong, 2015.

Sparks (2004) reported lead (Pb) as one of the serious hazardous pollutants exists in our environment [32], in the same direction some studies claimed the existence of lead in Indian river such as a high level of lead contamination found in the water of the Yamuna River [33] and remarkable amount of iron, manganese and lead etc. observed in the water of the Ganga River in Kolkata [34]. However, Pb(II) is one of the most required and used in various industries including battery, electroplating, paint, steel, inorganic fertilizers and pesticides [35–36]. According to the data from International Agency for Research on Cancer (IARC, WHO), lead was recognized as group 2A carcinogen [37] while National Toxicological Program (NTP) belongs to Department of Health and Human Services (US DHHS), US, in

their 14th report on carcinogens has classified lead and its compound as “Reasonably anticipated to be Human carcinogens” [38] .

Therefore, Heavy metals contamination reveals an intense threat to our health and environment because of their non-biodegradability and high toxicity. Various approaches have been explored to remove heavy metal pollutants from our environment such as: reverse osmosis [39], adsorption [40], filtration [41], biosorption [42], electro-coagulation [43], membrane processing [44], ion exchange [45] etc.



**Figure 1.1:** Effective eco-friendly techniques for elimination and recovery of harmful heavy metal and another important element from wastewater. Reproduced with permission [46]. Copyright 2022, Elsevier.

All procedures have their own ability and advantage in heavy metal removal procedure but in case of comparison studies bioremediation techniques for heavy metal removal is much effective rather than the chemical and physical process. Besides, Physical and chemical techniques are not eco-friendly, very costly, and are usually dominated by the waste concentration. Whereas, bioremediation process employed biological systems, biomaterials for removing toxic pollutants like heavy metals, dyes from water, soil, air, industrial waste water which refers a low cost and predominantly ecologically acceptable method [47–50].

It has been well known for a long time that several living and dead microorganisms such as bacteria, algae, fungi, yeast etc. can eliminate heavy toxic ions from solutions reported by Sterritt and Lester in 1996 [51]. Protein, polysaccharides, lipids from the microbial cell walls play a critical role in attaching various metal ions with amino, carboxylate, hydroxyl and phosphate groups forming nontoxic complexed compounds [52–53]. Therefore, resistant bacteria hold out against the exposure of toxic, hazardous heavy metals and remove them by evolving mechanisms such as bio-reduction/bio-oxidation, bioaccumulation, biosorption and biotransformation [54–56].

In the same path thermophilic bacteria and biomolecules also delivered its role to eliminate toxic heavy metals from ambient environment suggested by the study of O. Chaalal et al. (2003) where a noble thermophilic bacterium was found in the hot spring of United Arab Emirates, have ability to remove Lead compounds contaminants from water [57]. Another thermophilic bacterium *Geobacillus thermodenitrificans* collected from Damodar River, India also capable to binding the heavy metals from industrial waste water [58]. Different studies suggested that various parameter effected the procedure of heavy metal removal by the specific thermophilic bacteria such as pH, initial metal concentration and particle size etc. [59]. A lead-tolerant thermophilic bacterium identified as *Aeribacillus pallidus* MRP280 provided evidence of removal and absorption ability of Pb (II) especially from lead-contaminated water depending on particular temperature, pH, contact time and cell density. Thus, it can be stated that the utility of thermophilic bacteria provides exclusive satisfaction for lead elimination beneath of industrial circumstances where excessive temperature is needed for conducting the processes [60].

Therefore, amplification of the activity of thermophilic biomaterials towards environmental bioremediation needs to develop a proper applicable design and more particular parameter for lead contamination removal.



Now, these microorganism including thermophiles shows their ability in the formation of nanoparticles using their enzymes. Researchers reported that nanoparticles are synthesized when the specific microorganisms can able to grab target metal ions from their habitant and transform them into nanomaterials using enzymes (Li et al. 2011) produced by the cell activities whereas the process is classified into two categories as intracellular and extracellular synthesis depending on the area where nanoparticles are formed [61–62]. Natural molecules such as proteins, amino acids, released from the cells of the organisms coated and stabilized the prepared nanoparticles and the capping proteins properly linked to the surface of the nanoparticles using free amino groups to prevents the aggregation of nanoparticles such that the essential properties of the nanoparticles can be preserved [63–64].

**1.3 Nanoparticles and their applications:** Nanoparticles also called ultrafine particle described as a particle of matter having diameter between 1 and 100 nanometres [65–67]. As building blocks, nano-sized materials access a crucial participation in the area of nanotechnology claims their applications in different areas, including medicine, catalysis, engineering and environmental remediation and received enormous attention due to their unique featured in thermal, electrical, magnetic and catalytic properties [68]. In 2008, the International Organization for Standardization (ISO) confirmed formation of one-dimensional nanomaterials i.e., nanotubes and nanofibers and two-dimensional nanomaterials i.e., nanoplates and nanodiscs followed by various process.

Nanoparticles are highly mobile in the free state, possess enormous specific surface area and may evidence quantum effects which leads nanoparticles having a wide limit of configuration. Nanoparticles provides an extensive range of potential and proper applications in nano-biomedicine as drug and gene delivery agents [69–70] tissue engineering

[71], biosensors [72], Photocatalytic activity [73], antibacterial activity [74], in the field of electronics [75] and also in heavy metal removal technique [76].

There are many physical and chemical techniques for nanoparticle synthesis but bio-inspired synthesis of nanoparticles achieved a massive attention owing to their eco-friendly and cost-effective technique [77]. Thermophilic microorganisms also provide their contribution in nanoparticle synthesis such as thermophilic bacteria BKH1 used as bio-agent for silica nanoparticles (SiO<sub>2</sub>-NPs) formation whereas another bacteria MDH1 have contributed in the synthesis of gold nanoparticles [17, 19].

On the other side, to control environmental pollution caused by the extreme burning of fossil fuels, we must be focused on green renewable energy source.

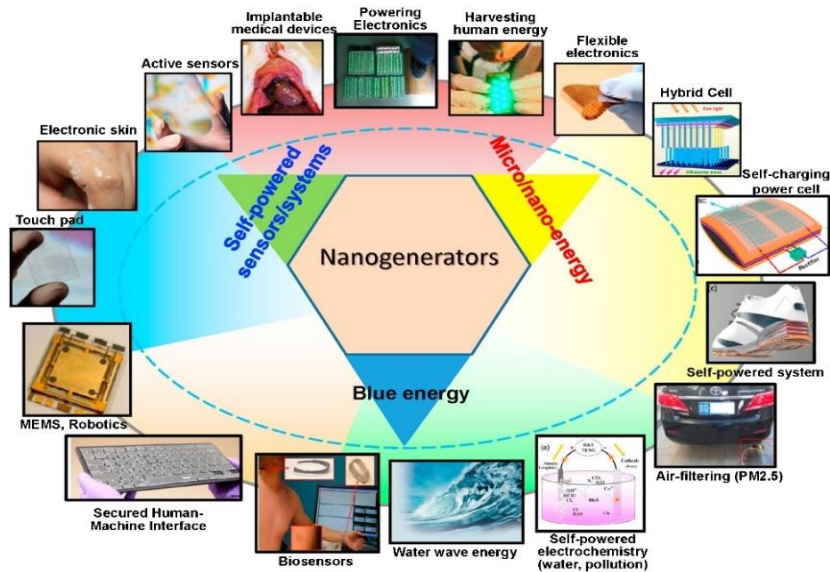
**1.4 Renewable Energy Harvester:** To overcome this energy deficiency and save our future generation and mother earth, renewable energy is the ultimate accomplishment. However, one alternative to fossil fuel which is zero-emission clean nuclear energy but some unfortunate nuclear energy inversion happened in the past time. In 1986, the Chernobyl Nuclear Power Plant disaster and in 2011 the Fukushima Daiichi disaster raised a questionable remark on nuclear energy [78]. The anti-nuclear movement was started at international level and many countries such as Norway, Spain, Germany, Australia, Denmark, Italy, Sweden, Switzerland etc. stay opposed to nuclear power expansion.

In the other side, renewable energy derived from natural sources such as wind, sunlight, rain, waves, tides, geothermal heat and biomass which are replenished with higher rate in parallel with their consumption is our last hope to green energy revolution [79]. However, the large scale ambient renewable energy is extensively available in the earth, many technologies are being developed to significantly capture it and properly utilize to accomplish the energy requirement. These indigenous, inexhaustible renewable energies have

great impact to reduce environmental pollution mainly air pollution created by the burning of fossil fuels and significantly improve public health and climate change issues [80]. In 2022, the International Energy Agency (IEA) demands that all countries should invest more in the technologies reliable with renewable energy source to control the increasing price of fossil fuel along with secure our energy system effectively for future and also cherish our climate goals that retain the average global temperature bellow 2.0 °C [81–82]. Furthermore, there also exists some wasted energy in the form light, heat, vibration, movement, or sound that could also be impactful if captured. It is efficient that if we can recover the waste energy even a minimal of this energy would create an effective environmental and economic impacts. This harvested waste energy from ambient environment can be used for several applications. The scavenging energy-based technologies can be used in the field of self-powered electronics to constantly supply power to the device and in sensor networks.

Till to the 21<sup>st</sup> century many approaches have been developed for power generation and harvest energy. The common techniques for power generation are performed by electromagnetic generators (EMGs) which based on Faraday's law of electromagnetic induction but this technology can significantly generate and harvest only high-frequency mechanical energies [83]. However, in the ambient environment, some kind of broader range highly efficient energy source like low-frequency mechanical energies including human body motions, water waves and various kind of thermal and chemical energy are also available which cannot be properly and significantly harvest through EMGs. In this scenario, there come the concept of nanogenerator through which these small-scale green energies in the ambient environment can be harvested and able to generate power [84].

**1.5 Nanogenerator:** Nanogenerator is classified as an evolving energy harvesting nanotechnology that can harvest small-scale energies in ambient environment and converts various kind of mechanical and thermal energy occurred by small-scale physical change such as human motion like walking, running, breathing, heartbeat, vibration, wind; even waste energy into electricity. Nanogenerators were first fabricated for increase the effectiveness of self-powered device following piezoelectric and triboelectric effect where tiny mechanical energy was converted into electrical energy, that have a significant application in various directions like internet of things, bio-medical fields and crucial security systems, environmental/ infrastructural monitoring [83].



**Figure 1.2:** An epitome of various applications of nanogenerators as energy source. Reproduced with permission [85] Copyright 2017, Elsevier.

A nanogenerator includes three typical obtainments: Piezoelectric, Pyroelectric, and triboelectric nanogenerators and all have their applications in sustainable green energy harvest and sufficient power generation. As from figure 1 nanogenerators applications covers mainly three directions such as (i) micro-/nano-energy source (ii) self-powered sensors (iii) blue energy.

Furthermore, a nanogenerators can be used as an integrated part of a self-powered system along with energy storage unit like supercapacitors and batteries, for powering several functional devices [86].

Now till date a huge improvement in the performance and the feature of the nanogenerators was achieved based on piezoelectric and triboelectric effect.

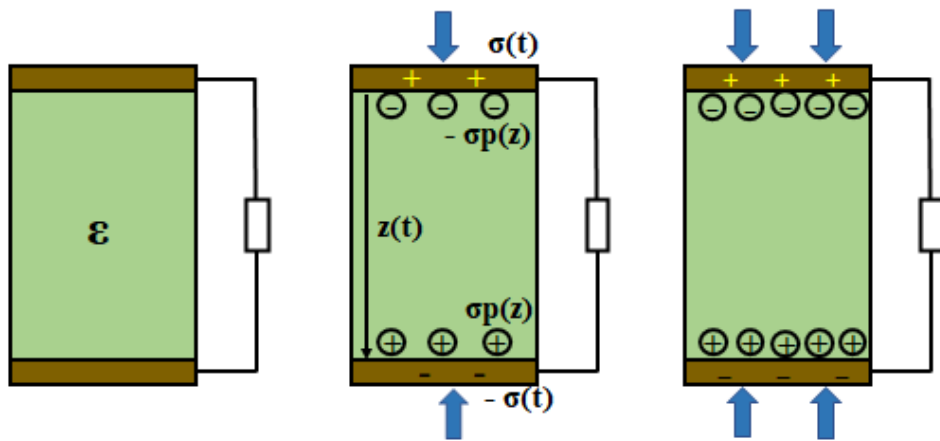
**1.6 Piezoelectric nanogenerator:** Piezoelectric nanogenerator is generally invented as an energy harvesting device capable of converting mechanical energy into electrical power via action of a piezoelectric material. The word piezoelectricity describes electricity conducting from pressure and latent heat.

Piezoelectric effect describes as a linear electromechanical interaction in crystalline materials in between the mechanical and electrical states with no inversion symmetry [87]. As piezoelectric effect mentioned as a reversible process then the materials experience the internal generation of mechanical stress developing from applied electric field.

Pierre and Jacques Curie successfully conducted the first effective experimental work on piezoelectricity in 1880. Quartz is a single crystal in which the demonstration of piezoelectric effect was first time revealed. Subsequently, this effect became one of the most valuable concepts for fabrication of self-powered nanogenerator, a mechanical energy harvesting device.

**1.6.1 Working Principle:** Figure 1.3(i) illustrates the working principle of piezoelectric nanogenerator in respect with enhancing applied stress. The two surfaces of the dielectric piezoelectric material are enveloped by a top and bottom electrode. At the two ends of the material, covered by electrode experiences a vertical mechanical deformation shows in figure 1.3(ii) results the generation of piezoelectric polarization charges. Figure 1.3(iii) shows the high polarization charge density with increase of applied force. The polarization charges

created the electrostatic potential is equilibrated by the motion of electrons conducted from one electrode to another electrode through an external applied load. This phenomenon represents the conversion process of mechanical energy into proper electrical power. Now, Considering the strain in the material resulting from applied force then  $\sigma_p(z)$  represents the density of the piezoelectric polarization charges on the material surface along with the free electrons charge density in the electrode,  $\sigma(x)$  which described as the function of the thickness,  $z$  of the material having piezoelectric properties.



**Figure 1.3:** Description of the working principle of piezoelectric nanogenerator with the enhance of the applied external stress.

When a mechanical stress is exerted on a piezoelectric material, a change in electrical polarization happens within the material which is able to induce an electric current in an external circuit and significantly be employed as an electromechanical generator. To satisfy its applicability as electrical energy harvester, the piezoelectric material must provide the significant ability of producing both charge and voltage. However, most of the piezoelectric material acquires a well-defined polar axis to accomplish technological importance and the applied strain corresponding to this polar axis contributes a major influence to the energy harvesting performance of the piezoelectric material.

**1.6.2 Theoretical background:** The Maxwell equations provides the essential theory to describe the fundamental physics for sustainable green energy harvesting executing piezoelectric effect.

The fundamental Maxwell's equations are following:

$$\nabla \cdot \mathbf{D} = \rho_f \text{ (Gauss's law)}$$

$$\nabla \cdot \mathbf{B} = 0 \text{ (Gauss's law for magnetism)}$$

$$\nabla \times \mathbf{E} = -\partial \mathbf{B} / \partial t \text{ (Faraday's law)}$$

$$\nabla \times \mathbf{H} = \mathbf{J}_f + \partial \mathbf{D} / \partial t \text{ (Ampere's circuital law with Maxwell's addition)}$$

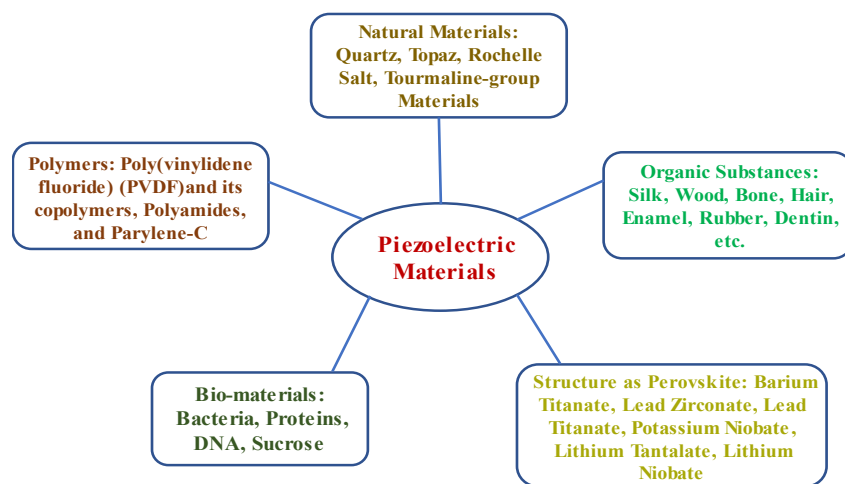
where the E is electric field; B denoted as the magnetic field; H as magnetizing field;  $\rho_f$  represents the free electric charge density;  $\mathbf{J}_f$ , the free electric current density and D denoted as displacement field.

And the Maxwell's displacement current, describes as,

$$\mathbf{J}_D = \partial \mathbf{D} / \partial t = \epsilon_0 \partial \mathbf{E} / \partial t + \partial \mathbf{P} / \partial t$$

From Maxwell analysis we know the first term  $\epsilon_0 \partial \mathbf{E} / \partial t$  gives the idea of electromagnetic wave, originated wireless communication and later the information technology. Zhong Lin Wang reported that the second term  $\partial \mathbf{P} / \partial t$  provides in the Maxwell's displacement current equation is directly connected to the output electric current of the nanogenerator, giving the evidence of nanogenerators as an accomplishment of Maxwell's displacement current in energy and sensors [83].

**1.6.3 Piezoelectric materials:** Piezoelectric materials are those materials which acquire ability to transform mechanical strain and vibration energy into effective electrical power. This property allows the material to implement in piezoelectric nanogenerator fabrication for self-powered energy harvesting. Owing to the research performed on these materials, there is a wide range of piezoelectric materials with different characteristics and specifications and energy harvesting abilities. Quartz is the first material exhibited piezoelectric properties as discovered.



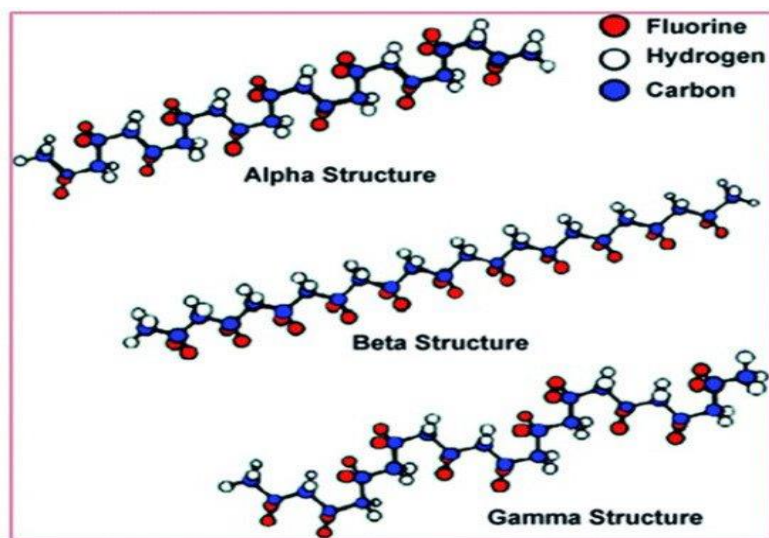
**Figure 1.4:** Illustration of Various Piezoelectric Materials

These materials show piezoelectric properties along with its advantages and disadvantages in applications. Among these well-known materials, Poly(vinylidene fluoride) (PVDF) recognised as one of the favourable piezoelectric material for its high mechanical strength with good processability which manifests strongest piezoelectric properties in contrast with other commercial polymer [88–91].



**1.7 Poly(vinylidene fluoride) (PVDF):** PVDF is a highly non-reactive, semi-crystalline (crystallinity  $\sim 50\%$ ) thermoplastic fluoropolymer with good ferroelectric feature, resulted from the polymerization of vinylidene difluoride whose molecular repeat unit is  $(\text{CH}_2 - \text{CF}_2)$ , exhibits the strongest piezo- and pyro- electric activity amid all known polymers [92–93].

PVDF crystallizes into four crystalline phases such as  $\alpha$ -,  $\beta$ -,  $\gamma$ -,  $\delta$ - phase. The all-trans (TTTT) structure represents  $\beta$  phase (phase I), most important distinct crystalline structure. However,  $\alpha$  phase (called phase II) is the common polymorph, contains alternating trans-gauche TGTG molecules arranged in antiparallel manner [94]. Now, PVDF also belongs to an intermediate structure  $\text{T}_3\text{GT}_3\text{G}$  in a parallel packing fashion to create the  $\gamma$  phase denoted as phase III [95]. Furthermore,  $\alpha$  phase in parallel version creates  $\delta$  phase, also represents as phase  $\alpha_p$  or IV [96]. Figure 1.4 represents the molecular configuration and different crystalline forms of PVDF. Such kind of polymer chain endorsement can be described in the sequence of dihedral bond angles such as the trans bond (T) contains a dihedral angle of  $180^\circ$  and the left and right gauche bonds ( $G$  and  $G$ ) holds  $\pm 60^\circ$  of dihedral angle approximately.



**Figure 1.5:** Schematic diagram of crystalline phase of PVDF. Reproduced with permission [91].  
Copyright 2018, MDPI.

The repeated switching of the polarization between opposite but energetically equivalent directions towards the 2-fold b-axis which leads the most favourable phase,  $\beta$ -phase as polar and uniaxial ferroelectric. The unit cell of the  $\beta$  phase consists of two  $-(\text{CH}_2-\text{CF}_2)-$  formula units parallel to the chains, directed to the c-axis (Figure 1.4) [97]. From figure it also clear that the complete crystalline  $\alpha$  phase configuration creates with opposing polar sublattices of the trans-gauche chains evolving no net polarization in both parallel and perpendicular to the chain axis. Here, in  $\alpha$  phase, unit cell contains four  $-(\text{CH}_2-\text{CF}_2)-$  units where two in the plane perpendicular to the c axis and two along the c-axis parallel to the chains [98].

Furthermore, the  $\beta$  phase is the one which contains highest dipolar moment per unit cell ( $8 \times 10^{-30}$  C m) in comparison with other phases that increase the efficiency of electro-active PVDF as piezoelectric material in self-power device fabrication [99].

Different strategies have been therefore developed such as Solvent casting, Langmuir Blodgett Electrospinning, Spin-coating etc. to obtain the electroactive phases of PVDF besides some external entity was incorporated into PVDF to nucleate electro-active  $\beta$  phase without electrical poling [17,18]. And finally, these PVDF-based piezoelectric nanogenerator achieves an extensive accomplishment in energy generation and storage, sensors and healthcare monitoring systems, filtration membranes [100].

Therefore, thermophilic microorganisms such as bacteria and their protein contribute an enormous efficiency from heavy metal removal to green energy harvester development technique, controlling the deficiency of sustainable energy and environmental pollution.

In this work, thermophilic bacterial (MDH1) protein was used to conduct the performance of heavy metal removal from contaminated water. The extracellular protein with molecular weight  $\sim 30$  kDa was directly added to the lead nitrate solution to eliminate the lead particles from the solution. The significant chemical functional groups of protein were able to bind to

the lead ions which was precipitated as the form lead oxide nanoplates and separated from the solution. The filtered supernatant was further brought to study the non-toxicity featured through the growth of *E. Coli* bacterium on culture plate. Furthermore, the prepared lead oxide nanoplates exhibit photo catalytic activity due to which it can degrade several toxic dyes such as Methyl Orange (MO) and Bromophenol Blue (BB) and effectively able to eliminate the dyes from industrial effluents. Thus, the MDH1 microbial protein is very convenient for cleaning of lead contamination from drinking water as well as of MO and BB dye contamination includes industrial effluents, foods and several agricultural products.

Besides, another environmentally accessible thermophilic bacterial (BKH2) protein was utilized to prepare highly biocompatible porous bio-organic piezoelectric PVDF films depending different standard purified protein concentration and further these films were employed to design a piezoelectric nanogenerator as energy harvester which was successfully implemented towards clinical healthcare monitoring applications. Here, organic polymer PVDF was selected to interact with bacterial protein. The bacterial purified protein incorporated with the PVDF chain to nucleate self-polarised electro-active  $\beta$ -phase along with increased the crystallinity and properly engineered microstructure to form porous, flexible and spongy films. These bio-organic films were brought to investigate biocompatibilities using MTT assay and *E. coli* bacterium growth analysis in the presence of these films, confirmed by optical microscope, FESEM, fluorescence microscope and digital image analysis. Structural characterizations of these films were performed by FESEM, clearly shows the porous structure, FTIR spectra represents the  $\beta$ -phase, DSC thermogram showing thermal stability of the films. Some electrical performance also studies to ensure the electro-active properties of the films including frequency-dependent dielectric properties and polarization level by polarization (P) – electric field (E) hysteresis loop studies. These studies reported the significant increase of piezoelectric co-efficient and piezoelectric figure of merit

of the Protein-PVDF films in comparison with Neat PVDF films which leads the bio-organic films based nanogenerator towards energy harvesting applications. The proof-of-concept of device designing is also analysed, that is the bio-organic film based nanogenerator is efficient to generate maximum output power of as high as  $640 \text{ mW/m}^2$  with energy conversion efficiency of 62.5% which is further applied for driving several commercial light emitting diodes (LEDs) and also properly charge capacitors. With high piezoelectric pressure sensitivity and good biocompatible nature, the device was implemented real time health care monitoring includes from subtle pulse pressure waveform detection to vocal cord vibration simulating. This study recommends attractive prospects towards the development of efficacious, autonomous and sustainable electromechanical device for next generation self-powered biomedical devices.

Chapter 2  
Review of Literature

## 2.1 Bacteria

The existence of bacteria on earth is originated from the beginning of the life on earth. The evolution of bacteria has developed since before Precambrian time, around 3.5 billion years ago while they survive without oxygen [101]. After the oxygen appeared in the atmosphere due to the action of cyanobacteria about 1.8 billion years ago, the bacteria were widespread on the earth. Thus, bacteria got enough time to adapt their ambient environments and able to creates numerous descendant forms.

The prokaryotic microorganism, bacteria possesses a single cell, come in various shapes such as they can be spheres, rods, or spirals. With a few micrometres in length bacteria are ubiquitous, exists in most of its habitants such as water, soil, under water, deep biosphere of Earth's crust and also survive in extreme environments as radioactive waste and hot springs and meanwhile in human body. Approximately  $2 \times 10^{30}$  bacteria exist on earth, forming a biomass with its impactful advantage and disadvantage in human life [102]. Because of their two different types of cell wall, classified as gram-positive and gram-negative based on the reaction of cell wall with gram strain. The metabolism process of bacteria depends on light using photosynthesis or using oxidation process breaking down chemical compounds. For research, bacteria are grown in laboratory using solid or liquid media depending on their requirement in purpose [103].

Most of the bacteria in human body or in the environment are harmless and have beneficial effect on immune system, are called non-pathogenic bacteria. They are all significant to soil ecology, pollution treatment i.e., breaking down toxic waste and essentially recycling nutrients.

### **2.1.1 Discovery of Thermophile**

Bacteria which can survive at high temperature i.e., above 65 °C denoted as thermophile, collected from high temperature marine habitats such as hot spring and from terrestrial. Some studies suggested that they are the first living object on the earth since the birth of the earth when the temperature of the earth was quite hot and that's why sometimes they called as the "Universal Ancestor". Therefore, Horiike et al. reported, thermophilic eubacteria are belonged to have been among the earliest bacteria [104]. In 1965, Thomas Brock reported his unexpected discovery of high-temperature bacteria in the boiling hot springs (above 90 °C) of Yellowstone National Park, USA [105]. After Brock's discovery, different thermophilic bacteria were discovered from different countries like Iceland, Italy, New Zealand and also India. These bacteria not only live in hot water but also, they are capable to well grow in more than one extreme such as lives with high level of calcium carbonate, sulfur and acidic water or alkaline springs.

Hot spring or geothermal spring is a spring which contains water at temperature considerably higher than the surrounding temperature. These are created by the geothermally heated groundwater which emergence on the surface of the Earth. Large amount of different type of dissolved minerals are found into the water of these hot spring which vary from acid sulfate to alkaline chloride to bicarbonate and also to iron-rich spring [106–107]. Furthermore, the presence of microbial communities in the Iron-rich hot springs produce clumps of oxidized iron using iron in the hydrothermal fluids [108]. Akira et al. (1999) demonstrated that quinone Profiles of Hot Spring Microbial Mats were changed with a thermal gradient such as cyanobacteria, oxygenic phototrophic bacteria and chemotropic sulfur bacteria considering different temperature, pH and sulfide concentration [109]. There are many hot springs identified in India where different species of bacteria were discovered and applied in different research area. Some of them are Gauri Kund (Uttarakhand), Manikaran (Himachal Pradesh),

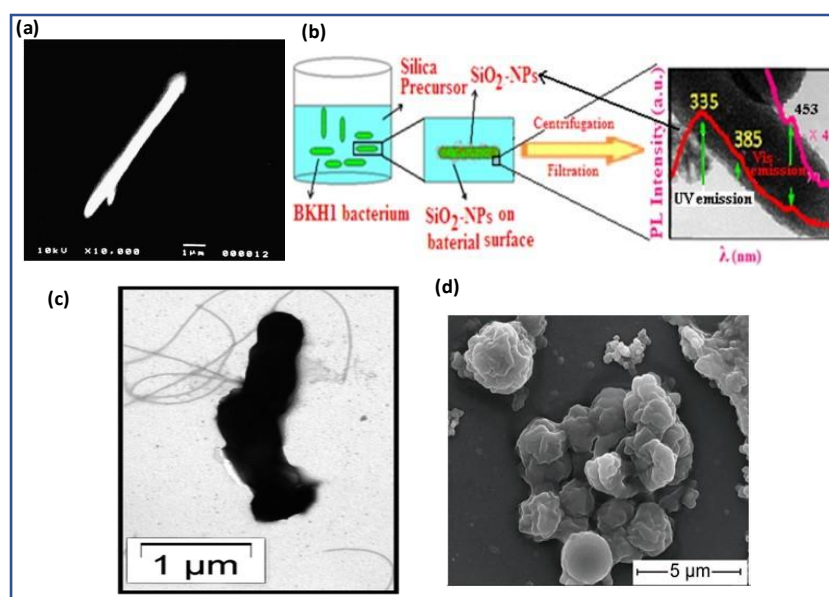
Vasisht (Himachal Pradesh), Vajreshwari (Maharashtra), Taptapani (Odisha), Atri (Odisha). Yumeasamdong (Sikkim), Panamik (Ladakh), Thingbu and Tsachu (Arunachal Pradesh) etc. Furthermore, there is a place at Bakreshwar (23.88 °N 87.37 °E) in Birbhum district of West Bengal where many hot springs were identified such as Bhairav Kunda (temp. 65 °C), Dudh Kunda (temp. 66 °C), Khar Kunda (temp. 58-66 °C), Brahma Kunda (temp. 43-45 °C), Agni kunda, Paphara Kunda (temp. 80 °C), Baitarini Kunda (temp. 72 °C) etc. Due to their unique chemical resources various type of thermophilic and hyper-thermophilic bacteria are identified. Another important hot spring located at Metaldanga in Birbhum district of West Bengal. This is one of the virgin hot springs with temperature 42 °C with almost same feature as Bakreshwar hot spring, lies in the same zone.

### **2.1.2 Importance of thermophilic enzyme**

According to the studies of Thomas Brock in 1997, the enzyme extracted from thermophilic bacteria is stable at near-boiling temperatures which has been proved to be vital in polymerase chain reaction (PCR), utilized to replicate specific pieces of DNA. Today, we all know the importance of PCR technique in applications from rapid diagnosis of disease to forensic medicine [110]. These hyperthermophilic enzymes hopefully more preferable as industrial catalysts because they does not need any toxic metal/heavy ions for functionality which opening the path of feasibility to conduct eco-friendly process in various platform, studied by Comfort et al. in 2004 [111]. Turner et al. (2007) described in their studies on thermophiles and enzymes that the thermostable enzymes acquired a great potential and utilization in biorefining, a method of assembling essential technologies among renewable raw elements, industrial intermediates and effective ultimate products [112]. Some thermo-active anaerobic bacteria collected from Icelandic hot springs have an admirably good ability to produce ethanol from lignocellulolytic hydrolysates which can be used as biofuel reported by Sommer et al. (2003) [113]. Sharma et al. (2013) worked on the Culturable Diversity of



Thermophilic Microorganisms in Hot Springs of Northern Himalayas and collected 101 thermophilic microbial which are the good source of amylase, cellulase and xylanase, possess enough potential for production of Industrially Important Enzymes [114]. Therefore, thermophilic microorganisms have been documented as an important source of industrial enzymes. Another some important thermophilic bacteria were discovered by Mousumi et al. (2010) and Manas et al. (2015) from Bakreshwar hot spring named as BKH1, BKH2 respectively as shown in the Figure 2.1 (a), (c) and collected a unique protein, Bioremediase provided an evolutionary impact on Bio-concrete technology [16, 18]. Mousumi et al. (2010) reported that the thermophilic protein (bioremediase) acquires silica leaching activity, developed a new construction material that used in self-healing concrete technology [16]. Furthermore, Shilpi et al. (2015) demonstrated a study where the thermophilic bacteria BKH2 and its protein was used as biological template for silica nanoparticles ( $\text{SiO}_2$ -NPs) formation which provides a green and cost-efficient technique for nanoparticle synthesis which is described in Figure 2.1 (b) [17]. Thermophilic bacteria MDH1(FESEM image shown in Figure 2.1(d)) and its protein collected from hot spring of Metaldanga, India provided a green technique for gold nanoparticle synthesis, described by Nurul et al (2016) [19].



Chapter 2  
Review of Literature

stations and high-tension lines etc [119–121]. Now, the various plants growing in the heavy metal polluted zone, provides a change in their metabolism and biochemical processes which caused lower biomass production, growth reduction and metal accumulation [122]. Water is an fundamental substance for the existence of life on the earth but due to heavy metal incorporation, changes the pH, organic content and size of the particles in water becomes undrinkable and the aquatic plants response to such disturbance by deterioration in diversity, consistency, and composition of species [123]. Aktar et al. (2010) conducted their studies on the existance of heavy metals in the water of Ganga River where Cd and Pb were detected in the range of 0.005 to 0.006 and 0.05 to 0.53 mg L<sup>-1</sup>, respectively [34]. Singh et al. in 2014 reported the largest concentration of Pb in Yamuna River water was around 392 µg L<sup>-1</sup>, defined bioconcentration in various fish which had human health risk implications [33]. Humans encountered with enough amounts of heavy metals may encounter with several diseases such as cancers, depression, hematic, cardiovascular problems gastrointestinal and renal failure and tubular and glomerular dysfunction [124]. The exposure of low or high concentration of arsenic via drinking water or contaminated food may be fatal to the human health which affects more than 150 million people all over the world [125–126]. Argos et al. (2010) have reported that heavy metal arsenic pollution in groundwater has been a serious life threat to the human being in Bangladesh, India, South-East, South-West and North-East USA, China, Mexico, Argentina etc [127]. The threatening effects of Arsenic poisoning on human life includes melanosis, leuco-melanosis, hyperkeratosis, dorsum, keratosis, gangrene and skin cancer, whereas Watanabe et al. (2003) worked on Effects of Arsenic on Younger Generations, reported the chronic arsenic disclosure are insecure for skin manifestations, new-borns and infants are affected especially from the breast milk that concern in child growth and development [128–129]. On the other hand, mercury also consider one of the most toxic substances on the planet along with arsenic and lead that continues to be

incorporated into our waterways and soil, consumed in our food and water and spilled into our atmosphere [130]. World health organization (WHO) reported in their studies the possible health damage which occurred due to mercury exposure that includes tremors, insomnia, neuromuscular effects, memory loss, and headaches and also damage our nervous, digestive and immune systems, lungs and kidneys [131]. Lead is a static toxic metal to be present all over the environment includes, air, soil, water and also derived from different industrial products like leaded gasoline, cosmetics, paints, ceramics, hair dye, airplanes, water pipes, farm equipment, shielding for x-ray machines, etc. to the environment which is considered as a dominant environmental toxin with non-biodegradable featured [132–133]. Dapul et al. in 2014 reported Lead Poisoning in Children and found a dangerous consequences of Lead exposure on children's health as children in the embryonic state may acquire lead from their mother through the blood which creates universal concern [134]. However, Zelikoff et al. in 1993 studied that lead induced oxidative stress with extreme generation of free radicals, and damaged the cell membrane, results inflammatory signalling cascades [135].

Therefore, heavy metal contamination develops a threatening circumstance to environment and also on human life. Different strategies have been developed to control the heavy metal pollution over the planet Earth.

### **2.3 Various Heavy metal removal technique**

To eliminate heavy metal pollutant from environment and also from direct industrial waste water diverse conventional physicochemical and green biological techniques are developed based on their efficiency. Some examples of conventional methods of heavy metal removal include adsorption [40], chemical precipitation [136], membrane separation [44], filtration [41], ion exchange [45], flotation [137], ion exchange [45], reverse osmosis [39], and electrochemical technologies [43] etc.

Heavy metal	Operation Methods	C <sub>0</sub> (mg L <sup>-1</sup> )	Optimum pH	RE (%)	Ref.
<b>Adsorption</b>					
Pb	Clinoptilolite	1,036	4.0	55	[138]
Pb, Cd	8-hydroxyquinoline reformed Carbon Nanotube	Not available	7	Pb > 80% Cd > 80%	[139]
<b>Ultrafiltration</b>					
Zn, Cd	SDS; Polysulfone; MEUF	50	Not provided	99	[140]
<b>Nanofiltration</b>					
Cd, Cr, Pb	polybenzimidazole	Not available	Not available	95,98,93	[141]
<b>Reverse Osmosis</b>					
Cd, Cr, Pb	thin-film composite membrane TW30-1812-50	Not available	Not available	Not available	[142]
<b>Coagulation/Flocculation</b>					
Co, Ni, Cu	Chitosan, montmorillonite, system	20–100	7	Not available	[143]
<b>Precipitation</b>					
Cd, Ni, Pb	Sodium decanoate	--	4-8	>90	[136]
Pb, Cu, Cr, Zn	CaO	100	7–11	>99.3	[144]
<b>Ionic liquids</b>					
Cu, Cr, Pb, Zn Cu, Pb, Zn	[PR4] [MTBA] [PR4] [TS]	5–1,000 µg/L (Cu, Cr, Pb) and 25– 5,000 µg/L (Zn)	6.5 and 20 g/L IL, Standard solution	>78, 35–99, >85, 20–43 46–95, 56–92, >97	[145]
<b>Floatation</b>					
Cd, Pb,	Tea saponin	10–5 mol/L	6	Cd-89.95%	[146]
<b>Ion Exchange</b>					
Ni, Pb	Amberjet	800, 1,000	Not available	>98	[147]

**Table 2.1:** Some examples of conventional method of heavy metal removals.

The conventional methods are considerable in terms of heavy metal separation but the long-term performance costs are disappointing in case of large-scale applications. At the same time, the above processes need various chemical which are not only costly and inaccessible but sometimes also risky for ambient environment. Therefore, considering all the drawbacks

of these conventional techniques of heavy metal removal, there is a demand for sustainable unconventional and cost-effective alternatives which is also environmentally benign. In this circumstances, biological agents provide favourable and growing interest in heavy metal removal because of their eco-friendly nature. So, using biological ways and means new technologies have been developed to remove heavy metal ions from polluted industrial wastewater and from ambient environment, considering a higher production at lower prices than conventional approaches [148].

Bioremediation is one of such technique of removal of harmful contaminants such as toxic heavy metals or transformation of these toxic metals into less hazardous substances and/or eradication of poisonous elements from a polluted environment [149]. This bio-based treatment process depends on utilizing various plants and other organisms including algae, fungi, bacteria, and cyanobacteria etc., conductive to adsorb, degrade, transform, and/or eliminate pollutants from contaminated ambient environment [150]. There are different bioremediation techniques developed by the researchers depending on their own advantages and disadvantages that are discussed in table 2.2.

Water source	Metal(s) studied	Description of the treatment system	Metal removal process	Performance	Ref.
Lab-sim. aq. sol.	Cr	<b>Phytoremediation:</b> using vetiver grass ( <i>Chrysopogon zizanioides</i> )	Dil. Cr SS → adsorption, diffusion, and accumulation into roots (at low pH) → root to shoot translocation (at high pH)	Rem%: up to 100%	[151]
Lab-sim. aq. sol.	Pb(II), Cd(II)	<b>Biosorption:</b> using two metal resistant-bacterial strains of <i>Bacillus</i> sp.	Dil. M <sup>n+</sup> SS → Cd(II) ions bioaccumulated in periplasmic space/cell surface; <i>in situ</i> chemical precipitation of Cd(II) (as cadmium sulfate and cadmium phosphate) and Pb(II) (as insoluble crystals of lead sulfide)	Rem%: up to 93.8% (Pb(II)/ <i>Bacillus</i> sp. Q3), up to 78% (Cd(II)/ <i>Bacillus</i> sp. Q5)	[152]

Water source	Metal(s) studied	Description of the treatment system	Metal removal process	Performance	Ref.
Lab-sim. aq. sol.	Cr(VI)	<b>Bio-reduction:</b> using <i>Trichoderma lixii</i> isolate CR700	Cr(VI) in aq. sol. → surface adsorption, diffusion and bioaccumulation of total Cr → Cr(VI) intracellular reduction (Cr(VI) $\xrightarrow{\text{red}}$ Cr(III)) → extracellular precipitation of Cr(III) as Cr <sub>2</sub> O <sub>3</sub>	Red%: up to 99.4%; Acc.: 2.12 ± 0.15 mg/g of dried biomass	[153]
Lab-sim. aq. sol.	As(III)	<b>Bio-oxidation:</b> using <i>Pseudomonas monteilii</i> (IT6) and <i>Bacillus infantis</i> (S12) bacterial strains	As(III) in aq. sol. → As(III) $\xrightarrow{\text{red}}$ As(V)	Oxid%: 92% (IT6) and 96% (S12)	[154]
Lab-sim. AMD	Cd(II), Cu(II), Fe(III), Ni(II), Pb(II), Zn(II)	<b>Bio-precipitation:</b> sulfide precipitation using SRB-based sulfidogenic anaerobic IFBR	Dil. M <sup>n+</sup> SS → SO <sub>4</sub> <sup>2-</sup> reduction using SRB with sodium lactate as electron donor → metals sulfide precipitation as NPs in nanopowder form	Rem%: up to >95% (Cd(II), Cu(II), Pb(II), Zn(II)), up to 90% (Fe(III)), up to 85% (Ni(II))	[155]
Lab-sim. aq. sol.	Cd, Cr, Pb	<b>Bio-flocculation:</b> using <i>Pseudomonas koreensis</i> and <i>Pantoea</i> sp.	Incubation and flocculating activity → bio-flocculant purification; M <sup>n+</sup> in SS → metals removal <i>via</i> bio-flocculation → recovery of insoluble bio-flocculants by centrifugation	Rem% ( <i>Pantoea</i> sp.): removed 51.2% (Cd), 52.5% (Cr), 80.5% (Pb); Rem% ( <i>P. koreensis</i> ): 48.5% (Cd), 42.5% (Cr), 73.7% (Pb)	[156]
Phosphorites	U, Sm, Th, La, Ce	<b>Bioleaching:</b> using <i>Aspergillus niger</i>	Phosphorites → siderophores production by <i>Aspergillus niger</i> → metals bioleaching <i>via</i> chelation with siderophores	Rem%: 69.5% (U), 66.7% (Sm), 55% (Th), 51% (La), 50.1% (Ce)	[157]

Water source	Metal(s) studied	Description of the treatment system	Metal removal process	Performance	Ref.
Real pulp and paper industry WW	Fe, Mn, Zn, Pb, Ni, Cu, Cd, As	<b>Microbial-assisted phytoremediation:</b> using <i>Bacillus</i> sp. PS-6 combined with <i>Phragmites communis</i> plants	Metals in aq. sol. → metabolite, indole acetic acid, siderophore, ligninolytic, hydrolytic enzyme production activity by <i>Bacillus</i> sp. → enhanced metals phytoremediation by <i>Phragmites communis</i> via biosorption	Total Acc. (mg/kg): 240.83 (Mn), 286.18 (Fe), 139.68 (Zn), 112.42 (Pb), 103.98 (Ni), 95.48 (Cu), 85.59 (Cd), 74.29 (As)	[158]

**Table 2.2:** The various bioremediation-based strategies regarding the removal of heavy metal pollutants from environment. Reproduced with permission [46]. Copyright 2022, Elsevier.

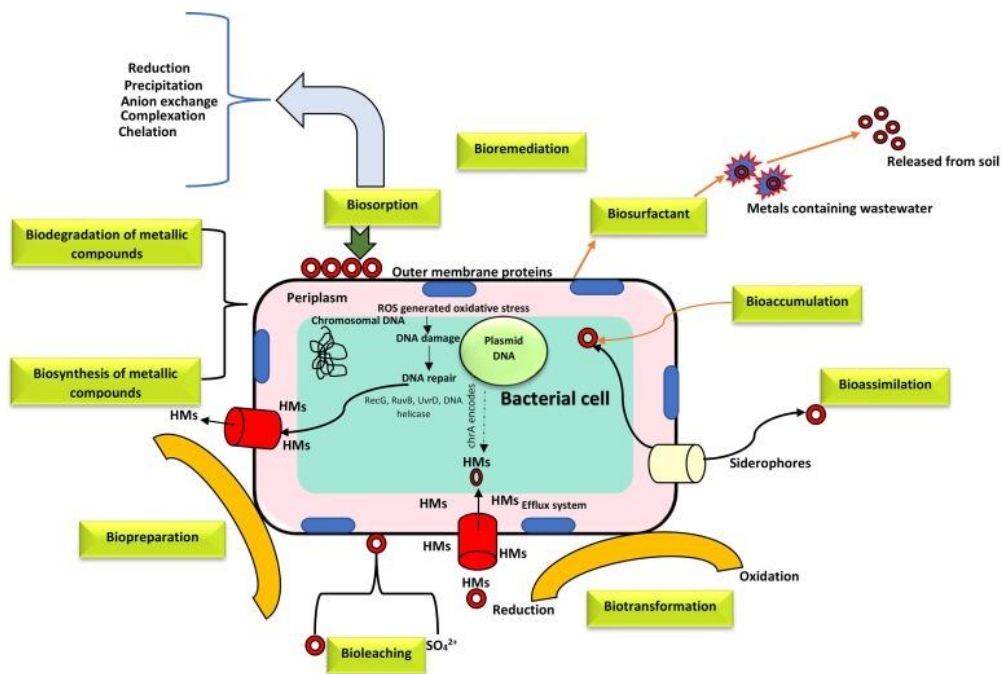
Like other microorganism environmental bacteria/protein acquires a good ability to remove heavy metal pollutant from environment and also from industrial wastewater utilizing bioremediation technique.

## 2.4 Role of bacteria/protein in heavy metal removal:

Accounting for a large fraction of all living biomass on earth, bacteria are operated as a waste by-product in commercial fermentation processing, and various bacteria such as *Bacillus*, *Escherichia*, *Pseudomonas*, *Streptomyces*, *Micrococcus*, etc. species examined for heavy metals uptake [159–160]. Bacteria possess diverse resistance mechanisms which provide them survival strategy to reduce toxic metal even in high concentrated aqueous and soil systems. In 2001 Huang et al. reported heavy metals removal technique from aqueous solutions using two bacterial species, *E. coli* and *B. subtilis* as effective agents of Pb(II), Cd(II) and Cr(VI) removal and observed under the optimal conditions 63.39 % and 69.90 % Cd(II), 68.51% and 67.36% Pb(II), 60.26% and 54.56% Cr(IV) can be removed by *E. coli* and *B. subtilis* respectively [161]. Kang et al. (2016) described bioremediation process of heavy metals utilizing four bacterial strains, identified from bacterial mixtures denoted as



*Viridibacillus arenosi* B-21, *Sporosarcina soli* B-22 along with *Enterobacter cloacae* KJ-46, and *E. cloacae* KJ-47. These bacterial strains showed impressive remediation of 98.3% for Pb, 85.4% for Cd, and 5.6% for Cu from contaminated soils [162]. Sharma et al. (2021) demonstrated in their review study that belongs to efficiency of bacteria and bacterial assisted phytoremediation of toxic heavy metals from polluted sites as well as wastewater [163]. Their studies showed various types of bacterial interactions with heavy metals in contaminated wastewater (depicted in figure 2.2) and development of biochemical transformations, and enhanced phytodegradation, represents bacterial support during phytoremediation.

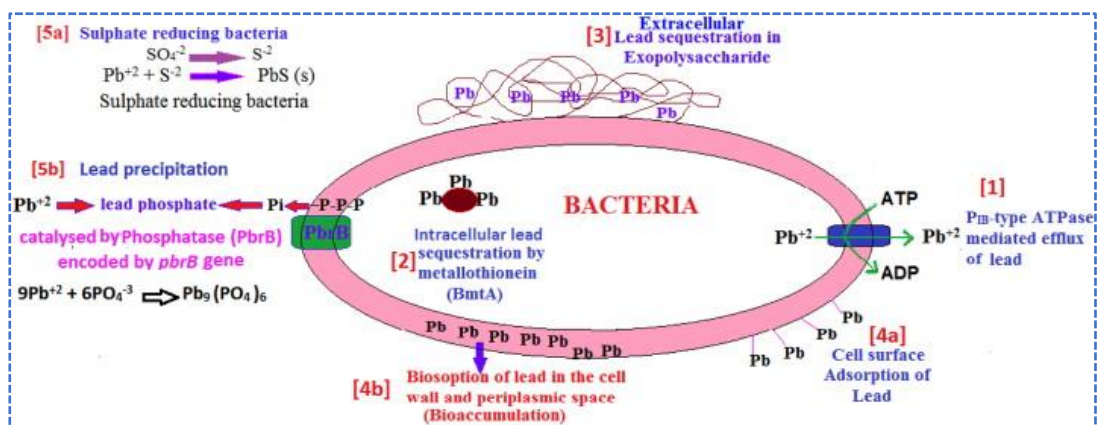


**Figure 2.2:** Schematic description of various types of bacterial interactions with heavy metals in contaminated wastewater. Reproduced with permission [163]. Copyright 2021, Elsevier.

On the other hand, direct application of microorganisms or its enzymes and biosurfactants, is a novel way to increase remediation effectiveness. Saier et al. (1994) discovered RND (resistance-nodulation-cell division) protein which belongs to novel families of bacterial membrane protein that involved in heavy metal resistance named *R. metallidurans* [164]. Furthermore, the importance of bacterial protein in heavy metal removal process was

described by Sharma et al. (2021) in their studies on phytoremediation of heavy metals from toxic industrial wastewater by microbial community and metal-binding proteins [165]. The metal binding proteins include phytochelatins, metallothioneins, cysteines (gcgpcgcg) (CP), Cd-binding peptides (CdBPs), and histidines (ghhphg)<sub>2</sub> (HP) enhance the accumulation and resistance or tolerance of toxic heavy metals which provide great potential for the detoxification of heavy metals [166].

Just like other bacteria, thermophilic bacteria claim their importance in the elimination of heavy metal pollutant from ambient environment. Ozdemir et al. in 2013 reported two strains of thermophilic bacteria, named as *Geobacillus thermantarcticus* and *Anoxybacillus amylolyticus*, which induced to remove heavy metals such as Cd<sup>2+</sup>, Cu<sup>2+</sup>, Co<sup>2+</sup>, and Mn<sup>2+</sup> ions using biosorption technique [167]. In the same biological way, Ilyas et al. (2014) developed an eco-friendly heavy metal (Cu, Zn, Ni, Cd, Al, Cr, Pb) removal technique, bioleaching from recycling industry electronic waste using thermophilic bacteria *Sulfobacillus thermosulfidooxidans* and *Thermoplasma acidophilum* as template [168]. The wastewater produced from the industries provides a noticeable role in lead (Pb(II)) contamination to the environment. Whereas in 1996 Levinson et al. described lead resistance in *Staphylococcus aureus* strain which tolerated higher Pb(NO<sub>3</sub>)<sub>2</sub> concentration and accumulated the metal as an intracellular lead-phosphate [169]. A review studies performed by Naik et al. (2013) demonstrated the lead resistant properties of bacterial strain followed by various mechanisms such as efflux mechanism, biosorption, precipitation, extracellular sequestration, alteration in cell morphology, increased intracellular bioaccumulation of lead that may lead the performance of bioremediation of lead in contaminated sites, described in Figure 2.3 [170].



**Figure 2.3:** Lead resistant mechanisms in bacteria, (1) PIB-type ATPase mediated efflux of lead, (2) Lead sequestration by metallothionein (BmtA), (3) Lead sequestration in exopolysaccharide, (4a) Cell surface adsorption of lead, (4b) Biosorption of lead in cell wall and periplasmic space (bioaccumulation), (5a) Lead precipitation by sulphate reducing bacteria, (5b) Lead precipitation catalysed by Phosphatase enzyme (PbrB). Reproduced with permission [170]. Copyright 2013, Elsevier.

The metal-resistance mechanisms in wild bacteria described by Chen et al. (2019) provides the pathway for the creation of genetically engineered bacteria for remediation purposes in which Pb(II) biosorption nature of *Serratia Se 1998* collected from Pb-contaminated soil which was observed through macroscopic and microscopic techniques [171]. A lead tolerant thermophilic bacterium, *Aeribacillus pallidus* MRP280 was utilized as a biosorbent for lead removal from aqueous solution, reported by Rakhmawati et al. (2021) where maximum  $96.78 \pm 0.19\%$  and  $88.64 \pm 0.60\%$  of lead were removed using living and non-living biomass, respectively at  $55\text{ }^{\circ}\text{C}$  [172].

On the other side, microorganisms specially bacteria have the ability of nanoparticle formation which provides further applications in various scientific fields.

## 2.5 Role of bacterial/protein in nanotechnology

Microorganisms grabbed target ion from ambient environment and then transfer the metal ion into the element metal using its enzymes described as the process of biosynthesis of nanoparticles followed intracellular or extracellular synthesis [173–174]. Li et al. (2011)



complexes [176]. Gandhi et al. (2018) used the extract of *Cuminum cyminum* seed powder to reduce lead nanoparticles which showed effective antimicrobial activities against pathogenic fungi and bacteria and anti-algal activity against spirulina culture [177]. Borhade et al. (2012) and Bratovic (2020) in their articles described the applications of lead oxide nanoparticles in photocatalytic degradation of methyl blue dye and also may act as anticancer and antimicrobial drugs [178–179]. Miri et al. (2018) reported the cytotoxic activity of the synthesized PbO-NPs investigated on Neuo2A cancer cell line that indicated the concentrations under 30  $\mu\text{g/mL}$  provide insignificant toxicity [180]. Therefore, in a study Ramanathan et al. (2013) established a link between heavy metal resistance and nanoparticle synthesis capability in bacterial systems followed by aqueous phase synthesis of copper nanoparticles [181].

The above discussions describe the importance of bacterial and its protein in heavy metal removal process. Nevertheless, these bacteria also have ability in energy harvesting applications based on piezoelectric nanogenerator.

## **2.6 Role of bacteria in energy harvesting**

From the very long-time bacteria have been utilized as energy source, one of the favourable sources of green energy. Mink et al. (2014) reported a micro-sized microbial fuel cells (MFCs) acted as energy harvesters that transform biomass from liquids into usable power using bacteria [182]. Brochu et al. (2021) described in their paper a two-cycle bacteria energy recovery system (BERS) which may able to power two embedded sensors includes a sound sensor and an ultra-low portable pH sensor which provide a constant 0.14 mW power without using any electrical components for signal conditioning [183]. A bacterial cellulose based green energy harvester from mechanical vibration was developed by Trigona et al. (2020) where bacterial cellulose was saturated with ionic liquid, and conducting polymers as


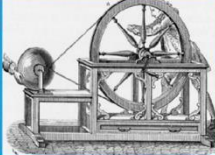
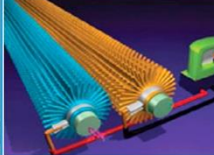
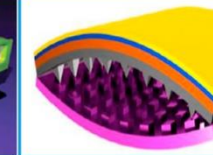
electrodes which generated electrical signal when a mechanical deformation is imposed [184].

Therefore, above studies discussed the effectivity of bacteria as green energy harvester. Now a day, the world suffers from energy crisis and extreme fossil fuel pollution which may overcome by the development of bacteria-based energy harvester includes piezoelectric nanogenerator.

## **2.7 Nanogenerator**

The first proposed idea of self-powering nanogenerator was came in 2006 and the first practical nanogenerator was fabricated by Wang et al. through the discovery of ZnO nanowire based piezoelectric nanogenerators [185]. This study inspires the researcher to work in the field of nano energy. Within the 4 years of its discovery the improvement in the performance of nanogenerator was noticed for example the open circuit voltage raised from the original 9 mV to 1 V [186–188]. The discovered self-powered PENGs not only harvest energy from the working environment with maintenance-free and sustainable operation but also work as active sensors which triggered by mechanical deformation and an electrical signal was generated which include no extra power source at the sensor tip [189]. Furthermore, in 2012 based on triboelectric effect the triboelectric nanogenerator (TENG) was first ever invented [190]. Employing the combination of triboelectric effect and electrostatic induction, a triboelectric nanogenerator converts the external mechanical energy into electrical power, act as an energy harvesting device.

Mechanical energy harvesting in ambient environment generally be performed using several effects mainly electromagnetic induction, electrostatic, piezoelectric and triboelectric. Each of these mechanical energy harvesting effects consisted with its own significance in uniqueness and effective applications, as compared and summarized in figure 2.5.

Mechanical energy harvesting	Electromagnetic	Electrostatic	Piezoelectric	Triboelectric
				
<b>Harvesting principle</b>	Electromagnetic induction	Electrostatic induction	Piezoelectric effect & Electrostatic induction	Contact electrification & Electrostatic induction
<b>Impedance type</b>	Resistive	Capacitive	Capacitive	Capacitive
<b>Pros</b>	High efficiency, easy to scale up	Light weight	Easy to scale down to nanoscale	Large output power, high efficiency, low weight, cost effective materials, simple fabrication
<b>Cons</b>	Heavy magnet required, low output for small-scale devices	Precharge required, low output, high matched impedance	Low output & low efficiency, pulsed output, high matched impedance	Pulsed output, high matched impedance

**Figure 2.5:** A comparative description of electromagnetic, electrostatic, piezoelectric and triboelectric effect in energy harvesting application. Reproduced with permission [85]. Copyright 2017, Elsevier.

## 2.8 Piezoelectric Nanogenerator

Piezoelectric nanogenerator is a promising technology for utilising ambient mechanical energy in electrical power generation in view of the fact that piezoelectric effect is entirely based on the intrinsic polarisation of the materials regardless of the direct contact with another material as in the case of triboelectric nanogenerator and its energy harvesting nature does not need any external voltage source, magnetic field which is essential in case of electrostatic and electromagnetic energy harvesting, respectively [191–192]. Furthermore, without effecting by environment element such as humidity, the piezoelectric nanogenerators can be successfully fabricated in comparatively small dimensions along with properly

compact structures which can effortlessly integrated into microelectromechanical systems [193–195].

The first piezoelectric nanogenerator was invented in 2006 by Wang et al. based on zinc oxide nanowire (NW) arrays [185] and gradually many approaches and invention was conducted to improve the performance, sustainability and applicability of piezoelectric nanogenerator in different field of science.

### **2.8.1. ZnO nanowires-based PENG:**

Wang et al. demonstrated an approach in 2006 to converting mechanical energy into proper electrical power utilizing aligned zinc oxide nanowires (NWs) depending on the coupling of piezoelectric and semiconducting features of ZnO along with the origination of a Schottky barrier in between the contacts of metal and ZnO. This experiment resulted the estimation of the piezoelectric power generation to be 17 to 30% [185].

Next to it, an integrated multilayer nanogenerator was fabricated by Xu et al. in 2008 utilizing the paired nanotip-to-nanowire brushes which was composed of metal-coated pyramid shaped ZnO nanotip (NTP) arrays along with hexagonal prism-shaped ZnO NW arrays, methodized at temperature less than 100 °C using a chemical approach on the two surfaces of the common substrate, respectively (Figure 2.6 d). They used ultrasonic waves to excite the layer-by-layer matched brush architecture which generated current and demonstrated a four-layered integrated NG which produced an output power density of 0.11  $\mu\text{W}/\text{cm}^2$  at a voltage of 62 mV [186].

In 2009, Choi et al. developed a transparent and flexible piezoelectric nanogenerator using vertically-aligned ZnO nanowires [196]. But because of some shortcoming regarding mechanical durability of the electrodes which effects the device's performance stability and lifetime, the same research group fabricated a PENG based on conductive single walled

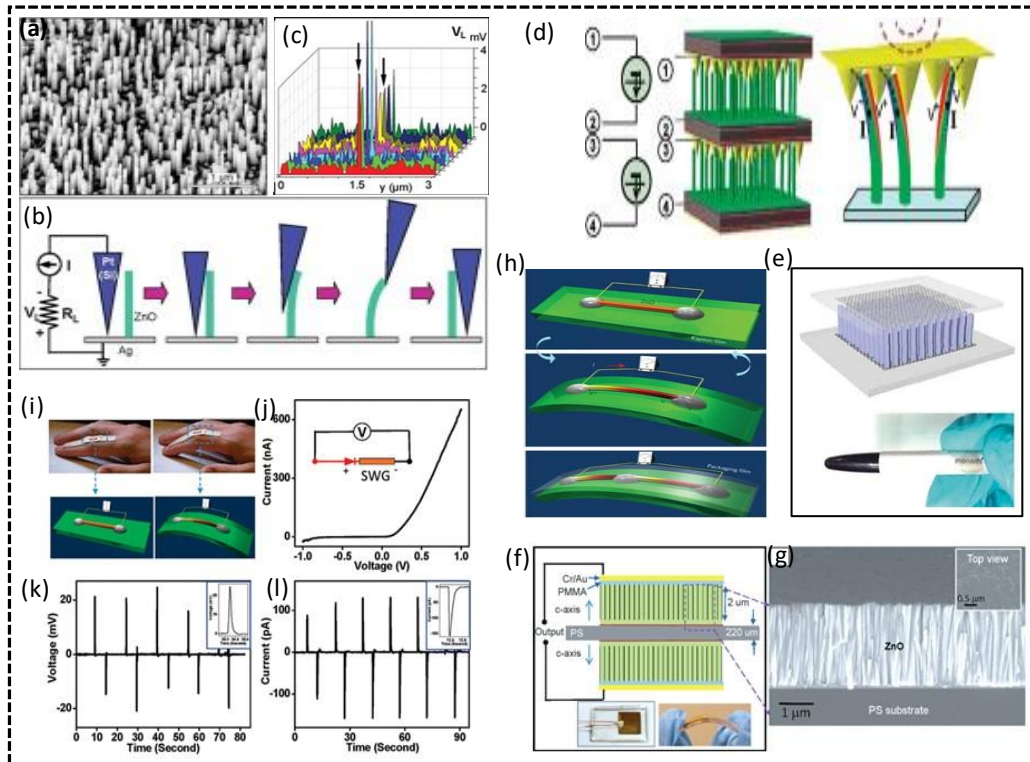


carbon nanotube (CNT) network sheets which act as a contact electrode [197]. According to the studies Choi et al. fabricated a transparent and entirely rollable PENG containing 1D ZnO nanorods which grown epitaxially on a 2D graphene electrode (Figure 2.6 e). Graphene electrode with its extraordinary mechanical and electrical properties and effectively high carrier mobility at ambient temperature along with a Schottky contact to the ZnO nanorods, the NG possesses a superior charge-scavenging performance [198].

In the same way, Hu et al. demonstrated a PENG made of a free cantilever beam with a flexible polymer substrate, vertical ZnO NW arrays textured films on top and bottom surfaces along with electrodes [[199]. An almost thin layer of poly(methyl methacrylate) (PMMA) was coated over the surface of the ZnO film to act as an insulating layer and then placed a conducting metal electrode (shown in Figure 2.6 (f, g)). The measured output voltage gained 10 V when strained to 0.12% with a strain rate of  $3.56\% \text{ S}^{-1}$  and the output current reached  $0.6 \mu\text{A}$  with corresponding power density  $10 \text{ mW/cm}^3$ . This study proves the importance of ZnO nanowire-based PENG for building self-powered systems.

The above discussions were based on vertically aligned piezoelectric ZnO nanowires but there raised some problems including mechanical robustness, output stability, environmental and lifetime adaptability of such devices. Therefore, Yang et al. reported through their studies that they fabricated a flexible power generator whose action is based on cyclic stretching–releasing of a piezoelectric fine wire and without involving in sliding contacts the fine wire was firmly fixed to metal electrodes at both ends which is further encased on a flexible substrate. They demonstrated, a single wire has a strain of 0.05-0.1% originated an oscillating output voltage up to 50 mV through repeatedly stretching and releasing and the energy conversion efficiency of the wire can be developed as high as 6.8% (Figure 2.6 h) [200]. Furthermore, the same group demonstrated the application of the single wire generator (SWG) in energy harvesting from small scale dynamic muscle movement and convert

biomechanical energy in electricity (Figure 2.6 (i-l)) with output voltage up to 25 mV and output current 150 pA from a single SWG device. They connected four SWGs in series which generated output voltage of 0.1-0.15 V [187].



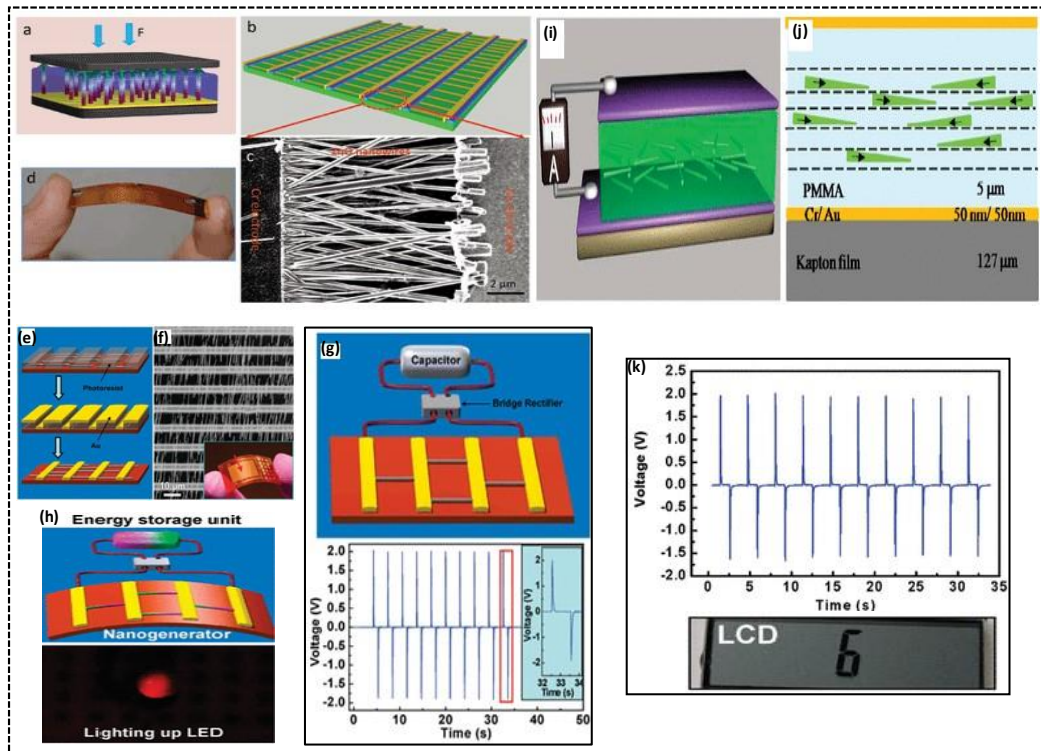
**Figure 2.6:** Piezoelectric nanogenerators based on ZnO nanowire arrays. (a-c) Experimental design for converting nanoscale mechanical energy into electrical energy by a vertical piezoelectric (PZ) ZnO NW. Reproduced with permission [185]. Copyright 2006, Science. (d) Fabrication technique of the multi-layered NGs and rational growth of ZnO NW and NTP arrays [186]. Copyright 2008, American Chemical Society. (e) fully rollable PENG consisting of 1D ZnO nanorods which grown epitaxially on a 2D graphene electrode. Reproduced with permission [198]. Copyright 2010, Wiley-VCM. (f, g) PENG made of a free cantilever beam with a flexible polymer substrate, vertical ZnO NW arrays textured films on top and bottom surfaces along with electrodes Reproduces with permission [199]. Copyright 2011, American Chemical Society. (h) Design of a laterally packaged piezoelectric fine wire (PFW) generator on a flexible substrate. Reproduced with permission [200]. Copyright 2009, Nature Publishing Group. (i-l) Piezoelectric Energy harvesting from the movement of human index finger using an SWG representing by the I-V characteristic of the SWG. [187]. Copyright 2009, American Chemical Society.

Now, to fabricate self-powered nanowire devices with achieving high power output, Xu et al. (2010) innovated a nanogenerator in accordance with vertically or laterally aligned ZnO nanowire arrays where exists solid bonds or contacts among the electrodes and the ends of the nanowires. So, they fabricated a multiple lateral-nanowire-array integrated nanogenerator (LING) and a maximum output voltage of 1.26 V at a low strain of 0.19% was achieved by integrating 700 rows of lateral ZnO nanowire arrays. In addition, a vertically integrated nanogenerator (VING) with three layers of ZnO nanowire arrays was also induced which produced output voltage of 0.243 V along with a peak power density of  $2.7 \text{ mW cm}^{-3}$ . Figure 2.7 (a-d) represents the schematic and characteristic images of vertically integrated nanogenerator (VING) and multiple lateral-nanowire-array integrated nanogenerator (LING) [201].

After that, Zhu et al. (2010) introduced a lateral ZnO nanowire array based flexible high output nanogenerator (HONG) by scalable sweeping printing method. In this method, horizontally aligned arrays were configured through the transferring of vertically aligned NWs to a receiving substrate and then electrodes are properly placed to connect all of the NWs together (Figure 2.2 (e,f). This study demonstrated; a single layer structure of HONG generated open-circuit voltage of up to 2.03 V with output power density of  $\sim 11 \text{ mW/cm}^3$  (Figure 2.2 g). Furthermore, the generated electric energy was beneficially stored by using capacitors, and essentially employed to light up commercial light-emitting diode (LED) (Figure 2.2 h) [202].

In that way, another study was conducted by Hu et al. (2010) where a cost-effecting piezoelectric nanogenerator was developed utilizing the conical shape of the as-grown ZnO nanowires that produced an output power which was capable to continuously drive a commercial small liquid crystal display conducted by Hu et al [203] . With the unipolar assembly of the conical nanowires, a macroscopic piezoelectric potential was developed

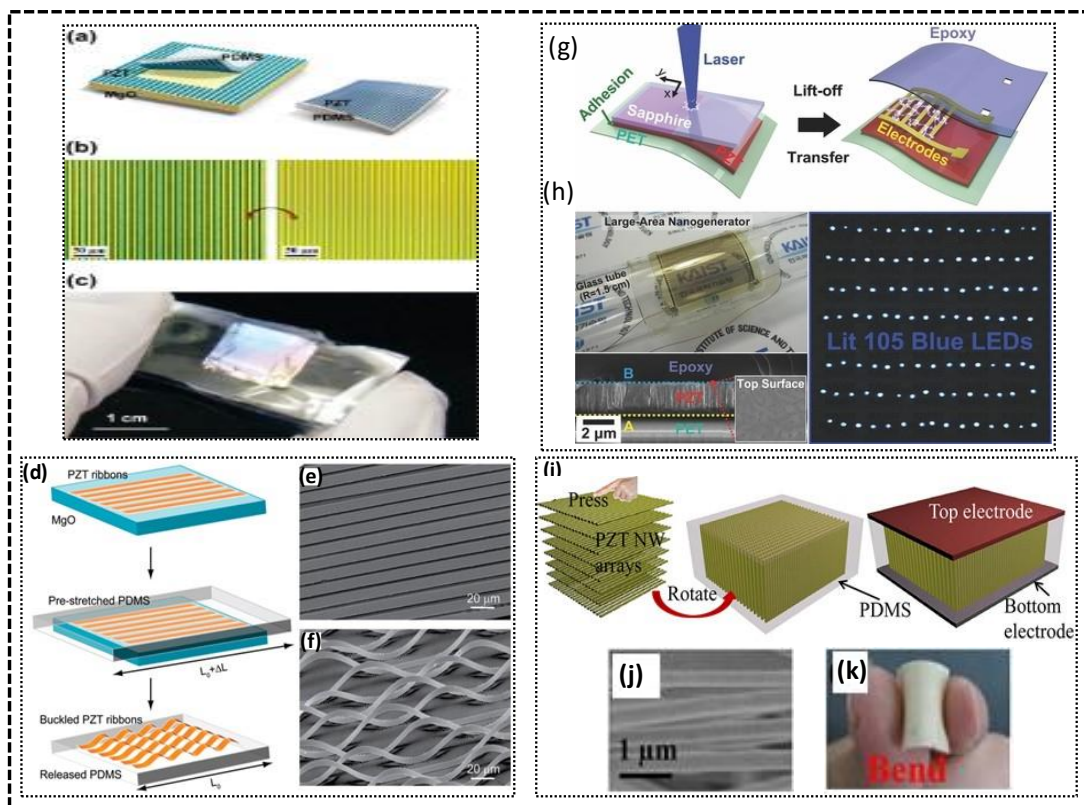
across thickness due to induced mechanical deformation, which drives the flow of the inductive charges between the top and bottom electrodes (Figure 2.2 i,j). Due to a compressive strain of 0.11% an output voltage of 2 V was produced at a straining rate of  $3.67\% \text{ s}^{-1}$  which can drive many small commercial electronics like a liquid crystal display (LCDs) (Figure 2.2 k).



**Figure 2.7:** Flexible PENG based on ZnO nanowire arrays. (a-d) Structure and optical images of vertically integrated nanogenerator (VING) and multiple lateral-nanowire-array integrated nanogenerator (LING). Reproduced with permission [201]. Copyright 2010, Nature Publishing Group. Images (e-h) shows lateral ZnO nanowire array based flexible high output nanogenerator (HONG) by scalable sweeping printing method. Reproduced with permission [202]. Copyright 2010, American Chemical Society. (i-k) piezoelectric nanogenerator based on the conical shape of the as-grown ZnO nanowires, produced an output power which continuously drive a commercial small liquid crystal display (LCD). Reproduced with permission [203]. Copyright 2010, American Chemical Society.

## 2.8.2 PZT-Based PENGs

Lead zirconate titanate (PZT) is a very important ceramic material with good piezoelectric properties along with high dielectric constant and piezoelectric coefficient, exhibits a higher output voltage and current that's way it has been widely appreciated for a sensor and actuator [204–207]. However, there also have some drawback because of its brittle nature of a thin film, not very much suitable for flexible and stretchable modes.



**Figure 2.8:** PZT based piezoelectric nanogenerator. (a-c) Schematic representation and optical microscopy image of crystalline PZT ribbons on a flexible PDMS substrate. Reproduced with permission [208]. Copyright 2012, American Chemical Society. (d-f) Represents the schematic diagram of wavy/buckled piezoelectric PZT ribbons and corresponding SEM images. Reproduced with permission [209]. Copyright 2011, American Chemical Society. (g, h) Fabrication process and optical image of a flexible PZT thin film-based PENG using the laser lift-off method, allowed more than 100 commercial blue LEDs to illuminate. Reproduced with permission [210]. Copyright 2014, Wiley-VCH. (i-k) fabrication process and SEM, optical image of a vertically aligned ultralong (PZT)

nanofibers based high output PENG using electrospinning technique. Reproduced with permission [211]. Copyright 2013, American Chemical Society.

To overcome this drawback and increase its efficiency for flexible energy conversion, Qi et al. (2010) approached a method in which crystalline piezoelectric PZT ribbons holding nanometer scale thickness was implemented on rubber substrates across large areas. In this approach, crystalline PZT ribbons were prepared on MgO source wafers using RF sputtering method and post annealed to form the perovskite crystal structure. Then the MgO wafer was etched to free the PZT ribbons and transferred onto printed flexible polydimethylsiloxane (PDMS) rubber, shown in Figure 2.8 (a-c) [208]. The printed PZT piezoelectric ribbons-based PENG was produced the maximum output voltage and current of 0.25V and 40 nA, respectively, at a tapping frequency of 3.2 Hz.

However, to enhance piezoelectricity and stretchability of this PZT Ribbons based nanogenerator from their previous studies Qi et al. (2011) fabricated the energy harvesting devices from buckled PZT Ribbons. Using the advantage of nanoscale thickness of piezoelectric ribbons, transformed them in wavy shape pattern and incorporated them with stretchable PDMS rubber to accommodate significantly higher compressive and tensile strains, as illustrated in Figure 2.8 (d-f) [209]. Therefore, the fabricated NG can be stretched up to 8% strain and can be able to generate output current of 60 pA, consisting of 10 ribbons and corresponding current density of  $2.5 \mu\text{A mm}^{-2}$ .

Now, Park et al. (2014) also demonstrated an approach to fabricate piezoelectric PZT thin film based nanogenerator with high flexibility and high efficiency in energy harvesting, synthesized via a laser lift-off (LLO) process [210]. By using XeCl laser irradiation on sapphire, the whole area of the PZT thin films were transferred into a flexible polyethylene terephthalate (PET) substrate with no structural damage (Figure 2.8 (g, h)). Therefore, due to slight mechanical deformation, the PZT thin film-based PENG converted a high output performance of 200 V and  $150 \mu\text{A cm}^{-2}$ . And the short circuit current reached up to 8  $\mu\text{A}$ ,

generated from a large-area PENG (3.5 cm × 3.5 cm) by human finger motion which allowed more than 100 commercial blue LEDs to illuminate.

In the same area, Gu et al. (2013) reported a work in which a vertically aligned ultralong (PZT) nanofibers based high output PENG was fabricated using electrospinning technique (Figure 2.8 (i, k)) [211]. This integrated PZT nanofiber-based NG measured maximum output voltage of 209 V, showing much higher values compared to the past record and also produced maximum current of 53  $\mu\text{A}$  with current density of 23.5  $\mu\text{A}/\text{cm}^2$ . The PENG also powered commercial LEDs straight away without energy storage which provide an effective progress in self-powered device development program.

### **2.8.3 Composite Materials-Based PENG**

Lead zirconate titanate (PZT) is well known for its excellent piezoelectric properties and the nanogenerators based on PZT achieved a great success in the self-powered energy harvesting technique. But however, due to the toxicity of lead and its compounds, general awareness is essential for the sustainable development of eco-friendly lead-free materials as asserted from the legislation approved by the European Union in this effect [212–213].

Researcher approved several kinds of materials as a potentially attractive alternatives of PZTs for specific applications. Basically, the lead-free systems include: perovskite materials such as BaTiO<sub>3</sub> (BT), BNT, NaTaO<sub>3</sub>, KNbO<sub>3</sub> etc., and non-perovskites materials such as bismuth layer-structured ferroelectrics (BLSF), tungsten-bronze type ferroelectrics, etc [214–218].

Now, Composite material-based PENGs composed of mainly nano-materials with piezoelectric properties dispersed into an elastomeric matrix, provides a promising effect on flexible, large scale energy harvesting applications because of their mechanical robustness and cost effectiveness.

In 2010, Park et al. conducted a study on Nanogenerator based on piezoelectric perovskite lead-free BaTiO<sub>3</sub> thin film. Using radio frequency magnetron sputtering, BaTiO<sub>3</sub> thin films

were deposited on a Pt/Ti/SiO<sub>2</sub>/(100) Si substrate and poled to increase piezoelectric property and then transferred in a flexible substrate (Figure 2.9 a) [219]. The flexible BaTiO<sub>3</sub> PENG generated an output voltage of 1.0 V and essential output current density of 0.19  $\mu\text{A}/\text{cm}^2$  by periodically bending deformation.

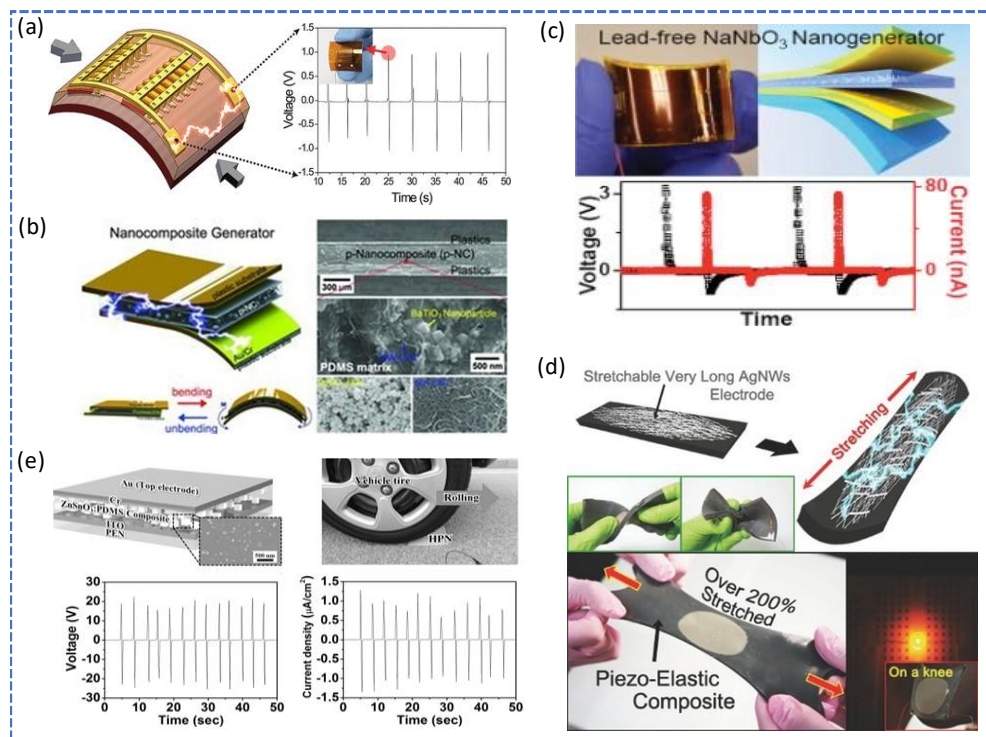
Another approach was reported by Park et al. (2012) in which a simple nanocomposite generator (NCG) was fabricated based on BaTiO<sub>3</sub> nanoparticles and graphitic carbons (i.e., carbon nanotubes and reduced graphene oxide). Now, to produce a piezoelectric composite (p-NG) the two materials (BaTiO<sub>3</sub> nanoparticles and graphitic carbons) were deposited in polydimethylsiloxane (PDMS) by mechanical agitation shown in figure 2.9 (b) [220]. Under the repeated bending and unbending cycles, the piezoelectric NCG device produced an open-circuit voltage ( $V_{oc}$ ) of  $\sim 3.2$  V and a short-circuit current ( $I_{sc}$ ) of 350 nA.

Another lead-free composite material based piezoelectric nanogenerator was fabricated by Jung et al. (2011) using Au/Cr-coated NaNbO<sub>3</sub> nanowire and poly(dimethyl siloxane) (PDMS) polymer composite polymer film (Figure 2.9 (c)) [221]. the fabricated device generated an output voltage of 3.2 V and output current of 72 nA under a compressive strain of 0.23%. Their report suggests that NaNbO<sub>3</sub> nanowires should be an useful alternative of large-scale lead-free PENG applications.

In 2015, A Hyper-Stretchable Elastic-Composite piezoelectric Energy Harvester was demonstrated where a very long Ag nanowires (VAgNWs) were used as stretchable electrodes illustrated in figure 2.9 (d) [222]. In this work, rubber-based piezoelectric elastic composite material was prepared which consists of PMN-PT particles and multiwalled carbon nanotubes (MWCNTs) in a silicone elastomer matrix and the very long nanowire percolation electrodes, consists of the VAgNWs to fabricate the PENG with outstanding energy harvesting performance. This stretchable energy harvester provides over ten times larger stretchability ( $\approx 200\%$ ) and high-power output with voltage of 4 V and current of 500



nA compared to the previous stretchable piezoelectric nanogenerator. This Hyper-Stretchable Elastic-Composite piezoelectric nanogenerator provided wearable energy-harvesting clothes for highly stretchable stockings by converting biomechanical stretching energy to electricity. Another successful work was performed in area of high-performance, flexible piezoelectric nanogenerator by Lee et al. (2014) using combination of piezoelectric single-crystal  $\text{ZnSnO}_3$  nanocubes along with PDMS polymer neglecting electrical poling process (Figure 2.9 (e)) [223]. The reported unique feature of the NG was that it provided large power output under vertical compression only. Due to high unidirectional behaviour, the device provided a large area piezoelectric power generation utilizing vertical mechanical compression such as human walking, moving vehicles, railway transport. Benefiting from its unique features, a large output voltage of about 20 V and an output current density of  $1 \mu\text{A cm}^{-2}$  are successfully accomplished under rolling of a vehicle tire while using a single cell of this PENG.



**Figure 2.9:** (a)  $\text{BaTiO}_3$  thin films were deposited on a Pt/Ti/SiO<sub>2</sub>/(100) Si substrate to fabricate PENG using radio frequency magnetron sputtering. Reproduced with permission [219]. Copyright

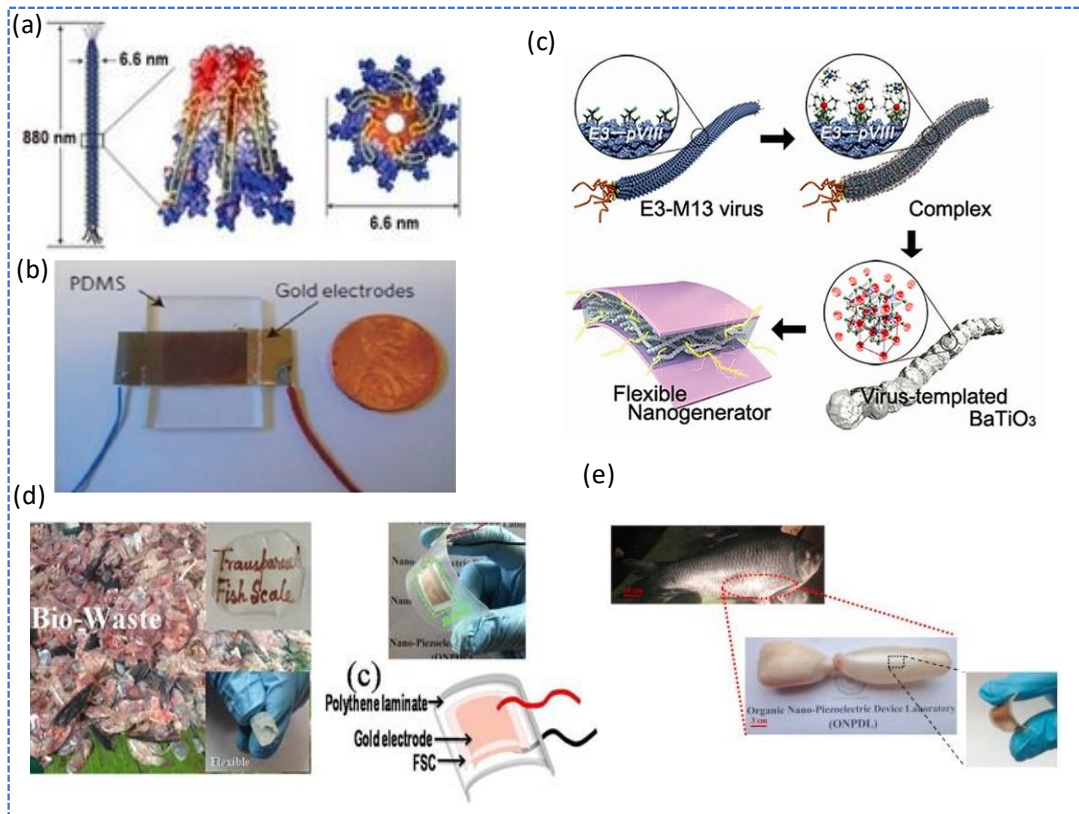
2010, American Chemical Society. (b) a simple nanocomposite generator (NCG) was fabricated based on BaTiO<sub>3</sub> nanoparticles and graphitic carbons (i.e., carbon nanotubes and reduced graphene oxide). Reproduced with permission [220]. Copyright 2012, Wiley-VCH. (c) Lead-free NG based on Au/Cr-coated NaNbO<sub>3</sub> nanowire and poly(dimethyl siloxane) (PDMS) polymer composite polymer film. Reproduced with permission [221]. Copyright 2011, American Chemical Society. (d) A Hyper-Stretchable Elastic-Composite PENG based on PMN-PT particles and multiwalled carbon nanotubes (MWCNTs) in a silicone elastomer matrix and a very long Ag nanowires with outstanding energy harvesting performance. Reproduced with permission [222]. Copyright 2015, Wiley-VCM. (e) structure of piezoelectric single-crystal ZnSnO<sub>3</sub> nanocubes and PDMS polymer composite based hybrid piezoelectric nanogenerator. Reproduced with permission [223]. Copyright 2014, Wiley-VCM.

#### **2.8.4 Bio-materials based PENGs**

Apart from these conventional piezoelectric materials, some living entity like bacteria, virus and natural materials like protein, DNA plays very important role in fabrication of eco-friendly piezoelectric energy harvester because of their biocompatible feature. But due to their low piezoelectric coefficient, they are not so much used for large scale applications. In this regard, Lee and co-worker developed a bio-piezoelectric device utilising liquid-crystalline properties of M13 bacteriophage (phage) as represents in Figure 2.10 (a, b) [224]. To enhance the piezoelectric response, the major coat proteins of the phase was genetically engineered and modulate the dipole strength of the phase. Hence, the virus based thin films exhibited piezoelectric strength up to 7.8 pm V<sup>-1</sup> and fabricated phase-based piezoelectric nanogenerator produces output voltage of 400 mV along with output current of 6 nA which was used to operate a liquid-crystal display. According their studies, phase-based piezoelectric materials essentially delivered a simple sustainable approach to harvest piezoelectric energy.

In this area of bio-piezoelectric nanogenerator, Jeong et al. (2013) proposed an approach, Considering the genetically programmed self-assembly process, an anisotropic BaTiO<sub>3</sub> (BTO) nanocrystals was synthesized on an M13 viral template to fabricated a high performance, flexible piezoelectric nanogenerator (Figure 2.10 (c)) [225]. They reported

that, the virus-enabled flexible nanogenerator provides a high output voltage as 6 V and high current as 300 nA even not using any additional structural stabilizers. Their studies approved bio-templating approach as a superficial method to develop a biocompatible and eco-friendly piezoelectric nanogenerator.



**Figure 2.10:** (a, b) Schematic and optical diagram of Genetically modified bacterial viruses (M13 phages) based bio-piezoelectric device. Reproduced with permission [224]. Copyright 2012, Nature Publishing Group. (c) Schematic diagram of flexible PENG, fabricated using an anisotropic BaTiO<sub>3</sub> (BTO) nanocrystals and an M13 viral template by genetically programmed self-assembly process. Reproduced with permission [225]. Copyright 2013, American Chemical Society. (d) Describe the fabrication of bio-waste fish-scale based flexible bio-piezoelectric nanogenerator. Reproduced with permission [226]. Copyright 2016, American Institute of Physics. (e) Diagram of bio-piezoelectric nanogenerator using fish swim bladder as piezoelectric material. Reproduced with permission [227]. Copyright 2016, Elsevier.

Regarding to the studies on bio-piezoelectric nanogenerator Ghosh et al. describes a different approach using bio-waste transparent fish scale (FSC) as piezoelectric material to fabricate energy harvesting device shown in figure 2.10 (d) [226]. Due to its self-assembled and ordered collagen nano-fibrils structure, the fish scale acted as a self-poled piezoelectric component with intrinsic piezoelectric strength of 5.0 pC/N which generated output voltage and short circuit current of 4 V and 1.5  $\mu$ A respectively and corresponding maximum output power density of 1.14 IW/cm<sup>2</sup> using continuous compressive normal stress of 0.17 MPa. The same group conducted another studies based on fish swim bladder (FSB) consisted with piezoelectric well-aligned natural collagen nano-fibrils (Figure 2.10 (e)) [227]. The fish swim bladder film based piezoelectric nanogenerator exhibits a high output voltage about 10 V and current about 51 nA and this generated electricity instantly illuminated 50 commercial blue light emitting diodes (LEDs). Their studies provide a sustainable and eco-friendly power source in portable electric devices sincerely neglecting bulky battery counterpart.

### **2.8.5 Disadvantage and solution**

To control pollution and energy deficiency the world needs sustainable energy source, one of them belongs to piezoelectric energy harvester. However, the energy harvesting performance relates to different condition and circumstances such as ambient environment, materials properties etc. Piezoelectric energy harvesting behaviour is directly coincide with piezoelectric coefficient but applied stress or strain also provide an important factor. Hence the coupling between the mechanical energy source and the piezoelectric material plays an important role in ascertaining the energy harvesting performance. Another important feature that effects the energy harvesting performance most is the elasticity of the material i.e., how effectively the material could be sustained under an applied force or how smoothly and repeatedly endure a recoverable strain. Now, another dominating factor affects the applicability of piezoelectric material as an energy harvester is the bio-compatibility,

sustainability and eco-friendly nature of the material. Mainly, the strategies where inorganic materials are used to fabricate high-performance energy harvester rely on the methods obtained from the semiconductor industry and mostly, they are lead-based materials which are not bio/eco-compatible options for human society and bio-medical applications.

In this circumstance, polymer based organic piezoelectric materials such as PVDF or its similar copolymers with the highest dielectric constant are effectively used for piezoelectric energy harvesting applications with their adequate mechanical strength, high flexibility, ease of processing and along with high chemical resistance. Owing these characteristics, the PVDF based piezoelectric nanogenerator provides large applicability not only in energy harvesting but also in implantable sensing systems.

#### **2.8.6 PVDF based PENGs:**

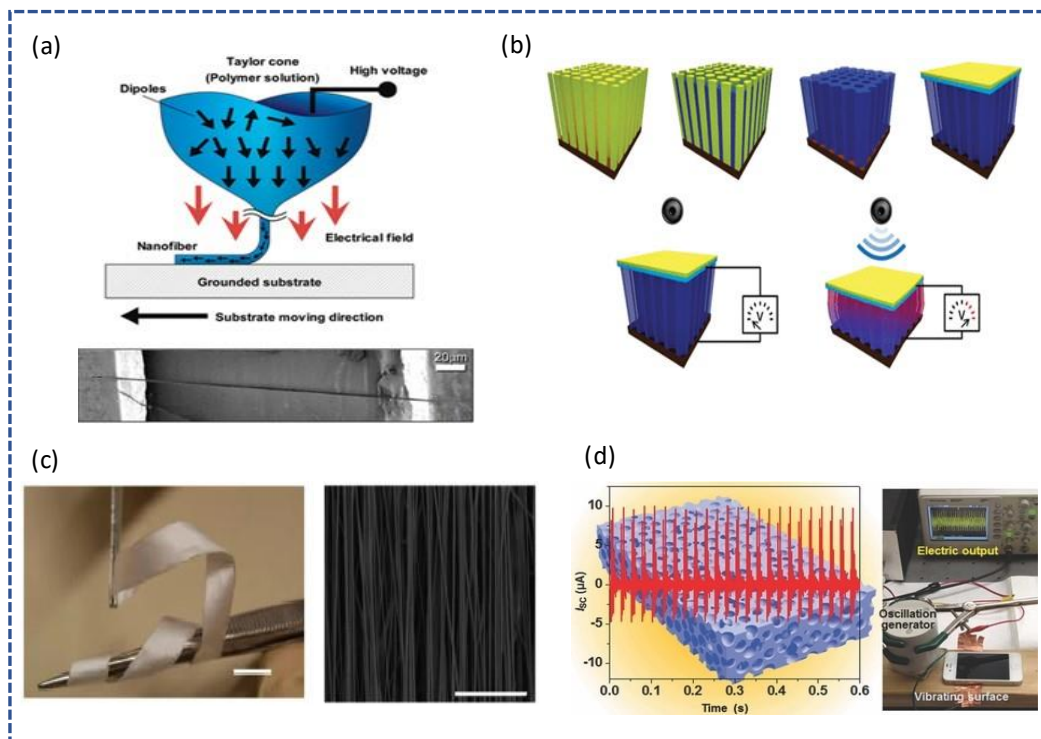
Many strategies have been reported for fabricating PVDF based flexible piezoelectric nanogenerator. In this regard, in 2010 Chang et al. proposed an idea of fabrication of piezoelectric nanogenerator based on poly(vinylidene fluoride) (PVDF) nanofibers. They used near-field electrospinning (NFES) technique to produce piezoelectric PVDF nanofibers on working substrates utilizing mechanical stretching and electrical poling process (Figure 2.11 (a)) [228]. Electrospinning technique provides strong electric field ( $> 10^7$  V/m) and stretching forces which naturally align dipoles in the nanofiber crystal and the nonpolar  $\alpha$ -phase is transformed into polar  $\beta$ -phase which derives the polarity of the electrospun nanofiber. Therefore, the output electrical response of a single PVDF based piezoelectric device was 5-30 mV of voltage and 0.5-3 nA current under stretched and released repeatedly. Another study was performed by Cha et al. (2011) in which they fabricated a porous PVDF nanostructure based piezoelectric nanogenerator by lithography free, template accommodate preparation method. They prepared nano-porous PVDF films utilising ZnO nanowires as a template exhibiting an efficient conversion of Sonic Wave driven mechanical oscillations to

electricity, shown in Figure 2.11 (b) [229]. This PVDF piezoelectric nanogenerator effectively generated rectified power density of  $0.17 \text{ mW/cm}^3$  and output current enhanced to be 5.2 times and 6 times comparable from bulk PVDF nanogenerator.

To take a further study, Persano et al. prepared flexible, free-standing sheets of highly aligned P(VDF-TrFe) nanofibers using electrospinning onto a fast-rotating collector, represents in Figure 2.11 (c) [230]. The mechanical robust material handed easily without fraction produced current up to 40 nA and output voltage about 1.5 V and also offered high sensitivity for identifying pressure, although at exceptionally small values (0.1 Pa).

To overcome the drawbacks of previous studies, Chen et al. (2015) fabricated a self-connected, vertically integrated P(VDF-TrFE) nanogenerator using electrohydrodynamic (EHD) pulling technology, with a molecular poling orientation [231]. The as-prepared P(VDF-TrFE) based PENG exhibited an output voltage of 4 V and a current of  $2.6 \mu\text{A}$  indicating that the piezoelectric voltage was enhanced to 5.4 times compare to the bulk film. The device was successfully utilised to power a seven-segment indicator large-scale LCDs and also multi-coloured LEDs. The reported study not only employed a technique for fabricating 3D piezoelectric polymers but also open a new era of self-connected piezoelectric nanogenerator for self-powered electronics.

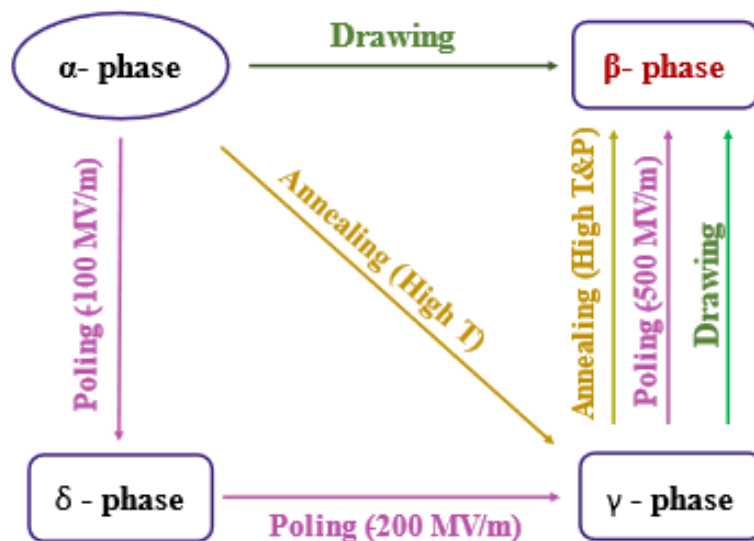
Now to increase the effectiveness of PVDF based piezoelectric nanogenerator Mao et al. (2014) demonstrated a sponge-Like mesoporous piezoelectric PVDF thin film based nanogenerator where film was prepared upon a flat surface by casting a mixture of PVDF solution and ZnO nanoparticles (Figure 2.11 (d)) [232]. The mesoporous PVDF piezoelectric nanogenerator with dimensions  $2 \text{ cm} \times 1 \text{ cm}$  capable of produce average peak voltage up to 11 V and current up to  $9.8 \mu\text{A}$ .



**Figure 2.11:** (a) Schematic and SEM image of piezoelectric nanogenerator based on poly(vinylidene fluoride) (PVDF) nanofibers using near-field electrospinning (NFES) technique with electrical poling process. Reproduced with permission [228]. Copyright 2010, American Chemical Society. (b) Schematic diagram of nanoporous PVDF films using ZnO nanowire as template-based PENG exhibiting an efficient conversion of Sonic Wave driven mechanical oscillations to electricity. Reproduced with permission [229]. Copyright 2011, American Chemical Society. (c) Photograph and SEM image of free-standing sheets of highly aligned P(VDF-TrFe) nanofibers using electrospinning onto a fast-rotating collector. Reproduced with permission [230]. Copyright 2013, Nature Publishing Group. (d) Structure of sponge-like mesoporous PVDF thin film based piezoelectric nanogenerator. Reproduced with permission [232]. Copyright 2014, Wiley-VCM.

### 2.8.7 Limitations:

Polymer-based piezoelectric nanogenerators provide promising effect in multi-functional applications along with high output power generation but need electrical poling. The main drawback of this type of nanogenerator is that it demands additional electrical poling to achieve good performance which requires mechanical stretching process to align the dipoles of the polar electroactive  $\beta$ -phase of PVDF structures. Figure 2.7 shows different traditional schemes to accomplish electro-active  $\beta$ -phase in PVDF. The electric poling process of PVDF needs electric field in the order of 200 MV/m and corresponding temperature around 100 °C to convert non-polar  $\alpha$ -phase to polar  $\beta$ - and  $\gamma$ -phase.



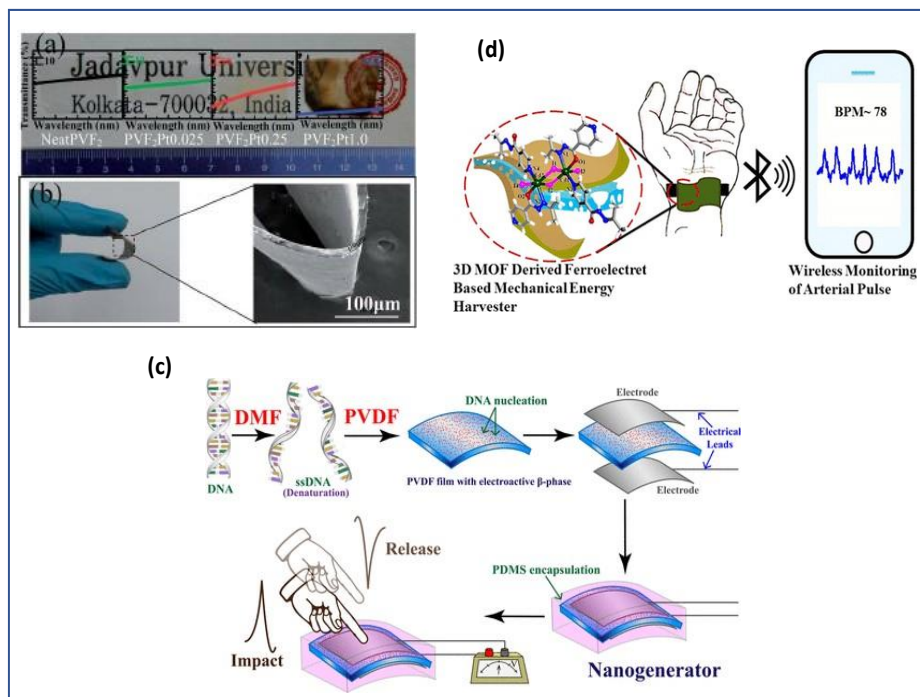
**Figure 2.12:** Different phase transformation process of PVDF

In the other hand, to originate electro-phase the PVDF films were stretched to an extend which develops irregularities, lack of flexibility and sometimes defects the material that may affect the properties of the material [233]



Till to date, many approaches were reported to fabricate piezoelectric nanogenerator without electrical poling in which some external entities were incorporated within PVDF to nucleate electroactive  $\beta$ -phase.

Ghosh et al. (2014) prepared platinum nanoparticles incorporated PVDF film without electrical poling where Pt-NPs promotes the electroactive phase transformations in PVDF which is further used in energy harvester (depicted in figure 2.13 (a) (b)) [234]. Condensed nanostructured DNA based self-poled  $\beta$ -phase containing PVDF film was prepared by Tamang et al. (2015) which was further used to fabricate piezoelectric nanogenerator provides instantaneous output power density of  $11.5 \mu\text{W}/\text{cm}^2$ , used in portable electronic devices (Figure 2.13 (c)) [235]. Another studies were performed by Singha et al. (2020) developed a three dimensional MOF-derived PVDF composite ferroelectret film-assisted mechanical energy harvester (MEH), generated power density of  $32 \mu\text{W}/\text{cm}^2$  that used for self-powered Remote Healthcare Monitoring Approach (Figure 2.13 (d)) [236].



**Figure 2.13:** (a), (b) represents digital photograph of Neat PVDF and Pt-NPs doped PVDF films, (b) digital photograph (left panel) represents good flexible feature of Pt-NPs doped PVDF film and FE-SEM image (right panel) of the film. Reproduced with permission [233]. Copyright 2014, The Royal Society of Chemistry. (c) Schematic diagram of fabrication of DNA assisted PVDF film based piezoelectric nanogenerator. Reproduced with permission [234]. Copyright 2015, American Chemical Society. (d) Schematic diagram of MOF-derived PVDF composite ferroelectret film-assisted mechanical energy harvester (MEH). Reproduced with permission [235]. Copyright 2020, American Chemical Society.

Therefore, these reviews introduced the state of the art of research on the recovery of environmental pollution created by heavy metals and extreme burning of fossil fuels and various approaches to controlling the energy crisis. We find a way of removing heavy metals using eco-friendly biomaterials and trying to enhance their activity. These studies have prepared the field of research on self-powered piezoelectric energy harvesters and their various scope of applications in the range from powering consumer electronics to sensors in bio-medical systems. However, we receive an opportunity to improve the performance of the piezoelectric nanogenerator by using different kinds of biocompatible materials and introducing them to various scientific fields of applications.

## Aims & Objectives

In the context of present scenario, we have idealised some noble eco-friendly approaches in order to overcome the long-standing problems includes critical environmental pollution and serious energy crisis.

- Isolation, purification & characterisation of thermophilic bacterial (MDH1 & BKH2) protein.

### **Aimed to remove heavy metal pollutants**

- Use MDH1 bacterial protein in the removal of lead contamination from aqueous solution.
- Utilized as-formed nanoplates in photocatalytic activity to remove MO, BB dye contamination.
- Study the non-toxicity of lead-free supernatant solution over the growth of *E. coli* bacterium.

### **Aimed to recover energy crisis and fossil fuel originated pollution using renewable energy harvester**

- Use BKH2 bacterial protein with organic polymer PVDF in fabrication of self-poled bio-organic and highly biocompatible porous films.
- Design and developed the Protein-PVDF film based self-powered, flexible piezoelectric nanogenerator
- Study biocompatibility nature of the films and nanogenerator over the growth of *E. coli* bacterium and MTT assay with WI 38 cell.
- Apply the piezoelectric nanogenerator as energy harvester to power consumer electronics.
- Implement the bio-organic self-powered device towards clinical applications of real-time healthcare monitoring from subtle pulse pressure waveform detection to vibrotactile information collection.

Chapter 3  
**Materials and Methods**

In this session, the studies introduced the materials and the methods that were utilized in heavy metal removal process as well as bio-organic piezoelectric nanogenerator fabrication. At first, the study briefly described the method to culture thermophilic bacteria and the purification technique of bacterial protein samples. Next, the chapter reveals the technique of lead contamination removal and dye degradation technique and describes the bacterial protein-based PVDF nano-fiber preparation method using the electro-spinning technique which can be used as a bio-filter for heavy metal filtration from contaminated water. Then, the chapter focus on the purified protein-based electroactive film preparation and bio-organic piezoelectric nanogenerator fabrication technique.

The experimental work related to Bacteria culture, purified protein sample preparation, and heavy metal removal was performed in the Biophysics laboratory, department of Physics, Jadavpur University. The experimental studies of bio-organic Piezoelectric nanogenerators were delivered in the ONPDL department of Physics, Jadavpur University. Characterization of the samples was performed in the different instrumental facilities of the department of Physics, Jadavpur University. Some important characterizations were conducted at IIT Kharagpur and the Institute of Nanoscience and Technology (INST), Mohali, India.

Materials like Ferric chloride, Sodium di-hydrogen phosphate, Potassium chloride, Sodium chloride, Yeast Extract, and Peptone were purchased from Sigma-Aldrich, USA. Tris Buffer, Sephadex G-100, and Lead nitrate were also purchased from Sigma-Aldrich, USA. Methyl Orange (MO) and Bromophenol blue (BB) dye were purchased from Merck, Germany. Millipore deionized water was used in this study. PVDF (Sigma-Aldrich, USA, Mw= 275,000) in N, N-dimethyl formamide (DMF, Merck, India). Silver Paste from Sigma-Aldrich, USA and Polydimethylsiloxane (PDMS) (Sylgard 184, Dow Corning Corp., USA).

### **3.1. Bacterial purified protein sample preparation**

At the beginning of the experimental procedure, it is very important to describe the detailed description of the bacterial strain used for these studies. In our studies, we used two non-pathogenic hot spring bacteria; BKH2 collected from Bakreshwar of Birbhum district hot spring and another MDH1 collected from Metaldanga of Birbhum district, West Bengal, India [8–9]. The major examination of these two bacteria was performed by our senior lab fellows and I mainly focussed on the applications of these bacteria and their extracellular protein in energy harvesting systems and heavy metal removal processes. These two bacteria are features as gram-negative, non-pathogenic, and facultative anaerobic and also both the bacteria grow well in the same culture media but at two different temperature 65°C (for BKH2) and 42°C (for MDH1).

#### **3.1.1. Study of BKH2 and MDH1 Bacterium**

##### ***3.1.1.1. Source***

Different types of hot springs with different temperatures are located at Bakreshwar in Birbhum district, West Bengal, India, which belong to different non-pathogenic bacterial species. The temperature of hot springs varies from 35° C to 72.5° C and discharges differ from 90 lpm to 480 lpm. One of the hot springs situated at Bakreshwar (latitude 23.8800° N and longitude 87.3700° E) has a temperature of 65° C and another situated at Metal Danga (24.0763° N, 87.7099° E) has temperature 42° C of Birbhum district, West Bengal. The thermal water of the two hot springs is alkaline (pH 9.0 at Bakreshwar and pH 8.0 at Metaldanga) in nature, and contains low to moderate HCO<sub>3</sub>, SO<sub>4</sub>, and Sodium. Bakreshwar thermal water contains high Sodium (Na) (with a range of 30-100 ppm) and lower Calcium (Ca), Silica (SiO<sub>2</sub>), and Magnesium (Mg).

### ***3.1.1.2. Sample Collection***

Both the bacterium was collected from our Biophysics laboratory stock where they are cultured and maintained in a proper procedure. Two novel bacterial strains were properly identified and separated from the mixed population of bacterial strains through serial dilution technique from the soil of Bakreshwar and Meatal Danga hot springs having a temperature of 65° C and 42° C respectively. They were inoculated in the semi-synthetic medium as specified by previous studies conducted by lab seniors, growing the bacteria at a specified temperature under anaerobic conditions. Pure culture of the strains one named BKH2 (grown at 65° C) and another as MDH1 (grown at 42° C) was developed along with identification of the strains was performed by analysing the 16 S-rRNA gene sequences.

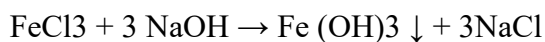
### ***3.1.1.3. Growth Medium for Hot Spring Bacteria (BKH2 And MDH1)***

These isolated bacteria need proper growth and maintenance such that we can utilize them for our further studies. Therefore, a specific semi-synthetic media was prepared which acceptably preserved the bacterial population in the growth medium. Most of the hot spring bacteria hold some unique necessity of oxidizing agent. In the process of bacterial culture media, two different media solutions were prepared named Media 1 and Media 2 and the final medium was prepared by mixing them in 1:9 ratios by fixing pH at 8.0 [16].

#### **Composition of Media 1:**

Medium 1 comprise with 0.1 M Ferric chloride ( $\text{FeCl}_3$ ) solution. Firstly, 100 ml of  $\text{FeCl}_3$  (0.1 M) solution was prepared by dissolving the  $\text{FeCl}_3$  reagent into sterile deionized water and keeping the pH of the solution at 8.0 by adding 5(N) NaOH and 6(N) HCL (if required). Clear precipitation of ferric hydroxide [ $\text{Fe}(\text{OH})_3$ ] was formed that was collected through a centrifugation process at 5000 x g for 10 minutes and the precipitate sample needed to wash two or more times by sterile deionized water to remove chloride ions ( $\text{Cl}^-$ ). Finally, the

required precipitate was then again dissolved in sterile deionized water and adjusted the volume to 100 ml.



Medium 1 holds iron in + III state as FeO(OH)

### **Composition of Medium 2:**

The materials used in the preparation of the bacterial Medium 2 are Sodium di-hydrogen phosphate: 0.6 g/litre, Sodium carbonate: 2.5 g/litre, Potassium chloride: 0.33 g/litre, Peptone: 0.5% (5.0 g/litre), Yeast extract: 0.02% (200 mg/litre). These required materials were dissolved properly in sterile deionized water and ready to use as Medium 2. After that, the two semi-synthetic media (medium1 and medium 2) were mixed properly in the ratio of 1:9 to obtain the final bacterial culture medium. The final semi-synthetic medium was then filtered to eliminate other extra precipitates and the final pH of the growth culture medium was stabled at 8.0 by adding 6(N) HCL.

### **Growth condition:**

Being anaerobic, both the bacterium was cultured in properly sealed gas-pressure vials each containing 40 ml of growth medium. Before incubation with bacteria, the extra air content in the sealed bottle was totally replaced by carbon dioxide gas (CO<sub>2</sub>) treated by a syringe-needle system. Initially, the inoculum (1%) of the previous mother culture was added to the newly prepared semi-synthetic medium for the expected growth of the bacterial population. The inoculated final bacterial cultures were incubated at 65°C for BKH2 and 42° C for MDH1 for 6 to 8 days.



#### ***3.1.1.4. The BKH2 Bacterium***

The novel anaerobic, non-pathogenic BKH2 bacterium, cultured at 65° C, shows gram-negative and rod-shaped featured in morphological analysis. They are characterized as 2–3 mm long and 0.6–0.7 mm width rods shaped by HRTEM analysis. To confirm the authenticity of the strain, the bacteria were processed for 16S with primers used for 16S-rRNA amplification. According to the analysis of NCBI BLAST, the partial 16S-rRNA gene sequence (961 nucleotides) of the isolated bacterium revealed that they belong to the ‘Burkholderiaceae’ family and contains 97% identity to the bacterium ‘Cupriavidus metallidurans’ [18]. The phylogenetic tree was also prepared depending on the BLAST results. The bacterium was named BKH2 with GenBank accession no.: KP231522 and submitted to NCBI.

#### ***3.1.1.5. The MDH1 Bacterium***

Another novel bacterium named MDH1 was found to grow well at 42 °C, identified as facultative anaerobic, gram-negative and non-pathogenic. Scanning electron microscope (SEM) images confirmed their coccoid shape with a diameter of 2-3 nm. The separated MDH1 bacterial strain was associated with “Pseudomonadaceae” family and 99% similarities with *Pseudomonas putida* H8234 [19], as per the Phylogenetic analysis of the partial 16 S-rRNA gene sequence of the bacterium (1421 nucleotides; GenBank accession number KT600031).

### **3.1.2. Isolation and purification of bacterial Protein**

This thermophilic bacterium (BKH2 and MDH1) secretes some extracellular proteins in its growth medium. These proteins are the biomaterial of interest for conducting the studies. But there are some impurities in bacterial growth media mixed with proteins that may be

hampered by the further experimental reactions that's why it needs to purify the protein mixture.

### ***3.1.2.1 Isolation of Crude Protein from Bacterial Growth Medium***

To separate crude protein from culture media, the well-grown bacteria cultures of 5-6 days old BKH2 and MDH1 were centrifuged at 5000 x g for 15 minutes using Eltek Centrifugation Machine (TC 4100D). The precipitated bacterial cells were collected in a fresh container and stored at -80° C freezer for further requirement and the supernatant which contained crude proteins of BKH2 and MDH1 bacterium. The protein was dried as dust form using a Lyophilizer Machine (EYELA FDU-1200, Japan). Now the dust crude proteins of the bacterium were ready for purification process.

### ***3.1.2.2 Purification of Crude Protein***

The double step column chromatography technique was used to get sufficient purified protein and, in this study, Sephadex G-100 gel filtration column (100 cm x 1 cm) was employed to separated protein from impurities [10]. Column Chromatography introduces as a technique which is utilise to separate substances that are applied into the column packed with an adsorbent and depending on the affinity for the adsorbent the substance passes through the well packed column at variant rate after then collected in fraction solution at different times. Easily, it is described as solid-liquid technique where two phases, stationary phase introduces as solid and mobile phase is liquid. Same like in Sephadex G-100 gel filtration column, Sephadex G-100 used as stationary phase and 5 mM Tris-HCL buffer with pH 8.0 as mobile phase. Next, each BKH2 and MDH1 crude proteins (50 µg) were carefully loaded into the Sephadex G-100 column remained pre-equilibrated with Tris-HCL buffer. Proteins were properly eluted through the filtration column at a definite flow rate of 12 ml/h and each solution fraction contained 1 ml solution were collected using Fraction Collector (Eyela DC-1000). The purification technique was conducted twice to acquire proper highly purified

protein of interest. After the double step purification, the solution fractions containing the purified from of each sample were identified by measuring their optical density against fraction at 280 nm using Elico SL-196 UV-Visible Spectrophotometer. Then the eluted purified proteins were again concentrated as dust form through lyophilization. In this way the purified proteins dust sample of each bacterium were prepared and stored at -80°C freezer for future work.

### **3.1.3 Purified Protein justification by Lowry Method**

Protein concentration of both the BKH2 and MDH1 bacterium were justified by Lowry Method [237]. The Lowry protein assay is considered as a biochemical assay which determine the total concentration of protein in a protein mixed solution.

#### **Chemical required:**

The reagent needed for this experiment was categorised as: Reagent A with 2% NaCO<sub>3</sub> in 0.1 N NaOH, Reagent B with 0.5 % CuSO<sub>4</sub>, 5 H<sub>2</sub>O in 1% NaK-Tartarate, Reagent C as Reagent A and Reagent B in 50:1 ratio, Reagent D as Reagent C without NaOH, Reagent E as Folin reagent: Distilled water in 1:2 ratios. Now, the BSA solution was prepared by dissolving 1 mg of BSA (Bovine serum albumin) in 1ml of double distilled water. BKH2 and MDH1 protein was used as sample of interest.

#### **Procedure:**

At the starting of the experiment, different amount of BSA solution as 0 ml (0 µg), 0.005 ml (5 µg), 0.01 ml (10 µg), 0.02 ml (20 µg), 0.05 ml (50 µg), 0.1 ml (100 µg) were taken in series of clean test tubes. Then 1 ml of prepared Reagent C was added to the BSA solutions and allowed to remain for 10 minutes at ambient temperature.

After the required time 0.1 ml of prepared Reagent E was mixed with each solution and adjust the volume of each solution at 1 ml with distilled water. All prepared reagent mixed properly and rapidly and safely kept at room temperature for almost 30 mins. Elico SL-196

UV-Visible Spectrophotometer with 660 nm wavelength was used to measure the BSA protein concentration and based on the spectrometric data a standard BSA protein curve was prepared. After that 0.01 ml, 0.02 ml, 0.03 ml, 0.04 ml, 0.05 ml, 0.06 ml, 0.07 ml of purified BKH2 and MDH1 bacterium protein were taken in series of clean test tubes and previous experiment was conducted as described in the above procedure. Now using Spectrophotometry, the optical density of the final protein solution was measured also at 660 nm and the exact concentration of each protein was calculated using BSA standard curve and averaged all the data to get the final protein concentration.

These two thermophilic bacterial (MDH1 & BKH2) purified proteins was implemented towards lead contamination removal and bio-organic piezoelectric film fabrication process.

### **3.1.4 Sodium Dodecyl Sulfate-Polyacrylamide Gel Electrophoresis (SDS-PAGE)**

#### **technique:**

SDS-PAGE is an analytical method, developed to isolate components of a protein mixture based on their size. The proteins are denatured using SDS and then the negatively charged protein were loaded onto a gel and placed in an electric field. After applying a particular voltage, it will move towards the anode and be separated by a molecular sieving effect based on size. Due to their different size, each biomolecule moves differently through the gel matrix: smaller biomolecules move farther down the gel, while larger molecules remain closer to the point of origin. Biomolecules may therefore be separated roughly according to size, which depends mainly on molecular weight under denaturing conditions, but also depends on higher-order conformation under native conditions. After the visualization by a staining technique, the size of a protein can be calculated by comparing its migration distance with that of a known molecular weight ladder (marker).

**Procedure:**

The SDS-PAGE technique was conducted using 12 % acrylamide gel at a constant voltage of 100 volts. Protein samples were boiled in a buffer containing a reducing agent for 3 mins. The whole solution along with the Sigma protein molecular marker was then loaded onto 12 % gel. After the pre-requisite time span, molecular masses of different protein bands were properly stained with Coomassie brilliant blue R-250 which was followed by a de-staining procedure to visualize the particular band.

**3.2 Lead contamination removal**

A green sustainable technique was developed for the removal of lead contamination from environment where biomaterials were used as lead removing agent. The purified thermophilic bacterial (MDH1) protein was introduced into the toxic, nondegradable lead-compound solution with motive to remove lead from the solution and conducted some characterization technique. Here, Lead nitrate (purchased from Sigma-Aldrich, USA) aqueous solution was used, Methyl Orange (MO) and Bromophenol blue (BB) dye were used in dye degradation activity. Millipore deionized water was used in this study. *E. coli* bacterium was collected from laboratory stock culture which was utilized for toxicity measurement.

**3.2.1 lead removal from lead nitrate solution**

About 100 µg bacterial (MDH1) protein powder was added to 100 ml lead nitrate precursor solution [0.6 M Pb(NO<sub>3</sub>)<sub>2</sub>] and kept at ambient temperature (37°C) for 24 hours. A white precipitation was formed which was collected through centrifugation at 4000 g using Eltek centrifugation machine (TC 4100D). The supernatant was separated through filtration (Whatman filter paper, Pore size 11 µm) and the precipitated sample was dried at room temperature to get the powder form for morphological and other experimental studies. The supernatant was stored for further analysis.

### **3.2.2 Identification of lead oxide precipitate**

Inductively coupled plasma - optical emission spectrometry (ICP-OES Optima 2100 DV, Perkin-Elmer) was used to confirm lead elimination from the reaction solution. The morphological characterization of the precipitate was done by Field Emission Scanning Electron Microscope (FESEM, FEI, INSPECT F50, US) as well as by Transmission Electron Microscope (JEOL JEM 2100F, US). Energy Dispersive Spectrometer (EDX) analysis was performed for elementary detection of the nanoplates sample. The crystallographic properties of lead precipitate were studied by using X-ray diffraction (XRD) measured by X-ray diffractometer (Bruker, D8 Advance) with  $\text{CuK}\alpha$  radiation ( $\lambda = 1.54 \text{ \AA}$ ) operated at 40 kV voltage and 40 mA current. Fourier Transform Infrared Spectroscopy (FTIR) spectroscopy in Attenuated Total Reflection (A529-P/ QMIRacle-ATR-unit, Bruker, Germany) mode with 4  $\text{cm}^{-1}$  spectral resolution was employed to identify the functional groups present in the lead precipitate.

### **3.2.3 Toxicity study of the supernatant on bacterial growth**

The supernatant of the reaction solution was separated from precipitate through centrifugation followed by filtration through Whatman filter paper (pore size 11  $\mu\text{m}$ ). The toxic nature of the lead ions and the supernatant were studied by observing the zone of inhibition on *E. coli* (JM101) bacterial growth in Luria-Broth (LB) agar plate. LB medium containing agar (1.5%) was poured into Petri disc and allowed to get solidified. 100  $\mu\text{l}$  of pre-grown *E. coli* culture was spread on the agar plate and left at room temperature for at least 15 min. Three exactly identical wells were made on the agar plate using the cork borer under sterilized condition. One well was filled with 50  $\mu\text{l}$  of 0.6 M  $\text{Pb}(\text{NO}_3)_2$  solution and the rest of two wells were filled with different volumes of supernatant (20  $\mu\text{l}$  and 50  $\mu\text{l}$ ). The Petri agar plate was kept for incubation at 37°C for 24 h. After the stipulated time period, the zone of inhibition produced at the well was observed and photographed.

### 3.2.4. Photo-Catalytic activity of lead oxide

The photo catalytic activity of the lead oxide nanoplates was demonstrated by degrading hazardous dyes like Methyl Orange (MO) and Bromophenol Blue (BB). At first, 50 mg of each dye was added to 1 L of distilled water and used as stock solution. After that, 10 mg of powdered lead precipitate was added to 100 ml of each dye solution and mixed on magnetic stirrer for 15 minutes. 3 ml of the mixed solution was used to evaluate the catalytic degradation of each dye by measuring the corresponding absorbance spectrum of those dyes (300 - 700 nm) at different time intervals in UV-Visible Spectrophotometer (ELICO, SL 210). Degradation percentage of MB and BB dye in presence of lead oxide nanoplates was calculated through the formula:

$$\% \text{ of Degradation} = \frac{(C_0 - C)}{C_0} \times 100 \quad (1)$$

where  $C_0$  is the initial concentration of dye solution and  $C$  is the concentration of dye solution in presence of lead oxide nanoplates in different time intervals.

Further, some primary work was conducted to prepare a membrane based on bacterial (MDH1) protein to remove lead contamination from aqueous solution. In this regard, electrospun nanofiber membranes have attracted a favourable attention due to their high specific surface area, high porosity with small-sized pores, among other characteristics.

### 3.2.5 Preparation of electrospun nano-fiber

In order to fabricate bacterial protein based PVDF nano-fiber, the PVDF pellets were dissolved in 3:2 volume ratio of DMF and acetone respectively with solvent concentration of 12 % w/v. Then purified bacterial (MDH1) protein was added properly to the DMF/acetone solution and left in magnetic stirrer for proper mixing. Electrospinning performance was conducted by placing 10 ml of the protein-DMF/acetone solution within 15 ml plastic syringe (DISPOVAN) tipped with a 22 G stainless steel needle. The electric field was applied across

the metal tip and collector of  $0.6 \text{ kVm}^{-1}$  and the solution were injected through the syringe at a constant rate of  $1.2 \text{ ml h}^{-1}$ . The produced nano-fiber mat was collected onto the *aluminium* foil which was utilized to cover the collector. Now, the as-prepared protein based electrospun nano-fiber was characterized by morphologically using FESEM.

### **3.3 Bio-organic film preparation and Bio-Piezoelectric Nanogenerator fabrication using bacterial protein**

Herein, this chapter evolves Purified BKH2 Bacterial Protein as a representative of piezoelectric biomaterial along with semi-crystalline polymer PVDF in bio-organic Piezoelectric nanogenerator fabrication process. The thermophilic bacterial (BKH2) protein is a high temperature tolerance and is a biopolymer with promising electrical and physical properties, incorporated with PVDF matrix to prepare a free standing flexible porous film contain self-poled  $\beta$ -phase and based on this porous film, a flexible piezoelectric nanogenerator was fabricated. The materials used in the fabrication process of the films and nanogenerators and their valuable effect was also discussed. However, various procedures include biocompatibility investigation of the films and the nanogenerator was briefly discussed over the growth of E. Coli bacterium and WI 38 cells.

#### **3.3.1 Materials and film preparation**

The purified BKH2 bacterial protein [18] with different concentrations were used in bio-organic films preparation experiment where 6 wt% (w/v) PVDF-DMF solution were prepared by dissolving PVDF (Sigma-Aldrich, USA,  $M_w = 275,000$ ) in N, N-dimethyl formamide (DMF, Merck, India). To find the comparative studies three different concentrations of purified bacterial protein (BP) such as 0.25, 0.5 and 1 wt% were added with 10 ml of PVDF-DMF solutions and placed the solutions in magnetic stirrer for proper mixing. In film fabrication process Solution casting procedure is our favourable choice as it provides almost



uniform thin film which is important for nanogenerator fabrication. Therefore, using the solution casting procedure, the films were deposited on clean glass substrates and subsequently dried at 60° C for 6 h. Free-standing, almost uniform and flexible films were prepared with the labelling of “Neat PVDF” where Bacterial Protein was not added and PVDF-BP-0.25, PVDF-BP-0.50, and PVDF-BP-1.0 where 0.25 wt%, 0.50 wt% and 1.0 wt% of purified BP were added into PVDF-DMF solutions respectively. These films were properly collected for further characterization and nanogenerator fabrication.

### **3.3.2 In-vitro biocompatibility study**

Biocompatibility describes a material efficiency to compatible with living organism mainly with human body. Mainly, the term biocompatible reflects how biomaterials and biomaterial material doped organic material interact properly with human body and how those interactions invent the biomaterial-based device in the field of clinical success in the long run [238]. Therefore, biocompatibility studies of the prepared bio-organic films are immensely important to conduct the further development of the films in nanogenerator towards bio-medical fields and energy harvester. To accomplish this requirement, we deliver a pathway for the practical approach towards identification of biocompatibility of as prepared Protein-PVDF films and these films based piezoelectric nanogenerator. There are many methods already developed in biocompatibility confirmation texts, with maintaining similarities we describe some methods and practical tests like - growth of common non-pathogenic *E. coli* bacteria in liquid and solid Luria Broth (LB) media and cell viability test with WI 38 cells in presence of the films and films-based nanogenerators as evidence of super biocompatible nature of the protein-based PVDF films and these films-based bio-organic nanogenerator.

*E. coli* Bacteria has mostly selected bacteria for conducting biocompatibility tests by analysing their growth period. Here, in this study, we analyse the effect of both Neat PVDF and Protein-PVDF films on the growth of *E. coli* bacteria such that we can draw a

comparison study. Therefore, we conducted the study on both LB media and LB agar media in presence of films and performed some characteristic studies like FESEM and Fluorescence Microscopy. Cell survivability study always remain one of the best methods to established biocompatibility feature of materials. Here in this study, we used WI 38 cells which was isolated from lung tissue for biocompatibility identification over Protein-PVDF films and Nanogenerators.

### ***3.3.2.1. Preparation of E. Coli Bacterium Culture Media***

LB is a widely used *E. coli* bacterial culture medium, here Luria-Broth (LB) liquid media (25 ml) was prepared using the standard method in two different conical fluxes in which the same amount of i.e., 10 µl of pre overnight *E. coli* culture was transferred [239]. Then, Neat PVDF and PVDF-BP films were placed into the media and incubated overnight at 37°C under continuous shaking. After 24 h, the films were separated for further study.

Next, Luria-Broth (LB) agar solid media was prepared also using the standard method [239]. In this method, the LB medium containing agar (1.5%) was poured into two Petri discs and allowed to get solidified. Then attached both Neat PVDF and PVDF-BP-0.25 films on the two different agar media plates and 100 µl ( $10^6$  bacterial cell/ml) of pre-grown *E. coli* culture was spread on both the agar plates containing the films and left at room temperature for 15 min. The Petri agar plate was kept for incubation at 37°C for 24 h. after the stipulated time period, the culture plate was collected for proper characterization. The films were separated very slowly from the culture media and prepared for FESEM and Fluorescence Microscopic characterization.

### ***3.3.2.2 Sample Preparation for FESEM And Fluorescence Microscopy Measurement***

The separated both Neat PVDF and Protein-PVDF films from LB liquid and LB agar plates were placed on glass slide for air drying. Then the dried films were employed for FESEM

measurement. And for Fluorescent Microscopy measurement the films were stained by Ethidium Bromide (EtBr) such that a clear image of *E. coli* bacteria can be obtained.

### **3.3.2.3 Biocompatibility Study Using MTT Assay**

MTT assay described cell survivability study in presence of Protein-PVDF film and the device itself. In general, the MTT assay is performed to account cellular metabolic activity as a significant of cell viability, proliferation and cytotoxicity. This colorimetric assay is centred on the reduction of a yellow tetrazolium salt (3-(4,5-dimethylthiazol-2-yl)-2,5-diphenyltetrazolium bromide (MTT) to purple formazan crystals by metabolically active cells.

In this experiment, WI 38 cells were seeded on 35 mm tissue culture plates and next day cells were treated with Neat PVDF, Protein-PVDF film (PVDF-BP) and nanogenerator (NG), overnight. Cells were then washed with 1X PBS twice and further incubated for 4 hours with MTT solution (450 $\mu$ g/ml). MTT solution was discarded and after addition of extraction buffer (Isopropanol, Tween20, HCl), a crystal violet colour was observed. The absorbance of the resulting formazan crystals was measured at 570 nm using a spectrophotometer, and the values were compared with untreated cells.

### **3.3.3 Nanogenerator fabrication**

In order to fabricate the bio-organic piezoelectric nanogenerator, metal-insulator-metal (MIM) structure was used where, conducting carbon films as top and bottom electrodes (of size: 20  $\times$  15 mm) were attached on both sides of the dielectric bio-organic PVDF films. The electrical output leads were joined to each of the carbon electrodes. Finally, the electrode-PVDF electrode stack was encapsulated within Polydimethylsiloxane (PDMS) (Sylgard 184, Dow Corning Corp., USA) based elastomer for enhancing the robustness and to contribute compact structure to the fabricated device. The PDMS was prepared by mixing base and curing agents in the ratio of 10:1 and placing the resulting material in vacuum desiccators to

eliminate air bubbles followed by heating at 60° C for 3 h. The total thickness of the nanogenerator was 200 μm.

### **3.3.4 Nanogenerator performance study**

To study the output performance of nanogenerator, human finger was imparted on the film. The applied axial stress  $\sigma_s$  by repeated finger tapping on the device surface from different heights can be ascertained depending on the evolved axial strain  $\varepsilon$ , in the Protein-PVDF film from the equation,  $\sigma_s = \frac{V_R}{|g_{33}|L}$  with  $\varepsilon = \frac{\sigma_a}{Y}$ . Where, Y is the young's modulus of the film,  $V_R$  is the rectified output voltage,  $g_{33}$  is the converse piezoelectric coefficient and L is the thickness of the film. A digital storage oscilloscope (Agilent DSO3102A) and pico-ammeter (Keithley 6485) was used to measure the output voltage and current respectively.

## **3.4 Materials and its performance Characterization and instrumental description**

Here, the material characterization of both lead oxide nanoplates and bio-organic film along with nanogenerator performance characterization was discussed along with instrument descriptions. The detail surface morphological studies of lead oxide nanoplates and films were performed by Field Emission Scanning Electron Microscopy (FESEM, FEI, INSPECT F50) and under the acceleration voltage of 10 kV. The structural compositions of bacterial protein doped PVDF films and nanoplates were extensively investigated using Fourier transform infrared spectroscopy in Attenuated Total Reflection (A529-P/QMIRacle-ATR-unit (Pike), TENSOR II, Bruker) mode. Inductively Coupled Plasma (ICP-OES Optima 2100 DV, Perkin-Elmer, Canada) and XRD (Bruker, D8 Advance) were used to identify the elemental composition and crystalline structure of nanoplates respectively. Additionally, to study the thermal properties of the bioorganic films, Differential Scanning Calorimeter (DSC) was carried out on a Perkin Elmer, STA-8000 instrument in liquid N<sub>2</sub> environment. Tensile

strength of the films was also measured by a universal testing machine (Tinius Olsen H50KS) at a strain rate of 1 mm/ min. The polarization (P) versus electric field (E) hysteresis loops were obtained from the ferroelectric testing system (P-E, PLC100V, Radiant Technology Precision) connected to a high voltage interface, employing bipolar triangular electric field (E) along the thickness direction at room temperature. The dielectric properties were measured using precision impedance analyzer (Wayne Kerr, 6500B). Finite element method based theoretical simulation was performed using COMSOL multiPhysics software (version 5.5).

In this thesis, the materials characterizations have been done with the following instruments unless and until it is mentioned.

#### **3.4.1 UV-VIS Spectrophotometer**

UV-visible spectroscopy introduces as an absorption or reflectance spectroscopy, performances in ultraviolet and visible regions of the electromagnetic spectrum. UV-Visible spectroscopy refers as an analytical technique that measures the intensity of light that is absorbed by or transmitted through a sample in contrast with a reference sample. This property is influenced by the sample composition and proper concentration which may provide the sample identification.

In this study, the UV-vis absorption spectrum of protein concentration and photocatalytic activity of lead oxide nanoplates were recorded by UV-VIS Spectrophotometer (ELICO, SL 210).

#### **3.4.2 Field emission scanning electron microscopy (FE-SEM)**

Field emission scanning electron microscopy (FE-SEM) is an advanced and essential technology used to capture the micro- or nanostructure image of the materials. FESEM define as an electron microscope that captures the surface images of the sample by scanning it with a high energy beam of electron according to a zig-zag pattern. Electrons are liberated from a

field emission gun that can produce up to 1000x the emission of a tungsten filament. The performance of FESEM needs high vacuum and the emitted secondary and backscattered electrons are utilized for imaging the sample surface. Within the high vacuum chamber, the primary electrons are deflected by the electronic lenses and bombard the objects and then secondary electrons are emitted whose angle and velocity relate to the surface structure of the object. These secondary electrons are captured by the detector and produce an electronic signal which is amplified and transformed into a monitor or a digital image.

In this work, FE-SEM, INSPECT F50 was used to characterize the surface morphology of the protein-PVDF films and lead oxide nanoplates and Energy Dispersive X-ray Spectroscopic (EDS) analysed the chemical components of the sample, recorded with Bruker Nano X-flash detector (410-M) belonging to the FE-SEM chamber.

### **3.4.3 Transmission Electron Microscopy (TEM)**

High-resolution transmission electron microscopy is a powerful technique that conducts the direct imaging of the atomic structure of samples. Besides the other surface morphology and particle size distribution techniques, (like XRD, FESEM) the HRTEM acquires most popular and effective for measuring small particle sizes approximate ranging from small (<2 nm) to large (>20 nm) and possesses good accessibility, direct visibility and ease of use. In HRTEM, an electron gun produces a stream of electrons which is focused using condenser lenses into thin, monochromatic beam which strikes the specimen and transmitted through it and again focused using objective lenses into an image. The intermediate and projector lenses enlarge the image depending on the magnification and the images strikes on phosphor image screen to enable for users.

Here, HRTEM (JEOL JEM 2100F) was used to identified the structure the lead oxide nanoplates.

#### **3.4.4 X-ray diffraction (XRD)**

X-ray diffraction (XRD) is a highly versatile technique that delivers detailed information about the crystallographic structure, physical properties, and chemical composition of a material and useful for stress measurements as well as for texture analysis. This technique is based on the constructive interference of monochromatic X-rays and a crystalline or semi-crystalline sample. In XRD, the produced X-rays are collimated and aimed towards the sample and then interacted with the sample, produces diffracted rays which is then detected, processed, and counted. Therefore, the proper intensity of the diffracted rays scattered at different angles of element is impressed to display a proper diffraction pattern. XRD performs on the principle of Bragg's equation, that explained in terms of the reflection of collimated X-ray beam incidence on a crystal plane of the specimen which is to be characterized.

To identify the degree of crystallinity and the crystallographic features of the nanoplates, x-ray diffraction (XRD) measurements were conducted by using an x-ray diffractometer (Bruker, D8Advance) using CuK $\alpha$  radiation ( $\lambda = 0.15178$  nm).

#### **3.4.5 ICP (Inductively Coupled Plasma) Spectroscopy**

Inductively Coupled Plasma Optical Emission Spectroscopy (ICP-OES) is an analytical technique utilized to measure the exact concentration of certain elements present in a sample. It is a type of emission spectroscopy that employs the inductively coupled plasma to generate excited atoms and ions that emit electromagnetic radiation at wavelength are proportional to the concentrations of the particular element within the sample. In ICP-OES, the source of energy is heat from an argon plasma that works at temperature of 10,000 kelvin.

Here, the lead identification study was conducted using Inductively Coupled Plasma Optical Emission Spectroscopy (ICP-OES Optima 2100 DV, Perkin-Elmer).

### **3.4.6 Fourier transform infrared spectroscopy (FT-IR)**

Fourier Transform Infrared (FTIR) spectroscopy is an analytical methodology that clarifies the structure of individual molecules and the chemical composition of molecular mixtures. FTIR is the most effective approach to understand the molecular structure of material along with the pathways, kinetic and mechanism of chemical reactions. FTIR spectroscopy operates using modulated, mid-infrared energy to interrogate a sample. The infrared light was absorbed by the molecules of the sample at a specific frequency which is directly associated with atom-to-atom vibrational bond energies in the molecule. When the energy of mid-infrared light and the bond energy of the vibration become equivalent then the molecular bond can absorb that energy. Different molecular bonds vibrating with different energies absorb different wavelengths of the IR radiation and the particular intensity and frequency of these individual absorption bands represent the overall spectrum that design the characteristic fingerprint of the molecule. The attenuated total reflection (ATR) is defined as a sampling technique used besides traditional infrared spectroscopy, which eventually qualifies specimen to be observed directly in either solid or liquid state, without additional preparation.

In this study, the crystalline modifications and molecular bonds of the samples were analysed by Fourier transform infrared spectroscopy (FT-IR) (TENSOR II, Bruker). The spectra were recorded in transmission and Attenuated Total Reflection (ATR) (A529-P/ QMIRacle-ATR-unit (Pike), TENSOR II, Bruker) mode under  $4\text{ cm}^{-1}$  spectral resolution and 100 scans.

### **3.4.7 Dielectric and ferroelectric characterizations**

For the electrical characterizations, conducting carbon electrodes on both surfaces of the films were prepared. The relative dielectric constant ( $\epsilon_r$ ) and loss tangent ( $\tan \delta$ ) responses of the films were conducted using a precision impedance analyser (Wayne Kerr, 6500B) as a function of frequency (from 20 Hz–10 MHz). Polarization–electric field (P–E) hysteresis



loops were performed utilizing a standard ferroelectric testing system (P-LC100V, Radiant Technology Precision) connected to a high-voltage source.

### **3.4.8 Piezoelectric characterizations**

The output voltages and current were recorded using a National Instruments (NI) DAQ board (USB 6000) via an online interface with a PC with a sampling rate of  $1000\text{ s}^{-1}$  and a pico ammeter (Keithley 6485) respectively. Sometimes digital storage oscilloscope (Agilent DSO3102A) and digital pico-ammeter (DPA 111) also used for voltage and current measurements respectively. For capacitor charging performance, the output voltage was rectified using a 1N4001 silicon diode. The vertical forces were recorded by a 3-axial force pressure sensor (FlexiForce A201).

Chapter 4

**Results and Discussions**

## **4.1 Removal of Lead Contamination through the Formation of Lead-Nanoplates by a Thermophilic Bacterial Protein**

The hazardous heavy metals contamination provides serious concern for all over the world in terms of their environmental load and health impacts that mixes to the environment by the disposal of untreated or partially treated industrial effluents, heavy metal-containing fertilizers and pesticides used in agricultural fields etc. Among the other heavy metals, lead listed one of the most harmful heavy metal due to its nondegradable nature that causes mental retardation, kidney disease and also damage our nervous system, mainly pregnant women and young children are more susceptible to lead toxicity [240–241].

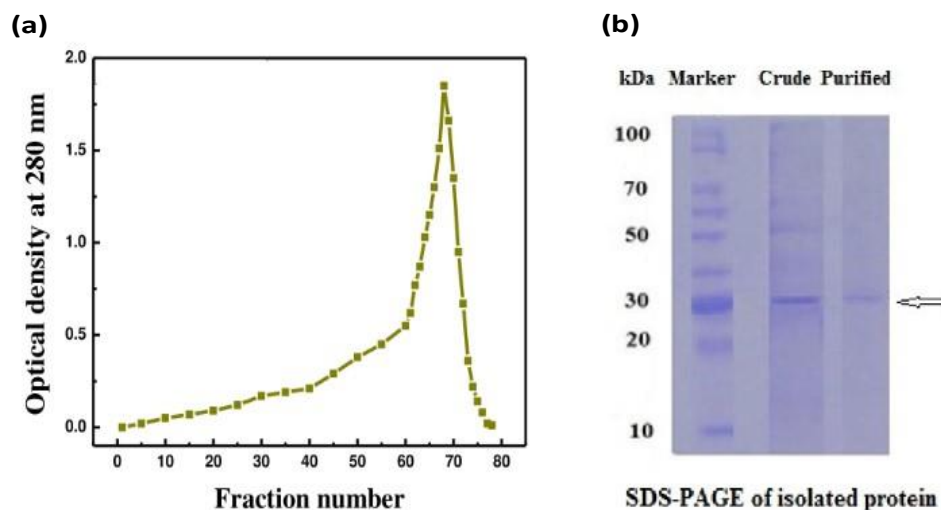
Therefore, in order to make the environment sustainable and healthier for all living systems, contaminated water bodies and cultivated land need to be rectified to make them free from heavy metals contamination. Several technologies have been employed for the removal of heavy metals or heavy metallic ion pollutants from effluent streams and lands. These technologies and physico-chemical methods employed for removing potentially harmful heavy metals are often ineffective or expensive particularly when the concentration of heavy metals is very low. While biological methods like bioremediation i.e., biosorption or bioaccumulation for removal of heavy metals may be an attractive alternative over and above the physico-chemical methods [149].

In this chapter, an extracellular bacterial (MDH1) protein has been explored for removal of lead contamination because the bacterial protein has the ability to bind with lead ion and remove it as nano-precipitation from the contaminated environment. The precipitated nanoplates are exploited against dye degradation for having its Photo-catalytic activity which is an added advantage of this treatment. The use of the microbial protein is a useful green approach for removal of lead contaminations and toxic dyes from environment since it

includes sustainable remediation technologies to rectify and re-establish the natural condition of environment.

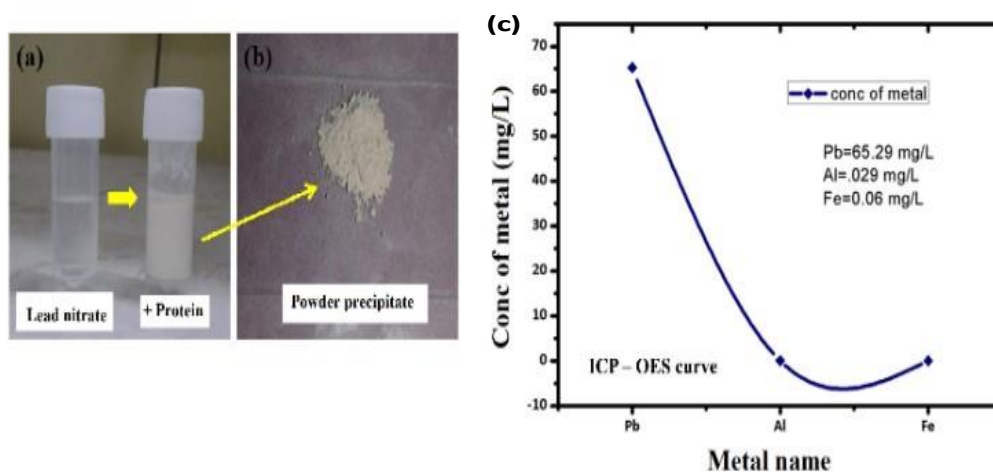
#### 4.1.1 Protein purification and SDS-PAGE analysis

The protein used in this work was isolated from the well grown MDH1 bacterial cultured medium and purified through double steps purification of Sephadex G-100 column chromatographic technique. The availability of protein in the collected eluted fraction was identified by measuring the optical densities of the solution at 280 nm using UV-Vis Spectrophotometer. The protein contained fraction which exhibited the highest optical density at 280 nm was found to possess lead removal activity from lead-compound solution shown in figure 4.1 (a). Now, sodium dodecyl sulfate–polyacrylamide gel electrophoresis in short SDS-PAGE is an electrophoresis technique which allows protein separation in respect to mass between 5 and 250 kDa. Figure 4.1 (b) represents SDS-PAGE analysis confirmed the molecular weight of the isolated protein was 30 kDa approximately which have the ability to react with aqueous lead solution and precipitated them.



**Figure 4.1:** (a) Protein purification curve (b) SDS-PAGE analysis of MDH1 bacterial protein

#### 4.1.2 The Inductively Coupled Plasma (ICP) analysis of powder precipitate



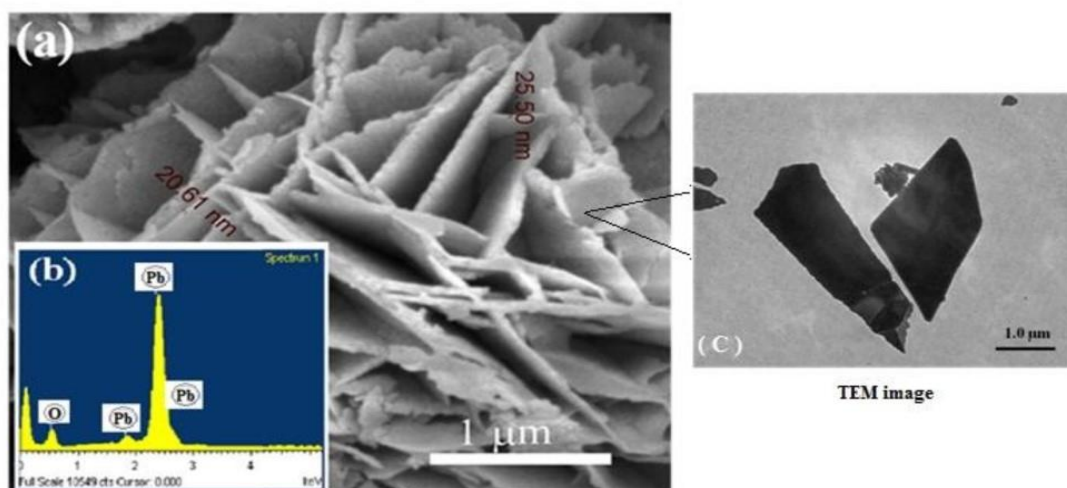
**Figure 4.2:** (a)-(b) represents lead oxide nanoplates formation in powder form (c) ICP-OES analysis of powder precipitate shows existence of lead in the sample.

When the protein was added to the lead nitrate solution, some elemental precipitation was formed immediately (Figure 4.2 (a) and Figure 4.2 (b)). The precipitate was separated through centrifugation followed by filtration through Whatman filter paper (25 mm) and dried to make powder form as shown in Figure 4.2 (b). Abundance of lead was detected in the precipitated powder when analysed by ICP spectrum of the sample (Figure 4.2 (c)). The ICP-OES spectrum of the powder precipitate confirmed that the precipitate sample contains almost 65.29 mg/L lead, formed by the reaction of MDH1 microbial protein and lead nitrate solution. ICP-OES is one of the most versatile methods for inorganic elemental analysis and use to determine the concentration of the heavy metals present in the solution [242]. Several bacterial strains (such as BKH1, BKH2, BKH4 etc.) isolated from hot springs of Bakreshwar similarly secrete several proteins in the growth medium which have the characteristic biomineralization property for which these bacteria can be used for the synthesis of nanoparticles and the development of high performance self-healed bio-concrete materials

[16-18]. Similarly, the whole cells of bacterium MDH1 was able to synthesis gold nanoparticles [19]. Therefore, the formation of lead nanoplates by the MDH1 bacterial protein is not at all a surprising phenomenon.

### 4.1.3 Surface morphology studies

The morphological structure of the powder precipitate was detected by FESEM and TEM analyses and the photomicrographs of the powder precipitate are shown in Figure 4.3. The FESEM image from Figure 4.3 (a) and that of TEM from Figure 4.3 (c) clearly confirmed the presence of nanoplates like structures in the precipitate. The thickness of the plates was measured from 20 to 25 nm. Presence of strong peaks of lead and oxygen in the EDX spectra, revealed that the as-prepared precipitate was lead-oxide nanoplates.

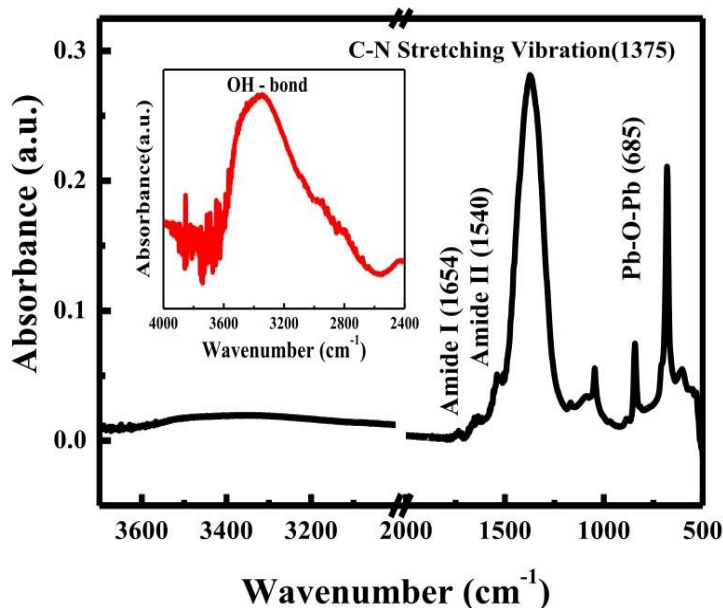


**Figure 4.3:** (a) surface morphology from FESEM image shows nanoplate structure (b) elemental representation of lead oxide using EDX analysis (c) TEM image of nanoplates.

### 4.1.4 FTIR Spectrum analysis

The FTIR spectrum of the precipitate sample confirmed the presence of different chemically functional groups in the lead oxide nanoplates represents in Figure 4.4. A sharp peak around

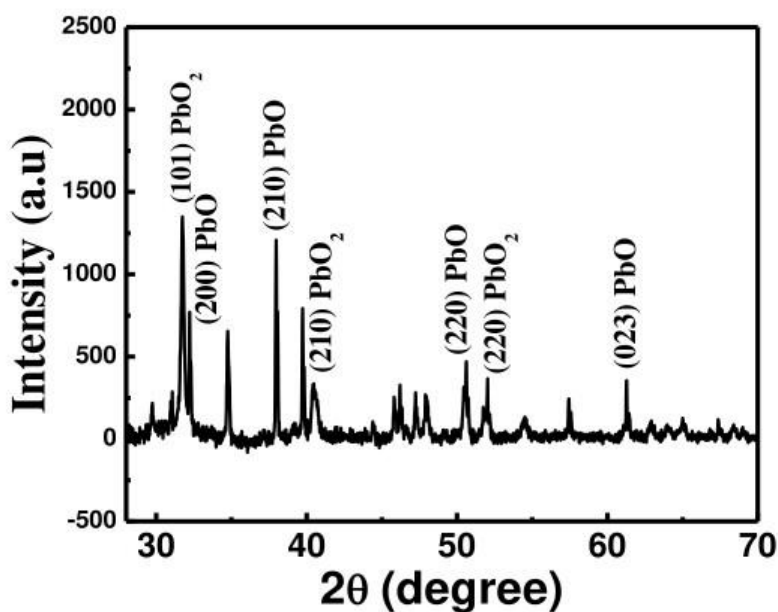
685  $\text{cm}^{-1}$  represents the asymmetric bending vibration of Pb-O-Pb bond and another intense peak at 1375  $\text{cm}^{-1}$  indicated the C - N stretching vibration. A very broad peak appeared at 3100 - 3600  $\text{cm}^{-1}$  region in the FTIR spectrum signified OH stretching vibration in H-bonded water which is shown in the inset of Figure 4.4 with enlarged view. The FTIR spectra evidenced the presence of Amide I and Amide II bonds which appeared due to the addition of microbial protein to the lead nitrate solution. The peaks between 1600 - 1700  $\text{cm}^{-1}$  were the stretching vibration of C=O bond of Amide I. The amide II band occurred at 1500 - 1600  $\text{cm}^{-1}$  and was mainly derived from the N-H bending vibration. FTIR study thus confirmed that the Amide I (1654  $\text{cm}^{-1}$ ) and Amide II (1540  $\text{cm}^{-1}$ ) both have the stronger ability to bind metallic atoms. It signifies that the protein may be responsible for forming a surface layer on the metallic lead oxide nanoplates that helps in stabilization of lead oxide nanoplates.



**Figure 4.4:** FTIR Spectrum of lead oxide nanoplates and inset image shows the enlarged view of the H-bond of nanoplates.

#### 4.1.5 XRD analysis:

The very sharp peaks in XRD pattern suggested the crystalline feature of lead oxide nanoplates (Figure 4.5). In comparison with standard XRD card (JCPDS data file), the main intense peak at  $31.8^\circ$  corresponds to the diffraction from (101) lattice plane and peaks at  $52^\circ$  and  $40.4^\circ$  correspond to (220) and (210) lattice planes respectively which shows a clear indication of  $\text{PbO}_2$  nanoplates formation as per the JCPDS analysis (card no. 080185). Another intense peak at  $37.9^\circ$  corresponds to (210) and at  $32.2^\circ$ ,  $50.7^\circ$  and  $61.1^\circ$  and correspond to (200), (220) and (023) planes respectively represent the  $\text{PbO}$  formation according to JCPDS analysis (card no. 050570). Therefore, the XRD pattern of the powder sample evidently indicates the formation of two forms of lead oxides. Both forms are insoluble in water. This type of reaction is known as disproportionation reaction.

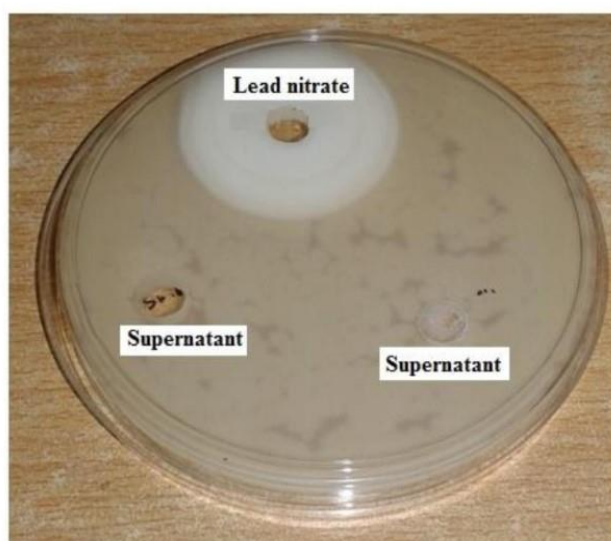


**Figure 4.5:** Crystalline structure analysis of lead oxide nanoplates using XRD



#### 4.1.6 Nontoxicity test of Supernatant

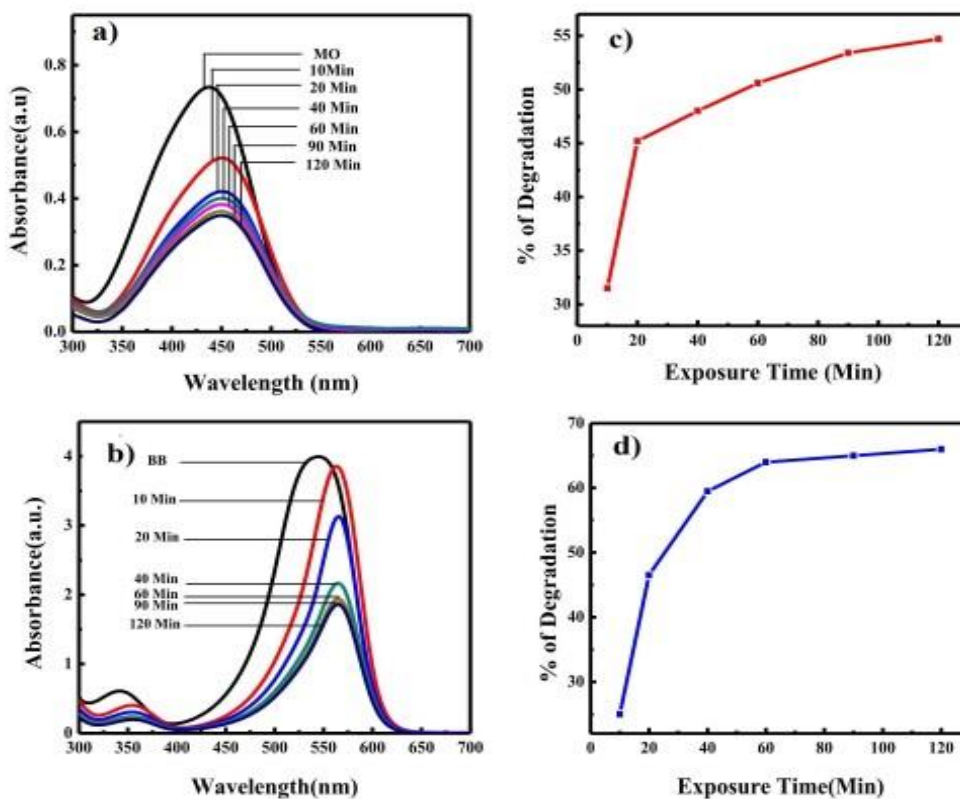
The supernatant, obtained after filtration of lead oxide nanoplates from the solution was carried out for essential non-toxicity measurement experiment along with original lead nitrate solution to create a comparison study. Lead ion is a very toxic compound which has bactericidal effect. It thus created a clear zone of inhibition on the culture plate against the *E. coli* (JM101) bacterial growth (Figure 4.6). But no such zone of inhibition was observed when supernatant was added to the wells of the *E. coli* bacterial growth containing agar plate. This result tells us that the bactericidal effect of the lead ions is lost due to the absence of lead ions in the supernatant. The MDH1 bacterial protein dissociates lead ions from its solution through the formation of lead oxide nanoplates.



**Figure 4.6:** Non-toxic effect of supernatant on *E. coli* bacterial growth

### 4.1.7 Dye degradation activity

The lead oxide nanoplates possess the photo-catalytic activity due to which it degraded Methyl Orange (MO) and Bromophenol Blue (BB) dyes which was described in Figures 7.7 (a)-(d) respectively. The release of dye effluents from textile industry is a major source of water pollution which created a harmful effect on aquatic system. Methyl Orange (MO) and Bromophenol Blue (BB) dyes are the pollutants of waste water, foods, cosmetics, agriculture and have a potential threat to the environment. The treatments for removing MO and BB dyes are therefore highly desirable. The catalytic degradation of these dye using nanoparticles is one of the most important and useful method for removing dyes from our environment.



**Figure 4.7:** Photocatalytic activity of lead oxide nanoplates on (a) MO; (b) BB and Percentage of dye degradation of (a) MO; (b) BB

This result showed that lead-oxide nanoplates acquired the Photo-catalytic ability for which it degraded MO and BB dye as described in Figures 7.7 (a)-(d) respectively. A huge drop in the pick of both MO and BB absorbance spectra was observed after a 120 min time span which indicate the degradation of dyes gradually in presence of lead oxide nanoplates. Furthermore, the percentage of degradation ability of lead-oxide nanoplates was calculated using Equation (1) and represents in the spectra shown in Figure 4.7 (c) and Figure 4.7 (d) respectively. These data and spectrum conclude the fact that bio-synthesized lead-oxide nanoplates are one of the effective photo catalysts.

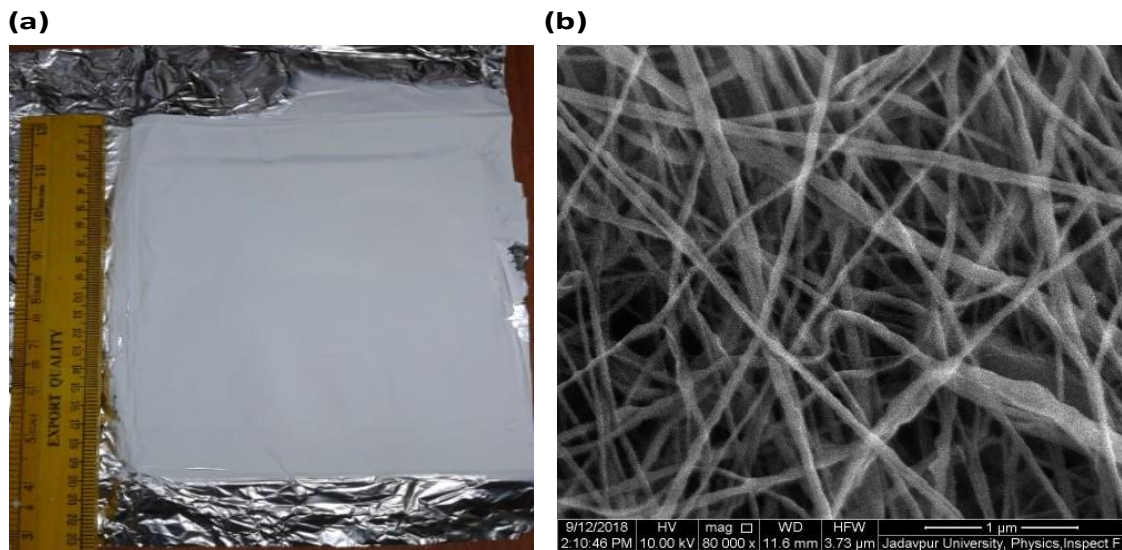
#### **4.1.8 Conclusion**

The work demonstrated here is a facile and eco-efficient route for the removal of lead contamination from aqueous solution by using a simple biological template. MDH1 microbial protein achieved successful activity of formation of lead-oxide nanoplates from lead nitrate solution and precipitate them. The lead oxide nanoplates also possess photo catalytic property due to which it degraded MO and BB dyes and can be used for the removal of those dyes from several industrial effluents. The MDH1 microbial protein is thus very useful for cleaning of lead contaminated water as well as BB and MO contaminated industrial effluents, foods and several agricultural products.

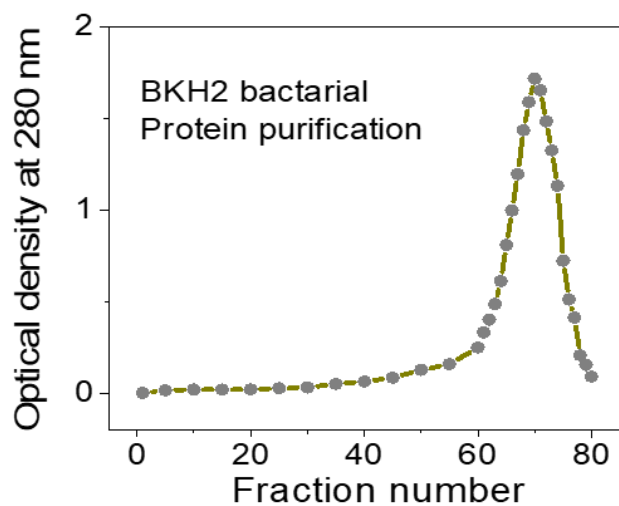
#### **4.1.9 Surface morphology study of electrospun nano-fiber:**

The bacterial (MDH1) protein based electrospun nano-fiber shown in the digital image (figure 4.8 (a)) implies proper formation of nanofiber with 20 cm in length. Figure (b) represents the FESEM image of the surface structure of nano-fiber illuminated the proper formation of fiber of nanoscale range assisted with bacterial protein. The image clearly evidenced the efficient porous structure of the nano-fiber which can be used as membrane that offer significant flux of liquid through it and may be beneficial for lead removal

technique as bio-filter. The further investigation will be continued in future regarding further characterization of the fiber, porosity measurement and fabrication of bio-filter.



**Figure 4.8:** (a) shows the digital photograph of electrospun Protein-PVDF nanofiber (b) FESEM image of porous protein-based nanofiber.



**Figure 4.9:** The BKH2 bacterial protein purification curve.

## 4.2. Bio-Organic Piezoelectric Nanogenerator

Energy harvesting from mechanical vibration in the sustainable and living environment is an efficient approach for flexible “battery free” and self-powered devices or piezoelectric nanogenerator and their effective applicability as sensor in medical field. This is the most impactful requirement not only for fully independent and sustainable function of low power-consuming electronic devices and systems but also in real time sustainable biomedical health monitoring system.

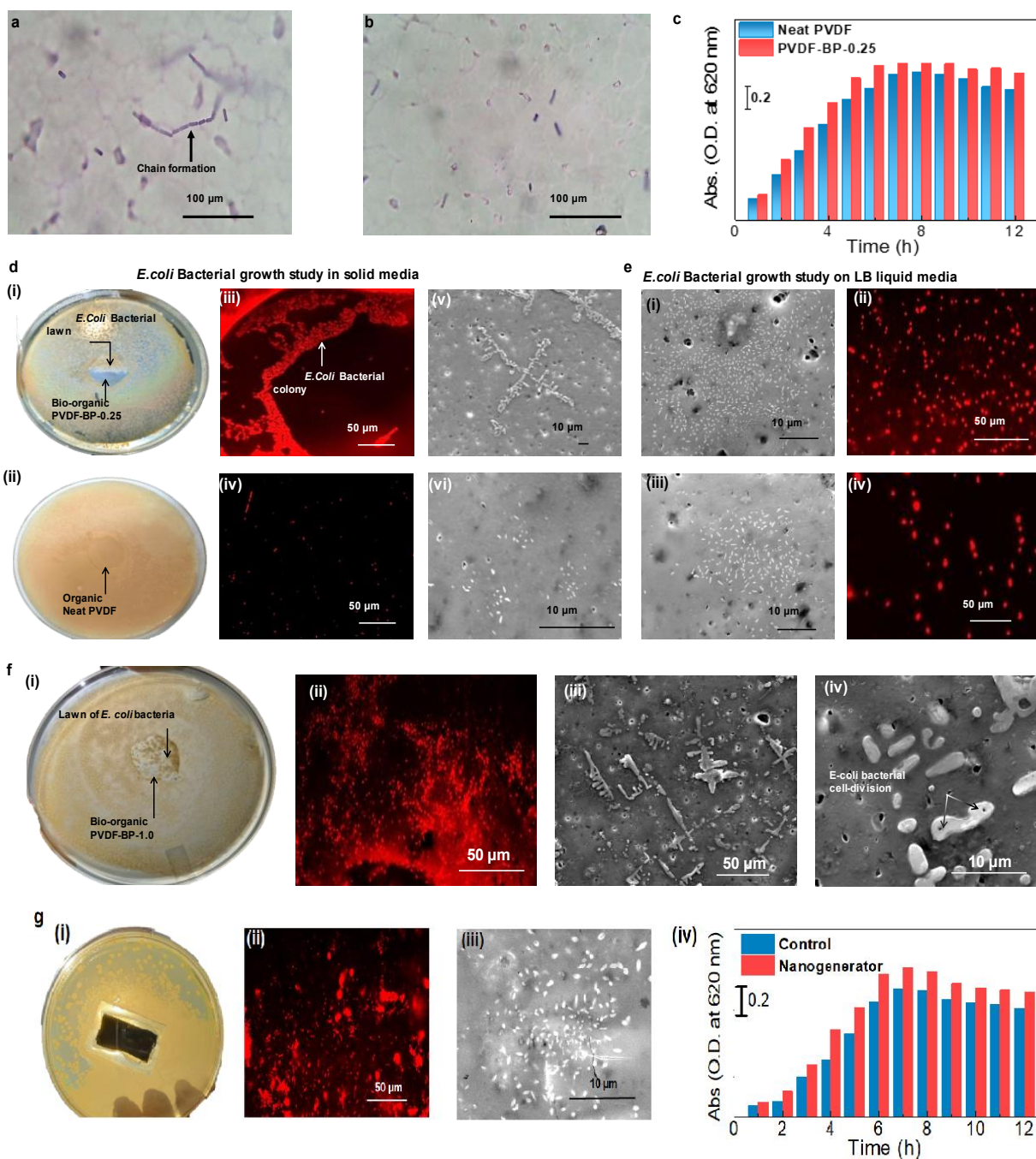
In this approach, we have incorporated the bacterial purified protein with PVDF matrix to acquire the porous composite self-poled  $\beta$ -phase containing films and based on this porous film, a flexible nanogenerator was fabricated. The BKH2 bacterial protein purification curve in Figure 4.9, showing a single major peak while plotting the optical density value of protein content fractions with fraction numbers, confirm the presence of protein in the collected fractions. The thermophilic bacterial (BKH2) protein is a high temperature tolerance and is a biopolymer with promising electrical and physical properties. We know biological materials like protein shows ferroelectricity, along with piezo-and pyroelectricity [244] and thus doped protein with PVDF we get a good response of electric properties of the films. Therefore, along with the formation of electroactive  $\beta$ -phase that we confirmed by FTIR analysis and with a good mechanical property through stress-strain measurement, the as-prepared film exhibits a good piezoelectric property. Consequently, Protein-PVDF composite film possess proper dielectric properties and also strong ferroelectric behaviour along with large piezoelectric charge coefficient. In addition, the biocompatibility and nontoxic nature, the protein leads as a nucleating agent over hydrated salts and nanoparticles. The biocompatibility study was conducted over the growth of *E. coli* bacterium and WI 38 cells in presence of films and the device. Now this biocompatible film-based NG exhibit a good ability of conversion of mechanical energy applied as finger touch into electrical energy and

produce open circuit voltage of 8.24 V and also capable to puts on several LEDs instantly without using external batteries.

#### **4.2.1 Biocompatibility analysis of Protein-PVDF films and Bio-Organic nanogenerator**

Now a days biocompatibility feature of the material is the main essential condition for the material, uses in every consumer electronic device as energy harvester and in bio medical devices as sensors for real health care system as they are directly connected to the human body. Biocompatibility which shows the materials ability not to produce any toxic effect when directly attached to the human body parts, must be tested before applied in any energy harvesting devices and in biomedical devices. Among the many developed methods, we used growth of *E. coli* bacteria and survivability of WI 38 cells along with Protein-PVDF films and these films based piezoelectric nanogenerators. In the materials and methods section, we briefly discussed the preparation and culture method of both *E. coli* bacteria and WI38 cells with films and NG, now we analyse all the results and discuss the effect of the films and NG in the sustainable growth of *E. coli* bacterial and WI 38 cells such that we can use them in health care monitoring systems.

First, discuss the growth of *E. coli* bacteria in liquid LB growth media along with the films and the NG. In this experiment as we used different concentration of protein then the studied was performed using lowest and highest concentration of protein (i.e., 0.25 and 1 wt. % respectively) based films (PVDF-BP-0.25 and PVDF-BP-1.0 respectively) and 1 wt% protein doped PVDF film-based NG. Figure 4.10 a represents the optical microscopic image of the surface of PVDF-BP-0.25 film where a clear chain formation of rod-shaped *E. coli* bacterium was observed and some rod-shaped *E. coli* bacterium also scattered through the surface of the film whereas in Neat PVDF film surface shows in figure 4.1b, only few *E. coli* bacteria were appeared in a scatter manner.



**Figure 4.10:** Biocompatibility tests: (a) Optical microscopy images showing growth of the *E. coli* bacterium over the surface of the PVDF-BP-0.25 bio-organic film and (b) Neat PVDF film. (c) Cell proliferation of the *E. coli* bacterium over the surface of PVDF-BP-0.25 and Neat PVDF films demonstrating the biocompatibility nature. (d) *E. coli* bacterial growth study from solid medium LB agar plate. (i) Digital images of LB agar plate along with PVDF-BP-0.25 film and (ii) Neat PVDF film. (iii) The immunofluorescence microscopy images of PVDF-BP-0.25 and (iv) Neat PVDF film. (v) The FE-SEM images of PVDF-BP-0.25 and (vi) Neat PVDF films. (e) Growth study of *E. coli*

bacteria on the surface of the films collected from liquid LB media (i) FE-SEM image and (ii) immunofluorescence microscopy images of *E. coli* bacteria over the surface of PVDF-BP-0.25. (iii) The FE-SEM and (iv) immunofluorescence microscopy images of *E. coli* bacteria over the surface of Neat PVDF film. (f) (i) Digital images of LB agar plate along with PVDF-BP-0.25 film-based bio-organic nanogenerator, (ii) immunofluorescence microscopy image and (iii) FE-SEM images of *E. coli* bacteria over the surface of nanogenerator. (iv) Cell proliferation of the *E. coli* bacterium in liquid LB media in the presence of nanogenerator and without nanogenerator (control).

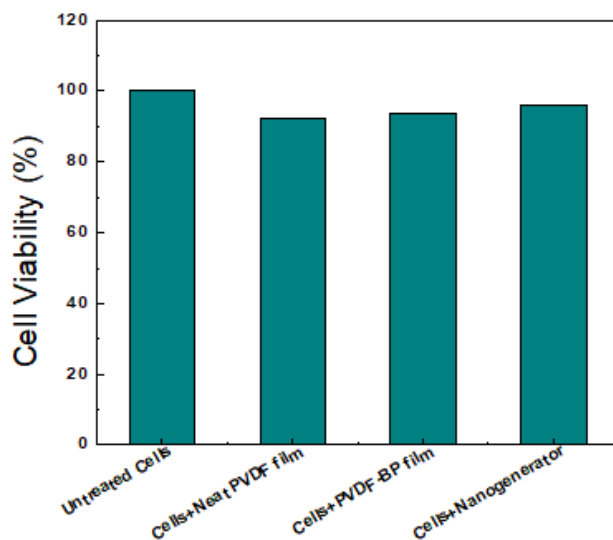
It signifies a good cell adhesion of *E. coli* bacterium on the surface of the PVDF-BP-0.25 film and this cell adhesion functionality of *E. coli* bacterium further helps the cells to proliferate with time. Now, the growth curve of *E. coli* bacterium in presence of PVDF-BP-0.25 film express in figure 4.10 c clearly shows the exponential growth where the bacterium begins to grow and divide at a constant pace and also the growth occurs very rapidly. After the exponential phase in respect to time, the saturation phase arises which is marked by a plateau in growth. The saturation phase generally is the counterbalance between the growth and death of cells resulting in no net increase in cell numbers. In this curve, after the clear saturation phase (the counterbalance between the growth and the death of cells~7 h) no net increase in cell numbers was observed and the bacterium moved towards death phase. If we draw the comparison of growth curve enlightened in the figure 4.9c between Protein-PVDF films and Neat PVDF film, a clear difference was observed. PVDF-BP-0.25 film is more effective in the growth of *E. coli* bacteria rather than Neat PVDF film which indicates that cell proliferation was more intense over PVDF-BP-0.25 film in parallel with Neat PVDF film. Therefore, from the growth curve analysis of *E. coli* bacterium, the life cycle of the *E. coli* bacterium was found that gives the clear and strong evidence behind the biocompatibility of the films. In order to strengthen our observations, we need to conduct more studies over the growth of *E. coli* bacteria ( $\sim 10^6$  cell/ml initially) in both liquid LB media and solid LB media with the PVDF-BP-0.25 and Neat PVDF film along with collect the information from the FESEM and fluorescence microscopy images of the film. Figure 4.10 d(i, iii, v) shows the



growth of *E. coli* bacterium in a solid medium LB agar plate with PVDF-BP-0.25 film and figure 4.10 d(ii, iv, vi) represents *E. coli* bacterial growth with Neat PVDF in solid media. The digital image of LB agar plate (figure 4.10 d(i)) clearly shows *E. coli* bacterial colony formation on the media along with the PVDF-BP-0.25 film. Also, a most interesting fact was noticed, an appreciable *E. coli* bacterial colony formation on the surface of the bio-organic film. But, in Neat PVDF film attached LB agar plate (figure 4.10 d(ii)), no such kind of *E. coli* bacterial colony was observed on the surface of the film. Therefore, the film was collected carefully for its morphological studies through FESEM and fluorescence microscopy analysis. The immunofluorescence microscopy image (fig 4.10 d(iii)) of the surface of PVDF-BP-0.25 film exhibits large content *e. coli* bacterial colony formation over PVDF-BP-0.25 film whereas in figure 4.10 (iv)), the fluorescence image of Neat PVDF film surface, a small content of *E. coli* bacterial growth was appeared on the film surface and no colony formation was noticed. FESEM image of PVDF-BP-0.25 film also affirmed the colony formation of *E. coli* bacterium over the film's surfaces and in contrast a lower content of bacterial growth was observed on the Neat PVDF film surface (figure 4.10 d(vi)). Now, the same outcomes were observed in the *E-coli* bacterial outgrowth over the films conducting with LB liquid media which results significantly larger bacterial growth over bio-organic PVDF-BP-0.25 film as asserted in FE-SEM (Figure 4.10 e(i)) and fluorescence microscopy images (Figure 4.10 e(ii)) contrasted to Neat PVDF film (Figure 4.10 e(iii), (iv)) which are also significantly compatible with the optical microscopy images shown in Figure 4.10 a, b. In point of fact, higher concentration of add-on bacterial protein in PVDF film raised the biocompatibility which was further assessed by growing *E. coli* bacterial culture ( $\sim 10^6$  cell/ml initially) over PVDF-BP-1.0 film shown in Figure 4.10 f(i-iii) where an effective lawn of *E. coli* bacterium over PVDF-BP-1.0 film surface in solid LB agar culture plate is more eminent due to over population together with the content of bacterial growth was

enhanced. Nevertheless, during *E. coli* bacterial growth period an obvious meaningful cell division over PVDF-BP-1.0 film was occurred that clearly observed from FESEM analysis (Figure 4.10 f(iv)), showing the suitability of *E. coli* bacterium with bio-organic PVDF-BP-1 film. These accumulative results inaugurate the fact that bacterial protein-based bio-organic PVDF-BP films are more biocompatible in contrast with Neat PVDF film hence more relevant in biomedical devices. Furthermore, it is also obligate to check the biocompatibility of the PVDF-BP film-based bio-organic nanogenerator as they are going to attached directly with human body. Hence, *E. coli* bacterial growth experiment also conducted over PVDFBP-0.25 film-based nanogenerator firstly observed in solid LB agar plate media (Figure 4.10 g(i)) which expressed good content of bacterial enhancement over the surface of NG, evidenced from immunofluorescence microscopic image shown in Figure 4.10 g(ii)) and also from sufficient FESEM (Figure 4.10 g(iii)) image. In addition, the exponential growth curve of *E. coli* bacterium in presence with nanogenerator in LB liquid media culture evolves larger bacterial growth in comparison with control media which was developed without nanogenerator as shown in Figure 4.10 g(iv). This result conveys the biocompatible functionality of the thermophilic bacterial protein-based bio-organic nanogenerator. The biocompatibility of a material is defined as the material property, which, after implantation in a living organism, does not produce adverse reactions or toxicity and must not induce inflammatory reactions [245]. In this study, the lowest concentration (0.25 wt%) of hot spring bacterial protein doped PVDF film was selected for comparison in order to illustrate strong attribute of BKH2 bacterial protein while lower content towards flourishing the biocompatibility feature of the bio-organic film and nanogenerator.

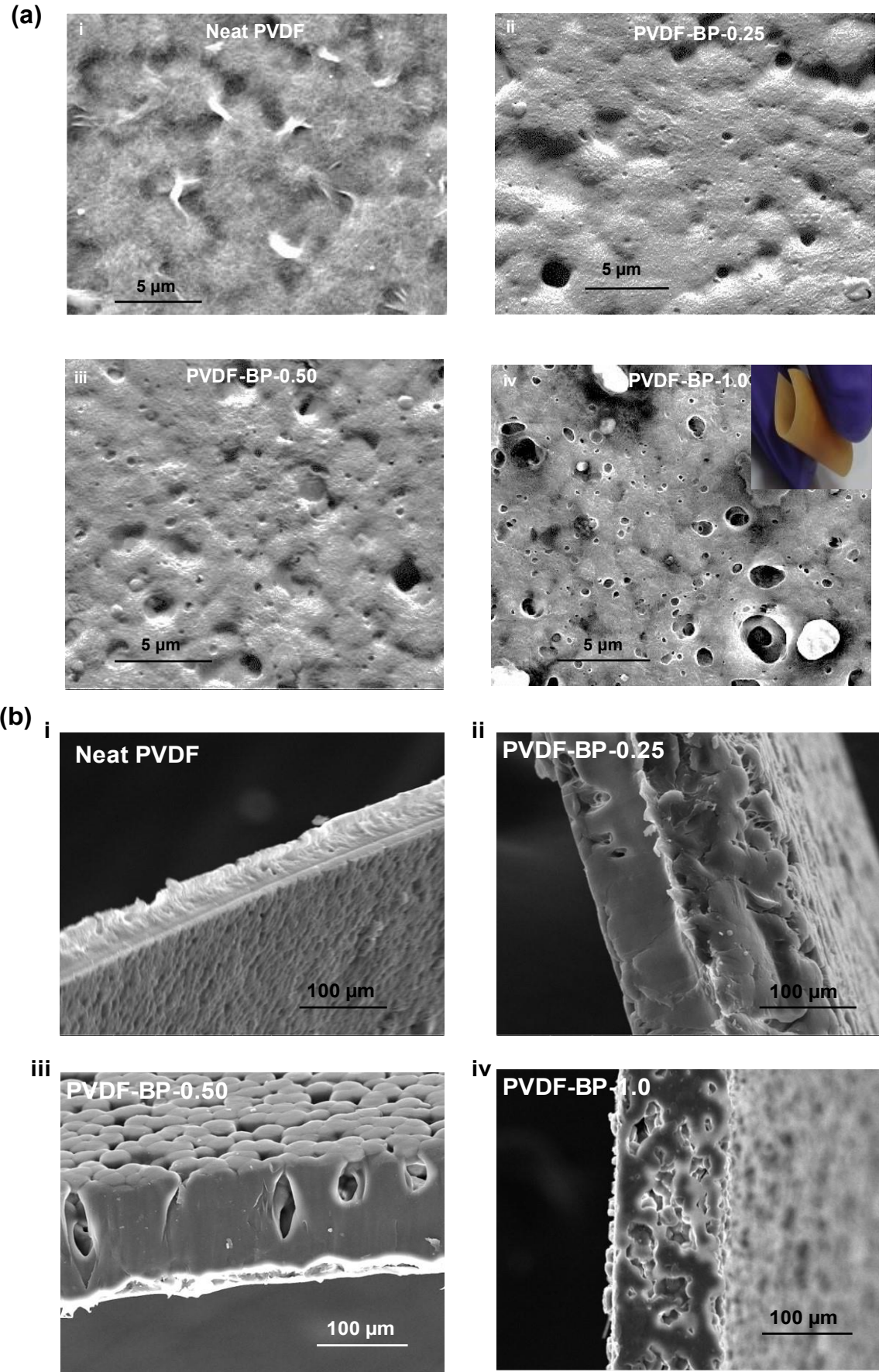
## Biocompatibility study using MTT assay:



**Figure 4.11:** Cell viability study of films and device using MTT assay

The biocompatibility effects of Neat PVDF film, PVDF-BP film and Nanogenerator were examined in normal cell line WI38. The survivability assay was carried out using MTT where oxidoreductase enzymes present in the cells reduced MTT dye into purple coloured formazan. As mentioned in Figure 4.11, we had observed that Neat PVDF, PVDF-BP film and Nanogenerator did not result in significant cell death when applied to normal cells. The percentage of cell viability of films and NG are almost same as that of untreated cells whereas the percentage of cell viability of nanogenerator and Protein-PVDF film increases in comparison with neat PVDF film, evidence from above graph. This result supports the biocompatibility studies conducted by the growth of *E. coli* bacterium however, in both the cases the biocompatibility enhances in the presence of PVDF-BP films and NG in comparison with Neat PVDF. Therefore, these films and the device is wholly compatible to direct human body contact and beneficial for real time health care monitoring.

### 4.2.2 Surface Morphology of films



**Figure 4.12** (a) (i-iv) Surface morphology by FE-SEM representing the porous microstructure over the bio-organic films with different protein concentrations. The inset in (iv) shows the flexibility demonstration of the spongy film. (b) The cross-sectional FE-SEM images of (i) Neat PVDF, (ii) PVDF-BP-0.25, (iii) PVDF-BP-0.50 and (iv) PVDF-BP-1.0 films. The images representing the fact that with increasing BP content into PVDF the porosity was increased.

To understand the good cell adhesion feature of PVDF-BP films in comparison with Neat PVDF film and to obtain a detail analysis of the surface morphology of the films, FESEM image description is one of the best choices. Figure 4.12 a (i-iv) represents the surface images of Neat PVDF and protein doped PVDF films respectively which clearly shows the different surface structure of the films. The Protein-BP films exhibit formation of porous microstructure over the surface of the protein based PVDF films and Figure 4.12 a(ii-iv) shows the porous microstructure increased with higher content of additive bacterial protein into PVDF. Not only over the surface, the porous microstructure also clearly observed across the volume of the PVDF-BP films evidenced from Figure 4.12 b(ii-iv). Therefore, we can say this porous structure was favourable for *E. coli* bacterial cell adhesion along with cell proliferation. Higher porosity furnishes a high surface area for cell – matrix interaction which provides enough space for extracellular matrix regeneration and uniform, proficient cell seeding [246]. Apart from, Neat PVDF film exhibits smooth surface including  $\alpha$ -spherulite fibril growth structure which provides a little effect on *E. coli* cell adhesion and no formation of porous structure was observed over the surface (figure 4.12 a(i)) and across the volume (Figure 4.12 b(i)). Now, find the proper information regarding porosity, we calculated the percentage of porosity of the films using the equation:

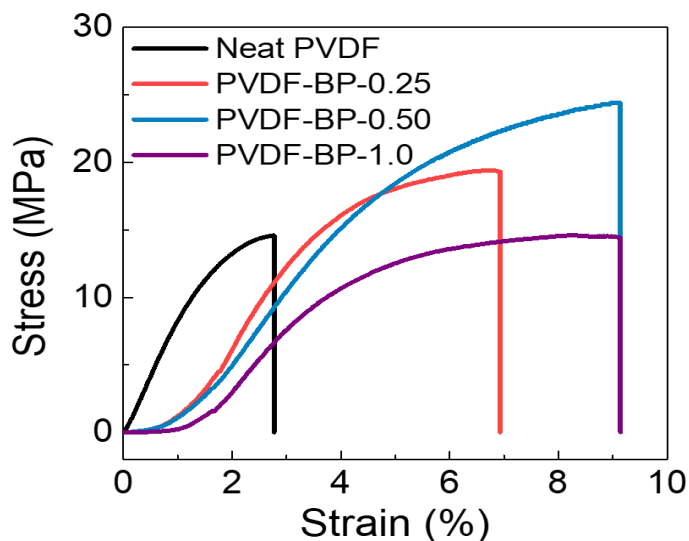
$$\text{Porosity (\%)} = \left(1 - \frac{\rho_m}{\rho_b}\right) \times 100 \quad (2)$$

where,  $\rho_m$  is the material density of the porous PVDF-BP films and  $\rho_b$  represents bulk density of the non-porous PVDF film ( $1.7 \text{ g/cm}^3$ ). Here, the material density of different protein concentration-based films like PVDF-BP-0.25, PVDF-BP-0.50 and PVDF-BP-1.0

films belongs to  $\rho_m \sim 1.56, 1.5, 1.39$  g/cm<sup>3</sup> respectively. Finally, the porosity of the films was evaluated as 8%, 12% and 18% for the PVDF-BP-0.25, PVDF-BP-0.50 and PVDF-BP-1.0 films respectively. This result evidenced the increased of porosity along with the increase of protein content within PVDF. Along with the porous structure, a prominent protein layer all over the surface of the PVDF matrix also occurred and enhanced with higher content of bacterial protein. As a consequence of the porous microstructure, the protein-based PVDF films become quite soft, spongy and flexible shown in inset image of Figure 4.12 a (iv). Furthermore, the porous feature of the PVDF-BP films contributes a momentous effect on their mechanical and electric characteristics.

#### **4.2.3 Stress-Strain analysis:**

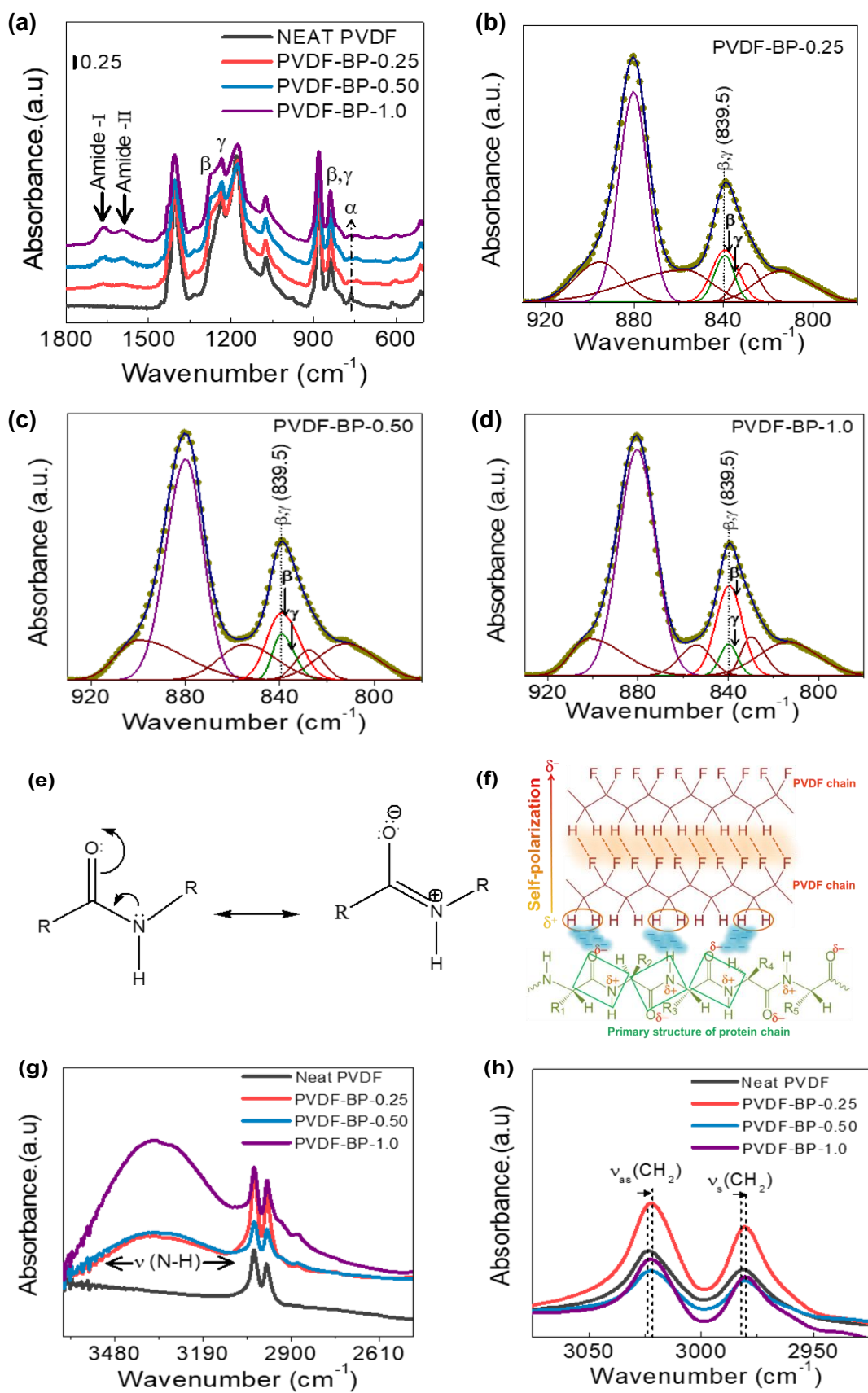
The softness of the bio-organic films was evaluated using stress ( $\sigma_u$ )-strain ( $\epsilon_u$ ) analysis (Figure 4.13). Owing to higher porosity, the PVDF-BP films become less stiff than that of Neat PVDF. As a result, break point of strain was increased from  $\epsilon_u \sim 2.77\%$  from Neat PVDF to  $\epsilon_u \sim 6.93\%, 9.14\%, 9.15\%$  for PVDF-BP-0.25, PVDF-BP-0.50 and PVDF-BP-1.0 films respectively. However, the PVDF-BP films possess lower young's modulus (Y) in comparison to Neat PVDF film. With higher BP content as porosity increases in the PVDF-BP films, numerically Y decreases such as Y  $\sim 620$  MPa, 543 MPa, 468 MPa for PVDF-BP-0.25, PVDF-BP-0.50 and PVDF-BP-1.0 films respectively which are comparatively lower than that of Neat PVDF (Y  $\sim 832$  MPa).



**Figure 4.13** Stress-strain curve of Neat PVDF and protein based PVDF films shows the softness of the films.

#### 4.2.4 FTIR analysis

In order to implement the developed films towards energy harvesting, the prerequisite electroactive phase ( $\beta$ -,  $\gamma$ -phases) contents were investigated. It has been observed that Neat PVDF film was composed of  $\gamma$ - ( $1234\text{ cm}^{-1}$ ) and non-polar  $\alpha$ -phases ( $763\text{ cm}^{-1}$ ), while PVDF-BP films were consisting of  $\beta$ - ( $1272\text{ cm}^{-1}$ ) and  $\gamma$ - phases ( $1234\text{ cm}^{-1}$ ) and non-polar  $\alpha$ -phase was completely demolished (Figure 4.14 a).





**Figure 4.14** (a) FT-IR spectra of the developed films. (b), (c), (d) represents Deconvolution of the FTIR spectra of bacterial protein incorporated PVDF films within the range  $930\text{ cm}^{-1}$  to  $780\text{ cm}^{-1}$ . (e) C–N double bond character in peptide bond due to resonating structure of amino acid. (f) Schematic representing the H-bonding interaction between the PVDF chain and resonating structure of peptide bonds followed by self-polarization of bio-organic material. (g) FT-IR spectra of the Neat PVDF and PVDF-BP films in the region of  $3500\text{--}3000\text{ cm}^{-1}$  showing broad peak, confirmed the broad intensified N-H stretching vibration in PVDF-BP films. (h) The FT-IR spectra in the frequency region of  $3075\text{--}2925\text{ cm}^{-1}$  representing frequency shifting of the CH<sub>2</sub> asymmetric ( $\nu_{as}$ ) and symmetric ( $\nu_s$ ) stretching vibration modes in PVDF-BP films.

The relative proportion of electroactive phase content ( $F_{EA}$ ) was quantified using the Beer-Lambert law,

$$F_{EA} = \frac{I_{EA}}{\left(\frac{K_{839}}{K_{763}}\right)I_{763} + I_{EA}} \times 100 \quad (3)$$

where  $I_{EA}$  is the absorbance intensity at  $839.53\text{ cm}^{-1}$  and  $I_{763}$  is the absorbance intensity at  $763\text{ cm}^{-1}$ ;  $K_{763}$  ( $\sim 6.1 \times 10^4\text{ cm}^2\text{ mol}^{-1}$ ) and  $K_{839}$  ( $\sim 7.7 \times 10^4\text{ cm}^2\text{ mol}^{-1}$ ) are the absorption coefficients at the respective wave numbers [246]. The calculated results show numerically  $F_{EA} \sim 82\%$ ,  $85\%$  and  $88\%$  for PVDF-BP-0.25, PVDF-BP-0.50 and PVDF-BP-1.0 films respectively. In the figures 4.13 b, c, d, the sharp peak contributed for  $\beta$ -phase and broad peak for  $\gamma$ -phase. The equations 4, 5 are used to quantify the individual relative proportion of  $\beta$  and  $\gamma$ -phases.

$$F(\beta) = F_{EA} \times \left(\frac{A_{\beta}}{A_{\beta} + A_{\gamma}}\right) \times 100\% \quad (4)$$

$$F(\gamma) = F_{EA} \times \left(\frac{A_{\gamma}}{A_{\beta} + A_{\gamma}}\right) \times 100\% \quad (5)$$

where,  $A_{\beta}$  and  $A_{\gamma}$  are the integral area under the  $\beta$  and  $\gamma$  marked deconvolution curves (Figure 4.14 b-d) respectively centered at  $839.5\text{ cm}^{-1}$  band. Using the curve deconvolution process [234], the estimated  $\beta$ -phase content was  $52\%$ ,  $58\%$  and  $66\%$  and  $\gamma$ -phase content were  $30\%$ ,  $27\%$  and  $22\%$  respectively for PVDF-BP-0.25, PVDF-BP-0.50 and PVDF-BP-1.0 films

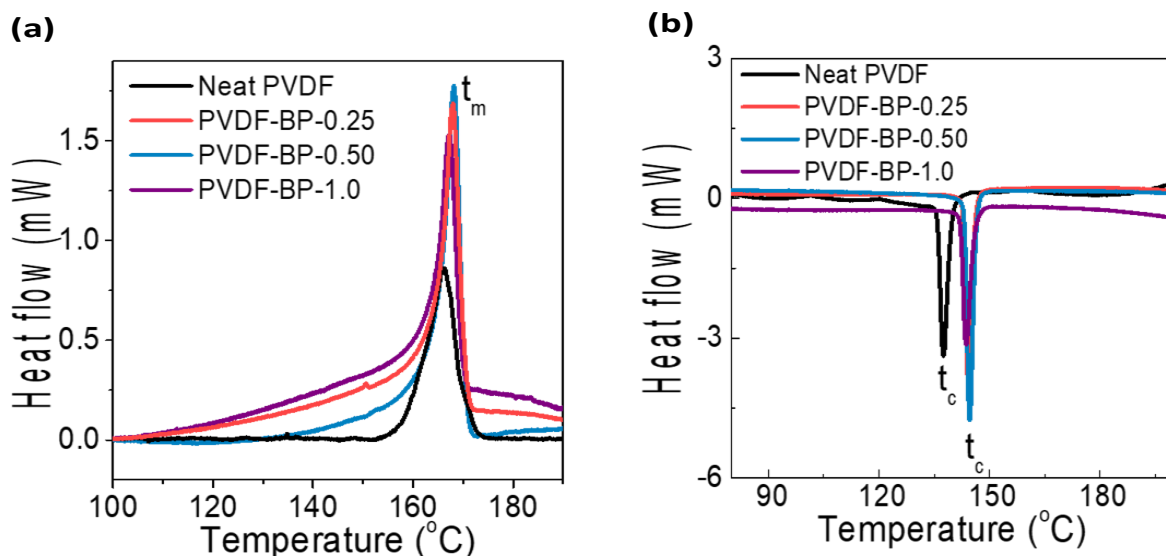
respectively (Figure 4.14 (b, c, d)). In addition to the electroactive phases, amide I ( $1661\text{ cm}^{-1}$ : resulting from  $\text{C} = \text{O}$  stretching/ hydrogen bonding coupled with  $\text{COO}^-$ ) and amide II ( $1596\text{ cm}^{-1}$ : N-H-bending ( $\delta(\text{N} - \text{H})$ ) coupled with  $\text{C} - \text{N}$  stretching ( $\nu(\text{C} - \text{N})$ )) [227] peaks become prominent within the PVDF-BP films and peak intensities increased with increased concentration of BP additive into PVDF. It is become evident that bacterial protein played a significant role for the porous microstructure formation (Figure 4.12) in the bio-organic PVDF films followed by electroactive  $\beta$ -phase nucleation (Figure 4.14 a) and subsequent stabilization of self-polarization (Figure 4.14 f). In our fabrication process, water molecules were removed from the bacterial protein during the freeze-drying (lyophilization process), although the presence of a tiny content of water molecules is unavoidable to the lab-based fabrication process where water molecules were interacted on the planer surface of peptide bond of the protein chain through dipole-dipole or ion-dipole interaction due to resonating structure and zwitter ionic behavior (Figure 4.14 e). Thus, the attached water molecules were slowly evaporated during the film crystallization ( $\sim 60\text{ }^\circ\text{C}$ ) which engineered the ununiformed porous structure formation through solvent-non-solvent phase separation process. As the BKH2 bacterial strain was thermophilic ( $65\text{ }^\circ\text{C}$ ) in nature, therefore during PVDF crystallization, the delocalization of  $\pi$  - electronic cloud occurred on the planer surface of peptide bond due to the resonating structure of the amino acid residues of protein chain. Eventually, strong  $\text{C} - \text{H} \cdots \pi$  interaction or dipole-dipole interaction occurred between  $-\text{CH}_2-$  dipoles of PVDF and  $\pi$  - electronic cloud of peptide bond (Figure 4.14 f). As a result of the hydrogen bonding interaction between  $-\text{C} = \text{O}$  moiety of peptide bond and H atoms of  $\text{CH}_2$  dipoles, a broad intensified N-H stretching vibration arising in the frequency range of  $3500\text{--}3000\text{ cm}^{-1}$  which is predominantly absent in Neat PVDF film (Figure 4.14 g). As a result of, the above-mentioned interactions, a clear frequency shifting of the  $\text{CH}_2$  asymmetric ( $\nu_{\text{as}}$ ) and symmetric ( $\nu_{\text{s}}$ ) stretching vibration modes in PVDF-BP films have been

observed with respect to Neat PVDF film (Figure 4.14 h). This phenomenon leads to the formation of self-poled electroactive  $\beta$ -phase and also has significance for spontaneous piezoelectricity generation [235, 252].

#### 4.2.5 DSC analysis:

For better understanding of the effect of bacterial protein on the thermal stabilization of the protein incorporated PVDF films, differential scanning calorimetry (DSC) was carried out. It is also evident from DSC curve that in the presence of protein the melting temperature ( $t_m$ ) of the protein doped PVDF film increases, compared to Neat PVDF. The melting temperature of Neat PVDF film points out at 166 °C which increased to 168 °C (for PVDF-BP-0.25), 168.3 °C (for PVDF-BP-0.50) and 167.5 °C (for PVDF-BP-1.0) (Figure 4.15 a). It is important to note that the melting DSC peaks more broadened with increasing content of BP into PVDF film. Theoretically, an infinitely narrow transition peak should arise for pure crystalline material, while, the peaks will be more broadened when external additives/impurities will be present within the crystalline material [247]. In our case, as the content of external BP additives into pure PVDF increases the melting DSC peaks are more broadened which is also consistent with the previous report [246]. In addition, protein doped PVDF films exhibit higher crystallization temperature ( $t_c$ ) with respect to Neat PVDF film (Figure 4.15 b). The crystallization temperature of Neat PVDF was at 137.5 °C and increases to 144.5 °C for PVDF-BP-0.25 furthermore, the crystalline temperature also increases for other two concentrations to 144.8 °C for PVDF-BP-0.50 and 143.7 °C for PVDF-BP-1.0 films. The crystallinity ( $\chi_c$ ) was evaluated using the melting enthalpy, as  $\chi_c = \frac{\Delta H_f/\varphi}{\Delta H_f^*}$  where,  $\Delta H_f$  was the melting enthalpy,  $\Delta H_f^* = 104.5 J/g$  is the melting enthalpy for a 100% crystalline PVDF,  $\varphi$  is the used weight fraction of PVDF ( $\sim 0.6$ ) [249]. The evaluated crystallinity was  $\chi_c \sim 45$ ,

53, 54 and 56% for Neat PVDF, PVDF-BP-0.25, PVDF-BP-0.50 and PVDF-BP-1.0 respectively.



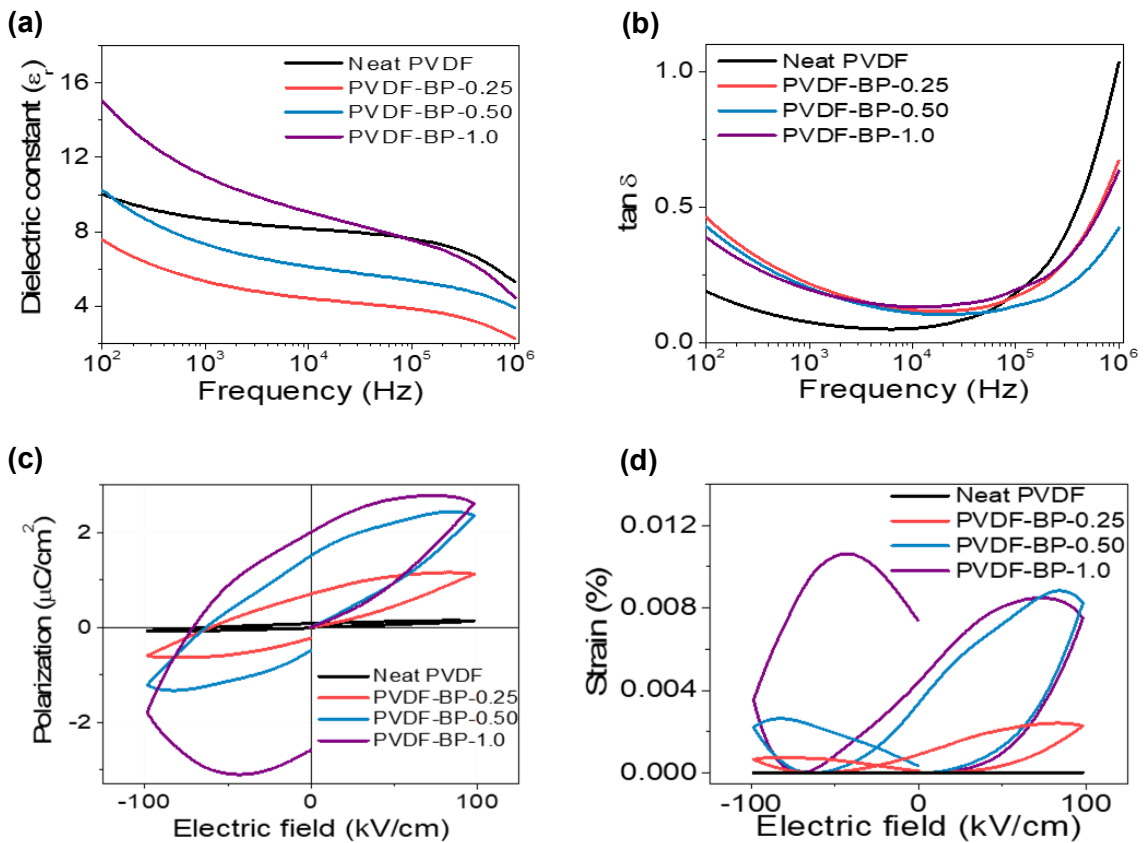
**Figure 4.15** (a) DSC thermograms under heating cycle and (b) cooling cycle.

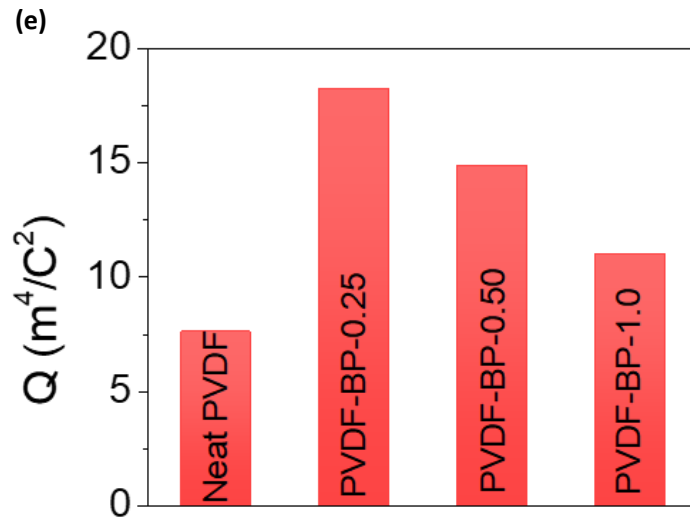
#### 4.2.6 Electrical properties of the films:

The electrical properties of the developed films were evaluated by measuring the frequency dependent dielectric constant ( $\epsilon_r$ ) (Fig. 4.16 a) and loss tangent ( $\tan \delta$ ) (Fig. 4.16 b) in the frequency range of 100 Hz – 1 MHz. Owing to the dipolar nature of PVDF, the  $\epsilon_r$  decreases with increasing frequency [250]. The Neat PVDF film possess  $\epsilon_r \sim 9$  and  $\tan \delta \sim 0.076$  at the frequency of 1 kHz, while the dielectric constants of the PVDF-BP-0.25, PVDF-BP-0.50 and PVDF-BP-1.0 were 5, 7 and 11 as well as  $\tan \delta$  were of 0.217, 0.2 and 0.196 respectively. It is interesting to note that with increasing content of BP, the  $\epsilon_r$  increases systematically while the change of  $\tan \delta$  were not significant. Owing to the porous structure, with lower content of BP (such as, PVDF-BP-0.25, and PVDF-BP-0.50) the  $\epsilon_r$  was numerically lower than that of Neat PVDF, while  $\epsilon_r$  were systematically increased with higher content of BP due to Maxwell-Wagner-Sillars (MWS) interfacial polarization effect. Therefore, there is some

competition between MWS effect and the porosity factor to control  $\epsilon_r$  of the PVDF-BP films. After certain concentration of BP (in this case PVDF-BP-1.0 film), MWS effect was the dominating factor over the porosity factor. As a result, the  $\epsilon_r$  of PVDF-BP-1.0 was numerically higher than that of Neat PVDF. In this case, owing to the higher content of protein, MWS effect was more prominent where, the ionic movements and hydrogen bonds bound to the protein structure plays an important role to increase dielectric constant compared to Neat PVDF [250]. As both the porosity and MWS effect arises due to the presence of BP into PVDF, therefore, the  $\epsilon_r$  of the PVDF-BP films were the combined effect of porosity and the MWS effect. Furthermore, polarization level of the developed films was measured by polarization (P) – electric field (E) hysteresis loop (Fig. 4.16 c). Benefitting from the higher electroactive phase content and higher degree of crystallinity, bacterial protein mixed PVDF films possess higher level of polarization at zero electric field (called remnant polarization,  $P_r$ ) compared to Neat PVDF. For example, PVDF-BP-1.0, PVDF-BP-0.5 and PVDF-BP-0.25 films possess higher  $P_r \sim 2, 1.5$  and  $0.7 \mu\text{C}/\text{cm}^2$  respectively compared to Neat PVDF ( $P_r \sim 0.07 \mu\text{C}/\text{cm}^2$ ). According to the macroscopic dimensional effect, the remnant polarization was directly proportional to the longitudinal piezoelectric coefficient ( $d_{33} = -\frac{P_r}{Y}$ ) which eventually useful for piezoelectric energy harvesting process [251]. As a result, bacterial protein incorporated PVDF film possess higher  $d_{33} \sim -11.3, -27.6$  and  $-42.7 \text{ pC}/\text{N}$  for PVDF-BP-0.25, PVDF-BP-0.5 and PVDF-BP-1.0 respectively compared to Neat PVDF film ( $d_{33} \sim -0.85 \text{ pC}/\text{N}$ ). Furthermore, the butterfly shaped symmetrical strain (S) – electric field (E) hysteresis loop directly reflects the converse piezoelectric effect of developed PVDF films (Figure 4.16 d). It was evaluated using the well-known electrostrictive relation of  $S=QP^2$ , where, Q denotes the magnitude of longitudinal electrostrictive coefficient which was estimated using the relation of  $d_{33} = 2Q\epsilon_r\epsilon_0P_r$  [251]. In obvious manner, the electrostrictive coefficients were higher for protein

mixed PVDF film in comparison to Neat PVDF film (Figure 4.16 e). Furthermore, bacterial protein mixed PVDF films consist of the higher piezoelectric voltage co-efficients  $g_{33} = \frac{d_{33}}{\epsilon_r \epsilon_0}$  [2] of 0.26, 0.44, 0.44  $\text{VmN}^{-1}$  for PVDF-BP-0.25, PVDF-BP-0.5 and PVDF-BP-1.0 respectively compared to Neat PVDF ( $g_{33} \sim 0.01 \text{VmN}^{-1}$ ). In overall, the piezoelectric figure-of-merit ( $F_oM_p \sim d_{33} \times g_{33}$ ) [2] validates the materials ability to design a piezoelectric energy harvester. The bacterial protein doped PVDF films possess 1000 times higher  $F_oM_p$  compared Neat PVDF film. For example, numerically the  $F_oM_p$  were of  $2.9 \times 10^{-12}$ ,  $12.1 \times 10^{-12}$  and  $18.8 \times 10^{-12} \text{Pa}^{-1}$  for PVDF-BP-0.25, PVDF-BP-0.5 and PVDF-BP-1.0 which were 1000 times higher than that of Neat PVDF film ( $F_oM_p \sim 8.5 \times 10^{-15} \text{Pa}^{-1}$ ). These results clearly indicated the suitability of the bacterial protein incorporated PVDF films as high-performance power generator.

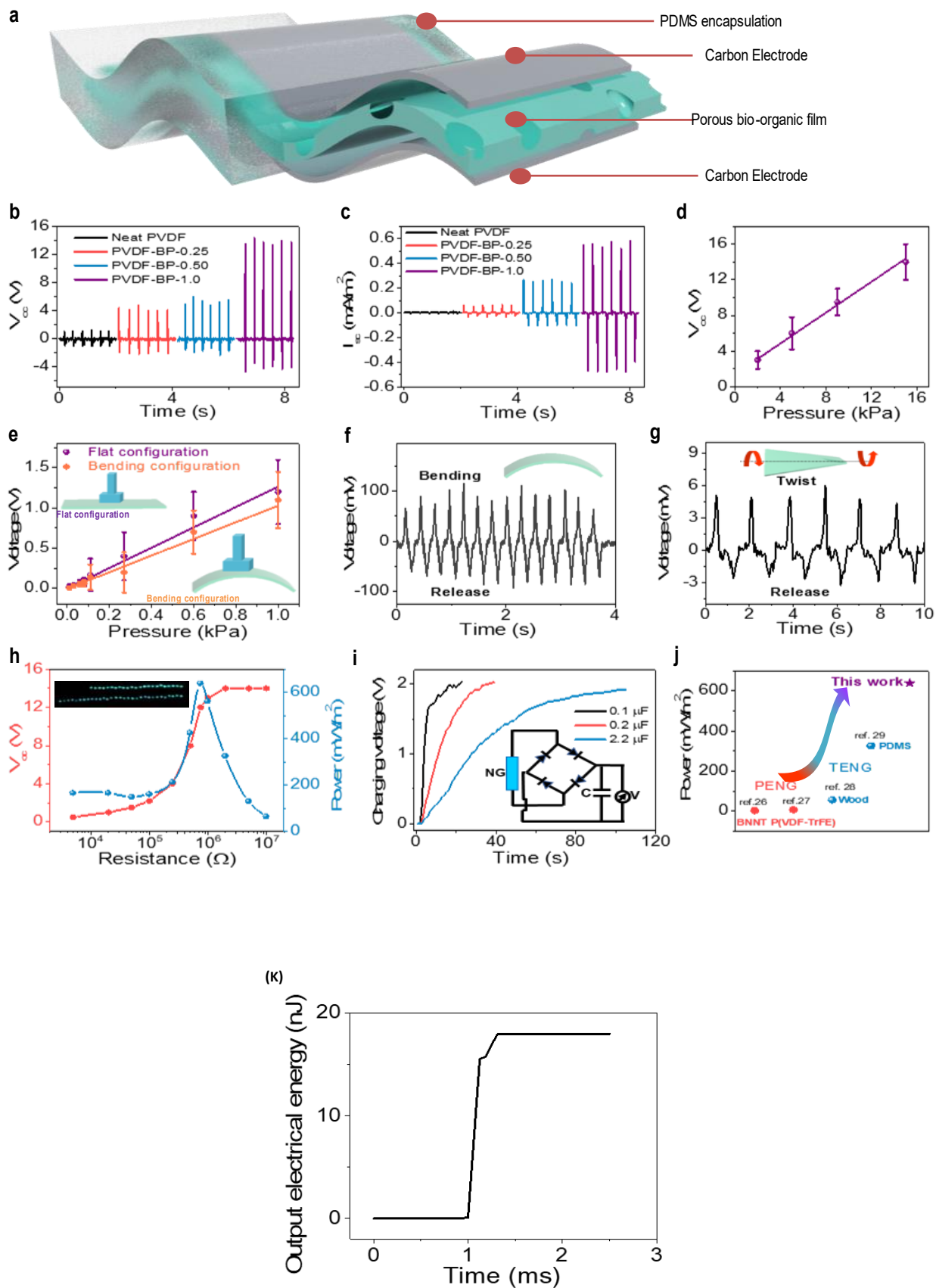




**Figure 4.16** Electrical properties of the Neat PVDF and the developed bio-organic films (a) Frequency dependent dielectric constant and (b) loss tangent (c) Electric field dependent polarization and (d) butterfly shaped piezoelectric strain hysteresis loops (e) The electrostrictive coefficients of the bio-organic PVDF-BP films and Neat PVDF film.

#### 4.2.7 Energy harvesting performance

The nanogenerator was prepared using the porous bacterial protein incorporated PVDF and non-porous Neat PVDF films considering the metal-insulator-metal structure followed by PDMS elastomer encapsulation for protection from any mechanical damage as shown schematically in Figure 4.17 a.





**Figure 4.17** The energy harvesting performance of the BONG. (a) Schematic of the designed BONG using the porous bio-organic film. (b) Generated open-circuit output voltage ( $V_{oc}$ ) and (c) short-circuit output current under 15 kPa pressure. (d) Pressure dependent output voltage in the range of 2–15 kPa pressure. (e) Voltage output within the pressure range of 10 Pa<sup>-1</sup> kPa pressure range under flat configuration and bending configuration of the device as shown schematically in the inset. (f) The voltage output from the device under repeated bending and releasing motions as schematically shown in the inset. (g) The voltage output from the nanogenerator under repeated twisting and releasing motion as shown schematically in the inset. (h) Output voltage and power variation across a range of load resistance of 5 k $\Omega$  – 10 M $\Omega$ . The inset shows operated 54 LEDs directly connected to BONG. (i) The charging performance of the commercial capacitors with the schematic of the used circuit in the inset. (j) The output power comparison of the BONG with the previously developed PENG and TENGs (k) The instantaneous output electrical energy per cycle from the BONG.

Owing to the higher figure-of-merit, the nanogenerator made by bio-organic PVDF-BP-1.0 shown the highest open-circuit output voltage ( $V_{oc}$ ) of 14 V (Figure 4.17 b) and short-circuit current output ( $I_{sc}$ ) of 0.56 mA/m<sup>2</sup> (Figure 4.17 c) compared to PVDF-BP-0.5 ( $V_{oc}$ ~ 6 V,  $I_{sc}$ ~ 0.26 mA/m<sup>2</sup>), PVDF-BP-0.25 ( $V_{oc}$ ~ 4 V,  $I_{sc}$ ~ 0.06 mA/m<sup>2</sup>) and Neat PVDF ( $V_{oc}$ ~ 1 V,  $I_{sc}$ ~ 0.01 mA/m<sup>2</sup>) under the repetitive finger imparting with compressive stress amplitude ( $\sigma_a$ ) of 15 kPa. As the  $V_{oc}$  and  $I_{sc}$  generated from the PVDF-BP-1.0 based bio-organic nanogenerator (BONG) were highest among the developed bio-organic films, therefore this device was used for further characterization unless otherwise mentioned. It was interesting to note that the  $V_{oc}$  from the PVDF-BP-1.0 increased linearly when the applied pressure to the nanogenerator was increased in the range of  $\sigma_a$ ~ 2–15 kPa (Figure 4.17 d). This linear increment evaluated the mechano-sensitivity ( $\sim \frac{V_{oc}}{\sigma_a}$ ) of the device as high as 0.86 V/kPa<sup>-1</sup> which was superior to the previously developed devices (Table 4.1). In order to evaluate the sensitivity, the linear fitting was done using the equation,  $y = 0.86x + 1.4$ , where the standard error in slope was 0.038, Pearson correlation coefficient was 0.998 and adjusted R-squared value was 0.994. In order to evaluate the pressure detection limit of the device, the sensitivity was further evaluated under low pressure region (<1 kPa) (Figure 4.17 e). The device can detect the

pressure as low as 10 Pa which is the detection limit of the device. The device sensitivity ( $\sim 1.26 \text{ V kPa}^{-1}$ ) was higher in the low pressure (10 Pa – 1 kPa) region compared to high pressure region ( $0.86 \text{ V kPa}^{-1}$  in the pressure region of 2 – 15 kPa). In fact, the pressure sensitivity was not much affected under bending condition (sensitivity  $\sim 1.03 \text{ V kPa}^{-1}$  under bending radius,  $r \sim 15 \text{ mm}$ ) indicating the suitability of the device for clinical applications as human body motions contain combined movements such as bending, pressuring, twisting. The superior sensitivity of the device was further demonstrated by repeated bending and releasing motions (Figure 4.17 f). Under the bending state, the tensile strain developed along the thickness direction of the device was  $\varepsilon_y = \frac{L}{2r} = 0.67\%$ , (where,  $L = 200\mu\text{m}$  was the thickness of the device and  $r = 15\text{mm}$  was the bending radius) and along the length direction of the device was  $\varepsilon_x = 0.29\%$  considering the poisson's ratio,  $\nu = \left| \frac{\varepsilon_x}{\varepsilon_y} \right| = 0.44$  of PVDF [12]. Under repeated bending-releasing motion, the generated voltage output was 100 mV which was higher in comparison to the generated voltage output ( $\sim 5 \text{ mV}$ ) from the device under repeated twisting-releasing motions (Figure 4.17 g) which is consistent with the previous literature [12]. Furthermore, the several  $V_{oc}$  from the nanogenerator were measured across the load resistance ( $R_L$ ) under the applied pressure,  $\sigma_a \sim 15 \text{ kPa}$  and the instantaneous power output ( $P_L$ ) was evaluated using the formula  $P_L = \frac{1}{A} \frac{V_L^2}{R_L}$ , where  $A$  is the electrode area ( $\sim 3 \text{ cm}^2$ ), and  $V_L$  is the voltage drop across the load resistance  $R_L$  ( $\sim 5 \text{ k}\Omega$ –  $10 \text{ M}\Omega$ ). The  $R_L$  dependent variation of the  $V_{oc}$  and  $P_L$  was shown in Figure 4.17 h. The BONG generated maximum output power as high as  $640 \text{ mW/m}^2$  across the  $R_L \sim 0.75 \text{ M}\Omega$ . The power output of the BONG is found to be superior to the previously developed several nanogenerators (Table 4.2). With this higher output power, the nanogenerator was capable to instantly illuminate 54 light emitting diodes (LEDs) (inset of Figure 4.17 h) directly connected to the BONG. Furthermore, the under continuous finger imparting to the nanogenerator, the generated

electricity was stored to the commercially available capacitors of several capacitance (0.1, 0.2 and 2.2  $\mu\text{F}$ ) very quickly (less than 2 min) (Figure 4.17 i). For example, the 0.1  $\mu\text{F}$  capacitor was charged to the saturated voltage ( $V_c \sim 2 \text{ V}$ ) within 23 s and stored the energy was of ( $E = \frac{1}{2} CV_c^2$ ) 0.2  $\mu\text{J}$ . Similarly, the 0.2 and 2.2  $\mu\text{F}$  capacitors were saturated within 39 and 105 s respectively and stored the energy of 0.4 and 3.97  $\mu\text{J}$  respectively. In this case, the bridge rectifier circuit was used as shown schematically in the inset of Fig. 5i. The capacitor charging performance of the BONG is very much superior to that of previously reported several piezoelectric nanogenerators (Table 4.3). In fact, the high power output of our developed bio-organic nanogenerator outperform to the previously developed high performance inorganic (Boron Nitride Nanotube (BNNT), power output~ 3.59  $\text{mW}/\text{m}^2$ ) [253] and organic (thin film PVDF-TrFE, power output  $\sim 8 \text{ mW}/\text{m}^2$ ) [254] piezoelectric nanogenerators as well as well studied wood (power output~ 57  $\text{mW}/\text{m}^2$ ) [255] and PDMS (power output~ 327  $\text{mW}/\text{m}^2$ ) [256] based triboelectric nanogenerators (TENG) (Figure 4.17 j) and therefore, can be implemented to the future biomedical electronics. Furthermore, the nanogenerator possesses the energy conversion efficiency ( $\eta_{\text{piezo}}$ ) of 62.5%. The energy conversion efficiency was calculated using the equation of  $\eta_{\text{piezo}} = \frac{E_{\text{elec}}}{W_{\text{mec}}} \times 100\%$  where,

$$E_{\text{elec}} = \int_{t_1}^{t_2} \frac{V(t)^2}{R_L} dt = 18 \text{ nJ}$$

was the instantaneous output electrical energy per cycle (Figure 4.17 k) and  $W_{\text{mec}} = F \times \varepsilon \times L = 28.8 \text{ nJ}$  was the input mechanical energy per cycle [257]. In calculating applied mechanical energy, applied force  $F$  was 4.5 N corresponds to  $\sigma_a \sim 15 \text{ kPa}$ , the developed axial strain was  $\varepsilon = \frac{\sigma_a}{Y} = 32 \times 10^{-6}$ , where  $Y \sim 468 \text{ MPa}$  of the PVDF-BP-1.0 film, total thickness of device  $L = 200 \mu\text{m}$ . The energy conversion efficiency of the bio-organic nanogenerator is very promising and superior to the previously developed nanogenerators (Table 4.4).

**Table 4.1:** Mechano-sensitivity comparison of the BONG with the reported piezoelectric based pressure sensors.

Material	Sensitivity (V/kPa)	Reference
Piezoelectric fiber array vertically integrated P(VDF- TrFE)	0.027	1
P(VDF-TrFE)/CMOS transistor	0.011	2
P(VDF-TrFE) film	$2.2 \times 10^{-5}$	3
Carbonized electrospun polyacrylonitrile/barium titanate (PAN-C/BTO) nanofiber film	0.324	4
Aligned P(VDF- TrFE)/MWCNT composites	0.121	5
Cellular fluorocarbon	1.54	6
P(VDF-TrFE) thin film	$7.5 \times 10^{-4}$	7
Eletrospun PVDF fabric	$8.2 \times 10^{-4}$	8
P(VDF-TrFE) nanotube	0.05	9
Electrospun PVDF/BaTiO <sub>3</sub> nanowire (NW)	0.017	10

nanocomposite fibers		
Laterally aligned PZT angle- crystal nanowires	0.14	11
PVDF-MWCNT- OMMT	0.0176	12
PVDF-ZnO nanofibers	0.00312	13
<b><i>PVDF-Bacterial protein based bio-organic film</i></b>	<b><i>0.86</i></b>	<b><i>This work</i></b>

**Table 4.2:** The generated voltage, current and power output comparison of the BONG with previously developed piezoelectric nanogenerators. (¥NM: Not Mentioned)

<b>Materials</b>	<b>Voltage/Current</b>	<b>Power</b>	<b>Ref.</b>
PVDF	76 mV and 39 nA	577.6 pW/cm <sup>2</sup>	14
PVDF/NaNbO <sub>3</sub>	3.4 V, 4.4 µA	¥NM	15
ZnO/PVDF	8.36 V, 0.17 µA	77.69 nWcm <sup>-2</sup>	16
PVDF/CH <sub>3</sub> NH <sub>3</sub> PbI <sub>3</sub>	2 V/50 nA	0.8 mW/m <sup>2</sup>	17
PVDF	1 V, 0.15 mA	52 µWcm <sup>-3</sup>	18
BaTiO <sub>3</sub> /PZT/CNT/PVDF	6V/ 4 nA	NM	19
PVDF-TrFE	16.2 mV	NM	20
PVDF	8 V/3.76 µA	NM	21
PVDF-MoS <sub>2</sub>	12 V, 12nA	0.01 µW/cm <sup>2</sup>	22
Random PVDF	2.21 V/ 4 µA	0.16 mW/cm <sup>3</sup>	23
PVDF/graphene oxide	7 V	0.62 µW/cm <sup>2</sup>	24

PVDF-ZnO nonorods	85 V/2.2 $\mu$ A	NM	25
<b><i>PVDF-Bacterial protein based bio-organic film</i></b>	<b><i>14 V, 56 nA/cm<sup>2</sup></i></b>	<b><i>64 <math>\mu</math>W/cm<sup>2</sup></i></b> <b><i>(640 mW/m<sup>2</sup>)</i></b>	<b><i>This work</i></b>

**Table 4.3:** A summary or comparison of device materials and capacitor charging performances of the BONG with the reported nanogenerators.

<b>Active material</b>	<b>Charging time(s), Capacitor value (<math>\mu</math>F)</b>	<b>Saturation voltage (V), Power stored (<math>\mu</math>W)</b>	<b>References</b>
P(VDF-TrFE)/BaTiO <sub>3</sub>	250, 0.068	35, 0.17	26
aligned PVDF NFs	60, 1.0	4, 1.3	27
P(VDF-TrFE)	1800, 47	16, 3.34	28
Pt-PVDF	80, 1	3, 0.06	29
PZT-NH <sub>2</sub> NPs	100, 2.2	4, 0.18	30
Hybridization sugar-encapsulated PVDF	100, 1	8, 0.32	31
PVDF/ BaTiO <sub>3</sub>	76, 1	1.40, 0.01	32
P(VDF-TrFE)/ BaTiO <sub>3</sub>	120, 4.7	1.5, 0.04	33
PVA/ ZnS nanorods	40, 1	0.72, 0.007	34
PVDF/ ZnS nanorods	130, 2.2	10, 0.85	35
PVDF-niobate-based	300, 2.2	5, 0.09	36
[P(VDF-TrFE)]	5, 0.1	3.2, 0.01	37

Ce <sup>3+</sup> / PVDF/Graphene	60, 4.7	0.75, 0.02	38
<b><i>PVDF-Bacterial protein based bio-organic film</i></b>	<b>105 sec, 2.2</b>	<b>2, 4.4</b>	<b>This work</b>

**Table 4.4:** A comparison list of device materials, and energy conversion efficiency of the BONG with the reported nanogenerators.

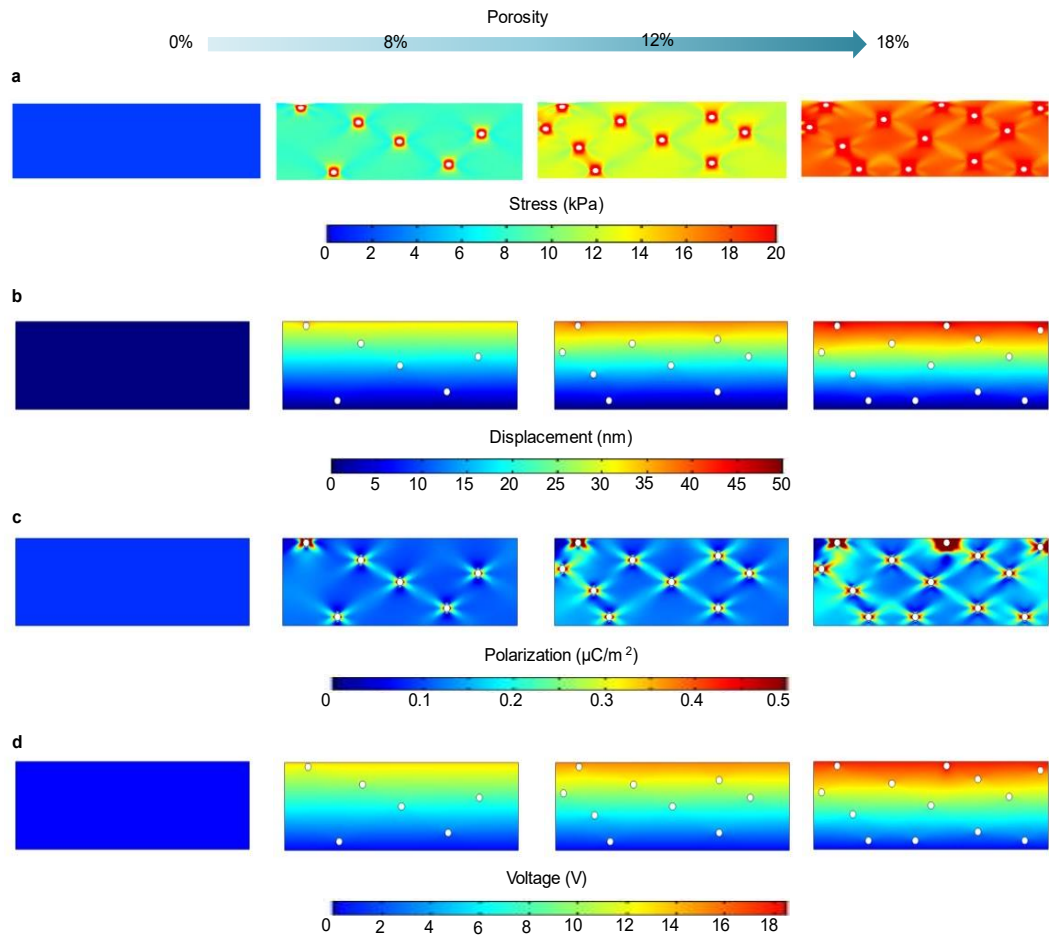
<b>Device materials</b>	<b>Energy conversion efficiency (%)</b>	<b>References</b>
PVDF fiber	21.8	39
KNbO <sub>3</sub> nanowires	0.9	40
Yb <sup>3+</sup> -PVDF	2.4	41
PVDF-Nanowire	0.2	42
Ferroelectric Pt-PVDF film	0.2	43
Fish swim bladder	0.3	44
Pt-PVDF fiber	0.7	45
Gelatin nanofiber	52.5	46
ZnO nanowire	30	47
PVDF)/PANI/g-C <sub>3</sub> N <sub>4</sub> blend nanocomposite fibers	19.7	48
PVDF–MoS <sub>2</sub> nanosheets	17.8	49
ZnSnO <sub>3</sub> microbelt	6.6	50
<b><i>PVDF-Bacterial protein based bio-organic film</i></b>	<b>62.5</b>	<b>This work</b>

## 4.2.9 Theoretical Simulation

In order to understand the high-power output generation capability of our developed nanogenerator, finite element method (FEM) based theoretical simulations were performed using the COMSOL Multiphysics. From the theoretical calculation, it was very evident that the geometrical porous microstructure formation played an important role for higher figure-of-merit, sensitivity as well as superior power generation capability. As the porosity was increased from 0 – 18% with the increased concentration bacterial protein from 0.25 to 1 wt% to the PVDF, the applied stress of 15 kPa was more concentrated/confined to the porous structure which is known as stress-concentration effect (Fig. 4.18 a) [257-259]. As a result of this confinement effect, the stress within the porous structure was enhanced than that of the applied stress amplitude and a stress gradient within the porous structure was formed (Figure 4.18 a). On the other hand, no such effect was observed in the Neat PVDF of 0% porosity. Consequently, the displacement of the porous PVDF films was increased with increasing porosity and of course larger than that Neat PVDF (Figure 4.18 b). Owing to the higher displacement/compressibility for PVDF-BP-1.0 film, the positive and negative current output (which is proportional to the input strain) for pressing and releasing stress respectively were similar (Figure 4.18 c) which was not the case for other PVDF-BP films. This higher displacement functionality with stress-concentration effect synergistically enhanced the stress induced polarization which was also found to be confined to the porous microstructures (Figure 4.17 c). Thus, the polarization was higher for PVDF of higher porosity. With this enhanced polarization, the PVDF with 18% porosity (experimentally, PVDF-BP-1.0) generated highest output voltage of 18 V under 15 kPa of pressure which was consistent with our experimental results ( $V_{oc} \sim 14$  V) (Figure 4.18 d). In obvious manner, the environmental



bacteria engineered porous structure PVDF generated higher output voltage than that of non-porous Neat PVDF film.

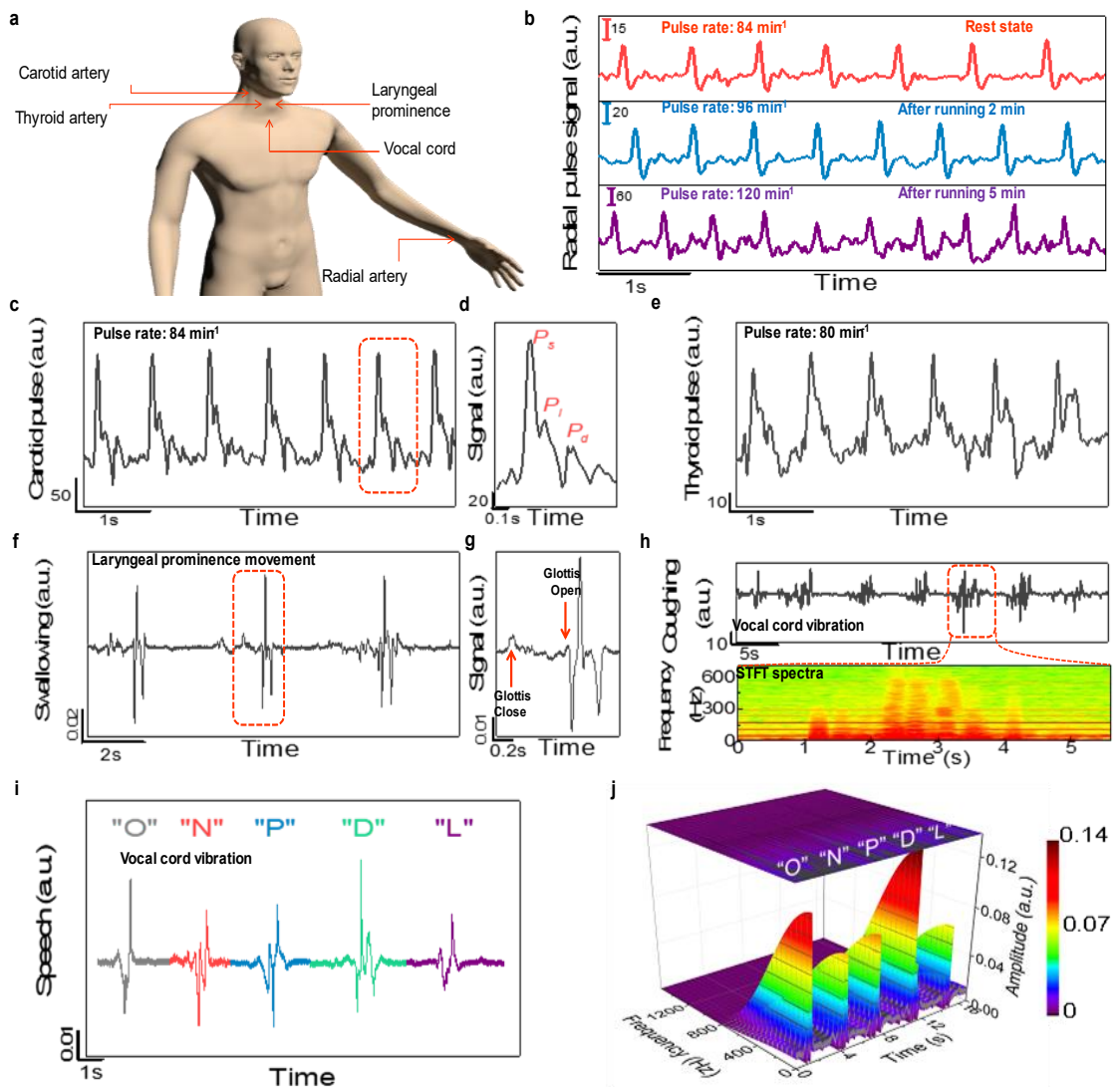


**Figure 4.18** Finite element based theoretical simulation. (a) The applied stress distribution, (b) the displacement distribution, (c) stress induced polarization distribution and (d) generated voltage distribution within the bio-organic films of different porosity as mentioned in the top portion.

#### 4.2.10 Self-Power Healthcare Monitoring

With the superior sensitivity of the PVDF-BP-1.0 film-based BONG, the device was implemented towards real-time healthcare monitoring sensor by attaching to the several body-parts of human body as shown in Fig 4.19 a. For example, upon attaching to the human wrist, the device can sense the radial artery pulse wave under different physical conditions.

The device can detect the heart beat pulse rate of  $84 \text{ min}^{-1}$  which was increased to  $96 \text{ min}^{-1}$  and  $120 \text{ min}^{-1}$  when the device was attached to the wrist after exercising (running) for 2 and 5 min respectively (Figure 4.19 b). The radial artery pulse wave characteristic was composed of four systolic waves, such as, A-wave (initially positive), B-wave (early negative), C-wave (re-increasing), D-wave (late re-decreasing), and one diastolic wave, which was E-wave (positive) [260].



**Figure 4.19** Clinical applications of the BONG. (a) Schematic representing the healthcare monitoring positions of a human body used in our study. (b) Radial artery pulse measurement under rest and running physical activities. (c) Carotid artery pulse measurement with (d) an enlarge signal of one

cycle. (e) Thyroid artery pulse signal measurement. (f) Laryngeal prominence movement signals with (g) one cycle signal showing glottis open and closing response. (h) Repeated coughing action signals (upper panel) with STFT of one signal (lower panel). (i) Vocal cord vibration signal during speaking different words of 'O', 'N', 'P', 'D', 'L' and (j) their 3-D STFT spectrogram.

The important parameters to indicate the cardiovascular dysfunction are represented by the ratio of peak heights such as E- and D- waves to A- wave (i.e.,  $P_{A/E}$ , and  $D/A$ , respectively) and the time delay ( $\tau_{EA}$ ) between the A- and E-wave. In this case, the parameters are continuously decreasing with increasing heart rate (i.e., from calm state to exercise conditions), such as at calm state  $P_{A/E} \sim 16$ ;  $D/A \sim -0.1$ ;  $\tau_{EA} \sim 0.58$ , after 2 min exercise  $P_{A/E} \sim 7.8$ ;  $D/A \sim -0.03$ ;  $\tau_{EA} \sim 0.54$  and after 5 min exercise  $P_{A/E} \sim 3.9$ ;  $D/A \sim -0.02$ ;  $\tau_{EA} \sim 0.33$ , which represented the diastolic dysfunction with increasing exercise, leading to the symptoms of heart failure. Therefore, our device can successfully discriminate the different physical activities. In addition, our developed BONG based sensor was capable to detect the carotid artery pulse wave when mounted to the neck of the volunteer (Figure 4.19 c). In this case, the device shows the same pulse rate ( $84 \text{ min}^{-1}$ ) as measured by radial artery pulse wave, thus representing high fidelity towards healthcare monitoring. A single pulse in Figure 4.18 d shows the main characteristic feature of pulse pressure wave consisting of main wave ( $P_s$ ) followed by predicrotic wave ( $P_i$ ) in systolic phase and the dicrotic wave ( $P_d$ ) in diastolic phase [260]. An artery augmentation index (AI) of 44% was extracted from the measured carotid pulse wave. The AI is an important cardiologic parameter generally used in clinical treatments which represents the elasticity of the human blood vessels and calculated as,  $AI = \frac{P_i}{P_s} \times 100\%$  [254]. The extracted AI value indicated a healthy young man and consistent with previously measured data [261]. Furthermore, upon mounting to the skin beneath the collarbone, the sensor can precisely detect the thyroid artery pulse wave (Figure 4.19 e). The characteristic waves of pulse pressure shape were similar to the carotid artery pulse wave and detected the pulse rate ( $\sim 80 \text{ min}^{-1}$ ) and AI value ( $\sim 49\%$ ) were almost consistent with the

measured values from carotid pulse wave. Furthermore, by fastening the device to the throat, the motion of the laryngeal prominence (the Adam's apple) of a healthy young man was observed during the swallowing of saliva action repeatedly (Figure 4.19 f) via identifying the glottis opening and closing processes (Figure 4.19 g). Therefore, the device might be useful in a breathing monitor for the early detection of sudden infant death syndrome (SIDS) in sleeping infants, alerting parents to any potential problems [262]. Furthermore, the device has shown high fidelity in sensing the vocal cord vibration during repeated coughing actions (upper panel of Figure 4.19 h). The processed data by short-time Fourier transform (STFT) spectrogram (lower panel of Figure 4.19 h) evidenced that the frequency band spectrum of coughing sound covers the frequency range up to 700 Hz which is in the same frequency characteristics of healthy young people coughing sound [263]. Therefore, the sensor could be used in diagnosis patient's damaged vocal cords, chronic obstructive pulmonary disease (COPD) such as, asthma, chronic bronchitis etc. by assessing frequency band of coughing action and even for early intervention of COVID-19 [251, 264]. In order to analyze the damaged vocal cords, another potential method is to noninvasively monitor the epidermis as well as muscle movement deformation around the throat during phonation. We attached the sensor as a speech pattern recognition system, firmly to the human speaker's neck. Interestingly, when different words (such as 'O' , 'N' , 'P' , 'D' , 'L' ) were spoken by the volunteer, the device was also capable to detect the vocal cord vibration synchronous to the speaking words and generated the electrical signal (Figure 4.19 i). In this case, the sensor mimics the vocal cord deformation in order to generate vibrotactile output signal waveform. The time-dependent position and amplitude of signal waveforms and corresponding STFT processed 3D-spectrograms agree with acoustic profile of each alphabet (Figure 4.19 j). It is evident that the maximum amplitude of all words is almost within the frequency range of 0–800 Hz (i.e., within the limit of vocal cord vibration frequency) [2]. Therefore, the developed

sensor has the potential to develop vibrotactile hearing aids, aiding in speech rehabilitation training.

#### **4.2.11 Conclusion**

we have demonstrated the concept and a set of design rules to establish a bio-piezoelectric platform having good biocompatibility and piezoelectricity via integrating the biologically active bacteria and organic PVDF polymer. The bacterial protein engineered the microstructure of PVDF to develop porous bio-organic film and also interacted with the polymer chain to enhance the electroactive phase content and crystallinity. With appropriate content of bacterial protein, much improved piezoelectric co-efficient ( $d_{33} \sim -42.7$  pC/N) and figure of merit ( $F_oM_p \sim 18.8 \times 10^{-12}$  Pa<sup>-1</sup>) were achieved in the bio-organic film which eventually benefited towards power generation ( $\sim 640$  mW/m<sup>2</sup>) that outperformed the previously developed piezoelectric and even triboelectric nanogenerators. This impressive bio-organic film based nanogenerator was not only demonstrated to be useful in powering consumer electronics but also implemented in the direction of realtime physiological signal detection based clinical applications. Deployed as piezoelectric energy harvester, our rationally designed bacterial protein engineered bio-organic film open a new avenue for next generation sustainable and autonomous biomedical systems with minimal invasiveness.

Chapter 5

**Conclusion and Future Outlook**

## **5.1 General Conclusion of thesis:**

The main focus of this thesis belongs to describe favourable technique to diminish environmental pollution includes air pollution, soil or water pollution created by extreme use of fossil fuels and heavy metals. Various physical, chemical or biological processes have been developed to control the environmental pollution depending on their own benefits. In this regard, natural bacteria are an ideal choice which account for most of the biomass on earth. Bacteria, a living bio-factories possess a unique feature to experience evolutionary adaption in relatively short time period and effectively engineered the materials microstructure and properties rather than other inorganic and chemical catalyst. Owing their ecological and biological importance, there are multifaceted applications of bacteria including but not limited to agricultural, medical and industrial, also employed as bioremediation agent of heavy metal removal and energy material in self-powered piezoelectric energy harvester. Whereas thermophilic bacteria have its own utility being survive at extreme high temperature provides the image of first life on earth. In this work, some thermophilic bacteria such as MDH1, BKH2 were used to remove heavy metal contamination from aqueous solution and in fabrication of piezoelectric nanogenerator for energy harvesting.

Now a days heavy metal contamination reaches a serious threat to human life because of extreme exposure of heavy metals from different sources like untreated industrial wastewater. Thermophilic bacteria able to survive in extreme environment possesses heavy metal tolerance and reduce ability. A noble thermophilic bacterium named MDH1 was collected from hot spring of Metaldanga of temperature 42° C, cultivated in laboratory. The MDH1 bacterium secretes some extra-cellular protein in its growth media which was collected and purified and used as biological template for the removal of lead from lead nitrate aqueous solution. Lead, one of the most fatal elements for human health was found everywhere in the

environment. Pursuing the eco-friendly route, bacterial protein removed the lead from lead nitrate solution as precipitation of lead oxide nanoplates. Whereas, the well grown *E. coli* bacterium in presence of the supernatant solution provides the evidence of the non-toxicity of the lead-free solution. Furthermore, the precipitated lead oxide nanoplates were utilized in dye degradation activity where using photocatalytic property, MO and BB dyes were properly degraded by the nanoplates. Therefore, the MDH1 microbial protein is very impactful for cleaning of lead contaminated water as well as BB and MO contaminated industrial effluents, foods and several agricultural products.

On the other side, extreme burn of fossil fuel not only generates environmental pollution but the world faces a high level of energy crisis. Therefore, to overcome these problems renewable energy source such as piezoelectric energy harvester is the only favourable option in which environmental mechanical vibration convert to electrical energy and increase applicability not only in portable electrical devices but also in biomedical field. In this work, a noble thermophilic bacterium named BKH2 collected from Bakreshwar hot spring of temperature 65 °C was cultivated in laboratory whose extra-cellular protein was used to prepare piezoelectric film along with organic piezoelectric materials such as poly(vinylidene fluoride) (PVDF). The bacterial protein engineered the microstructure of PVDF to develop highly bio-compatible porous bio-organic film and interacted with the PVDF chain to nucleate self-polarized  $\beta$ -phase and enhanced crystallinity. This bio-organic film was used to fabricate self-powered, flexible and biocompatible bio-organic piezoelectric nanogenerator operated as energy harvester. With appropriate content of bacterial protein, much improved piezoelectric co-efficient and figure of merit were achieved in the bio-organic film which eventually benefited towards power generation that outperformed the previously developed piezoelectric and even triboelectric nanogenerators. This impressive bio-organic film based nanogenerator was not only demonstrated to be useful in powering consumer electronics such



as driving commercial LEDs and charge capacitors but also implemented in the direction of real-time physiological signal detection based clinical applications. Deployed as piezoelectric energy harvester, our rationally designed bacterial protein engineered bio-organic film open a new avenue for next generation sustainable and autonomous biomedical systems with minimal invasiveness.

Thus, owing to the effective feature of the environmental thermophilic bacteria, the two-challenging problem of the planet i.e., pollution and energy crisis can be minimised successfully and make our environment healthy and sustainable.

## **5.2 Future work:**

In case of environmental safety, there are a lot of work that will be performed regarding heavy metal removal and renewable energy generation.

### **Heavy metal removal:**

In this work, a green technique was used to remove the lead from lead nitrate solution as the form of lead oxide nanoplates. Now, this technique will be used for the removal of lead from lead contaminated drinking water in a large scale. This green technique will also be applied in the removal of arsenic, mercury and another toxic heavy metal from contaminated drinking water which is one of the main challenges of human life.

Therefore, the future work related to heavy metal removal is as follows:

- (i) Use this bacterium based green technique in large scale removal of lead from the contaminated drinking water.
- (ii) Remove arsenic, mercury and another toxic heavy metal from contaminated water, soil, and also from agricultural items to prevent the carcinogenic effect of these water into the human body.
- (ii) the thermophilic bacterial protein could be directly applied to the industrial waste water to remove toxic materials such that they can't be mixed into the environment.
- (iv) A Membrane might be designed using bacteria and its protein which can be used as bio-filter that can filter heavy metals from contaminated water, food and wastewater.

### **Energy harvester:**

Although some promising applications of the piezoelectric nanogenerator has been demonstrated here and the bio-organic film was utilized in piezoelectric process of energy harvesting. But there is no doubt that there exist another attractive energy harvesting process and applications waiting for being discovered. To conduct future research, several possible and effective investigation topics are summarized as follows:

(i) Pyroelectric nanogenerator, a thermal energy harvesting device provides potential in waste heat energy harvesting. The bio-organic film will be used in pyroelectric nanogenerator to harvest waste heat energy and implement them in temperature imaging, environmental monitoring and personal electronics.

(ii) In recent times, triboelectric nanogenerator is also promising technology for mechanical-to-electrical energy conversion. Therefore, the bio-organic film may be impactful in the fabrication of triboelectric nanogenerator which will be applied in green energy harvesting, wearable electronics and biomedical monitoring.

(iii) The bio-organic film based piezo- and pyro-electric energy harvesters could be directly integrated to the solar cell to obtain higher renewable energy generation.

(iv) furthermore, the film could be used in electronic skin (e-skin) fabrication which refers to stretchable, flexible and self-healing electronics that could be able to mimic functionalities of human or animal skin.

(v) Using the combination of bacterial protein and PVDF, the nano-fiber would be fabricated through electrospinning technique which applied in piezo-, tribo-electric energy harvester to get better results.

The intension of this work to implement the nanogenerator in a large-scale area such that the energy deficiency might be recovered by the eco-friendly green renewable energy source.

Chapter 6

# References

1. World Health Organization. Regional Office for Europe. & Joint WHO/Convention Task Force on the Health Aspects of Air Pollution., *Health risks of heavy metals from long-range transboundary air pollution* (World Health Organization Regional Office Europe, 2007).
2. J. Duruibe & J. Egwurugwu, *Heavy Metal Pollution and Human Biotoxic Effects Corrosion study, and waste management View project Effects of Formalin Inhalation on Physical Characteristics and Renal Profile of Albino Wistar Rats View project* (2007).
3. W. Treder & G. Cieslinski, Effect of silicon application on cadmium uptake and distribution in strawberry plants grown on contaminated soils. *Journal of Plant Nutrition*, **28** (2005) 917–929. <https://doi.org/10.1081/PLN-200058877>.
4. K. H. Vardhan, P. S. Kumar, & R. C. Panda, A review on heavy metal pollution, toxicity and remedial measures: Current trends and future perspectives. *Journal of Molecular Liquids*, **290** (2019). <https://doi.org/10.1016/j.molliq.2019.111197>.
5. C. Zou, Q. Zhao, G. Zhang, & B. Xiong, Energy revolution: From a fossil energy era to a new energy era. *Natural Gas Industry B*, **3** (2016) 1–11. <https://doi.org/10.1016/j.ngib.2016.02.001>.
6. A. Zecca & L. Chiari, Fossil-fuel constraints on global warming. *Energy Policy*, **38** (2010) 1–3. <https://doi.org/10.1016/j.enpol.2009.06.068>.
7. K. T. Konstantinidis, A. Ramette, & J. M. Tiedje, The bacterial species definition in the genomic era. *Philosophical Transactions of the Royal Society B: Biological Sciences* (Royal Society, 2006), pp. 1929–1940. <https://doi.org/10.1098/rstb.2006.1920>.
8. W. F. Martin & F. L. Sousa, Early microbial evolution: The age of anaerobes. *Cold Spring Harbor Perspectives in Biology*, **8** (2016). <https://doi.org/10.1101/cshperspect.a018127>.
9. A. L. Koch, *Control of the Bacterial Cell Cycle by Cytoplasmic Growth* (2002).
10. H. Sutar, *A Review on: Bioremediation Publication Preview Source Electrical Behaviour and Spherulites Morphology of HDPE/PP Polyblends with HDPE as Base*

*Material View project Study the characteristics of nano-graphene incorporated polypropylene View project* (2012).

11. R. Saraswat, D. Saraswat, & M. Yadav, A REVIEW ON BIOREMEDIATION OF HEAVY METALS BY MICROBES. *International Journal of Advanced Research*, **8** (2020) 200–210. <https://doi.org/10.21474/IJAR01/11281>.
12. A. Spain, C. by, & E. Alm, *Implications of Microbial Heavy Metal Tolerance in the Environment* (2003).
13. P. Turner, G. Mamo, & E. N. Karlsson, Potential and utilization of thermophiles and thermostable enzymes in biorefining. *Microbial Cell Factories*, **6** (2007). <https://doi.org/10.1186/1475-2859-6-9>.
14. C. Trigona, S. Graziani, G. di Pasquale, A. Pollicino, R. Nisi, & A. Licciulli, Green energy harvester from vibrations based on bacterial cellulose. *Sensors (Switzerland)*, **20** (2020). <https://doi.org/10.3390/s20010136>.
15. A. Chien, D. B. Edgar, & J. M. Trela, *Deoxyribonucleic Acid Polymerase from the Extreme Thermophile Thermus aquaticus* (1976).
16. M. Biswas, S. Majumdar, T. Chowdhury, B. Chattopadhyay, S. Mandal, U. Halder, & S. Yamasaki, Bioremediase a unique protein from a novel bacterium BKH1, ushering a new hope in concrete technology. *Enzyme and Microbial Technology*, **46** (2010) 581–587. <https://doi.org/10.1016/j.enzmictec.2010.03.005>.
17. S. Show, A. Tamang, T. Chowdhury, D. Mandal, & B. Chattopadhyay, Bacterial (BKH1) assisted silica nanoparticles from silica rich substrates: A facile and green approach for biotechnological applications. *Colloids and Surfaces B: Biointerfaces*, **126** (2015) 245–250. <https://doi.org/10.1016/j.colsurfb.2014.12.039>.
18. M. Sarkar, N. Alam, B. Chaudhuri, B. Chattopadhyay, & S. Mandal, Development of an improved E. coli bacterial strain for green and sustainable concrete technology. *RSC Advances*, **5** (2015) 32175–32182. <https://doi.org/10.1039/c5ra02979a>.
19. N. Alam, M. Sarkar, T. Chowdhury, D. Ghosh, & B. Chattopadhyay, Characterization of a Novel MDH1 Bacterium from a Virgin Hot Spring Applicable for Gold Nanoparticle (GNPs) Synthesis. *Advances in Microbiology*, **06** (2016) 724–732. <https://doi.org/10.4236/aim.2016.69071>.

20. S. J. Hawkes, *Information • Textbooks • Media • Resources What Is a “Heavy Metal”?* (1997).
21. M. Edelstein & M. Ben-Hur, Heavy metals and metalloids: Sources, risks and strategies to reduce their accumulation in horticultural crops. *Scientia Horticulturae*, **234** (2018) 431–444. <https://doi.org/10.1016/j.scienta.2017.12.039>.
22. P. S. Kumar & R. Gayathri, *ADSORPTION OF Pb 2+ IONS FROM AQUEOUS SOLUTIONS ONTO BAEL TREE LEAF POWDER: ISOTHERMS, KINETICS AND THERMODYNAMICS STUDY Nomenclatures* (2009).
23. M. Jaishankar, T. Tseten, N. Anbalagan, B. B. Mathew, & K. N. Beeregowda, Toxicity, mechanism and health effects of some heavy metals. *Interdisciplinary Toxicology*, **7** (2014) 60–72. <https://doi.org/10.2478/intox-2014-0009>.
24. R. Reza, ; G Singh, & \* R Reza, Heavy metal contamination and its indexing approach for river water. *Int. J. Environ. Sci. Tech*, **7** (2010) 785–792.
25. M. S. Sankhla, M. Kumari, M. Nandan, R. Kumar, & P. Agrawal, Heavy Metals Contamination in Water and their Hazardous Effect on Human Health-A Review. *International Journal of Current Microbiology and Applied Sciences*, **5** (2016) 759–766. <https://doi.org/10.20546/ijcmas.2016.510.082>.
26. M. Zaynab, R. Al-Yahyai, A. Ameen, Y. Sharif, L. Ali, M. Fatima, K. A. Khan, & S. Li, Health and environmental effects of heavy metals. *Journal of King Saud University - Science*, **34** (2022). <https://doi.org/10.1016/j.jksus.2021.101653>.
27. H. B. Bradl, *Heavy Metals in the Environment Sources and Origins of Heavy Metals*.
28. B. V. Ghinwa M. Naja, *Toxicity and Sources of Pb, Cd, Hg, Cr, As, and Radionuclides in the Environment* (2017).
29. M. Hanna-Attisha, J. LaChance, R. C. Sadler, & A. C. Schnepf, Elevated blood lead levels in children associated with the flint drinking water crisis: A spatial analysis of risk and public health response. *American Journal of Public Health*, **106** (2016) 283–290. <https://doi.org/10.2105/AJPH.2015.303003>.
30. T. Akiyama, *Integral Leadership Education for Sustainable Development Creation of An Integral Framework of Everything: Explorations of Post-Cartesian Paradigm View project Development of Sustainability Assessment Method View project* (2012).

31. G. Theses, C. A. Pace, by A. Cynthia Pace, M. Professor, D. A. Himmelgreen, M. Schmink, H. P. da Silva, L. M. Whiteford, & R. K. Zarger, *Scholar Commons Ripple Effects of the Belo Monte Dam: A Syndemic Approach to Addressing Health Impacts for the Downstream Community of Gurupá* (2018).
32. *BIOGEOCHEMICAL PROCESSES CONTROLLING METAL BEHAVIOR IN THE CRITICAL ZONE.*
33. A. K. Singh, S. C. Srivastava, P. Verma, A. Ansari, & A. Verma, Hazard assessment of metals in invasive fish species of the Yamuna River, India in relation to bioaccumulation factor and exposure concentration for human health implications. *Environmental monitoring and assessment*, **186** (2014) 3823–3836. <https://doi.org/10.1007/s10661-014-3660-6>.
34. M. Wasim Aktar, M. Paramasivam, M. Ganguly, S. Purkait, & D. Sengupta, Assessment and occurrence of various heavy metals in surface water of Ganga river around Kolkata: A study for toxicity and ecological impact. *Environmental Monitoring and Assessment*, **160** (2010) 207–213. <https://doi.org/10.1007/s10661-008-0688-5>.
35. F. Y. Aljaberi, Studies of autocatalytic electrocoagulation reactor for lead removal from simulated wastewater. *Journal of Environmental Chemical Engineering*, **6** (2018) 6069–6078. <https://doi.org/10.1016/j.jece.2018.09.032>.
36. U. Zulfiqar, M. Farooq, S. Hussain, M. Maqsood, M. Hussain, M. Ishfaq, M. Ahmad, & M. Z. Anjum, Lead toxicity in plants: Impacts and remediation. *Journal of Environmental Management*, **250** (2019). <https://doi.org/10.1016/j.jenvman.2019.109557>.
37. *IARC (International Agency for Research on Cancer), October, 30, https://monographs.iarc.fr/list-of-classifications/, 2021. .*
38. *National Toxicological Program (NTP), U. S. Department of Health and Human Services (US DHHS), October, 30, 2021, http://ntp.niehs.nih.gov/go/roc. .*
39. M. M. Rao, D. K. Ramana, K. Seshaiyah, M. C. Wang, & S. W. C. Chien, Removal of some metal ions by activated carbon prepared from Phaseolus aureus hulls. *Journal of*



*Hazardous Materials*, **166** (2009) 1006–1013.  
<https://doi.org/10.1016/j.jhazmat.2008.12.002>.

40. R. Ahmad & S. Haseeb, Kinetic, isotherm and thermodynamic studies for the removal of Pb<sup>2+</sup> ion by a novel adsorbent *Luffa acutangula* (LAPR). *Desalination and Water Treatment*, **57** (2016) 17826–17835. <https://doi.org/10.1080/19443994.2015.1088476>.
41. J. Anna & E. M. V. Hoek, Removing cadmium ions from water via nanoparticle-enhanced ultrafiltration. *Environmental Science and Technology*, **44** (2010) 2570–2576. <https://doi.org/10.1021/es902310e>.
42. A. E. Ofomaja, E. B. Naidoo, & S. J. Modise, Biosorption of copper(II) and lead(II) onto potassium hydroxide treated pine cone powder. *Journal of Environmental Management*, **91** (2010) 1674–1685. <https://doi.org/10.1016/j.jenvman.2010.03.005>.
43. J. R. Parga, D. L. Cocke, J. L. Valenzuela, J. A. Gomes, M. Kesmez, G. Irwin, H. Moreno, & M. Weir, Arsenic removal via electrocoagulation from heavy metal contaminated groundwater in la Comarca Lagunera México. *Journal of Hazardous Materials*, **124** (2005) 247–254. <https://doi.org/10.1016/j.jhazmat.2005.05.017>.
44. K. K. Bhatluri, M. S. Manna, P. Saha, & A. K. Ghoshal, Supported liquid membrane-based simultaneous separation of cadmium and lead from wastewater. *Journal of Membrane Science*, **459** (2014) 256–263. <https://doi.org/10.1016/j.memsci.2014.02.019>.
45. Y. Chen, B. Pan, H. Li, W. Zhang, L. Lv, & J. Wu, Selective removal of Cu(II) ions by using cation-exchange resin-supported polyethyleneimine (PEI) nanoclusters. *Environmental Science and Technology*, **44** (2010) 3508–3513. <https://doi.org/10.1021/es100341x>.
46. A. Abidli, Y. Huang, Z. ben Rejeb, A. Zaoui, & C. B. Park, Sustainable and efficient technologies for removal and recovery of toxic and valuable metals from wastewater: Recent progress, challenges, and future perspectives. *Chemosphere*, **292** (2022). <https://doi.org/10.1016/j.chemosphere.2021.133102>.
47. S. Ray & M. Kanti Ray, *Bioremediation Of Heavy Metal Toxicity-With Special Reference To Chromium*.

48. A. Kulshreshtha, R. Agrawal, M. Barar, & S. Saxena, A Review on Bioremediation of Heavy Metals in Contaminated Water. *IOSR Journal of Environmental Science, Toxicology and Food Technology*, **8** (2014) 44–50. <https://doi.org/10.9790/2402-08714450>.
49. R. Dixit, Wasiullah, D. Malaviya, K. Pandiyan, U. B. Singh, A. Sahu, R. Shukla, B. P. Singh, J. P. Rai, P. K. Sharma, H. Lade, & D. Paul, Bioremediation of heavy metals from soil and aquatic environment: An overview of principles and criteria of fundamental processes. *Sustainability (Switzerland)*, **7** (2015) 2189–2212. <https://doi.org/10.3390/su7022189>.
50. A. Singh, D. B. Pal, A. Mohammad, A. Alhazmi, S. Haque, T. Yoon, N. Srivastava, & V. K. Gupta, Biological remediation technologies for dyes and heavy metals in wastewater treatment: New insight. *Bioresource Technology*, **343** (2022). <https://doi.org/10.1016/j.biortech.2021.126154>.
51. Sterritt, R. M., and J. M. Lester. 1996. Heavy metals immobilization by bacterial extracellular polymers. In *Immobilization of Ions by Bio-sorption*, H. Eccles and J. Hunt (eds.). London: Chemistry Society, 121–134. (n.d.).
52. G. Girma, Microbial Bioremediation of some Heavy Metals in Soils: An updated review. *Egyptian Academic Journal of Biological Sciences G. Microbiology*, **7** (2015) 29–45.
53. I. Fitri Purwanti, S. Budi Kurniawan, H. Sulistiyaning Titah, & B. Voijant Tangahu, Article ID: IJCIET\_09\_02\_091 Isolated from Aluminium Recycling Area. *International Journal of Civil Engineering and Technology (IJCIET)*, **9** (2018) 945–954.
54. A. A. Juwarkar & S. K. Yadav, Bioaccumulation and Biotransformation of Heavy Metals. *Bioremediation Technology* (Springer Netherlands, 2010), pp. 266–284. [https://doi.org/10.1007/978-90-481-3678-0\\_9](https://doi.org/10.1007/978-90-481-3678-0_9).
55. P. M. Fernández, S. C. Viñarta, A. R. Bernal, E. L. Cruz, & L. I. C. Figueroa, Bioremediation strategies for chromium removal: Current research, scale-up approach and future perspectives. *Chemosphere*, **208** (2018) 139–148. <https://doi.org/10.1016/j.chemosphere.2018.05.166>.

56. M. Ahemad, Remediation of metalliferous soils through the heavy metal resistant plant growth promoting bacteria: Paradigms and prospects. *Arabian Journal of Chemistry*, **12** (2019) 1365–1377. <https://doi.org/10.1016/j.arabjc.2014.11.020>.
57. O. Chaalal, A. Y. Zekri, & R. Islam, Uptake of heavy metals by microorganisms: An experimental approach. *Energy Sources*, **27** (2005) 87–100. <https://doi.org/10.1080/00908310490448136>.
58. S. K. Chatterjee, I. Bhattacharjee, & G. Chandra, Biosorption of heavy metals from industrial waste water by *Geobacillus thermodenitrificans*. *Journal of Hazardous Materials*, **175** (2010) 117–125. <https://doi.org/10.1016/j.jhazmat.2009.09.136>.
59. S. Ilyas, J. C. Lee, & B. S. Kim, Bioremoval of heavy metals from recycling industry electronic waste by a consortium of moderate thermophiles: Process development and optimization. *Journal of Cleaner Production*, **70** (2014) 194–202. <https://doi.org/10.1016/j.jclepro.2014.02.019>.
60. A. Rakhmawati, E. T. Wahyuni, & T. Yuwono, Potential application of thermophilic bacterium *Aeribacillus pallidus* MRP280 for lead removal from aqueous solution. *Heliyon*, **7** (2021). <https://doi.org/10.1016/j.heliyon.2021.e08304>.
61. K. Simkiss and K. M. Wilbur, *Biomineralization*, Academic, New York, NY, USA, 1989. (n.d.).
62. S. Mann, *Biomineralization: Principles and Concepts in Bioinorganic Materials Chemistry*, Oxford University Press, Oxford, UK, 2001. (n.d.).
63. X. Li, H. Xu, Z. S. Chen, & G. Chen, Biosynthesis of nanoparticles by microorganisms and their applications. *Journal of Nanomaterials*, **2011** (2011). <https://doi.org/10.1155/2011/270974>.
64. N. I. Hulkoti & T. C. Taranath, Biosynthesis of nanoparticles using microbes-A review. *Colloids and Surfaces B: Biointerfaces*, **121** (2014) 474–483. <https://doi.org/10.1016/j.colsurfb.2014.05.027>.
65. C. Y. Wu, Nanoparticles and the environment. *Journal of the Air and Waste Management Association*, **55** (2005) 708–746. <https://doi.org/10.1080/10473289.2005.10464656>.

66. J. Kreuter, Nanoparticles-a historical perspective. *International Journal of Pharmaceutics*, **331** (2007) 1–10. <https://doi.org/10.1016/j.ijpharm.2006.10.021>.
67. V. J. Mohanraj & Y. Chen, *Nanoparticles-A Review* (2006).
68. Y. Xia, Y. Xiong, B. Lim, & S. E. Skrabalak, Shape-controlled synthesis of metal nanocrystals: Simple chemistry meets complex physics? *Angewandte Chemie - International Edition*, **48** (2009) 60–103. <https://doi.org/10.1002/anie.200802248>.
69. B. Haley & E. Frenkel, Nanoparticles for drug delivery in cancer treatment. *Urologic Oncology: Seminars and Original Investigations*, **26** (2008) 57–64. <https://doi.org/10.1016/j.urolonc.2007.03.015>.
70. P. Couvreur, Nanoparticles in drug delivery: Past, present and future. *Advanced Drug Delivery Reviews*, **65** (2013) 21–23. <https://doi.org/10.1016/j.addr.2012.04.010>.
71. A. de la Isla, W. Brostow, B. Bujard, M. Estevez, J. R. Rodriguez, S. Vargas, & V. M. Castaño, Nanohybrid scratch resistant coatings for teeth and bone viscoelasticity manifested in tribology. *Materials Research Innovations*, **7** (2003) 110–114. <https://doi.org/10.1080/14328917.2003.11784770>.
72. M. Holzinger, A. le Goff, & S. Cosnier, Nanomaterials for biosensing applications: A review. *Frontiers in Chemistry*, **2** (2014). <https://doi.org/10.3389/fchem.2014.00063>.
73. D. Beydoun, R. Amal, G. Low, & S. Mcevoy, *Role of nanoparticles in photocatalysis* (1999).
74. L. Wang, C. Hu, & L. Shao, The antimicrobial activity of nanoparticles: Present situation and prospects for the future. *International Journal of Nanomedicine*, **12** (2017) 1227–1249. <https://doi.org/10.2147/IJN.S121956>.
75. I. Matsui, *Journal Review Nanoparticles for Electronic Device Applications: A Brief Review* (2005).
76. nano particle \_heavy metal rem. (n.d.).
77. J. Huang, L. Lin, D. Sun, H. Chen, D. Yang, & Q. Li, Bio-inspired synthesis of metal nanomaterials and applications. *Chemical Society Reviews*, **44** (2015) 6330–6374. <https://doi.org/10.1039/c5cs00133a>.

78. F. Gralla, D. J. Abson, A. P. Møller, D. J. Lang, U. Vilsmaier, B. K. Sovacool, & H. von Wehrden, Nuclear accidents call for transdisciplinary nuclear energy research. *Sustainability Science*, **10** (2014) 179–183. <https://doi.org/10.1007/s11625-014-0260-x>.
79. O. Ellabban, H. Abu-Rub, & F. Blaabjerg, Renewable energy resources: Current status, future prospects and their enabling technology. *Renewable and Sustainable Energy Reviews*, **39** (2014) 748–764. <https://doi.org/10.1016/j.rser.2014.07.113>.
80. N. Scovronick, M. Budolfson, F. Dennig, F. Errickson, M. Fleurbaey, W. Peng, R. H. Socolow, D. Spears, & F. Wagner, The impact of human health co-benefits on evaluations of global climate policy. *Nature Communications*, **10** (2019). <https://doi.org/10.1038/s41467-019-09499-x>.
81. “Record clean energy spending is set to help global energy investment grow by 8% in 2022 - News”. IEA. Retrieved 27 June 2022.
82. “Global energy transformation: A roadmap to 2050 (2019 edition)”. </publications/2019/Apr/Global-energy-transformation-A-roadmap-to-2050-2019Edition>. Archived from the original on 18 April 2019. Retrieved 9 December 2020.
83. Y. Zi, H. Guo, Z. Wen, M. H. Yeh, C. Hu, & Z. L. Wang, Harvesting Low-Frequency (<5 Hz) Irregular Mechanical Energy: A Possible Killer Application of Triboelectric Nanogenerator. *ACS Nano*, **10** (2016) 4797–4805. <https://doi.org/10.1021/acsnano.6b01569>.
84. Y. Zi & Z. L. Wang, Nanogenerators: An emerging technology towards nanoenergy. *APL Materials*, **5** (2017). <https://doi.org/10.1063/1.4977208>.
85. Z. L. Wang, On Maxwell’s displacement current for energy and sensors: the origin of nanogenerators. *Materials Today*, **20** (2017) 74–82. <https://doi.org/10.1016/j.mattod.2016.12.001>.
86. Y. Hu, Y. Zhang, C. Xu, L. Lin, R. L. Snyder, & Z. L. Wang, Self-powered system with wireless data transmission. *Nano Letters*, **11** (2011) 2572–2577. <https://doi.org/10.1021/nl201505c>.

87. G Gautschi, *Gautschi, G., 2006. Piezoelectric Sensorics: Force Strain Pressure Acceleration and Acoustic Emission Sensors Materials and Amplifiers. Springer Science & Business Media.*
88. W. M. Prest & D. J. Luca, The formation of the  $\gamma$  phase from the  $\alpha$  and  $\beta$  polymorphs of polyvinylidene fluoride. *Journal of Applied Physics*, **49** (1978) 5042–5047. <https://doi.org/10.1063/1.324439>.
89. B.-E. el Mohajir & N. Heymans, *Changes in structural and mechanical behaviour of PVDF with processing and thermomechanical treatments. 1. Change in structure.*
90. E. Fukada, *Special Issue Papers History and Recent Progress in Piezoelectric Polymers* (2000).
91. A. Salimi & A. A. Yousefi, FTIR studies of  $\beta$ -phase crystal formation in stretched PVDF films. *Polymer Testing*, **22** (2003) 699–704. [https://doi.org/10.1016/S0142-9418\(03\)00003-5](https://doi.org/10.1016/S0142-9418(03)00003-5).
92. P. Martins, A. C. Lopes, & S. Lanceros-Mendez, Electroactive phases of poly(vinylidene fluoride): Determination, processing and applications. *Progress in Polymer Science*, **39** (2014) 683–706. <https://doi.org/10.1016/j.progpolymsci.2013.07.006>.
93. L. Ruan, X. Yao, Y. Chang, L. Zhou, G. Qin, & X. Zhang, Properties and applications of the  $\beta$  phase poly(vinylidene fluoride). *Polymers*, **10** (2018). <https://doi.org/10.3390/polym10030228>.
94. R. Hasegawa, Y. Takahashi, Y. Chatani, & H. T. Adokoro, *Crystal Structures of Three Crystalline Forms of Poly(vinylidene fluoride)* (1972).
95. S. Weinhold, M. H. Litt, & J. B. Lando, *The Crystal Structure of the  $\gamma$  Phase of Poly(vinylidene fluoride)* (UTC, 1980).
96. M. Li, H. J. Wondergem, M. J. Spijkman, K. Asadi, I. Katsouras, P. W. M. Blom, & D. M. de Leeuw, Revisiting the  $\delta$ -phase of poly(vinylidene fluoride) for solution-processed ferroelectric thin films. *Nature Materials*, **12** (2013) 433–438. <https://doi.org/10.1038/nmat3577>.
97. K. Tashiro, Ferroelectric polymers. (1995) 63–182.

98. A. Bachmann & J. B. Lando, *A Reexamination of the Crystal Structure of Phase II of Poly(vinylidene fluoride)* (1981).
99. H. M. G. Correia & M. M. D. Ramos, Quantum modelling of poly(vinylidene fluoride). *Comput Mater Sci* (2005), pp. 224–229. <https://doi.org/10.1016/j.commatsci.2004.12.040>.
100. L. Lu, W. Ding, J. Liu, & B. Yang, Flexible PVDF based piezoelectric nanogenerators. *Nano Energy*, **78** (2020). <https://doi.org/10.1016/j.nanoen.2020.105251>.
101. J. R. Brown, W. Ford Doolittle, & N. Scotia, *Archaea and the Prokaryote-to-Eukaryote Transition* (1997).
102. H. C. Flemming & S. Wuertz, Bacteria and archaea on Earth and their abundance in biofilms. *Nature Reviews Microbiology*, **17** (2019) 247–260. <https://doi.org/10.1038/s41579-019-0158-9>.
103. Wheelis M, *Principles of modern microbiology* (Sudbury, Mass: Jones and Bartlett Publishers, 2008).
104. T. Horiike, D. Miyata, K. Hamada, S. Saruhashi, T. Shinozawa, S. Kumar, R. Chakraborty, T. Komiyama, & Y. Tateno, Phylogenetic construction of 17 bacterial phyla by new method and carefully selected orthologs. *Gene*, **429** (2009) 59–64. <https://doi.org/10.1016/j.gene.2008.10.006>.
105. *Bacterial Growth Rates above 900C in Yellowstone Hot Springs*.
106. B. D. Drake, K. A. Campbell, J. v. Rowland, D. M. Guido, P. R. L. Browne, & A. Rae, Evolution of a dynamic paleo-hydrothermal system at Mangatete, Taupo Volcanic Zone, New Zealand. *Journal of Volcanology and Geothermal Research*, **282** (2014) 19–35. <https://doi.org/10.1016/j.jvolgeores.2014.06.010>.
107. D. J. des Marais & M. R. Walter, Terrestrial Hot Spring Systems: Introduction. *Astrobiology*, **19** (2019) 1419–1432. <https://doi.org/10.1089/ast.2018.1976>.
108. M. N. Parenteau & S. L. Cady, Microbial biosignatures in iron-mineralized phototrophic mats at Chocolate Pots hot springs, Yellowstone National Park, United States. *Palaios*, **25** (2010) 97–111. <https://doi.org/10.2110/palo.2008.p08-133r>.

109. A. Hiraishi, T. Umezawa, H. Yamamoto, K. Kato, & Y. Maki, *Changes in Quinone Profiles of Hot Spring Microbial Mats with a Thermal Gradient* (1999).
110. T. D. Brock, The value of basic research: Discovery of *thermus aquaticus* and other extreme thermophiles. *Genetics*, **146** (1997) 1207–1210. <https://doi.org/10.1093/genetics/146.4.1207>.
111. D. A. Comfort, S. R. Chhabra, S. B. Connors, C. J. Chou, K. L. Epting, M. R. Johnson, K. L. Jones, A. C. Sehgal, & R. M. Kelly, Strategic biocatalysis with hyperthermophilic enzymes. *Green Chemistry*, **6** (2004) 459–465. <https://doi.org/10.1039/b406297c>.
112. P. Turner, G. Mamo, & E. N. Karlsson, Potential and utilization of thermophiles and thermostable enzymes in biorefining. *Microbial Cell Factories*, **6** (2007). <https://doi.org/10.1186/1475-2859-6-9>.
113. P. Sommer, T. Georgieva, & B. K. Ahring, *Potential for using thermophilic anaerobic bacteria for bioethanol production from hemicellulose* (2003).
114. N. Sharma, G. Vyas, & S. Pathania, Culturable Diversity of Thermophilic Microorganisms Found in Hot Springs of Northern Himalayas and to Explore Their Potential for Production of Industrially Important Enzymes. *Scholars Academic Journal of Biosciences (SAJB) Sch. Acad. J. Biosci*, **1** (2013) 165–178.
115. Fergusson JE, editor. *The Heavy Elements: Chemistry, Environmental Impact and Health Effects*. Oxford: Pergamon Press; 1990. (n.d.).
116. S. Shallari, C. Schwartz, A. Haskob, J. L. Morelat, & S. Shallan, *Heavy metals in soils and plants of serpentine and industrial sites of Albania* (1998).
117. Z. L. He, X. E. Yang, & P. J. Stoffella, Trace elements in agroecosystems and impacts on the environment. *Journal of Trace Elements in Medicine and Biology*, **19** (2005) 125–140. <https://doi.org/10.1016/j.jtemb.2005.02.010>.
118. Nriagu JO. A global assessment of natural sources of atmospheric trace metals. *Nature*. 1989;338:47–49. (n.d.).
119. A. Arruti, I. Fernández-Olmo, & Á. Irabien, Evaluation of the contribution of local sources to trace metals levels in urban PM<sub>2.5</sub> and PM<sub>10</sub> in the Cantabria region



- (Northern Spain). *Journal of Environmental Monitoring*, **12** (2010) 1451–1458. <https://doi.org/10.1039/b926740a>.
120. P. B. Tchounwou, C. G. Yedjou, A. K. Patlolla, & D. J. Sutton, Heavy metal toxicity and the environment. *EXS*, **101** (2012) 133–164. [https://doi.org/10.1007/978-3-7643-8340-4\\_6](https://doi.org/10.1007/978-3-7643-8340-4_6).
121. M. Jaishankar, T. Tseten, N. Anbalagan, B. B. Mathew, & K. N. Beeregowda, Toxicity, mechanism and health effects of some heavy metals. *Interdisciplinary Toxicology*, **7** (2014) 60–72. <https://doi.org/10.2478/intox-2014-0009>.
122. P. C. Nagajyoti, K. D. Lee, & T. V. M. Sreekanth, Heavy metals, occurrence and toxicity for plants: A review. *Environmental Chemistry Letters*, **8** (2010) 199–216. <https://doi.org/10.1007/s10311-010-0297-8>.
123. K. Karlsson, M. Viklander, L. Scholes, & M. Revitt, Heavy metal concentrations and toxicity in water and sediment from stormwater ponds and sedimentation tanks. *Journal of Hazardous Materials*, **178** (2010) 612–618. <https://doi.org/10.1016/j.jhazmat.2010.01.129>.
124. K. Steenland & P. Boffetta, *Lead and Cancer in Humans: Where Are We Now?* (2000).
125. H. B. K. R. P Ravenscroft, *Ravenscroft, P., Brammer, H. and Richards, K., 2011. Arsenic pollution: a global synthesis. John Wiley & Sons.* (2011).
126. R. Singh, S. Singh, P. Parihar, V. P. Singh, & S. M. Prasad, Arsenic contamination, consequences and remediation techniques: A review. *Ecotoxicology and Environmental Safety*, **112** (2015) 247–270. <https://doi.org/10.1016/j.ecoenv.2014.10.009>.
127. M. Argos MPH, T. Kalra MPH, P. J. Rathouz, B. Pierce, H. Ahsan, J. Graziano, T. Islam MBBS, A. Ahmed MBBS, M. Rakibuz-Zaman MBBS, R. M. Hasan, G. B. Sarwar, L.-D. Earth, H. Ahsan, M. Argos, T. Kalra, P. J. Rathouz, Y. Chen, B. Pierce, F. Parvez, T. Islam, A. Ahmed, M. Rakibuz-Zaman, R. Hasan, G. Sarwar, V. Slavkovich, A. van Geen, & J. Graziano, Arsenic exposure from drinking water, and all-cause and chronic-disease mortalities in Bangladesh (HEALS): a prospective cohort study. *www.thelancet.com*, **376** (2010) 252–58. <https://doi.org/10.1016/S0140>.

128. C. Watanabe, T. Inaoka, T. Matsui, K. Ishigaki, N. Murayama, & R. Ohtsuka, Effects of arsenic on younger generations. *Journal of Environmental Science and Health - Part A Toxic/Hazardous Substances and Environmental Engineering*, **38** (2003) 129–139. <https://doi.org/10.1081/ESE-120016885>.
129. WHO, 2011. Guidelines for Drinking-Water Quality. vol. 4. World Health Organisation, Geneva, pp. 315–318. (n.d.).
130. J. C. Clifton, Mercury Exposure and Public Health. *Pediatric Clinics of North America*, **54** (2007) 237.e1-237.e45. <https://doi.org/10.1016/j.pcl.2007.02.005>.
131. K. M. Rice, E. M. Walker, M. Wu, C. Gillette, & E. R. Blough, Environmental mercury and its toxic effects. *Journal of Preventive Medicine and Public Health*, **47** (2014) 74–83. <https://doi.org/10.3961/jpmph.2014.47.2.74>.
132. Centers for Disease Control, 2017. Support Document to the 2015 Priority List of Hazardous Substances That Will Be Candidates for Toxicological Profiles.
133. M. Boskabady, N. Marefati, T. Farkhondeh, F. Shakeri, A. Farshbaf, & M. H. Boskabady, The effect of environmental lead exposure on human health and the contribution of inflammatory mechanisms, a review. *Environment International*, **120** (2018) 404–420. <https://doi.org/10.1016/j.envint.2018.08.013>.
134. H. Dapul & D. Laraque, Lead Poisoning in Children. *Advances in Pediatrics*, **61** (2014) 313–333. <https://doi.org/10.1016/j.yapd.2014.04.004>.
135. Zelikoff, J.T., Parsons, E., Schlesinger, R.B., 1993. Inhalation of particulate lead oxide disrupts pulmonary macrophage-mediated functions important for host defense and tumor surveillance in the lung. *Environ. Res.* 62, 207–222. (n.d.).
136. P. Ghosh, A. N. Samanta, & S. Ray, Reduction of COD and removal of Zn<sup>2+</sup> from rayon industry wastewater by combined electro-Fenton treatment and chemical precipitation. *Desalination*, **266** (2011) 213–217. <https://doi.org/10.1016/j.desal.2010.08.029>.
137. E. A. Deliyanni, G. Z. Kyzas, & K. A. Matis, Various flotation techniques for metal ions removal. *Journal of Molecular Liquids*, **225** (2017) 260–264. <https://doi.org/10.1016/j.molliq.2016.11.069>.

138. V. J. Inglezakis, M. A. Stylianou, D. Gkantzou, & M. D. Loizidou, Removal of Pb(II) from aqueous solutions by using clinoptilolite and bentonite as adsorbents. *Desalination*, **210** (2007) 248–256. <https://doi.org/10.1016/j.desal.2006.05.049>.
139. S. A. Kosa, G. Al-Zhrani, & M. Abdel Salam, Removal of heavy metals from aqueous solutions by multi-walled carbon nanotubes modified with 8-hydroxyquinoline. *Chemical Engineering Journal*, **181–182** (2012) 159–168. <https://doi.org/10.1016/j.cej.2011.11.044>.
140. J. H. Huang, G. M. Zeng, C. F. Zhou, X. Li, L. J. Shi, & S. B. He, Adsorption of surfactant micelles and Cd<sup>2+</sup>/Zn<sup>2+</sup> in micellar-enhanced ultrafiltration. *Journal of Hazardous Materials*, **183** (2010) 287–293. <https://doi.org/10.1016/j.jhazmat.2010.07.022>.
141. W. P. Zhu, S. P. Sun, J. Gao, F. J. Fu, & T. S. Chung, Dual-layer polybenzimidazole/polyethersulfone (PBI/PES) nanofiltration (NF) hollow fiber membranes for heavy metals removal from wastewater. *Journal of Membrane Science*, **456** (2014) 117–127. <https://doi.org/10.1016/j.memsci.2014.01.001>.
142. T. Bakalár, M. Búgel, & L. Gajdošová, *Heavy metal removal using reverse osmosis* (2009).
143. E. Assaad, A. Azzouz, D. Nistor, A. v. Ursu, T. Sajin, D. N. Miron, F. Monette, P. Niquette, & R. Hausler, Metal removal through synergic coagulation-flocculation using an optimized chitosan-montmorillonite system. *Applied Clay Science*, **37** (2007) 258–274. <https://doi.org/10.1016/j.clay.2007.02.007>.
144. Q. Chen, Z. Luo, C. Hills, G. Xue, & M. Tyrer, Precipitation of heavy metals from wastewater using simulated flue gas: Sequent additions of fly ash, lime and carbon dioxide. *Water Research*, **43** (2009) 2605–2614. <https://doi.org/10.1016/j.watres.2009.03.007>.
145. M. Fuerhacker, T. M. Haile, D. Kogelnig, A. Stojanovic, & B. Keppler, Application of ionic liquids for the removal of heavy metals from wastewater and activated sludge. *Water Science and Technology*, **65** (2012) 1765–1773. <https://doi.org/10.2166/wst.2012.907>.

146. X. Z. Yuan, Y. T. Meng, G. M. Zeng, Y. Y. Fang, & J. G. Shi, Evaluation of tea-derived biosurfactant on removing heavy metal ions from dilute wastewater by ion flotation. *Colloids and Surfaces A: Physicochemical and Engineering Aspects*, **317** (2008) 256–261. <https://doi.org/10.1016/j.colsurfa.2007.10.024>.
147. T. M. Zewail & N. S. Yousef, Kinetic study of heavy metal ions removal by ion exchange in batch conical air spouted bed. *Alexandria Engineering Journal*, **54** (2015) 83–90. <https://doi.org/10.1016/j.aej.2014.11.008>.
148. J. Hazarika, K. Pakshirajan, A. Sinharoy, & M. B. Syiem, Bioremoval of Cu(II), Zn(II), Pb(II) and Cd(II) by *Nostoc muscorum* isolated from a coal mining site. *Journal of Applied Phycology*, **27** (2015) 1525–1534. <https://doi.org/10.1007/s10811-014-0475-3>.
149. Head, I.M., 1998. Bioremediation: towards a credible technology. *Microbiology*, **144**(3), pp.599-608. (n.d.).
150. J. D. García-García, R. Sánchez-Thomas, & R. Moreno-Sánchez, Bio-recovery of non-essential heavy metals by intra- and extracellular mechanisms in free-living microorganisms. *Biotechnology Advances*, **34** (2016) 859–873. <https://doi.org/10.1016/j.biotechadv.2016.05.003>.
151. F. F. Masinire, D. O. Adenuga, S. M. Tichapondwa, & E. M. N. Chirwa, Remediation of Chromium(VI) containing wastewater using *Chrysopogon zizanioides* (Vetiver Grass). *Chemical Engineering Transactions*, **79** (2020) 385–390. <https://doi.org/10.3303/CET2079065>.
152. P. Heidari & A. Panico, Sorption Mechanism and Optimization Study for the Bioremediation of Pb(II) and Cd(II) Contamination by Two Novel Isolated Strains Q3 and Q5 of *Bacillus* sp. *International Journal of Environmental Research and Public Health*, **17** (2020) 1–20. <https://doi.org/10.3390/ijerph17114059>.
153. V. Kumar & S. K. Dwivedi, Hexavalent chromium stress response, reduction capability and bioremediation potential of *Trichoderma* sp. isolated from electroplating wastewater. *Ecotoxicology and Environmental Safety*, **185** (2019). <https://doi.org/10.1016/j.ecoenv.2019.109734>.

154. S. Sher, A. Ghani, S. Sultan, & A. Rehman, Bacterial Strains Isolated from Heavy Metals Contaminated Soil and Wastewater with Potential to Oxidize Arsenite. *Environmental Processes*, **8** (2021) 333–347. <https://doi.org/10.1007/s40710-020-00488-7>.
155. M. Kumar & K. Pakshirajan, Continuous removal and recovery of metals from wastewater using inverse fluidized bed sulfidogenic bioreactor. *Journal of Cleaner Production*, **284** (2021). <https://doi.org/10.1016/j.jclepro.2020.124769>.
156. A. S. Ayangbenro, O. O. Babalola, & O. S. Aremu, Biofloculant production and heavy metal sorption by metal resistant bacterial isolates from gold mining soil. *Chemosphere*, **231** (2019) 113–120. <https://doi.org/10.1016/j.chemosphere.2019.05.092>.
157. Y. Osman, A. Gebreil, A. M. Mowafy, T. I. Anan, & S. M. Hamed, Characterization of *Aspergillus niger* siderophore that mediates bioleaching of rare earth elements from phosphorites. *World Journal of Microbiology and Biotechnology*, **35** (2019). <https://doi.org/10.1007/s11274-019-2666-1>.
158. P. Sharma, S. Tripathi, P. Chaturvedi, D. Chaurasia, & R. Chandra, Newly isolated *Bacillus* sp. PS-6 assisted phytoremediation of heavy metals using *Phragmites communis*: Potential application in wastewater treatment. *Bioresource Technology*, **320** (2021). <https://doi.org/10.1016/j.biortech.2020.124353>.
159. S. Iravani & R. S. Varma, Bacteria in Heavy Metal Remediation and Nanoparticle Biosynthesis. *ACS Sustainable Chemistry and Engineering*, **8** (2020) 5395–5409. <https://doi.org/10.1021/acssuschemeng.0c00292>.
160. M. R. Afrooz, B. K. Moghadas, & S. Tamjidi, Performance of functionalized bacterial as bio-adsorbent for intensifying heavy metal uptake from wastewater: A review study. *Journal of Alloys and Compounds*, **893** (2022). <https://doi.org/10.1016/j.jallcom.2021.162321>.
161. H. Min-sheng, P. Jing, & Z. Le-ping, *Removal of Heavy Metals from Aqueous Solutions Using Bacteria* (2001).

162. C. H. Kang, Y. J. Kwon, & J. S. So, Bioremediation of heavy metals by using bacterial mixtures. *Ecological Engineering*, **89** (2016) 64–69. <https://doi.org/10.1016/j.ecoleng.2016.01.023>.
163. P. Sharma, Efficiency of bacteria and bacterial assisted phytoremediation of heavy metals: An update. *Bioresource Technology*, **328** (2021). <https://doi.org/10.1016/j.biortech.2021.124835>.
164. M. H. Saier, R. Tarn, A. Reizer, & J. Reizer, *Two novel families of bacterial membrane proteins concerned with nodulation, celi division and transport* (1994).
165. P. Sharma, A. K. Pandey, A. Udayan, & S. Kumar, Role of microbial community and metal-binding proteins in phytoremediation of heavy metals from industrial wastewater. *Bioresource Technology*, **326** (2021). <https://doi.org/10.1016/j.biortech.2021.124750>.
166. H. Zhang, S. Zhao, D. Li, X. Xu, & C. Li, Genome-Wide Analysis of the ZRT, IRT-Like Protein (ZIP) Family and Their Responses to Metal Stress in *Populus trichocarpa*. *Plant Molecular Biology Reporter*, **35** (2017) 534–549. <https://doi.org/10.1007/s11105-017-1042-2>.
167. S. Özdemir, E. Kılınç, A. Poli, & B. Nicolaus, Biosorption of heavy metals (Cd<sup>2+</sup>, Cu<sup>2+</sup>, Co<sup>2+</sup>, and Mn<sup>2+</sup>) by thermophilic bacteria, *geobacillus thermantarcticus* and *anoxybacillus amylolyticus*: Equilibrium and kinetic studies. *Bioremediation Journal*, **17** (2013) 86–96. <https://doi.org/10.1080/10889868.2012.751961>.
168. S. Ilyas, J. C. Lee, & B. S. Kim, Bioremoval of heavy metals from recycling industry electronic waste by a consortium of moderate thermophiles: Process development and optimization. *Journal of Cleaner Production*, **70** (2014) 194–202. <https://doi.org/10.1016/j.jclepro.2014.02.019>.
169. H. S. Levinson, I. Mahler, P. Blackwelder, & T. Hood, Lead resistance and sensitivity in *Staphylococcus aureus*. *FEMS Microbiology Letters*, **145** (1996) 421–425. <https://doi.org/10.1111/j.1574-6968.1996.tb08610.x>.
170. M. M. Naik & S. K. Dubey, Lead resistant bacteria: Lead resistance mechanisms, their applications in lead bioremediation and biomonitoring. *Ecotoxicology and Environmental Safety*, **98** (2013) 1–7. <https://doi.org/10.1016/j.ecoenv.2013.09.039>.

171. H. Chen, J. Xu, W. Tan, & L. Fang, Lead binding to wild metal-resistant bacteria analyzed by ITC and XAFS spectroscopy. *Environmental Pollution*, **250** (2019) 118–126. <https://doi.org/10.1016/j.envpol.2019.03.123>.
172. A. Rakhmawati, E. T. Wahyuni, & T. Yuwono, Potential application of thermophilic bacterium *Aeribacillus pallidus* MRP280 for lead removal from aqueous solution. *Heliyon*, **7** (2021). <https://doi.org/10.1016/j.heliyon.2021.e08304>.
173. K. Simkiss and K. M. Wilbur, *Biom mineralization*, Academic, New York, NY, USA, 1989. (n.d.).
174. S. Mann, *Biom mineralization: Principles and Concepts in Bioinorganic Materials Chemistry*, Oxford University Press, Oxford, UK, 2001.
175. I. W. S. Lin, C. N. Lok, & C. M. Che, Biosynthesis of silver nanoparticles from silver(i) reduction by the periplasmic nitrate reductase c-type cytochrome subunit NapC in a silver-resistant *E. coli*. *Chemical Science*, **5** (2014) 3144–3150. <https://doi.org/10.1039/c4sc00138a>.
176. N. I. Hulkoti & T. C. Taranath, Biosynthesis of nanoparticles using microbes-A review. *Colloids and Surfaces B: Biointerfaces*, **121** (2014) 474–483. <https://doi.org/10.1016/j.colsurfb.2014.05.027>.
177. N. Gandhi, D. Sirisha, & S. Asthana, Ijesrt International Journal of Engineering Sciences & Research Technology Microwave Mediated Green Synthesis of Lead (Pb) Nanoparticles And Its Potential Applications. *International Journal of Engineering Sciences & Research Technology*, . <https://doi.org/10.5281/zenodo.1161701>.
178. A. v. Borhade, D. R. Tope, & B. K. Uphade, An efficient photocatalytic degradation of methyl blue dye by using synthesised PbO nanoparticles. *E-Journal of Chemistry*, **9** (2012) 705–715. <https://doi.org/10.1155/2012/362680>.
179. A. Bratovic, Synthesis, Characterization, Applications, and Toxicity of Lead Oxide Nanoparticles. *Lead Chemistry* (IntechOpen, 2020). <https://doi.org/10.5772/intechopen.91362>.
180. A. Miri, M. Sarani, A. Hashemzadeh, Z. Mardani, & M. Darroudi, Biosynthesis and cytotoxic activity of lead oxide nanoparticles. *Green Chemistry Letters and Reviews*, **11** (2018) 567–572. <https://doi.org/10.1080/17518253.2018.1547926>.

181. R. Ramanathan, M. R. Field, A. P. O'Mullane, P. M. Smooker, S. K. Bhargava, & V. Bansal, Aqueous phase synthesis of copper nanoparticles: A link between heavy metal resistance and nanoparticle synthesis ability in bacterial systems. *Nanoscale*, **5** (2013) 2300–2306. <https://doi.org/10.1039/c2nr32887a>.
182. J. E. Mink, R. M. Qaisi, B. E. Logan, & M. M. Hussain, Energy harvesting from organic liquids in micro-sized microbial fuel cells. *NPG Asia Materials*, **6** (2014). <https://doi.org/10.1038/am.2014.1>.
183. N. Brochu, B. Belanger-Huot, D. Humeniuk, L. Gong, M. A. Amirdehi, J. Greener, & A. Miled, Bacteria energy recovery system using natural soil bacteria in microbial fuel cells. *Energies*, **14** (2021). <https://doi.org/10.3390/en14154393>.
184. C. Trigona, S. Graziani, G. di Pasquale, A. Pollicino, R. Nisi, & A. Licciulli, Green energy harvester from vibrations based on bacterial cellulose. *Sensors (Switzerland)*, **20** (2020). <https://doi.org/10.3390/s20010136>.
185. Z. L. Wang, & J. Song, Piezoelectric nanogenerators based on zinc oxide nanowire arrays. *Science*, **312** (2006), 242-246.
186. S. Xu, Y. Wei, J. Liu, R. Yang, & Z. L. Wang, Integrated multilayer nanogenerator fabricated using paired nanotip-to-nanowire brushes. *Nano Letters*, **8** (2008) 4027–4032. <https://doi.org/10.1021/nl8027813>.
187. R. Yang, Y. Qin, C. Li, G. Zhu, & Z. L. Wang, Converting biomechanical energy into electricity by a muscle-movement- driven nanogenerator. *Nano Letters*, **9** (2009) 1201–1205. <https://doi.org/10.1021/nl803904b>.
188. S. Xu, Y. Qin, C. Xu, Y. Wei, R. Yang, & Z. L. Wang, Self-powered nanowire devices. *Nature nanotechnology*, **5** (2010), 366-373.
189. Y. Hu & Z. L. Wang, *Recent Progress in Piezoelectric Nanogenerators as Sustainable Power Source in Self-powered Systems and Active Sensors* (2019).
190. F. R. Fan, Z. Q. Tian, & Z. Lin Wang, Flexible triboelectric generator. *Nano Energy*, **1** (2012) 328–334. <https://doi.org/10.1016/j.nanoen.2012.01.004>.
191. X. D. Xie, Q. Wang, & S. J. Wang, Energy harvesting from high-rise buildings by a piezoelectric harvester device. *Energy*, **93** (2015) 1345–1352. <https://doi.org/10.1016/j.energy.2015.09.131>.



192. D. W. Wang, J. L. Mo, X. F. Wang, H. Ouyang, & Z. R. Zhou, Experimental and numerical investigations of the piezoelectric energy harvesting via friction-induced vibration. *Energy Conversion and Management*, **171** (2018) 1134–1149. <https://doi.org/10.1016/j.enconman.2018.06.052>.
193. H. Madinei, H. Haddad Khodaparast, S. Adhikari, & M. I. Friswell, Design of MEMS piezoelectric harvesters with electrostatically adjustable resonance frequency. *Mechanical Systems and Signal Processing*, **81** (2015) 360–374. <https://doi.org/10.1016/j.ymsp.2016.03.023>.
194. Y. Sun, J. Chen, X. Li, Y. Lu, S. Zhang, & Z. Cheng, Flexible piezoelectric energy harvester/sensor with high voltage output over wide temperature range. *Nano Energy*, **61** (2019) 337–345. <https://doi.org/10.1016/j.nanoen.2019.04.055>.
195. X. Zhou, K. Parida, O. Halevi, Y. Liu, J. Xiong, S. Magdassi, & P. S. Lee, All 3D-printed stretchable piezoelectric nanogenerator with non-protruding kirigami structure. *Nano Energy*, **72** (2020). <https://doi.org/10.1016/j.nanoen.2020.104676>.
196. M. Y. Choi, D. Choi, M. J. Jin, I. Kim, S. H. Kim, J. Y. Choi, S. Y. Lee, J. M. Kim, & S. W. Kim, Mechanically powered transparent flexible charge-generating nanodevices with piezoelectric ZnO nanorods. *Advanced Materials*, **21** (2009) 2185–2189. <https://doi.org/10.1002/adma.200803605>.
197. D. Choi, M. Y. Choi, H. J. Shin, S. M. Yoon, J. S. Seo, J. Y. Choi, S. Y. Lee, J. M. Kim, & S. W. Kim, Nanoscale networked single-walled carbon-nanotube electrodes for transparent flexible nanogenerators. *Journal of Physical Chemistry C*, **114** (2010) 1379–1384. <https://doi.org/10.1021/jp909713c>.
198. D. Choi, M. Y. Choi, W. M. Choi, H. J. Shin, H. K. Park, J. K. Seo, J. Park, S. M. Yoon, S. Chae, Y. H. Lee, S. W. Kim, J. Y. Choi, S. Y. Lee, & J. M. Kim, Fully rollable transparent nanogenerators based on graphene electrodes. *Advanced Materials*, **22** (2010) 2187–2192. <https://doi.org/10.1002/adma.200903815>.
199. Y. Hu, Y. Zhang, C. Xu, L. Lin, R. L. Snyder, & Z. L. Wang, Self-powered system with wireless data transmission. *Nano Letters*, **11** (2011) 2572–2577. <https://doi.org/10.1021/nl201505c>.

200. R. Yang, Y. Qin, L. Dai, & Z. L. Wang, Power generation with laterally packaged piezoelectric fine wires. *Nature Nanotechnology*, **4** (2009) 34–39. <https://doi.org/10.1038/nnano.2008.314>.
201. S. Xu, Y. Qin, C. Xu, Y. Wei, R. Yang, & Z. L. Wang, Self-powered nanowire devices. *Nature Nanotechnology*, **5** (2010) 366–373. <https://doi.org/10.1038/nnano.2010.46>.
202. G. Zhu, R. Yang, S. Wang, & Z. L. Wang, Flexible high-output nanogenerator based on lateral ZnO nanowire array. *Nano Letters*, **10** (2010) 3151–3155. <https://doi.org/10.1021/nl101973h>.
203. Y. Hu, Y. Zhang, C. Xu, G. Zhu, & Z. L. Wang, High-output nanogenerator by rational unipolar assembly of conical nanowires and its application for driving a small liquid crystal display. *Nano Letters*, **10** (2010) 5025–5031. <https://doi.org/10.1021/nl103203u>.
204. J. Kwon, W. Seung, B. K. Sharma, S. W. Kim, & J. H. Ahn, A high performance PZT ribbon-based nanogenerator using graphene transparent electrodes. *Energy and Environmental Science*, **5** (2012) 8970–8975. <https://doi.org/10.1039/c2ee22251e>.
205. S. Xu, B. J. Hansen, & Z. L. Wang, Piezoelectric-nanowire-enabled power source for driving wireless microelectronics. *Nature Communications*, **1** (2010). <https://doi.org/10.1038/ncomms1098>.
206. C. Dagdeviren, B. D. Yang, Y. Su, P. L. Tran, P. Joe, E. Anderson, J. Xia, V. Doraiswamy, B. Dehdashti, X. Feng, B. Lu, R. Poston, Z. Khalpey, R. Ghaffari, Y. Huang, M. J. Slepian, & J. A. Rogers, Conformal piezoelectric energy harvesting and storage from motions of the heart, lung, and diaphragm. *Proceedings of the National Academy of Sciences of the United States of America*, **111** (2014) 1927–1932. <https://doi.org/10.1073/pnas.1317233111>.
207. P. Janphuang, R. Lockhart, N. Uffer, D. Briand, & N. F. de Rooij, Vibrational piezoelectric energy harvesters based on thinned bulk PZT sheets fabricated at the wafer level. *Sensors and Actuators, A: Physical*, **210** (2014) 1–9. <https://doi.org/10.1016/j.sna.2014.01.032>.

208. Y. Qi, N. T. Jafferis, K. Lyons, C. M. Lee, H. Ahmad, & M. C. McAlpine, Piezoelectric ribbons printed onto rubber for flexible energy conversion. *Nano Letters*, **10** (2010) 524–525. <https://doi.org/10.1021/nl903377u>.
209. Y. Qi, J. Kim, T. D. Nguyen, B. Lisko, P. K. Purohit, & M. C. McAlpine, Enhanced piezoelectricity and stretchability in energy harvesting devices fabricated from buckled PZT ribbons. *Nano Letters*, **11** (2011) 1331–1336. <https://doi.org/10.1021/nl104412b>.
210. K. il Park, J. H. Son, G. T. Hwang, C. K. Jeong, J. Ryu, M. Koo, I. Choi, S. H. Lee, M. Byun, Z. L. Wang, & K. J. Lee, Highly-efficient, flexible piezoelectric PZT thin film nanogenerator on plastic substrates. *Advanced Materials*, **26** (2014) 2514–2520. <https://doi.org/10.1002/adma.201305659>.
211. L. Gu, N. Cui, L. Cheng, Q. Xu, S. Bai, M. Yuan, W. Wu, J. Liu, Y. Zhao, F. Ma, Y. Qin, & Z. L. Wang, Flexible fiber nanogenerator with 209 v output voltage directly powers a light-emitting diode. *Nano Letters*, **13** (2013) 91–94. <https://doi.org/10.1021/nl303539c>.
212. E. Ringgaard & T. Wurlitzer, Lead-free piezoceramics based on alkali niobates. *Journal of the European Ceramic Society*, **25** (2005) 2701–2706. <https://doi.org/10.1016/j.jeurceramsoc.2005.03.126>.
213. T. Takenaka & H. Nagata, Current status and prospects of lead-free piezoelectric ceramics. *Journal of the European Ceramic Society*, **25** (2005) 2693–2700. <https://doi.org/10.1016/j.jeurceramsoc.2005.03.125>.
214. K. Matsuo, R.-J. Kie, Y. Akimune, & T. Sugiyama, *Preparation of Lead-Free Sr<sub>2-x</sub>CaxNaNb<sub>5</sub>O<sub>15</sub> (x=0.1)-Based Piezoceramics with Tungsten Bronze Structure* (2002).
215. Y. Wang, J. Wu, D. Xiao, W. Wu, B. Zhang, L. Wu, & J. Zhu, Microstructure and electrical properties of [(K<sub>0.50</sub>Na<sub>0.50</sub>)<sub>0.95-x</sub>Li<sub>0.05</sub>Ag<sub>x</sub>](Nb<sub>0.95</sub>Ta<sub>0.05</sub>)O<sub>3</sub> lead-free ceramics. *Journal of the American Ceramic Society*, **91** (2008) 2772–2775. <https://doi.org/10.1111/j.1551-2916.2008.02529.x>.
216. D. Y. Wang, N. Y. Chan, S. Li, S. H. Choy, H. Y. Tian, & H. L. W. Chan, Enhanced ferroelectric and piezoelectric properties in doped lead-free (Bi<sub>0.5</sub>Na<sub>0.5</sub>)<sub>0.94</sub> Ba<sub>0.06</sub>

- TiO<sub>3</sub> thin films. *Applied Physics Letters*, **97** (2010). <https://doi.org/10.1063/1.3518484>.
217. K. il Park, S. Xu, Y. Liu, G. T. Hwang, S. J. L. Kang, Z. L. Wang, & K. J. Lee, Piezoelectric BaTiO<sub>3</sub> thin film nanogenerator on plastic substrates. *Nano Letters*, **10** (2010) 4939–4943. <https://doi.org/10.1021/nl102959k>.
218. M. M. Alam, S. K. Ghosh, A. Sultana, & D. Mandal, Lead-free ZnSnO<sub>3</sub>/MWCNTs-based self-poled flexible hybrid nanogenerator for piezoelectric power generation. *Nanotechnology*, **26** (2015). <https://doi.org/10.1088/0957-4484/26/16/165403>.
219. K. il Park, S. Xu, Y. Liu, G. T. Hwang, S. J. L. Kang, Z. L. Wang, & K. J. Lee, Piezoelectric BaTiO<sub>3</sub> thin film nanogenerator on plastic substrates. *Nano Letters*, **10** (2010) 4939–4943. <https://doi.org/10.1021/nl102959k>.
220. K. il Park, M. Lee, Y. Liu, S. Moon, G. T. Hwang, G. Zhu, J. E. Kim, S. O. Kim, D. K. Kim, Z. L. Wang, & K. J. Lee, Flexible nanocomposite generator made of BaTiO<sub>3</sub> nanoparticles and graphitic carbons. *Advanced Materials*, **24** (2012) 2999–3004. <https://doi.org/10.1002/adma.201200105>.
221. J. H. Jung, M. Lee, J. il Hong, Y. Ding, C. Y. Chen, L. J. Chou, & Z. L. Wang, Lead-free NaNbO<sub>3</sub> nanowires for a high output piezoelectric nanogenerator. *ACS Nano*, **5** (2011) 10041–10046. <https://doi.org/10.1021/nn2039033>.
222. C. K. Jeong, J. Lee, S. Han, J. Ryu, G. T. Hwang, D. Y. Park, J. H. Park, S. S. Lee, M. Byun, S. H. Ko, & K. J. Lee, A hyper-stretchable elastic-composite energy harvester. *Advanced Materials*, **27** (2015) 2866–2875. <https://doi.org/10.1002/adma.201500367>.
223. K. Y. Lee, D. Kim, J. H. Lee, T. Y. Kim, M. K. Gupta, & S. W. Kim, Unidirectional high-power generation via stress-induced dipole alignment from ZnSnO<sub>3</sub> nanocubes/polymer hybrid piezoelectric nanogenerator. *Advanced Functional Materials*, **24** (2014) 37–43. <https://doi.org/10.1002/adfm.201301379>.
224. B. Y. Lee, J. Zhang, C. Zueger, W. J. Chung, S. Y. Yoo, E. Wang, J. Meyer, R. Ramesh, & S. W. Lee, Virus-based piezoelectric energy generation. *Nature Nanotechnology*, **7** (2012) 351–356. <https://doi.org/10.1038/nnano.2012.69>.

225. C. K. Jeong, I. Kim, K. il Park, M. H. Oh, H. Paik, G. T. Hwang, K. No, Y. S. Nam, & K. J. Lee, Virus-directed design of a flexible BaTiO<sub>3</sub> nanogenerator. *ACS Nano*, **7** (2013) 11016–11025. <https://doi.org/10.1021/nn404659d>.
226. S. K. Ghosh & D. Mandal, High-performance bio-piezoelectric nanogenerator made with fish scale. *Applied Physics Letters*, **109** (2016). <https://doi.org/10.1063/1.4961623>.
227. S. K. Ghosh & D. Mandal, Efficient natural piezoelectric nanogenerator: Electricity generation from fish swim bladder. *Nano Energy*, **28** (2016) 356–365. <https://doi.org/10.1016/j.nanoen.2016.08.030>.
228. C. Chang, V. H. Tran, J. Wang, Y. K. Fuh, & L. Lin, Direct-write piezoelectric polymeric nanogenerator with high energy conversion efficiency. *Nano Letters*, **10** (2010) 726–731. <https://doi.org/10.1021/nl9040719>.
229. S. Cha, S. M. Kim, H. Kim, J. Ku, J. I. Sohn, Y. J. Park, B. G. Song, M. H. Jung, E. K. Lee, B. L. Choi, J. J. Park, Z. L. Wang, J. M. Kim, & K. Kim, Porous PVDF as effective sonic wave driven nanogenerators. *Nano Letters*, **11** (2011) 5142–5147. <https://doi.org/10.1021/nl202208n>.
230. L. Persano, C. Dagdeviren, Y. Su, Y. Zhang, S. Girardo, D. Pisignano, Y. Huang, & J. A. Rogers, High performance piezoelectric devices based on aligned arrays of nanofibers of poly(vinylidene fluoride-co-trifluoroethylene). *Nature Communications*, **4** (2013). <https://doi.org/10.1038/ncomms2639>.
231. X. Chen, H. Tian, X. Li, J. Shao, Y. Ding, N. An, & Y. Zhou, A high performance P(VDF-TrFE) nanogenerator with self-connected and vertically integrated fibers by patterned EHD pulling. *Nanoscale*, **7** (2015) 11536–11544. <https://doi.org/10.1039/c5nr01746g>.
232. Y. Mao, P. Zhao, G. McConohy, H. Yang, Y. Tong, & X. Wang, Sponge-like piezoelectric polymer films for scalable and integratable nanogenerators and self-powered electronic systems. *Advanced Energy Materials*, **4** (2014). <https://doi.org/10.1002/aenm.201301624>.
233. R. Gregorio & E. M. Ueno, *Effect of crystalline phase, orientation and temperature on the dielectric properties of poly (vinylidene fluoride) (PVDF)* (1999).

234. S. K. Ghosh, M. M. Alam, & D. Mandal, The in situ formation of platinum nanoparticles and their catalytic role in electroactive phase formation in poly(vinylidene fluoride): A simple preparation of multifunctional poly(vinylidene fluoride) films doped with platinum nanoparticles. *RSC Advances*, **4** (2014) 41886–41894. <https://doi.org/10.1039/c4ra06334a>.
235. A. Tamang, S. K. Ghosh, S. Garain, M. M. Alam, J. Haeberle, K. Henkel, D. Schmeisser, & D. Mandal, DNA-Assisted  $\beta$ -phase Nucleation and Alignment of Molecular Dipoles in PVDF Film: A Realization of Self-Poled Bioinspired Flexible Polymer Nanogenerator for Portable Electronic Devices. *ACS Applied Materials and Interfaces*, **7** (2015) 16143–16147. <https://doi.org/10.1021/acsami.5b04161>.
236. C. Sinha, D. Mandal, K. Roy, S. Jana, S. K. Ghosh, B. Mahanty, Z. Mallick, & S. Sarkar, Three-dimensional MOF-assisted self-polarized ferroelectret: An effective autopowered remote healthcare monitoring approach. *Langmuir*, **36** (2020) 11477–11489. <https://doi.org/10.1021/acs.langmuir.0c01749>.
237. O. H. Lowry, N. J. Rosebrough, A. L. Farr, & R. J. Randall, 1951. Protein measurement with the Folin phenol reagent. *J Biol Chem*, **193** (1951), 265-75.
238. U. Müller, In vitro biocompatibility testing of biomaterials and medical devices. *Medical device technology*, **19** (2008), 30-32.
239. M. P. Macwilliams & M.-K. Liao, *Luria Broth (LB) and Luria Agar (LA) Media and Their Uses Protocol* (2016).
240. S. J. Flora, G. Flora, & G. Saxena, *Environmental occurrence, health effects and management of lead poisoning*, *Lead*, (2006). <https://doi.org/10.1016/B978-044452945-9/50004-X>.
241. A. P. Neal & T. R. Guilarte, Molecular neurobiology of lead (Pb<sup>2+</sup>): Effects on synaptic function. *Molecular Neurobiology*, **42** (2010) 151–160. <https://doi.org/10.1007/s12035-010-8146-0>.
242. V. Chand & S. Prasad, ICP-OES assessment of heavy metal contamination in tropical marine sediments: A comparative study of two digestion techniques. *Microchemical Journal*, **111** (2013) 53–61. <https://doi.org/10.1016/j.microc.2012.11.007>.

243. V. v Lemanov, *Piezoelectric and Pyroelectric Properties of Protein Amino Acids as Basic Materials of Soft State Physics*.
244. Black, J., 2005. Biological performance of materials: fundamentals of biocompatibility. Crc Press. (n.d.).
245. Lawrence, B.J. and Madihally, S.V., 2008. Cell colonization in degradable 3D porous matrices. *Cell adhesion & migration*, 2(1), pp.9-16. (n.d.).
246. S. K. Ghosh & D. Mandal, Synergistically enhanced piezoelectric output in highly aligned 1D polymer nanofibers integrated all-fiber nanogenerator for wearable nano-tactile sensor. *Nano Energy*, **53** (2018) 245–257. <https://doi.org/10.1016/j.nanoen.2018.08.036>.
247. Chiu, M.H. and Prenner, E.J., 2011. Differential scanning calorimetry: An invaluable tool for a detailed thermodynamic characterization of macromolecules and their interactions. *Journal of Pharmacy and Bioallied Sciences*, 3(1), p.39. <https://doi.org/10.4103/0975-7406.76463>
249. M. Gu, J. Zhang, X. Wang, & W. Ma, Crystallization behavior of PVDF in PVDF-DMP system via thermally induced phase separation. *Journal of Applied Polymer Science*, **102** (2006) 3714–3719. <https://doi.org/10.1002/app.24531>.
250. L. Zhu, Exploring strategies for high dielectric constant and low loss polymer dielectrics. *Journal of Physical Chemistry Letters*, **5** (2014) 3677–3687. <https://doi.org/10.1021/jz501831q>.
251. S. K. Ghosh & D. Mandal, Envisioned strategy for an early intervention in virus-suspected patients through non-invasive piezo- And pyro-electric-based wearable sensors. *Journal of Materials Chemistry A*, **9** (2021) 1887–1909. <https://doi.org/10.1039/d0ta08547b>.
252. S. K. Ghosh, A. Biswas, S. Sen, C. Das, K. Henkel, D. Schmeisser, & D. Mandal, Yb<sup>3+</sup> assisted self-polarized PVDF based ferroelectric nanogenerator: A facile strategy of highly efficient mechanical energy harvester fabrication. *Nano Energy*, **30** (2016) 621–629. <https://doi.org/10.1016/j.nanoen.2016.10.042>.
- 253 I. Kim, H. Roh, J. Yu, N. Jayababu, & D. Kim, Boron Nitride Nanotube-Based Contact Electrification-Assisted Piezoelectric Nanogenerator as a Kinematic Sensor

- for Detecting the Flexion-Extension Motion of a Robot Finger. *ACS Energy Letters*, **5** (2020) 1577–1585. <https://doi.org/10.1021/acsenerylett.0c00451>.
254. A. Petritz, E. Karner-Petritz, T. Uemura, P. Schäffner, T. Araki, B. Stadlober, & T. Sekitani, Imperceptible energy harvesting device and biomedical sensor based on ultraflexible ferroelectric transducers and organic diodes. *Nature Communications*, **12** (2021). <https://doi.org/10.1038/s41467-021-22663-6>.
255. J. Luo, Z. Wang, L. Xu, A. C. Wang, K. Han, T. Jiang, Q. Lai, Y. Bai, W. Tang, F. R. Fan, & Z. L. Wang, Flexible and durable wood-based triboelectric nanogenerators for self-powered sensing in athletic big data analytics. *Nature Communications*, **10** (2019). <https://doi.org/10.1038/s41467-019-13166-6>.
256. Sun, J., Pu, X., Liu, M., Yu, A., Du, C., Zhai, J., Hu, W. and Wang, Z.L., 2018. Self-healable, stretchable, transparent triboelectric nanogenerators as soft power sources. *ACS nano*, *12*(6), pp.6147-6155. <https://doi.org/10.1021/acsnano.8b02479>
257. B. Mahanty, S. K. Ghosh, S. Jana, Z. Mallick, S. Sarkar, & D. Mandal, ZnO nanoparticle confined stress amplified all-fiber piezoelectric nanogenerator for self-powered healthcare monitoring. *Sustainable Energy and Fuels*, **5** (2021) 4389–4400. <https://doi.org/10.1039/d1se00444a>.
258. Roy, K., Jana, S., Ghosh, S.K., Mahanty, B., Mallick, Z., Sarkar, S., Sinha, C. and Mandal, D., 2020. Three-dimensional MOF-assisted self-polarized ferroelectret: an effective autopowered remote healthcare monitoring approach. *Langmuir*, *36*(39), pp.11477-11489. <https://doi.org/10.1021/acs.langmuir.0c01749>
259. Y. Park, Y. E. Shin, J. Park, Y. Lee, M. P. Kim, Y. R. Kim, S. Na, S. K. Ghosh, & H. Ko, Ferroelectric Multilayer Nanocomposites with Polarization and Stress Concentration Structures for Enhanced Triboelectric Performances. *ACS Nano*, **14** (2020) 7101–7110. <https://doi.org/10.1021/acsnano.0c01865>.
260. S. K. Ghosh, J. Park, S. Na, M. P. Kim, & H. Ko, A Fully Biodegradable Ferroelectric Skin Sensor from Edible Porcine Skin Gelatine. *Advanced Science*, **8** (2021). <https://doi.org/10.1002/advs.202005010>.
261. S. Munir, B. Jiang, A. Guilcher, S. Brett, S. Redwood, M. Marber, & P. Chowienczyk, Exercise reduces arterial pressure augmentation through vasodilation of



- muscular arteries in humans. *Am J Physiol Heart Circ Physiol*, **294** (2008) 1645–1650. <https://doi.org/10.1152/ajpheart.01171.2007.-Exercise>.
262. P. J. Fleming, R. Gilbert, Y. Azaz, J. Berry, P. T. Rudd, A. Stewart, & E. Hall, *Interaction between bedding and sleeping position in the sudden infant death syndrome: a population based case-control study*.
263. S. K. Ghosh, P. Adhikary, S. Jana, A. Biswas, V. Sencadas, S. D. Gupta, B. Tudu, & D. Mandal, Electrospun gelatin nanofiber based self-powered bio-e-skin for health care monitoring. *Nano Energy*, **36** (2017) 166–175. <https://doi.org/10.1016/j.nanoen.2017.04.028>.
264. A. H. Morice, G. A. Fontana, A. R. A. Sovijarvi, M. Pistolesi, K. F. Chung, J. Widdicombe, F. O’Connell, P. Geppetti, L. Gronke, J. de Jongste, M. Belvisi, P. Dicpinigaitis, A. Fischer, L. McGarvey, W. J. Fokkens, & J. Kastelik, The diagnosis and management of chronic cough. *European Respiratory Journal*, **24** (2004) 481–492. <https://doi.org/10.1183/09031936.04.00027804>.
265. X. L. Chen, H. M. Tian, X. M. Li, J. Y. Shao, Y. C. Ding, N. L. An and Y. P. Zhou, *Nanoscale*, A high performance P (VDF-TrFE) nanogenerator with self-connected and vertically integrated fibers by patterned EHD pulling. *Nanoscale*, **7** (2015), 11536.
266. R. S. Dahiya, D. Cattin, A. Adami, C. Collini, L. Barboni, M. Valle, L. Lorenzelli, R. Oboe, G. Metta, & F. Brunetti, Towards tactile sensing system on chip for robotic applications. *IEEE Sensors Journal*, **11** (2011) 3216–3226. <https://doi.org/10.1109/JSEN.2011.2159835>.
267. C. Li, P. M. Wu, S. Lee, A. Gorton, M. J. Schulz, & C. H. Ahn, Flexible dome and bump shape piezoelectric tactile sensors using PVDF-TrFE copolymer. *Journal of Microelectromechanical Systems*, **17** (2008) 334–341. <https://doi.org/10.1109/JMEMS.2007.911375>.
268. G. Zhao, X. Zhang, X. Cui, S. Wang, Z. Liu, L. Deng, A. Qi, X. Qiao, L. Li, C. Pan, Y. Zhang, & L. Li, Piezoelectric Polyacrylonitrile Nanofiber Film-Based Dual-Function Self-Powered Flexible Sensor. *ACS Applied Materials and Interfaces*, **10** (2018) 15855–15863. <https://doi.org/10.1021/acsami.8b02564>.

269. A. Wang, M. Hu, L. Zhou, & X. Qiang, Self-powered wearable pressure sensors with enhanced piezoelectric properties of aligned P(VDF-TrFE)/MWCNT composites for monitoring human physiological and muscle motion signs. *Nanomaterials*, **8** (2018). <https://doi.org/10.3390/nano8121021>.
270. B. Wang, C. Liu, Y. Xiao, J. Zhong, W. Li, Y. Cheng, B. Hu, L. Huang, & J. Zhou, Ultrasensitive cellular fluorocarbon piezoelectret pressure sensor for self-powered human physiological monitoring. *Nano Energy*, **32** (2017) 42–49. <https://doi.org/10.1016/j.nanoen.2016.12.025>.
271. T. Sharma, S. –S. Je, B. Gill and J. X. J. Zhang, *Sens. Actuators A: Physical*, 2012, **177**, 87.
272. Y. R. Wang, J. M. Zheng, G. Y. Ren, P. H. Zhang, & C. Xu, A flexible piezoelectric force sensor based on PVDF fabrics. *Smart Materials and Structures*, **20** (2011). <https://doi.org/10.1088/0964-1726/20/4/045009>.
273. V. Bhavanasi, D. Y. Kusuma, & P. S. Lee, Polarization orientation, piezoelectricity, and energy harvesting performance of ferroelectric PVDF-TrFE nanotubes synthesized by nanoconfinement. *Advanced Energy Materials*, **4** (2014). <https://doi.org/10.1002/aenm.201400723>.
274. W. Guo, C. Tan, K. Shi, J. Li, X. X. Wang, B. Sun, X. Huang, Y. Z. Long, & P. Jiang, Wireless piezoelectric devices based on electrospun PVDF/BaTiO<sub>3</sub> NW nanocomposite fibers for human motion monitoring. *Nanoscale*, **10** (2018) 17751–17760. <https://doi.org/10.1039/c8nr05292a>.
275. Q. L. Zhao, G. P. He, J. J. Di, W. L. Song, Z. L. Hou, P. P. Tan, D. W. Wang & M. S. Cao, *ACS Appl. Mater. Interfaces*, 2017, **9** (2017), 24696.
275. S. M. Hosseini & A. A. Yousefi, Piezoelectric sensor based on electrospun PVDF-MWCNT-Cloisite 30B hybrid nanocomposites. *Organic Electronics*, **50** (2017) 121–129. <https://doi.org/10.1016/j.orgel.2017.07.035>.
276. T. Yang, H. Pan, G. Tian, B. Zhang, D. Xiong, Y. Gao, C. Yan, X. Chu, N. Chen, S. Zhong, L. Zhang, W. Deng, & W. Yang, Hierarchically structured PVDF/ZnO core-shell nanofibers for self-powered physiological monitoring electronics. *Nano Energy*, **72** (2020). <https://doi.org/10.1016/j.nanoen.2020.104706>.

277. Z. Liu, C. Pan, L. Lin, J. Huang and Z. Ou, *Smart Mater. Struct.*, 2014, **23**, 025003.
278. W. Zeng, X. M. Tao, S. Chen, S. M. Shang, H. L. W. Chan & S. H. Choy, Highly durable all-fiber nanogenerator for mechanical energy harvesting. *Energy & Environmental Science*, 2013, **6** (2013), 2631. <https://doi.org/10.1039/C3EE41063C>.
279. M. Kim, Y. S. Wu, E. C. Kan, & J. Fan, Breathable and flexible piezoelectric ZnO@PVDF fibrous nanogenerator for wearable applications. *Polymers*, **10** (2018). <https://doi.org/10.3390/polym10070745>.
280. A. Sultana, Md. M. Alam, A. Biswas, T. R. Middy, & D. Mandal, Fabrication of wearable semiconducting piezoelectric nanogenerator made with electrospun-derived zinc sulfide nanorods and poly(vinyl alcohol) nanofibers. *Translational Materials Research*, **3** (2016) 045001. <https://doi.org/10.1088/2053-1613/3/4/045001>.
281. Y. Zhou, J. He, H. Wang, K. Qi, N. Nan, X. You, W. Shao, L. Wang, B. Ding, & S. Cui, Highly sensitive, self-powered and wearable electronic skin based on pressure-sensitive nanofiber woven fabric sensor. *Scientific Reports*, **7** (2017). <https://doi.org/10.1038/s41598-017-13281-8>.
282. X. Lu, H. Qu, & M. Skorobogatiy, Piezoelectric Micro- and Nanostructured Fibers Fabricated from Thermoplastic Nanocomposites Using a Fiber Drawing Technique: Comparative Study and Potential Applications. *ACS Nano*, **11** (2017) 2103–2114. <https://doi.org/10.1021/acsnano.6b08290>.
283. E. Yang, Z. Xu, L. K. Chur, A. Behroozfar, M. Baniyasi, S. Moreno, J. Huang, J. Gilligan, & M. Minary-Jolandan, Nanofibrous Smart Fabrics from Twisted Yarns of Electrospun Piezopolymer. *ACS Applied Materials and Interfaces*, **9** (2017) 24220–24229. <https://doi.org/10.1021/acсами.7b06032>.
284. M. H. You, X. X. Wang, X. Yan, J. Zhang, W. Z. Song, M. Yu, Z. Y. Fan, S. Ramakrishna, Y. Z. Long, S. Ramakrishna, & Y. Z. Long, A self-powered flexible hybrid piezoelectric–pyroelectric nanogenerator based on non-woven nanofiber membranes. *Journal of Materials Chemistry A*, **6**(2018), 3500.
285. K. Maity, B. Mahanty, T. K. Sinha, S. Garain, A. Biswas, S. K. Ghosh, S. Manna, S. K. Ray, & D. Mandal, Two-Dimensional Piezoelectric MoS<sub>2</sub>-Modulated Nanogenerator and Nanosensor Made of Poly(vinylidene Fluoride) Nanofiber Webs for Self-Powered

- Electronics and Robotics. *Energy Technology*, **5** (2017) 234–243. <https://doi.org/10.1002/ente.201600419>.
286. J. Fang, X. Wang, & T. Lin, Electrical power generator from randomly oriented electrospun poly(vinylidene fluoride) nanofibre membranes. *Journal of Materials Chemistry*, **21** (2011) 11088–11091. <https://doi.org/10.1039/c1jm11445j>.
287. K. Roy, S. K. Ghosh, A. Sultana, S. Garain, M. Xie, C. R. Bowen, K. Henkel, D. Schmeißer & D. Mandal, A self-powered wearable pressure sensor and pyroelectric breathing sensor based on GO interfaced PVDF nanofibers. *ACS Applied Nano Materials*, **2**, (2019).
288. J. Li, S. Chen, W. Liu, R. Fu, S. Tu, Y. Zhao, L. Dong, B. Yan & Y. Gu, High performance piezoelectric nanogenerators based on electrospun ZnO nanorods/poly (vinylidene fluoride) composite membranes. *The Journal of Physical Chemistry C*, **123**(2019), 11378–11387.
289. X. Guan, B. Xu, & J. Gong, Hierarchically architected polydopamine modified BaTiO<sub>3</sub>@P(VDF-TrFE) nanocomposite fiber mats for flexible piezoelectric nanogenerators and self-powered sensors. *Nano Energy*, **70** (2020). <https://doi.org/10.1016/j.nanoen.2020.104516>.
290. K. Maity, S. Garain, K. Henkel, D. Schmeißer, & D. Mandal, Natural Sugar-Assisted, Chemically Reinforced, Highly Durable Piezoorganic Nanogenerator with Superior Power Density for Self-Powered Wearable Electronics. *ACS Applied Materials and Interfaces*, **10** (2018) 44018–44032. <https://doi.org/10.1021/acsami.8b15320>.
291. M. M. Abolhasani, M. Naebe, K. Shirvanimoghaddam, H. Fashandi, H. Khayyam, M. Joordens, A. Pipertzis, S. Anwar, R. Berger, G. Floudas, J. Michels, & K. Asadi, Thermodynamic approach to tailor porosity in piezoelectric polymer fibers for application in nanogenerators. *Nano Energy*, **62** (2019) 594–600. <https://doi.org/10.1016/j.nanoen.2019.05.044>.
292. S. K. Ghosh & D. Mandal, Synergistically enhanced piezoelectric output in highly aligned 1D polymer nanofibers integrated all-fiber nanogenerator for wearable nano-tactile sensor. *Nano Energy*, **53**(2018), 245-257. <https://doi.org/10.1016/j.nanoen.2018.08.036>.

293. E. J. Lee, T. Y. Kim, S. W. Kim, S. Jeong, Y. Choi & S. Y. Lee, High-performance piezoelectric nanogenerators based on chemically-reinforced composites. *Energy & Environmental Science*, **11**(2018), 1425. <https://doi.org/10.1039/c8ee00014j>.
294. K. Maity, S. Garain, K. Henkel, D. Schmeißer, & D. Mandal, Natural sugar-assisted, chemically reinforced, highly durable piezoorganic nanogenerator with superior power density for self-powered wearable electronics. *ACS applied materials & interfaces*, *10*(2018), 44018-44032.
295. K. Shi, B. Sun, X. Huang, & P. Jiang, Synergistic effect of graphene nanosheet and BaTiO<sub>3</sub> nanoparticles on performance enhancement of electrospun PVDF nanofiber mat for flexible piezoelectric nanogenerators. *Nano Energy*, **52** (2018) 153–162. <https://doi.org/10.1016/j.nanoen.2018.07.053>.
296. S. Siddiqui, D. il Kim, E. Roh, L. T. Duy, T. Q. Trung, M. T. Nguyen, & N. E. Lee, A durable and stable piezoelectric nanogenerator with nanocomposite nanofibers embedded in an elastomer under high loading for a self-powered sensor system. *Nano Energy*, **30** (2016) 434–442. <https://doi.org/10.1016/j.nanoen.2016.10.034>.
297. A. Sultana, Md. M. Alam, A. Biswas, T. R. Middy, & D. Mandal, Fabrication of wearable semiconducting piezoelectric nanogenerator made with electrospun-derived zinc sulfide nanorods and poly(vinyl alcohol) nanofibers. *Translational Materials Research*, **3** (2016) 045001. <https://doi.org/10.1088/2053-1613/3/4/045001>.
298. A. Sultana, M. M. Alam, S. K. Ghosh, T. R. Middy, & D. Mandal, Energy harvesting and self-powered microphone application on multifunctional inorganic-organic hybrid nanogenerator. *Energy*, **166** (2019) 963–971. <https://doi.org/10.1016/j.energy.2018.10.124>.
299. C. Zhang, Y. Fan, H. Li, Y. Li, L. Zhang, S. Cao, S. Kuang, Y. Zhao, A. Chen, G. Zhu, & Z. L. Wang, Fully Rollable Lead-Free Poly(vinylidene fluoride)-Niobate-Based Nanogenerator with Ultra-Flexible Nano-Network Electrodes. *ACS Nano*, **12** (2018) 4803–4811. <https://doi.org/10.1021/acsnano.8b01534>.
300. L. Zhang, J. Gui, Z. Wu, R. Li, Y. Wang, Z. Gong, X. Zhao, C. Sun, & S. Guo, Enhanced performance of piezoelectric nanogenerator based on aligned nanofibers and three-dimensional interdigital electrodes. *Nano Energy*, **65** (2019). <https://doi.org/10.1016/j.nanoen.2019.103924>.

301. S. Garain, S. Jana, T. K. Sinha, & D. Mandal, Design of in Situ Poled Ce<sup>3+</sup>-Doped Electrospun PVDF/Graphene Composite Nanofibers for Fabrication of Nanopressure Sensor and Ultrasensitive Acoustic Nanogenerator. *ACS Applied Materials and Interfaces*, **8** (2016) 4532–4540. <https://doi.org/10.1021/acsami.5b11356>.
302. C. Chang, V. H. Tran, J. Wang, Y. K. Fuh, & L. Lin, Direct-write piezoelectric polymeric nanogenerator with high energy conversion efficiency. *Nano Letters*, **10** (2010) 726–731. <https://doi.org/10.1021/nl9040719>.
303. M. R. Joung, H. Xu, I. T. Seo, D. H. Kim, J. Hur, S. Nahm, C.-Y. Kang, S.-J. Yoon, H.-M. Park & J. Mater, Piezoelectric nanogenerators synthesized using KNbO<sub>3</sub> nanowires with various crystal structures. *Journal of Materials Chemistry A*. **2**(2014), 18547–18553
304. S. K. Ghosh, A. Biswas, S. Sen, C. Das, K. Henkel, D. Schmeisser, & D. Mandal, Yb<sup>3+</sup> assisted self-polarized PVDF based ferroelectric nanogenerator: A facile strategy of highly efficient mechanical energy harvester fabrication. *Nano Energy*, **30** (2016) 621–629. <https://doi.org/10.1016/j.nanoen.2016.10.042>.
305. R. A. Whiter, V. Narayan, & S. Kar-Narayan, A scalable nanogenerator based on self-poled piezoelectric polymer nanowires with high energy conversion efficiency. *Advanced Energy Materials*, **4** (2014). <https://doi.org/10.1002/aenm.201400519>.
306. S. K. Ghosh, T. K. Sinha, B. Mahanty, & D. Mandal, Self-poled Efficient Flexible “Ferroelectric” Nanogenerator: A New Class of Piezoelectric Energy Harvester. *Energy Technology*, **3** (2015) 1190–1197. <https://doi.org/10.1002/ente.201500167>.
307. S. K. Ghosh & D. Mandal, Efficient natural piezoelectric nanogenerator: Electricity generation from fish swim bladder. *Nano Energy*, **28** (2016) 356–365. <https://doi.org/10.1016/j.nanoen.2016.08.030>.
308. S. K. Ghosh & D. Mandal, Synergistically enhanced piezoelectric output in highly aligned 1D polymer nanofibers integrated all-fiber nanogenerator for wearable nano-tactile sensor. *Nano Energy*, **53** (2018) 245–257. <https://doi.org/10.1016/j.nanoen.2018.08.036>.
309. S. K. Ghosh, P. Adhikary, S. Jana, A. Biswas, V. Sencadas, S. D. Gupta, B. Tudu, & D. Mandal, Electrospun gelatin nanofiber based self-powered bio-e-skin for health care

- monitoring. *Nano Energy*, **36** (2017) 166–175.  
<https://doi.org/10.1016/j.nanoen.2017.04.028>.
310. Z. L. Wang, & J. Song, Piezoelectric nanogenerators based on zinc oxide nanowire arrays. *Science*, *312*(2006), 242-246. <https://doi.org/10.1126/science.1124005>
311. M. Khalifa & S. Anandhan, PVDF Nanofibers with Embedded Polyaniline-Graphitic Carbon Nitride Nanosheet Composites for Piezoelectric Energy Conversion. *ACS Applied Nano Materials*, **2** (2019) 7328–7339.  
<https://doi.org/10.1021/acsnm.9b01812>.
312. D. Bhattacharya, S. Bayan, R. K. Mitra, & S. K. Ray, Flexible biomechanical energy harvesters with colossal piezoelectric output ( $\sim 2.07$  V/kPa) based on transition metal dichalcogenides-poly(vinylidene fluoride) nanocomposites. *ACS Applied Electronic Materials*, **2** (2020) 3327–3335. <https://doi.org/10.1021/acsaelm.0c00632>.
313. J. M. Wu, C. Xu, Y. Zhang, & Z. L. Wang, Lead-free nanogenerator made from single ZnSnO<sub>3</sub> microbelt. *ACS nano*, *6*(2012), 4335-4340.  
<https://doi.org/10.1021/nn300951d>.

# Removal of Lead Contamination through the Formation of Lead-Nanoplates by a Hot Spring Microbial Protein

Chetana Ghosal, Nurul Alam, Abiral Tamang, Brajadulal Chattopadhyay\*

Department of Physics, Jadavpur University, Kolkata, India

Email: \*bdc\_physics@yahoo.co.in

**How to cite this paper:** Ghosal, C., Alam, N., Tamang, A. and Chattopadhyay, B. (2021) Removal of Lead Contamination through the Formation of Lead-Nanoplates by a Hot Spring Microbial Protein. *Advances in Microbiology*, 11, 681-693.

<https://doi.org/10.4236/aim.2021.1111049>

**Received:** October 26, 2021

**Accepted:** November 23, 2021

**Published:** November 26, 2021

Copyright © 2021 by author(s) and Scientific Research Publishing Inc. This work is licensed under the Creative Commons Attribution International License (CC BY 4.0).

<http://creativecommons.org/licenses/by/4.0/>



Open Access

## Abstract

Lead contamination still remains as serious threat to public health and environment because of its non-biodegradability and toxicity. A clean technique has been developed for removal of lead contamination through the formation of lead-oxide nanoplates using a bacterial protein (Molecular weight ~30 kDa) as biological template. The isolated hot-spring bacterial (the bacterium was named as MDH1) protein when adding to the solution of lead compound (e.g., lead nitrate), nanoplates of lead-oxide are formed as viewed by electron microscope. The as prepared lead-oxide-nanoplates are characterized by Inductively Coupled Plasma analysis, Energy Dispersive X-ray Spectroscopy and X-ray diffraction analyses. The lead-oxide-nanoplates and the filtered supernatant of the reactive solution both were separately used to observe the inhibition of growth of *E. coli* bacteria on culture plate. Lead-oxide-nanoplates produced clear zone of inhibition on the bacterial growth plate, whereas the filtered supernatant exhibited no such zone on the growth of *E. coli* bacteria revealing the fact that lead contamination was removed from the filtered supernatant. The prepared lead oxide nanoplates also possess dye degradation activity which is the added advantage of the process. The MDH1 bacterial protein acts as biological template which successfully removes lead contamination from lead-solution. The process is a clean and cost-effective one which can be used not only for removal of lead contamination but also for removal of different dyes from environment due to having dye-degradation attribute of the lead-oxide nanoplates.

## Keywords

Bacteria, Hot Spring, Protein, Dye Degradation, Lead-Oxide Nanoplates



## 1. Introduction

There are many heavy metals viz., lead, mercury, arsenic, chromium, cadmium etc. producing various hazardous effects to all over the world in terms of their environmental load and contaminations. These metals are undoubtedly serious causes of concern for our environment and societal health. The main anthropogenic sources of these heavy metal contaminations come from the disposal of untreated or partially treated industrial effluents, various toxic heavy metals containing sewage from different industries, heavy metal-containing fertilizers and pesticides used in agricultural fields etc. [1]. Amongst the various heavy metals or metalloids, Sparks (2004) considered lead (Pb) to be one of the major pollutants for our environment [2]. Several industrial activities, viz., production of batteries, production of pigments, melting of metal as well as manufacturing of lead arsenate insecticides or lead water pipes etc. are considered as the main sources of Pb contamination in the environment [3]. Several researchers have studied the heavy metal contamination in various Indian rivers. A very high concentration of lead ( $\sim 392 \mu\text{g/L}$ ) in the downstream water of the Yamuna River [4] and noticeable quantity of iron, lead and manganese etc. in the surface water of the Ganga River around Kolkata are obtained from their studies [5]. The most unfortunate situation is that the data obtained by the scientists against contamination are far exceeded from the limits to use the surface water of the Ganga River around Kolkata for drinking purposes. Exposure of several heavy metals (such as lead, mercury, chromium, arsenic, cadmium etc.) severely affects our health which also includes the prenatal development [6] [7]. Particularly, lead ions ( $\text{Pb}^{2+}$ ) cause mental retardation, affect kidney and create anemia in our body [8]. It is one of the most detrimental contaminants released in natural waters that also affect the central nervous system, hemoglobin synthesis, reproductive systems as well as gastrointestinal tract [9]. Airborne lead is poisonous to agricultural food by the deposition on fruits, soils and water [10]. It has also been reported that anemic pregnant women and young children are more susceptible to lead toxicity [11].

In order to make an eco-friendly environment, a clean and healthy atmosphere should be provided to all living systems, which will be free from several toxic heavy metals and other hazardous pollutants contamination. Several technologies and physico-chemical methods have been employed for the removal of heavy metals or heavy metallic ion pollutants from the effluent streams and lands. These are viz., ion exchange [12], adsorption [13], membrane processing [14], reverse osmosis [15], filtration [16], biosorption [17], electro-coagulation [18] etc. These technologies or physico-chemical methods employed for removing potentially harmful heavy metals are often ineffective or expensive particularly when the concentration of heavy metals is very low. Physical separation methods are also unable to separate heavy metal salts which are dissolved in waste water [19]. While biological methods like bioremediation *i.e.*, biosorption or bioaccumulation for removal of heavy metals may be an attractive alternative

over and above the physico-chemical methods due to its better efficacy and eco-friendliness [20].

The following study has been explored an extracellular bacterial protein (approximate molecular weight ~30 kDa) which has been used directly for removal of lead contamination from water. The protein is able to form lead oxide nanoplates when adding to the lead containing salts (e.g., nitrate solution). The lead oxide nanoplates are insoluble and thus easily precipitated at the bottom and separated out by filtration. The as prepared nanoplates can be exploited against dye degradation for having its photo-catalytic activity. This is an added advantage of this study.

## 2. Materials and Methods

The bacterial strain MDH1 (GenBank accession number: KT600031) has been isolated from a virgin hot spring of Metal Danga, Birbhum District, West Bengal, India and named as MDH1 and characterized in our laboratory [21]. The bacterial strain was purified through serial dilution technique and maintained by culturing in a semi-synthetic medium in our laboratory as described earlier [21]. Phylogenetic analysis of MDH1 strain has revealed that the bacterium is associated to the family “*Pseudomonadaceae*” with 99% homologous to *Pseudomonas putida* H8234. The bacterium is non-pathogenic, gram negative, coccoid shaped and facultative-anaerobic. Lead nitrate was purchased from Sigma-Aldrich. Methyl Orange (MO) and Bromophenol blue (BB) dye were purchased from Merck, Germany. Millipore deionized water was used in this study.

### *Isolation and purification of bacterial protein*

The bacterium MDH1 has been seen to secrete some extra cellular proteins in its growth medium. The desired protein was isolated from MDH1 bacterium cultured medium (6 - 7 days old), concentrated through lyophilization and purified through double-step Sephadex G-100 column chromatographic purification technique [22]. This purified protein was used in aqueous lead nitrate [Pb(NO<sub>3</sub>)<sub>2</sub>] solution (0.6 M) for the removal of lead from the solution through the formation of lead oxide nanoplates.

### *Removal of lead form lead nitrate solution*

About 100 µg bacterial (MDH1) protein powder was added to 100 ml lead nitrate precursor solution [0.6 MPb(NO<sub>3</sub>)<sub>2</sub>] and kept at ambient temperature (37°C) for 24 hours. A white precipitation was formed which was collected through centrifugation at 4000 g using Eltek centrifugation machine (TC 4100D). The supernatant was collected through filtration (Whatmann filter paper) and dried at room temperature to get the powder sample for morphological and other experimental studies. The supernatant was stored for further analysis.

### *Identification of lead oxide precipitate*

Inductively Coupled Plasma (ICP-OES Optima 2100 DV, Perkin-Elmer) data analysis was done to confirm the removal of lead from its solution through interaction with the bacterial (MDH1) protein. The morphological characterization

of the precipitate was done by Field Emission Scanning Electron Microscope (FESEM, FEI, INSPECT F50) as well as by Transmission Electron Microscope (JEOL JEM 2100F). Energy Dispersive Spectrometer (EDX) analysis was performed for elementary detection of the nanoplates sample. The crystallographic properties of lead precipitate were studied by using X-ray diffraction (XRD) measured by X-ray diffractometer (Bruker, D8 Advance) with  $\text{CuK}_\alpha$  radiation ( $\lambda = 1.54 \text{ \AA}$ ) operated at 40 kV voltage and 40 mA current. Fourier Transform Infra-red Spectroscopy (FTIR) spectroscopy in Attenuated Total Reflection (A529-P/QMIRacle-ATR-unit, Bruker) mode with  $4 \text{ cm}^{-1}$  spectral resolution was employed to identify the functional groups present in the lead precipitate.

#### *Toxicity study of the supernatant on bacterial growth*

The supernatant of the reaction solution was separated from lead oxide precipitate through centrifugation followed by filtration through Whatmann filter paper. The toxic nature of the lead ions and the supernatant were studied by observing the zone of inhibition on *E. coli* (JM101) bacterial growth in Luria-Broth (LB) agar plate. LB medium containing agar (1.5%) was poured into Petri disc and allowed to get solidified. 100  $\mu\text{l}$  of pre-grown *E. coli* culture was spread on the agar plate and left at room temperature for at least 15 min. Three exactly identical wells were made on the agar plate using the cork borer under sterilized condition. One well was filled with 50  $\mu\text{l}$  of 0.6 M  $\text{Pb}(\text{NO}_3)_2$  solution and the rest of two wells were filled with different volumes of supernatant (20  $\mu\text{l}$  and 50  $\mu\text{l}$ ). The supernatant was obtained after removing the lead oxide nanoplates by filtration as stated earlier. The Petri agar plate was kept for incubation at  $37^\circ\text{C}$  for 24 h. After the stipulated time period, the zone of inhibition produced at the well was observed and photographed.

#### *Photo-Catalytic activity of lead oxide*

The photo catalytic activity of the lead precipitate was demonstrated by degrading hazardous dyes like Methyl Orange (MO) and Bromophenol Blue (BB). At first, 50 mg of each dye was added to 1 L of distilled water and used as stock solution. After that, 10 mg of powdered lead precipitate was added to 100 ml of each dye solution and mixed on magnetic stirrer for 15 minutes. 3 ml of the mixed solution was used to evaluate the catalytic degradation of each dye by measuring the corresponding absorbance spectrum of those dyes (300 - 700 nm) at different time intervals in UV-Visible Spectrophotometer (ELICO, SL 210). Degradation percentage of MB and BB dye in presence of lead oxide nanoplates was calculated through the formula:

$$\% \text{ of Degradation} = \frac{(C_0 - C)}{C_0} \times 100 \quad (1)$$

where  $C_0$  is the initial concentration of dye solution and  $C$  is the concentration of dye solution in presence of lead oxide nanoplates in different time intervals.

### **3. Results**

The protein used in this work was isolated from the well grown MDH1 bacterial

cultured medium and purified through double steps purification of Sephadex G-100 column chromatographic technique (Figure 1). SDS-PAGE analysis showed that the molecular weight of the isolated protein was 30 kDa approximately. The protein when added to lead nitrate solution, formed a grey colour precipitate (Figure 2(a) and Figure 2(b)). The precipitate was separated through centrifugation followed by filtration through Whatman filter paper (25 mm) and dried to make powder form as shown in Figure 2. Abundance of lead was detected in the precipitated powder when analyzed by ICP spectrum analysis of the sample (Figure 2). The morphological structure of the powder precipitate was detected by FESEM and TEM analyses and the photomicrographs of the powder precipitate are shown in Figure 3. The photomicrograph of FESEM (Figure 3(a)) and that of TEM (Figure 3(b)) clearly confirmed the presence of nanoplates like structures in the precipitate. The thickness of the plates was measured from 20 to 25 nm. The FTIR spectrum of the as prepared precipitate confirmed the presence of different chemically functional groups in the lead oxide nanoplates (Figure 4). The FTIR spectra of the powder precipitate also exhibited the presence of Amide I and Amide II bonds as seen in Figure 4, which appeared due to the addition of microbial protein to the lead nitrate solution. The very sharp peaks of the XRD pattern of the powder precipitate similarly suggested that as prepared precipitate was crystalline in nature (Figure 5).

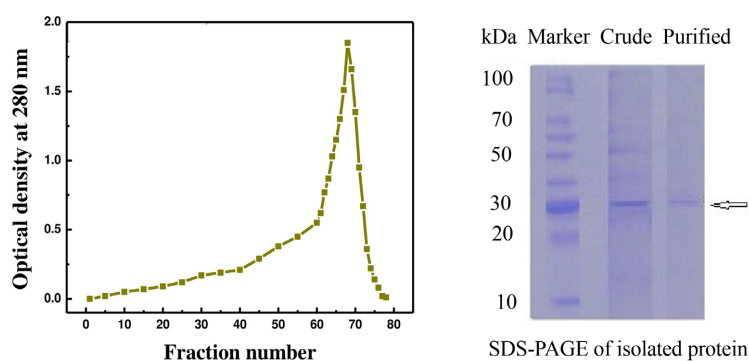


Figure 1. Purification and molecular weight determination of the protein.

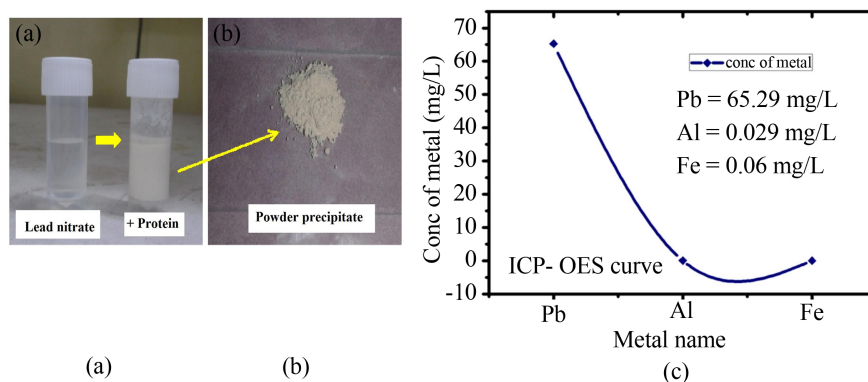
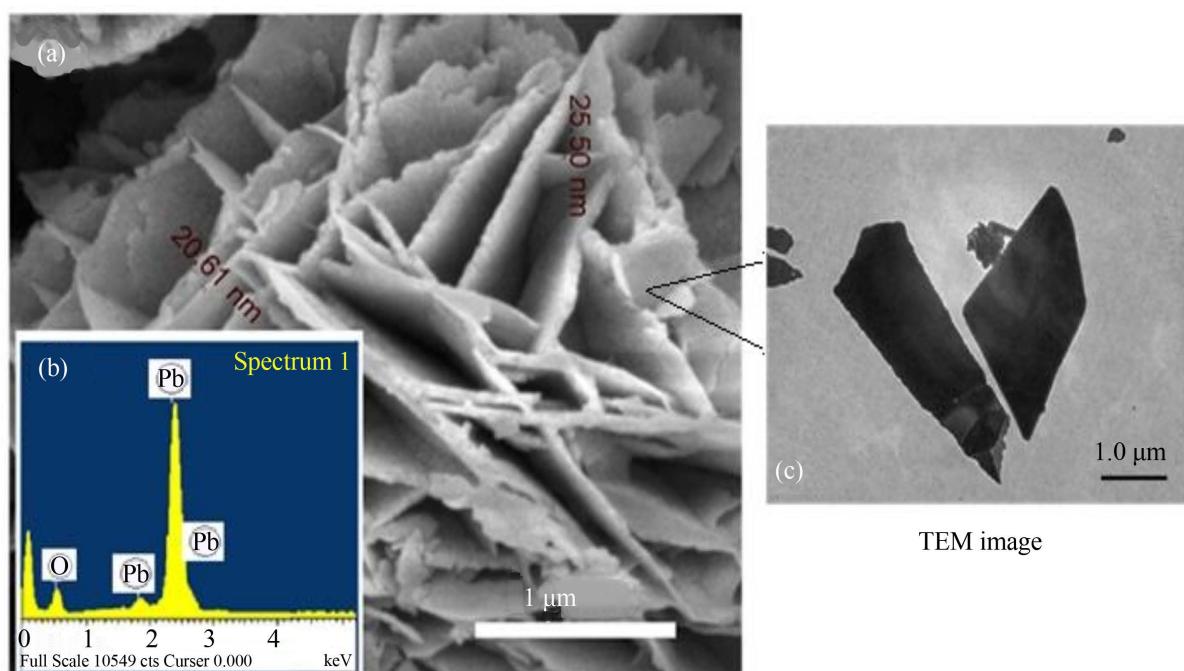
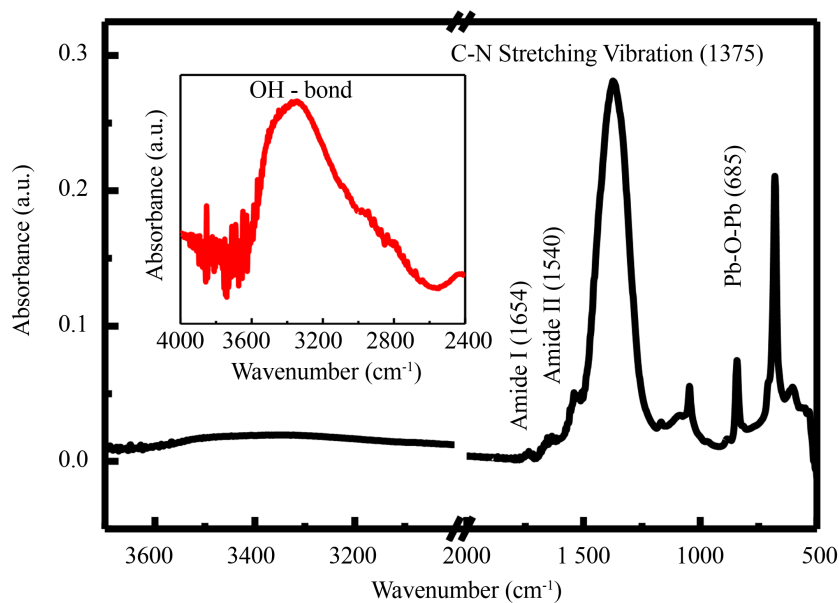


Figure 2. (a) and (b) Preparation of lead oxide precipitate; (c) ICP-OES characterization of lead oxide precipitate.

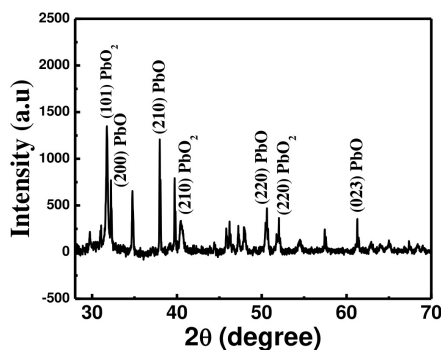


**Figure 3.** (a) FESEM image of lead oxide nanoplates; (b) EDX spectra of the nanoplates in the Inset of (a); (c) TEM image of lead oxide nanoplates.

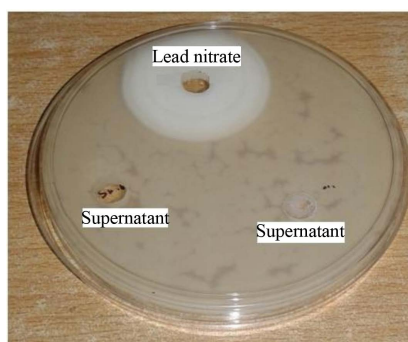


**Figure 4.** FTIR spectrum of lead oxide nanoplates. Inset shows the enlarged view of stretching vibration of OH bond.

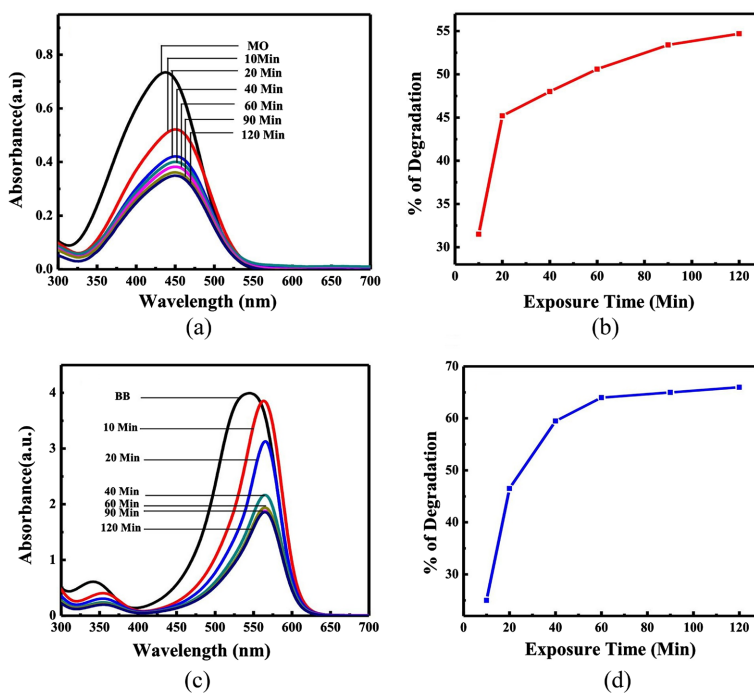
Lead nitrate assisted zone of inhibition in the growth plate of *E. coli* (JM101) bacterial cells was shown in **Figure 6**. There was no such zone of inhibition observed when only supernatant was added to the wells of the bacterial growth agar plate (**Figure 6**). The as prepared lead oxide nanoplates possess the photo-catalytic activity due to which it degraded methyl orange and bromophenol blue dyes which were described in **Figures 7(a)-(d)** respectively.



**Figure 5.** X-ray diffraction pattern of lead oxide nanoplates.



**Figure 6.** Zone of inhibition showing the non-toxic effect of the supernatant (which was obtained after removal of the lead ions by the precipitation of lead oxide nanoplates) on *E. coli* (JMJ 101) bacterial growth.



**Figure 7.** Photo-catalytic activity of the lead oxide nanoplates. where (a) Degradation of MO dye; (b) Degradation of BB dye; (c) % of Degradation of MO dye; (d) % Degradation of BB dye.

#### 4. Discussion

Heavy metals or metalloids are harmful to all living organisms because of their tendency to accumulate inside the biological system. It remains there over a prolonged period that causes several complications against survival. However, it is well known that a number of phytochemicals as well microorganisms are able to remove several heavy metals both from human beings and surroundings. Gu *et al.* (2017) have suggested a plausible microbiological process to remove metals from water [23]. Several bacteria are able to remove mercury from the sediment at a much higher rate of adsorption [24] [25]. Inorganic lead compounds are transformed into volatile tetra-methyl lead by some specific microorganism under anaerobic conditions [26]. Al-Rubaie and Al-Kubaisi (2015) have published a paper where they have described a process of lead removal from water by using aquatic plants [27]. Here an easy and amicable method is developed for removal of lead contamination which would be beneficial for us.

The process is comprised with the addition of a microbial protein to the lead nitrate solution. The protein was isolated from the well grown MDH1 bacterial cultured medium and purified through double steps Sephadex G-100 column chromatographic technique. The protein is secreted by the MDH1 bacteria and its molecular weight is approximately 30 kDa (Figure 1). The protein when adding to the lead nitrate solution, forms a precipitate which is grey in colour and insoluble in water (Figure 2). The as prepared precipitate was separated through centrifugation and followed by filtration through Whatmann filter paper and dried to make powder form. The ICP-OES spectrum of the powder precipitate confirmed that there was abundance of elementary lead present in the precipitated sample which was formed by the action of MDH1 microbial protein and lead nitrate solution (Figure 2). ICP-OES is one of the most versatile methods for inorganic elemental analysis and use to determine the concentration of the heavy metals present in the solution [28]. Several bacterial strains (such as BKH1, BKH2, BKH4 etc.) isolated from hot springs of Bakreshwar similarly secrete several proteins in the growth medium which have the characteristic biomineralization property for which these bacteria can be used for the development of high performance self-healed bio-concrete materials [22] [29] [30] [31]. The bacterium BKH1 is also able to produce silver nanoparticles [32]. Similarly, the whole cells of bacterium MDH1 show its ability for formation of gold nanoparticles [21]. Akhtar *et al.* (2013) has shown the biogenic synthesis of metallic nanoparticles by plant extracts. So the formation of lead nanoplates by the MDH1 bacterial protein is not at all a surprising phenomenon [33].

The morphological structure of the powder precipitate was seen by FESEM and TEM photomicrographs from (Figure 3). FESEM (Figure 3(a)) and TEM (Figure 3(b)) images clearly confirmed the nanoplates like structure present in the precipitate. The thickness of the plates was from 20 to 25 nm. Strong peaks of lead and oxygen only in the EDX spectra of the nanoplates revealed that the as prepared precipitate was the lead-oxide nanoplates. The FTIR spectrum (Figure

4) of the as prepared precipitate confirmed the presence of some chemically functional groups in the lead oxide nanoplates. A sharp peak at around  $685\text{ cm}^{-1}$  represented the asymmetric bending vibration of Pb-O-Pb bond. A very broad peak appeared at  $3100 - 3600\text{ cm}^{-1}$  region in the FTIR spectrum was signifying OH stretching vibration in H-bonded water which is shown in the inset of **Figure 4** with enlarged view. Another intense peak at  $1375\text{ cm}^{-1}$  indicated the C - N stretching vibration. The FTIR spectra exhibited the presence of Amide I and Amide II bonds as seen in **Figure 4**, which appeared due to the addition of microbial protein to the lead nitrate solution. The peaks between  $1600 - 1700\text{ cm}^{-1}$  were the stretching vibration of C=O bond of Amide I. The amide II band occurred at  $1500 - 1600\text{ cm}^{-1}$  and was mainly derived from the N-H bending vibration. FTIR study thus confirmed that the Amide I ( $1654\text{ cm}^{-1}$ ) and Amide II ( $1540\text{ cm}^{-1}$ ) both have the stronger ability to bind metallic atoms. It signifies that the protein may be responsible for forming a surface layer on the metallic lead oxide nanoplates that helps in stabilization of lead oxide nanoplates.

The crystalline nature of the powder precipitate was ascertained by XRD analysis (**Figure 5**). The very sharp peaks in the XRD spectra of powder precipitate are the clear evidence of the crystalline nature of the lead oxide nanoplates. In comparison with standard XRD card (JCPDS data file), the main intense peak at  $31.8^\circ$  corresponds to the diffraction from (101) lattice plane and peaks at  $52^\circ$  and  $40.4^\circ$  correspond to (220) and (210) lattice planes respectively. The XRD analysis of powder precipitate was the clear indication of  $\text{PbO}_2$  nanoplates formation as per the JCPDS analysis (card no. 080185). Another intense peak at  $37.9^\circ$  corresponds to (210) and at  $32.2^\circ$ ,  $50.7^\circ$  and  $61.1^\circ$  and correspond to (200), (220) and (023) planes respectively represent the PbO formation by JCPDS analysis (card no. 050570). So, the XRD pattern of the powder sample clearly indicates the formation two forms of lead oxides. Both forms are insoluble in water. This type of reaction is known as disproportion reaction.

Lead ion is a very toxic compound which has bactericidal effect. It thus created a clear zone of inhibition on the culture plate against the *E. coli* (JM101) bacterial growth (**Figure 6**). But no such zone of inhibition was observed when supernatant (which was obtained after filtration of lead oxide nanoplates from the solution) was added to the wells of the *E. coli* bacterial growth containing agar plate. This result tells us that the bactericidal effect of the lead ions is lost due to the absence of lead ions in the supernatant. The MDH1 bacterial protein dissociates lead ions from its solution through the formation of lead oxide nanoplates.

The release of dye effluents from textile industry is a major source of water pollution. Presence of dyes in waste water would have harmful effect on aquatic system. Methyl Orange (MO) and Bromophenol Blue (BB) dyes are the pollutants of waste water, foods, cosmetics, agriculture and have a potential threat to the environment. The treatments for removing MO and BB dyes are therefore highly desirable. The catalytic degradation of these dye using nanoparticles is one of the most important and useful method for removing dyes from our envi-



ronment. Our results showed that lead-oxide nanoplates had the Photo-catalytic ability for which it degraded MO and BB dye as described in **Figures 7(a)-(d)** respectively. The percentage of degradation ability of lead-oxide nanoplates was also calculated using Equation (1) and the percentage degradation spectra of MO and BB dyes were also shown in **Figure 7(c)** and **Figure 7(d)** respectively. These data and spectrum conclude the fact that bio-synthesized lead-oxide nanoplates are one of the effective photo catalyst. Chowdhury *et al.* (2015) have established that the hot spring bacterium BKH1 secretes bioremediase protein (molecular weight of 28 kDa) in the growth medium, which possess silica leaching activity [34]. They have proposed the mechanism of action of bioremediase protein against silica nanoparticles formation in biosilicification process. We also hypothesize similar type of action is taking place by the hot spring MDH1 bacterial protein against the formation of lead nanoplates. The actual mechanism of action of the protein against lead nanoplates formation will be established and reported in future.

## 5. Conclusion

The work demonstrated here is a facile and eco-efficient route for the removal of lead contamination from water by using a simple biological template. The results from different experiments confirm that the MDH1 microbial protein has the ability for formation of lead-oxide nanoplates from lead nitrate solution. The prepared lead oxide nanoplates also possess photo catalytic property due to which it can degrade several dyes (like MO and BB etc.) and be used for the removal of those dyes from several industrial effluents. The MDH1 microbial protein is thus very useful for cleaning of lead contaminated water as well as BB and MO contaminated industrial effluents, foods and several agricultural products.

## Funding Information

The financial support from WOS-A Scheme (Ref. SR/WOS-A/PM-43/2018) from Department of Science and Technology, Government of India, New Delhi is gratefully acknowledged. Authors are grateful for the experimental and technical supports provided by the Biophysics Laboratory, Department of Physics, Jadavpur University.

## Conflicts of Interest

There is no conflict of interest of any kind related to this work.

## Availability of Data and Material

All the data obtained from several experiments are presented within the text of the manuscript.

## Code Availability

NA.

## Authors' Contributions

BDC and AT conceived and designed the study. CG and SG conducted all the experimental work. CG also contributed new reagents or analytical tools. CG and AT analyzed the experimental data. BDC wrote the manuscript. All authors read carefully and approved the manuscript.

## Ethics Approval

NA.

## Consent to Participate

NA.

## Consent for Publication

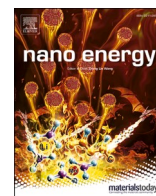
All the authors have given their consent to publish the article.

## References

- [1] Reza, R. and Singh, G. (2010) Heavy Metal Contamination and Its Indexing Approach for River Water. *International Journal of Environmental Science and Technology*, **7**, 785-792. <https://doi.org/10.1007/BF03326187>
- [2] Sparks, D.L. (2004) Toxic Metals in the Environment: The Role of Surfaces. *Elements*, **1**, 193-197. <https://doi.org/10.2113/gselements.1.4.193>
- [3] Jarosławiecka, A. and Piotrowska-Seget, Z. (2014) Lead Resistance in Micro-Organisms. *Microbiology*, **160**, 12-25. <https://doi.org/10.1099/mic.0.070284-0>
- [4] Singh, A.K., Srivastav, S.C., Verma, P., Ansari, A. and Verma, A. (2014) Hazard Assessment of Metals in Invasive Fish Species of the Yamuna River, India in Relation to Bioaccumulation Factor and Exposure Concentration for Human Health Implications. *Environmental Monitoring and Assessment*, **186**, 3823-3836. <https://doi.org/10.1007/s10661-014-3660-6>
- [5] Aktar, M.W., Paramasivam, M., Ganguly, M., Purkait, S. and Sengupta, D. (2010) Assessment and Occurrence of Various Heavy Metals in Surface Water of Ganga River around Kolkata: A Study for Toxicity and Ecological Impact. *Environmental Monitoring and Assessment*, **160**, 207-213. <https://doi.org/10.1007/s10661-008-0688-5>
- [6] Jaishankar, M., Tseten, T., Anbalagan, N., Mathew, B.B. and Beeregowda, K.N. (2014) Toxicity, Mechanism and Health Effects of Some Heavy Metals. *Interdisciplinary Toxicology*, **7**, 60-72. <https://doi.org/10.2478/intox-2014-0009>
- [7] Wai, K., Mar, O., Kosaka, S., Umemura, M. and Watanabe, C. (2017) Prenatal Heavy Metal Exposure and Adverse Birth Outcomes in Myanmar: A Birth-Cohort Study. *International Journal of Environmental Research and Public Health*, **14**, Article No. 1339. <https://doi.org/10.3390/ijerph14111339>
- [8] Neal, A.P. and Guilarte, T.R. (2010) Molecular Neurobiology of lead (Pb<sup>2+</sup>): Effects on Synaptic Function. *Molecular Neurobiology*, **42**, 151-160. <https://doi.org/10.1007/s12035-010-8146-0>
- [9] Liu, L.E., Liu, J., Li, H., Zhang, H., Liu, J. and Zhang, H. (2012) Equilibrium, Kinetic, and Thermodynamic Studies of Lead (II) Biosorption on Sesame Leaf. *BioResources*, **7**, 3555-3572.

- [10] Yamamura, S. (1984) Guidelines for Drinking Water Quality. World Health Organization, Geneva.
- [11] Flora, S.J.S., Flora, G. and Saxena, G. (2006) Environmental Occurrence, Health Effects and Management of Lead Poisoning. In: José, S.C. and José, S., Eds., *Lead*. Elsevier, Amsterdam, 158-228. <https://doi.org/10.1016/B978-044452945-9/50004-X>
- [12] Chen, Y., Pan, B., Li, H., Zhang, W., Lv, L. and Wu, J. (2010) Selective Removal of Cu (II) Ions by Using Cation-Exchange Resin-Supported Polyethyleneimine (PEI) Nanoclusters. *Environmental Science & Technology*, **44**, 3508-3513. <https://doi.org/10.1021/es100341x>
- [13] Ahmad, R. and Haseeb, S. (2016) Kinetic, Isotherm and Thermodynamic Studies for the Removal of Pb<sup>2+</sup> Ion by a Novel Adsorbent *Luffa acutangula* (LAPR). *Desalination and Water Treatment*, **57**, 17826-17835. <https://doi.org/10.1080/19443994.2015.1088476>
- [14] Bhatluri, K.K., Manna, M.S., Saha, P. and Ghoshal, A.K. (2014) Supported Liquid Membrane-Based Simultaneous Separation of Cadmium and Lead from Wastewater. *Journal of Membrane Science*, **459**, 256-263. <https://doi.org/10.1016/j.memsci.2014.02.019>
- [15] Rao, M.M., Ramana, D.K., Seshaiha, K., Wang, M.C. and Chien, S.C. (2009) Removal of Some Metal Ions by Activated Carbon Prepared from *Phaseolus aureus* Hulls. *Journal of Hazardous Materials*, **166**, 1006-1013. <https://doi.org/10.1016/j.jhazmat.2008.12.002>
- [16] Jawor, A. and Hoek, E.M. (2010) Removing Cadmium Ions from Water via Nanoparticle-Enhanced Ultrafiltration. *Environmental Science & Technology*, **44**, 2570-2576. <https://doi.org/10.1021/es902310e>
- [17] Ofomaja, A.E., Naidoo, E.B., Modise, S.J. (2010) Biosorption of Copper (II) and Lead (II) onto Potassium Hydroxide Treated Pine Cone Powder. *Journal of Environmental Management*, **91**, 1674-1685. <https://doi.org/10.1016/j.jenvman.2010.03.005>
- [18] Parga, J.R., Cocke, D.L., Valenzuela, J.L., Gomes, J.A., Kesmez, M., Irwin, G. and Weir, M. (2005) Arsenic Removal via Electrocoagulation from Heavy Metal Contaminated Groundwater in La Comarca Lagunera Mexico. *Journal of Hazardous Materials*, **124**, 247-254. <https://doi.org/10.1016/j.jhazmat.2005.05.017>
- [19] Kapoor, A. and Viraraghavan, T. (1995) Fungal Biosorption-an Alternative Treatment Option for Heavy Metal Bearing Wastewaters: A Review. *Bioresource Technology*, **53**, 195-206. [https://doi.org/10.1016/0960-8524\(95\)00072-M](https://doi.org/10.1016/0960-8524(95)00072-M)
- [20] Hussein, H., Fara, S. and Moawad, H. (2003) Isolation and Characterization of Pseudomonas Resistant to Heavy Metals Contaminants. *Arab Journal of Biotechnology*, **7**, 13-22. <https://doi.org/10.2225/vol7-issue1-fulltext-2>
- [21] Alam, N., Sarkar, M., Chowdhury, T., Ghosh, D. and Chattopadhyay, B.D. (2016) Characterization of a Novel MDH1 Bacterium from a Virgin Hot Spring Applicable for Gold Nanoparticle (GNPs) Synthesis. *Advances in Microbiology*, **6**, 724-732. <https://doi.org/10.4236/aim.2016.69071>
- [22] Biswas, M., Majumdar, S., Chowdhury, T., Chattopadhyay, B.D., Mandal, S., Halder, U. and Yamasaki, S. (2010) Bioremediase a Unique Protein from a Novel Bacterium BKH1, Ushering a New Hope in Concrete Technology. *Enzyme and Microbial Technology*, **46**, 581-587. <https://doi.org/10.1016/j.enzmictec.2010.03.005>
- [23] Gu, Z., Aikebaier, Y., Arefieva, V. and Mazirov, M. (2017) Using Microbiological Leaching Method to Remove Heavy Metals from Sludge. *Eurasian Journal of Soil Science*, **6**, 51. <https://doi.org/10.18393/ejss.284265>

- [24] Meger, S.A. (1986) Polluted Precipitation and the Geochronology of Mercury Deposition in Lake Sediment of Northern Minnesota. In: Martin, H.C., Ed., *Acidic Precipitation*, Springer, Dordrecht, 411-419.  
[https://doi.org/10.1007/978-94-009-3385-9\\_41](https://doi.org/10.1007/978-94-009-3385-9_41)
- [25] Pongratz, R. and Heumann, K.G. (1999) Production of Methylated Mercury, Lead, and Cadmium by Marine Bacteria as a Significant Natural Source for Atmospheric Heavy Metals in Polar Regions. *Chemosphere*, **39**, 89-102.  
[https://doi.org/10.1016/S0045-6535\(98\)00591-8](https://doi.org/10.1016/S0045-6535(98)00591-8)
- [26] Maher, W.A. (1981) Determination of Inorganic and Methylated Arsenic Species in Marine Organisms and Sediments. *Analytica Chimica Acta*, **126**, 157-165.  
[https://doi.org/10.1016/S0003-2670\(01\)83938-6](https://doi.org/10.1016/S0003-2670(01)83938-6)
- [27] Al-Rubaie, A.S.A. and Al-Kubaisi, A.R.A. (2015) Removal of Lead from Water by Using Aquatic Plants (*Ceratophyllum demersum* and *Eichhorina crassipes*). *International Journal of Current Microbiology and Applied Sciences*, **4**, 45-51.
- [28] Chand, V. and Prasad, S. (2013) ICP-OES Assessment of Heavy Metal Contamination in Tropical Marine Sediments: A Comparative Study of Two Digestion Techniques. *Enzyme and Microbial Technology*, **111**, 53-61.  
<https://doi.org/10.1016/j.microc.2012.11.007>
- [29] Sarkar, M., Adak, D., Tamang, A., Chattopadhyay, B.D. and Mandal, S. (2015) Genetically-Enriched Microbe-Facilitated Self-Healing Concrete—A Sustainable Material for a New Generation of Construction Technology. *RSC Advances*, **5**, 105363-105371.  
<https://doi.org/10.1039/C5RA20858K>
- [30] Sarkar, M., Chowdhury, T., Chattopadhyay, B.D., Gacchui, R. and Mandal, S. (2014) Autonomous Bioremediation of a Microbial Protein (Bioremediase) in Pozzolana Cementitious Composite. *Journal of Materials Science*, **49**, 4461-4468.  
<https://doi.org/10.1007/s10853-014-8143-1>
- [31] Sarkar, A., Chatterjee, A., Mandal, S. and Chattopadhyay, B.D. (2019) An Alkali-philic Bacterium BKH4 of Bakreshwar Hot Spring Pertinent to Bio-Concrete Technology. *Journal of Applied Microbiology*, **126**, 1742-1750.  
<https://doi.org/10.1111/jam.14236>
- [32] Show, S., Tamang, A., Chowdhury, T., Mandal, D. and Chattopadhyay, B.D. (2015) Bacterial (BKH1) Assisted Silica Nanoparticles from Silica Rich Substrates: A Facile and Green Approach for Biotechnological Applications. *Colloids and Surfaces B*, **126**, 245-250. <https://doi.org/10.1016/j.colsurfb.2014.12.039>
- [33] Akhtar, M.S., Panwar, J. and Yun, S.Y. (2013) Biogenic Synthesis of Metallic Nanoparticles by Plant Extracts. *ACS Sustainable Chemistry & Engineering*, **1**, 591-602.  
<https://doi.org/10.1021/sc300118u>
- [34] Chowdhury, T., Sarkar, M., Chaudhuri, B., Chattopadhyay, B.D. and Halder, U.C. (2015) Participatory Role of Zinc in Structural and Functional Characterization of Bioremediase: A Unique Thermostable Microbial Silica Leaching Protein. *Journal of Biological Inorganic Chemistry*, **20**, 791-803.  
<https://doi.org/10.1007/s00775-015-1266-2>



# Environmental bacteria engineered piezoelectric bio-organic energy harvester towards clinical applications

Chetana Ghosal<sup>a,1</sup>, Sujoy Kumar Ghosh<sup>a,1,2</sup>, Kritish Roy<sup>a</sup>, Brajadulal Chattopadhyay<sup>a,\*</sup>, Dipankar Mandal<sup>b,\*</sup>

<sup>a</sup> Department of Physics, Jadavpur University, Kolkata 700032, India

<sup>b</sup> Quantum Materials and Devices Unit, Institute of Nano Science and Technology, Knowledge city, Sector-81, Mohali 140306, India

## ARTICLE INFO

### Keywords:

Bacteria  
PVDF  
Piezoelectric  
Energy harvester  
Biocompatible  
Healthcare

## ABSTRACT

State-of-the-art biomedical applications including healthcare monitoring, in vivo real-time sensing and disease treatment largely relies on bio-piezoelectric platforms consisting of biocompatibility and piezoelectricity. However, the inability to design a high performance piezoelectric material with biocompatibility is the major challenges towards practical implementation. Here we present the concept and design principles of an biocompatible piezoelectric material with the assistance of environmental (hot spring) bacterial strain. The biological bacterial protein engineered the microstructure of organic polymer poly(vinylidene fluoride) (PVDF) in order to design the porous bio-organic films with increased biocompatibility, piezoelectric phase content and crystallinity. The porous microstructure significantly enhances the piezoelectric coefficient ( $d_{33} \sim -43$  pC/N) and piezoelectric figure of merit ( $FoM_p \sim 18.8 \times 10^{-12}$  Pa<sup>-1</sup>) of the bio-organic film compared with non-porous pure PVDF ( $d_{33} \sim -0.85$  pC/N,  $FoM_p \sim 8.5 \times 10^{-15}$  Pa<sup>-1</sup>). The proof-of-concept of device designing is also studied, that is nanogenerator composed of bio-organic film is capable to generate maximum output power of as high as 640 mW/m<sup>2</sup>, possesses energy conversion efficiency of 62.5% which is further used for driving several commercial light emitting diodes (LEDs) and charge capacitors. The enhanced piezoelectric performance is attributed via porosity formation and validated through finite element method (FEM) based theoretical simulation. With the good biocompatibility and piezoelectric pressure sensitivity (1.26 V kPa<sup>-1</sup> and 0.86 V kPa<sup>-1</sup> in the pressure range of 0.01 –1 kPa and 2 –15 kPa respectively), the device was implemented towards clinical applications of real-time healthcare monitoring from subtle pulse pressure waveform detection to vibrotactile information collection. With its natural biocompatibility, easy to prepare formulation and superior energy harvesting performance, the bio-organic film offers attractive prospects towards the development of effective, sustainable and autonomous electromechanical device for next generation self-powered biomedical devices.

## 1. Introduction

In our modern society, green sustainable energy is one of the major resources to foster our requirements in daily life. These renewable energy sources are a good complementary to the limited fossil fuels dependent energy challenges [1]. A sustainable energy resources without depending on any environmental conditions and irrespective of day and night time is mandatory to explore. For instance, piezoelectric nanogenerator (PENG) have obtained great attraction because of its self-powered flexible mechanical energy harvesting feasibility through

which environmental mechanical vibration convert to electrical energy and increase applicability in portable electrical devices [2]. In addition, sustainable PENG is one of the best choices towards biomedical applications from healthcare monitoring sensors to implantable devices for leading a healthy lifestyle [3–7]. In this context, organic piezoelectric materials, such as poly(vinylidene fluoride) (PVDF) and its co-polymers acquired significant attention for their suitable biocompatible, flexibility, light weight, chemical resistivity, and ease of large area processing in comparison to inorganic piezoelectric materials [8]. In order to implement PVDF towards clinical applications with energy harvesting

\* Corresponding authors.

E-mail addresses: [bdc\\_physics@yahoo.co.in](mailto:bdc_physics@yahoo.co.in), [brajadulal.chattopadhyay@jadavpuruniversity.in](mailto:brajadulal.chattopadhyay@jadavpuruniversity.in) (B. Chattopadhyay), [dmandal@inst.ac.in](mailto:dmandal@inst.ac.in) (D. Mandal).

<sup>1</sup> These authors contributed equally to this work.

<sup>2</sup> Present address: Laboratorio NEST, Istituto Nanoscienze-CNR and Scuola Normale Superiore, Piazza S. Silvestro 12, I-56127 Pisa, Italy.

capability, the  $\beta$ - and  $\gamma$ -crystalline phase is the prerequisite among polymorphs ( $\alpha$ ,  $\beta$ ,  $\gamma$  and  $\epsilon$ -phases). Noteworthy to mention that recent study indicating that rarely explored  $\delta$ -phase (which is basically polarized form of  $\alpha$ -phase) in PVDF is also fulfill the need of electroactive phase for fabricating the mechanical energy harvesters and sensors [9]. However, piezoelectric activity in PVDF cannot be planted effectively without electrical poling i.e., the PVDF layer is needs to be settled into electric field where the randomly oriented  $-\text{CH}_2 - / -\text{CF}_2 -$  dipoles would be aligned in the direction of electric field [8]. However, electrical poling is not always suitable due to its actual power expenditure, occurrence of repeated electrical failure and practical applications towards skin sensors and robotic interfaces. In this scenario, many different effective techniques are adopted to accomplish the self-polarized  $\beta/\gamma$ -phase generation without typical electric poling such as, phase-inversion technique [10], spin coating [8], and Langmuir–Schaefer (LS) method [11]. Among the available techniques, a simple and low-cost method is incorporation of external assisting agent to PVDF leading to self-polarized  $-\text{CH}_2 - / -\text{CF}_2 -$  dipoles due to the self-poling activity [2]. Additionally, recent attempts offered to prepare the porous self-polarized PVDF based highly sensitive PENGs which are more effective to the power generation. It also shows a good piezoelectric co-efficient ( $d_{33}$ ) comparable to the toxic, fragile lead zirconate titanate (PZT) [12–14] To date, many attempts have been observed where external additives were incorporated into PVDF in order to increase the piezoelectricity for high performance PENGs [2]. However, implementation of those materials towards clinical approach is still questionable due to lack of study on biocompatibility of those materials because in many cases the external additives are still invasive to human cell. In this regard, next to plants, natural bacteria account for most of the biomass on earth is an ideal choice [15]. Many of the microorganisms which exist in environment are not human pathogen. Unlike any other inorganic material or chemical catalyst, bacteria can be considered living biofactories, unique in their ability to undergo evolutionary adaption in relatively short time spans and engineered the materials microstructure and properties. Considering their ecological and biological relevance, there are multifaceted uses of bacteria as biological factories in diverse applications including but not limited to industrial, agricultural and medical applications.

In this work, environmentally available thermophilic BKH2 bacterial strain [16] was used to prepare highly biocompatible bio-organic piezoelectric PVDF film which was further used to design a piezoelectric energy harvester to implement into clinical healthcare monitoring applications (Fig. 1). The bacterial protein (BP) interacted with the PVDF chain to induce self-polarized  $\beta$ -phase, increased the crystallinity and engineered microstructure to form porous, spongy and flexible film. The designed nanogenerator with the developed bio-organic film generated high power throughput of  $640 \text{ mW/m}^2$ , possesses superior energy conversion efficiency of 62.5% and autonomously operated the consumer electronic components. Furthermore, with the superior sensitivity, the device was implemented towards physiological signal monitoring from subtle pressure sensing of human pulse wave to vocal cord vibration simulating.

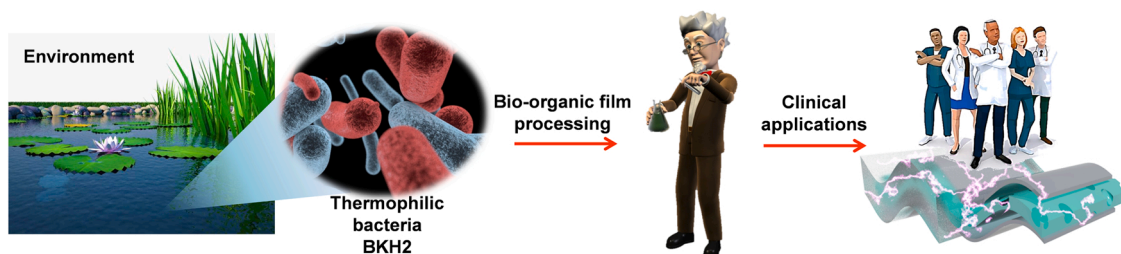
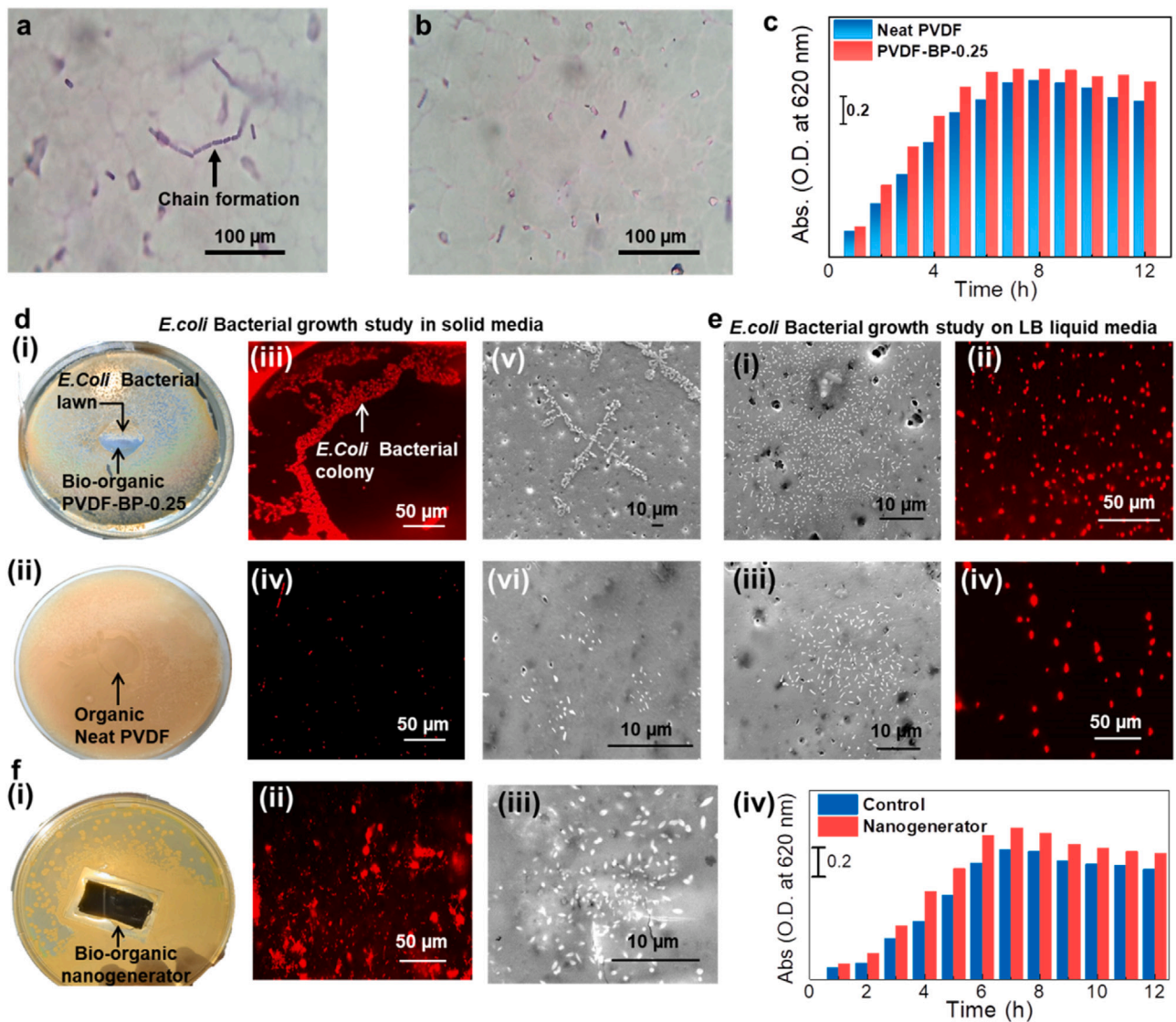


Fig. 1. The concept and design principles of the bio-organic films using the environmentally available bacteria—from biosynthesis to clinical applications.

## 2. Results and discussions

The biocompatibility of the bio-organic PVDF films was studied using the common nonpathogenic model Gram-negative bacteria *Escherichia coli* (*E. coli*). Fig. 2a represents chain formation of rod-shaped *E. coli* bacteria over PVDF-BP-0.25 bio-organic film (details regarding the naming and fabrication process of the bio-organic films are provided in the experimental section) whereas *E. coli* bacteria were present in scatter manner over Neat PVDF surface (Fig. 2b). It implies good cell adhesion of *E. coli* bacteria into PVDF-BP-0.25 film. This cell adhesion functionality further helps the cells to proliferate with time. The exponential growth of the *E. coli* bacteria cells with time over the film surfaces was represented in Fig. 2c. After the saturation phase (the counterbalance between the growth and death of cells  $\sim 7$  h) no net increase in cell numbers was observed. It is important to note that cells proliferation was more pronounced over PVDF-BP-0.25 film in comparison to Neat PVDF film. In order to strengthen our observations, further studies were conducted through *E. coli* bacteria ( $\sim 10^6$  cell/ml initially) culture over bio-organic PVDF-BP-0.25 and organic Neat PVDF films in both solid Luria Broth (LB) media and liquid LB media. The solid medium LB agar plate along with PVDF-BP-0.25 (Fig. 2d(i)) and Neat PVDF (Fig. 2d(ii)) represent large quantity of bacterial growth, forming a lawn of *E. coli* over PVDF-BP-0.25 due to over population on the agar plate which was not present on Neat PVDF film. The immunofluorescence microscopy images show large content *E. coli* colony formation over bio-organic PVDF-BP-0.25 film (Fig. 2d(iii)). In contrast, a small content of bacterial growth was observed over organic Neat PVDF film and no colony formation was observed (Fig. 2d(iv)). The FE-SEM images also show *E. coli* bacterial colony formation over PVDF-BP-0.25 film (Fig. 2d(v)) and lower content of bacterial growth over Neat PVDF film (Fig. 2d(vi)). In fact, higher concentration of BKH2 bacterial strain into PVDF film improved the biocompatibility which was further evaluated by considering the *E. coli* bacterial ( $\sim 10^6$  cell/ml initially) culture over bio-organic PVDF-BP-1.0 film where lawn of *E. coli* over PVDF-BP-1.0 film in LB agar plate is more prominent as well as content of bacterial growth was increased (Fig. S1). Even, *E. coli* bacterial cell division over PVDF-BP-1.0 film was clearly observed during bacterial growth. In addition, *E. coli* bacterial growth over the films using LB liquid media results larger bacterial growth over PVDF-BP-0.25 film as evidenced in FE-SEM (Fig. 2e(i)) and immunofluorescence microscopy images (Fig. 2e(ii)) compared to Neat PVDF film (Fig. 2e(iii),(iv)) which are also consistent with the optical microscopy images in Fig. 2a,b. These cumulative results establishes the fact that bio-organic PVDF-BP films are more biocompatible compared to Neat PVDF and more applicable in biomedical devices. In fact, *E. coli* bacteria culture over PVDF-BP-0.25 film based bio-organic nanogenerator (Fig. 2f(i)) using solid media LB agar plate demonstrated good content of bacteria growth over the surface as observed in immunofluorescence microscopy (Fig. 2f(ii)) and FE-SEM (Fig. 2f(iii)) images. In addition, *E. coli* bacterial growth over the nanogenerator using LB liquid media results larger bacterial growth compared to the control media (the media without nanogenerator) as shown in Fig. 2f(iv). This result indicates the biocompatible functionality of the bio-organic nanogenerator. The

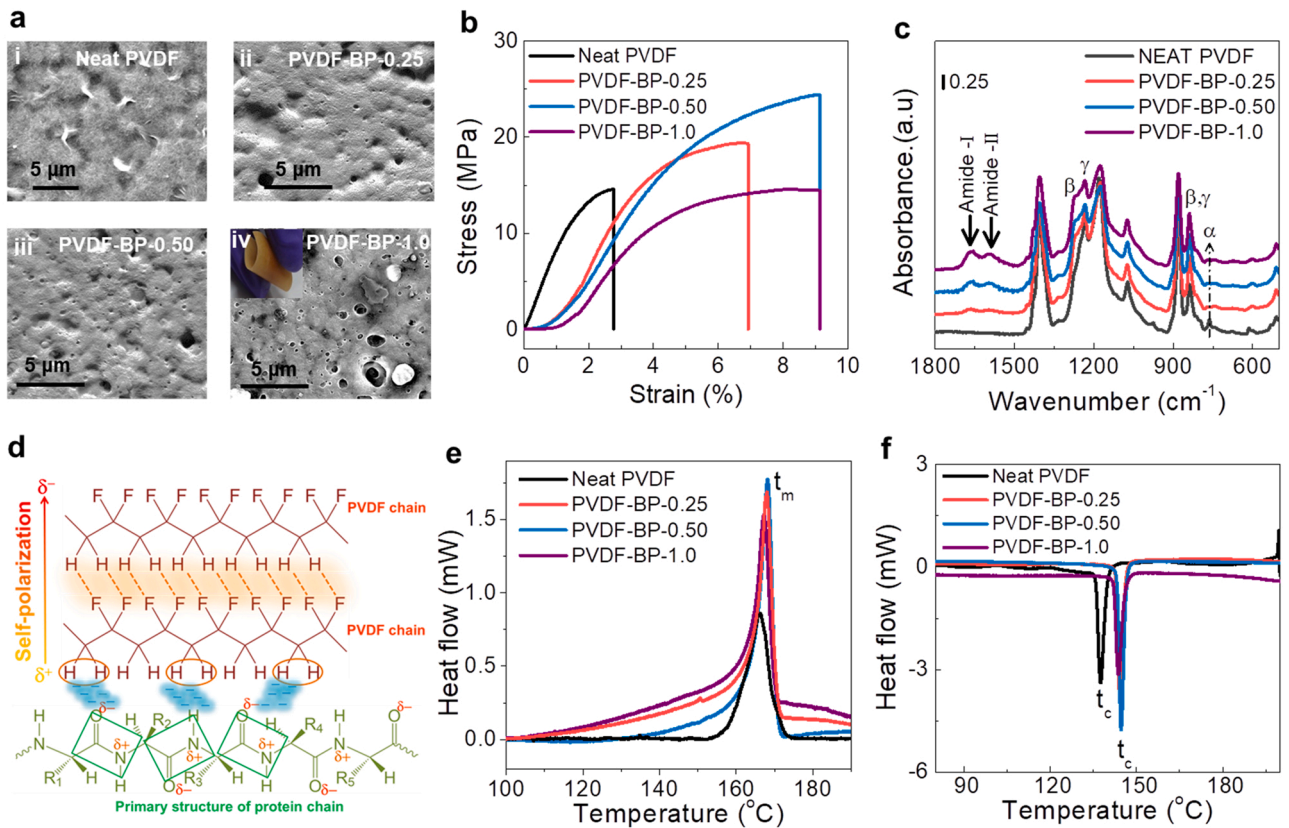


**Fig. 2.** Biocompatibility tests. (a) Optical microscopy images showing growth of the *E. coli* bacterium over the surface of the PVDF-BP-0.25 bio-organic film and (b) Neat PVDF film. (c) Cell proliferation of the *E. coli* bacterium over the surface of PVDF-BP-0.25 and Neat PVDF films demonstrating the biocompatibility nature. (d) *E. coli* bacterial growth study from solid medium LB agar plate. (i) Digital images of LB agar plate along with PVDF-BP-0.25 film and (ii) Neat PVDF film. (iii) The immunofluorescence microscopy images of PVDF-BP-0.25 and (iv) Neat PVDF film. (v) The FE-SEM images of PVDF-BP-0.25 and (vi) Neat PVDF films. (e) Growth study of *E. coli* bacteria on the surface of the films collected from liquid LB media (i) FE-SEM image and (ii) immunofluorescence microscopy images of *E. coli* bacteria over the surface of PVDF-BP-0.25. (iii) The FE-SEM and (iv) immunofluorescence microscopy images of *E. coli* bacteria over the surface of Neat PVDF film. (f) (i) Digital images of LB agar plate along with PVDF-BP-0.25 film based bio-organic nanogenerator, (ii) immunofluorescence microscopy image and (iii) FE-SEM images of *E. coli* bacteria over the surface of nanogenerator. (iv) Cell proliferation of the *E. coli* bacterium in liquid LB media in the presence of nanogenerator and without nanogenerator (control).

biocompatibility of a material is defined as the material property, which, after implantation in a living organism, does not produce adverse reactions or toxicity and must not induce inflammatory reactions [17]. In this case, the lowest concentration (0.25 wt%) of BP mixed PVDF film was chosen for comparison in order to represent strong effect of BKH2 bacterial strain even with lower content towards improving the biocompatibility feature of the bio-organic film.

The good cell adhesion property of the PVDF-BP film is understood by studying the surface morphology (Fig. 3a). The PVDF-BP films show formation of porous microstructure over surface (Fig. 3a(ii)-(iv)) and across volume (Fig. S2) which increased with higher content of additive BP into PVDF. This porous structure was beneficial for cell adhesion and cell proliferation. Higher porosity provides a high surface area for cell-matrix interactions, sufficient space for extracellular matrix regeneration, uniform and efficient cell seeding [18]. On the other side, Neat

PVDF film shows smooth surface with  $\alpha$ -spherulite fibril growth structure with a little effect on cell adhesion. The PVDF-BP films were composed of 8%, 12% and 18% porosity with addition of 0.25, 0.5 and 1 wt% of BP additive into PVDF respectively (Note S1). In addition to the porous structure, the protein layer on the surface of PVDF matrix also appeared and increased with higher content of BP. As a result, of the porous microstructure, the PVDF-BP films become soft, spongy and flexible (inset of Fig. 3a(iv)). Furthermore, the porosity of the PVDF-BP films has significant effect on their mechanical and electrical properties. The softness of the bio-organic films was evaluated using stress ( $\sigma_u$ )-strain ( $\epsilon_u$ ) analysis (Fig. 3b). Owing to higher porosity, the PVDF-BP films become less stiff than that of Neat PVDF. As a result, break point of strain was increased from  $\epsilon_u \sim 2.77\%$  from Neat PVDF to  $\epsilon_u \sim 6.93\%$ ,  $9.14\%$ ,  $9.15\%$  for PVDF-BP-0.25, PVDF-BP-0.50 and PVDF-BP-1.0 films respectively. However, the PVDF-BP films possess lower Young's



**Fig. 3.** Structural characterizations. (a) Surface morphology by FE-SEM representing the porous microstructure over the bio-organic films. The inset in (iv) shows the flexibility demonstration of the spongy film. (b) Stress-strain curve and (c) FT-IR spectra of the developed films. (d) Schematic representing the H-bonding interaction between the PVDF chain and resonating structure of peptide bonds followed by self-polarization of bio-organic material. (e) DSC thermograms under heating cycle and (f) cooling cycle.

modulus ( $Y$ ) in comparison to Neat PVDF film. With higher BP content as porosity increases in the PVDF-BP films, numerically  $Y$  decreases such as  $Y \sim 620$  MPa, 543 MPa, 468 MPa for PVDF-BP-0.25, PVDF-BP-0.50 and PVDF-BP-1.0 films respectively which are comparatively lower than that of Neat PVDF ( $Y \sim 832$  MPa).

In order to implement the developed films towards energy harvesting, the prerequisite electroactive phase ( $\beta$ - $\gamma$ -phases) contents were investigated. It has been observed that Neat PVDF film was composed of  $\gamma$ - ( $1234$   $\text{cm}^{-1}$ ) and non-polar  $\alpha$ -phases ( $763$   $\text{cm}^{-1}$ ), while PVDF-BP films were consist of  $\beta$ - ( $1272$   $\text{cm}^{-1}$ ) and  $\gamma$ - phases ( $1234$   $\text{cm}^{-1}$ ) and non-polar  $\alpha$ -phase was completely demolished (Fig. 3c). The relative proportion of electroactive phase content ( $F_{EA}$ ) was quantified using the Beer-Lambert law,

$$F_{EA} = \frac{I_{EA}}{\left(\frac{K_{839}}{K_{763}}\right)I_{763} + I_{EA}} \times 100 \quad (1)$$

where  $I_{EA}$  is the absorbance intensity at  $839.53$   $\text{cm}^{-1}$  and  $I_{763}$  is the absorbance intensity at  $763$   $\text{cm}^{-1}$ ;  $K_{763}$  ( $\sim 6.1 \times 10^4$   $\text{cm}^2 \text{mol}^{-1}$ ) and  $K_{839}$  ( $\sim 7.7 \times 10^4$   $\text{cm}^2 \text{mol}^{-1}$ ) are the absorption coefficients at the respective wave numbers [19]. The calculated results show numerically  $F_{EA} \sim 82\%$ ,  $85\%$  and  $88\%$  for PVDF-BP-0.25, PVDF-BP-0.50 and PVDF-BP-1.0 films respectively. Using the curve deconvolution process [20], the estimated  $\beta$ -phase content were  $52\%$ ,  $58\%$  and  $66\%$  and  $\gamma$ -phase content were  $30\%$ ,  $27\%$  and  $22\%$  respectively for PVDF-BP-0.25, PVDF-BP-0.50 and PVDF-BP-1.0 films respectively (Fig. S3). In addition to the electroactive phases, amide I ( $1661$   $\text{cm}^{-1}$ : resulting from C=O stretching/ hydrogen bonding coupled with COO<sup>-</sup>) and amide II ( $1596$   $\text{cm}^{-1}$ : N-H-bending ( $\delta(\text{N}-\text{H})$ ) coupled with C-N stretching ( $\nu(\text{C}-\text{N})$ ) [21] peaks become prominent within the PVDF-BP

films and peak intensities increased with increased concentration of BP additive into PVDF. It is become evident that bacterial protein played a significant role for the porous microstructure formation (Fig. S2) in the bio-organic PVDF films followed by electroactive  $\beta$ -phase nucleation (Fig. 3c) and subsequent stabilization of self-polarization (Fig. 3d). In our fabrication process, water molecules were removed from the bacterial protein during the freeze-drying (lyophilization process), although the presence of a tiny content of water molecules is unavoidable to the lab based fabrication process where water molecules were interacted on the planner surface of peptide bond of the protein chain through dipole-dipole or ion-dipole interaction due to resonating structure and zwitter ionic behavior (Fig. S4). Thus, the attached water molecules were slowly evaporated during the film crystallization ( $\sim 60$   $^{\circ}\text{C}$ ) which engineered the ununiform porous structure formation through solvent-non-solvent phase separation process. As the BKH2 bacterial strain was thermophilic ( $65$   $^{\circ}\text{C}$ ) in nature, therefore during PVDF crystallization, the delocalization of  $\pi$ -electronic cloud occurred on the planer surface of peptide bond due to the resonating structure of the amino acid residues of protein chain. Eventually, strong C-H $\cdots$  $\pi$  interaction or dipole-dipole interaction occurred between  $-\text{CH}_2$ -dipoles of PVDF and  $\pi$ -electronic cloud of peptide bond (Fig. 3d). As a result of the hydrogen bonding interaction between  $-\text{C}=\text{O}$  moiety of peptide bond and H atoms of  $\text{CH}_2$  dipoles, a broad intensified N-H stretching vibration arising in the frequency range of  $3500$ – $3000$   $\text{cm}^{-1}$  which is predominantly absent in Neat PVDF film (Fig. S5). As a result of, the above mentioned interactions, a clear frequency shifting of the  $\text{CH}_2$  asymmetric ( $\nu_{as}$ ) and symmetric ( $\nu_s$ ) stretching vibration modes in PVDF-BP films have been observed with respect to Neat PVDF film (Fig. S6). This phenomenon leads to the formation of self-poled electroactive  $\beta$ -phase and also has significance for



spontaneous piezoelectricity generation [12,22].

For better understanding of the effect of bacterial protein on the thermal stabilization of the protein incorporated PVDF films, differential scanning calorimetry (DSC) was carried out. It is also evident from DSC curve that in the presence of protein the melting temperature ( $t_m$ ) of the protein doped PVDF film increases, compared to Neat PVDF. The melting temperature of Neat PVDF film points out at 166 °C which increased to 168 °C (for PVDF-BP-0.25), 168.3 °C (for PVDF-BP-0.50) and 167.5 °C (for PVDF-BP-1.0) (Fig. 3e). It is important to note that the melting DSC peaks more broadened with increasing content of BP into PVDF film. Theoretically, an infinitely narrow transition peak should arise for pure crystalline material, while, the peaks will be more broadened when external additives/impurities will be present within the crystalline material [23]. In our case, as the content of external BP additives into pure PVDF increases the melting DSC peaks are more broadened which is also consistent with the previous report [19]. In addition, protein doped PVDF films exhibit higher crystallization temperature ( $t_c$ ) with respect to Neat PVDF film (Fig. 3f). The crystallization temperature of Neat PVDF was at 137.5 °C and increases to 144.5 °C for PVDF-BP-0.25 furthermore, the crystalline temperature also increases for other two concentrations to 144.8 °C for PVDF-BP-0.50 and 143.7 °C for PVDF-BP-1.0 films. The crystallinity ( $\chi_c$ ) was evaluated using the melting enthalpy, as  $\chi_c = \frac{\Delta H_f/\phi}{\Delta H_f^*}$  where,  $\Delta H_f$  was the melting enthalpy,  $\Delta H_f^* = 104.5 \text{ J/g}$  is the melting enthalpy for a 100% crystalline PVDF,  $\phi$  is the used weight fraction of PVDF ( $\sim 0.6$ ) [24]. The evaluated crystallinity was  $\chi_c \sim 45\%$ , 53%, 54% and 56% for Neat PVDF, PVDF-BP-0.25, PVDF-BP-0.50 and PVDF-BP-1.0 respectively.

The electrical properties of the developed films were evaluated by measuring the frequency dependent dielectric constant ( $\epsilon_r$ ) (Fig. 4a) and

loss tangent ( $\tan \delta$ ) (Fig. 4b) in the frequency range of 100 Hz – 1 MHz. Owing to the dipolar nature of PVDF, the  $\epsilon_r$  decreases with increasing frequency [25]. The Neat PVDF film possess  $\epsilon_r \sim 9$  and  $\tan \delta \sim 0.076$  at the frequency of 1 kHz, while the dielectric constants of the PVDF-BP-0.25, PVDF-BP-0.50 and PVDF-BP-1.0 were 5, 7 and 11 as well as  $\tan \delta$  were of 0.217, 0.2 and 0.196 respectively. It is interesting to note that with increasing content of BP, the  $\epsilon_r$  increases systematically while the change of  $\tan \delta$  were not significant. Owing to the porous structure, with lower content of BP (such as, PVDF-BP-0.25, and PVDF-BP-0.50) the  $\epsilon_r$  was numerically lower than that of Neat PVDF, while  $\epsilon_r$  were systematically increased with higher content of BP due to Maxwell-Wagner-Sillars (MWS) interfacial polarization effect. Therefore, there is some competition between MWS effect and the porosity factor to control  $\epsilon_r$  of the PVDF-BP films. After certain concentration of BP (in this case PVDF-BP-1.0 film), MWS effect was the dominating factor over the porosity factor. As a result, the  $\epsilon_r$  of PVDF-BP-1.0 was numerically higher than that of Neat PVDF. In this case, owing to the higher content of protein, MWS effect was more prominent where, the ionic movements and hydrogen bonds bound to the protein structure plays an important role to increase dielectric constant compared to Neat PVDF [25]. As both the porosity and MWS effect arises due to the presence of BP into PVDF, therefore, the  $\epsilon_r$  of the PVDF-BP films were the combined effect of porosity and the MWS effect.

Furthermore, polarization level of the developed films was measured by polarization (P) – electric field (E) hysteresis loop (Fig. 4c). Benefitting from the higher electroactive phase content and higher degree of crystallinity, bacterial protein mixed PVDF films possess higher level of polarization at zero electric field (called remnant polarization,  $P_r$ ) compared to Neat PVDF. For example, PVDF-BP-1.0, PVDF-BP-0.5 and PVDF-BP-0.25 films possess higher  $P_r \sim 2$ , 1.5 and 0.7  $\mu\text{C}/\text{cm}^2$

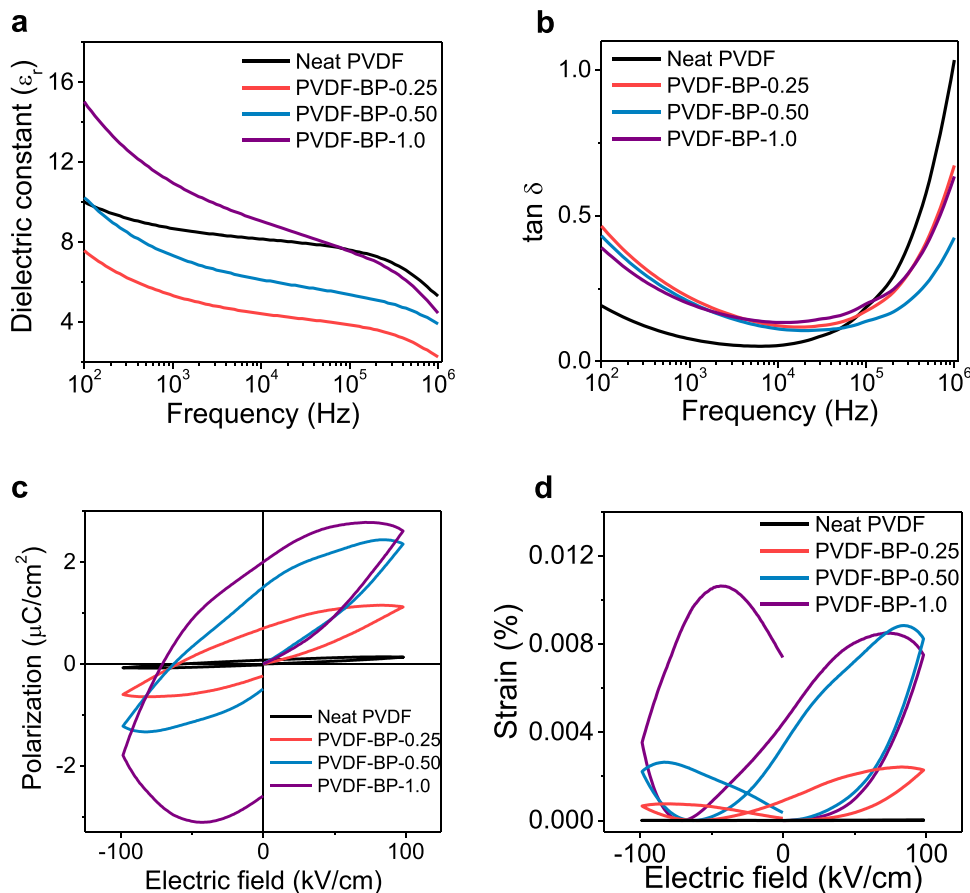


Fig. 4. Electrical properties of the Neat PVDF and the developed bio-organic films (a) Frequency dependent dielectric constant and (b) loss tangent (c) Electric field dependent polarization and (d) butterfly shaped piezoelectric strain hysteresis loops.

respectively compared to Neat PVDF ( $P_r \sim 0.07 \mu\text{C}/\text{cm}^2$ ). According to the macroscopic dimensional effect, the remnant polarization was directly proportional to the longitudinal piezoelectric co-efficient ( $d_{33} = -\frac{P_r}{\epsilon}$ ) which eventually useful for piezoelectric energy harvesting process [2]. As a result, bacterial protein incorporated PVDF film possess higher  $d_{33} \sim -11.3, -27.6$  and  $-42.7 \text{ pC}/\text{N}$  for PVDF-BP-0.25, PVDF-BP-0.5 and PVDF-BP-1.0 respectively compared to Neat PVDF film ( $d_{33} \sim -0.85 \text{ pC}/\text{N}$ ). Furthermore, the butterfly shaped symmetrical strain (S) – electric field (E) hysteresis loop directly reflects the converse piezoelectric effect of developed PVDF films (Fig. 4d). It was evaluated using the well-known electrostrictive relation of  $S=QP^2$ , where, Q denotes the magnitude of longitudinal electrostrictive coefficient which was estimated using the relation of  $d_{33} = 2QE_r\epsilon_0P_r$  [2]. In obvious manner, the electrostrictive coefficients were higher for protein mixed PVDF film in comparison to Neat PVDF film (Fig. S7). Furthermore, bacterial protein mixed PVDF films consist of the higher piezoelectric voltage co-efficients ( $g_{33} = \frac{d_{33}}{\epsilon_r\epsilon_0}$ ) [2] of 0.26, 0.44, 0.44  $\text{VmN}^{-1}$  for PVDF-BP-0.25, PVDF-BP-0.5 and PVDF-BP-1.0 respectively compared to Neat PVDF ( $g_{33} \sim 0.01 \text{ VmN}^{-1}$ ). In overall, the piezoelectric figure-of-merit ( $FoM_p \sim d_{33} \times g_{33}$ ) [2] validates the materials ability to design a piezoelectric energy harvester. The bacterial protein doped PVDF films possess 1000 times higher  $FoM_p$  compared Neat PVDF film. For example, numerically the  $FoM_p$  were of  $2.9 \times 10^{-12}, 12.1 \times 10^{-12}$  and  $18.8 \times 10^{-12} \text{ Pa}^{-1}$  for PVDF-BP-0.25, PVDF-BP-0.5 and PVDF-BP-1.0 which were 1000 times higher than that of Neat PVDF film ( $FoM_p \sim 8.5 \times 10^{-15} \text{ Pa}^{-1}$ ). These results clearly indicated the suitability of the bacterial protein incorporated PVDF films as high performance power generator.

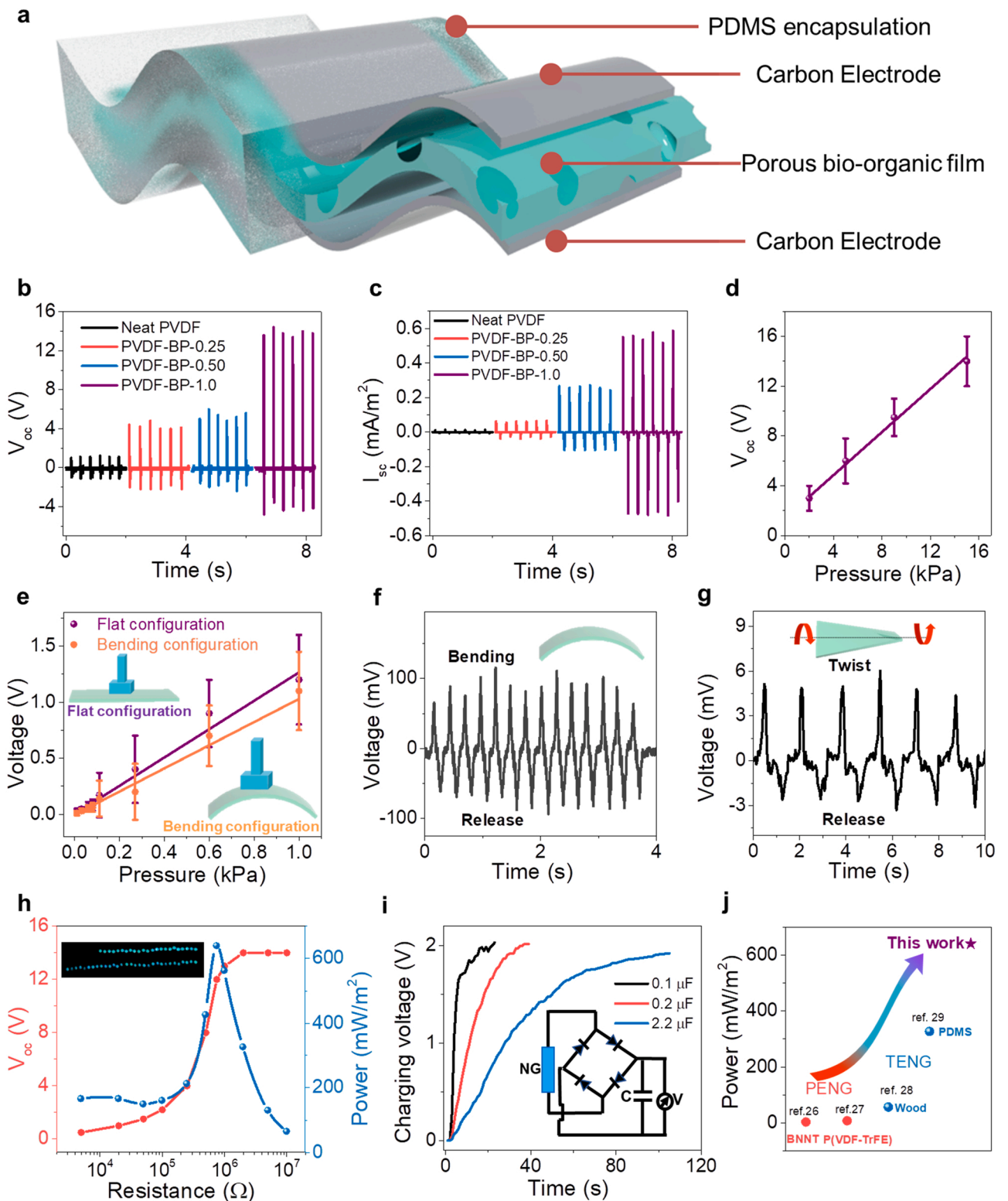
The nanogenerator was prepared using the porous bacterial protein incorporated PVDF and non-porous Neat PVDF films considering the metal-insulator-metal structure followed by PDMS elastomer encapsulation for protection from any mechanical damage as shown schematically in Fig. 5a. Owing to the higher figure-of-merit, the nanogenerator made by bio-organic PVDF-BP-1.0 shown the highest open-circuit output voltage ( $V_{oc}$ ) of 14 V (Fig. 5b) and short-circuit current output ( $I_{sc}$ ) of  $0.56 \text{ mA}/\text{m}^2$  (Fig. 5c) compared to PVDF-BP-0.5 ( $V_{oc} \sim 6 \text{ V}, I_{sc} \sim 0.26 \text{ mA}/\text{m}^2$ ), PVDF-BP-0.25 ( $V_{oc} \sim 4 \text{ V}, I_{sc} \sim 0.06 \text{ mA}/\text{m}^2$ ) and Neat PVDF ( $V_{oc} \sim 1 \text{ V}, I_{sc} \sim 0.01 \text{ mA}/\text{m}^2$ ) under the repetitive finger imparting with compressive stress amplitude ( $\sigma_a$ ) of 15 kPa. As the  $V_{oc}$  and  $I_{sc}$  generated from the PVDF-BP-1.0 based bio-organic nanogenerator (BONG) were highest among the developed bio-organic films, therefore this device was used for further characterization unless otherwise mentioned. It was interesting to note that the  $V_{oc}$  from the PVDF-BP-1.0 increased linearly when the applied pressure to the nanogenerator was increased in the range of  $\sigma_a \sim 2 - 15 \text{ kPa}$  (Fig. 5d). This linear increment evaluated the mechano-sensitivity ( $\sim \frac{V_{oc}}{\sigma_a}$ ) of the device as high as  $0.86 \text{ V}/\text{kPa}^{-1}$  which was superior to the previously developed devices (Table S1). In order to evaluate the sensitivity, the linear fitting was done using the equation,  $y = 0.86x + 1.4$ , where the standard error in slope was 0.038, Pearson correlation coefficient was 0.998 and adjusted R-squared value was 0.994. In order to evaluate the pressure detection limit of the device, the sensitivity was further evaluated under low pressure region ( $<1 \text{ kPa}$ ) (Fig. 5e). The device can detect the pressure as low as 10 Pa which is the detection limit of the device. The device sensitivity ( $\sim 1.26 \text{ V}/\text{kPa}^{-1}$ ) was higher in the low pressure (10 Pa–1 kPa) region compared to high pressure region ( $0.86 \text{ V}/\text{kPa}^{-1}$  in the pressure region of 2–15 kPa). In fact, the pressure sensitivity was not much affected under bending condition (sensitivity  $\sim 1.03 \text{ V}/\text{kPa}^{-1}$  under bending radius,  $r \sim 15 \text{ mm}$ ) indicating the suitability of the device for clinical applications as human body motions contain combined movements such as bending, pressuring, twisting. The superior sensitivity of the device was further demonstrated by repeated bending and releasing motions (Fig. 5f). Under the bending state, the tensile strain developed along the thickness direction of the device was  $\epsilon_y = \frac{\Delta r}{r} = 0.67\%$ , (where,  $L = 200 \mu\text{m}$  was the thickness of the device and  $r = 15 \text{ mm}$  was the

bending radius) and along the length direction of the device was  $\epsilon_x = 0.29\%$  considering the poisson's ratio,  $\nu = \left| \frac{\epsilon_x}{\epsilon_y} \right| = 0.44$  of PVDF [12].

Under repeated bending-releasing motion, the generated voltage output was 100 mV which was higher in comparison to the generated voltage output ( $\sim 5 \text{ mV}$ ) from the device under repeated twisting-releasing motions (Fig. 5g) which is consistent with the previous literature [12]. Furthermore, the several  $V_{oc}$  from the nanogenerator were measured across the load resistance ( $R_L$ ) under the applied pressure,  $\sigma_a \sim 15 \text{ kPa}$  and the instantaneous power output ( $P_L$ ) was evaluated using the formula  $P_L = \frac{1}{A} \frac{V_L^2}{R_L}$ , where A is the electrode area ( $\sim 3 \text{ cm}^2$ ), and  $V_L$  is the voltage drop across the load resistance  $R_L$  ( $\sim 5 \text{ k}\Omega - 10 \text{ M}\Omega$ ). The  $R_L$  dependent variation of the  $V_{oc}$  and  $P_L$  was shown in Fig. 5h. The BONG generated maximum output power as high as  $640 \text{ mW}/\text{m}^2$  across the  $R_L \sim 0.75 \text{ M}\Omega$ . The power output of the BONG is found to be superior to the previously developed several nanogenerators (Table S2). With this higher output power, the nanogenerator was capable to instantly illuminate 54 light emitting diodes (LEDs) (inset of Fig. 5h, Video S1) directly connected to the BONG. Furthermore, the under continuous finger imparting to the nanogenerator, the generated electricity was stored to the commercially available capacitors of several capacitance (0.1, 0.2 and 2.2  $\mu\text{F}$ ) very quickly (less than 2 min) (Fig. 5i). For example, the 0.1  $\mu\text{F}$  capacitor was charged to the saturated voltage ( $V_c \sim 2 \text{ V}$ ) within 23 s and stored the energy was of ( $E = \frac{1}{2} CV_c^2$ ) 0.2  $\mu\text{J}$ . Similarly, the 0.2 and 2.2  $\mu\text{F}$  capacitors were saturated within 39 and 105 s respectively and stored the energy of 0.4 and 3.97  $\mu\text{J}$  respectively. In this case, the bridge rectifier circuit was used as shown schematically in the inset of Fig. 5i. The capacitor charging performance of the BONG is very much superior to that of previously reported several piezoelectric nanogenerators (Table S3). In fact, the high power output of our developed bio-organic nanogenerator outperform to the previously developed high performance inorganic (Boron Nitride Nanotube (BNNT), power output  $\sim 3.59 \text{ mW}/\text{m}^2$ ) [26] and organic (thin film PVDF-TrFE, power output  $\sim 8 \text{ mW}/\text{m}^2$ ) [27] piezoelectric nanogenerators as well as well studied wood (power output  $\sim 57 \text{ mW}/\text{m}^2$ ) [28] and PDMS (power output  $\sim 327 \text{ mW}/\text{m}^2$ ) [29] based triboelectric nanogenerators (TEG) (Fig. 5j) and therefore, can be implemented to the future biomedical electronics. Furthermore, the nanogenerator possesses the energy conversion efficiency ( $\eta_{piezo}$ ) of 62.5%. The energy conversion efficiency was calculated using the equation of  $\eta_{piezo} = \frac{E_{elec}}{W_{mec}} \times 100\%$  where,  $E_{elec} = \int_{t_1}^{t_2} \frac{V(t)^2}{R_L} dt = 18 \text{ nJ}$  was the instantaneous output electrical energy per cycle (Fig. S8) and  $W_{mec} = F \times \epsilon \times L = 28.8 \text{ nJ}$  was the input mechanical energy per cycle [30]. In calculating applied mechanical energy, applied force F was 4.5 N corresponds to  $\sigma_a \sim 15 \text{ kPa}$ , the developed axial strain was  $\epsilon = \frac{\sigma_a}{Y} = 32 \times 10^{-6}$ , where  $Y \sim 468 \text{ MPa}$  of the PVDF-BP-1.0 film, total thickness of device  $L = 200 \mu\text{m}$ . The energy conversion efficiency of the bio-organic nanogenerator is very promising and superior to the previously developed nanogenerators (Table S4).

Supplementary material related to this article can be found online at [doi:10.1016/j.nanoen.2021.106843](https://doi.org/10.1016/j.nanoen.2021.106843).

In order to understand the high power output generation capability of our developed nanogenerator, finite element method (FEM) based theoretical simulations were performed using the COMSOL multiphysics (Note S2). From the theoretical calculation, it was very evident that the geometrical porous microstructure formation played an important role for higher figure-of-merit, sensitivity as well as superior power generation capability. As the porosity was increased from 0–18% with the increased concentration bacterial protein from 0.25 to 1 wt% to the PVDF, the applied stress of 15 kPa was more concentrated/confined to the porous structure which is known as stress-concentration effect (Fig. 6a) [30–32]. As a result of this confinement effect, the stress within the porous structure was enhanced than that of the applied stress amplitude and a stress gradient within the porous structure was formed



**Fig. 5.** The energy harvesting performance of the BONG. (a) Schematic of the designed BONG using the porous bio-organic film. (b) Generated open-circuit output voltage ( $V_{oc}$ ) and (c) short-circuit output current under 15 kPa pressure. (d) Pressure dependent output voltage in the range of 2–15 kPa pressure. (e) Voltage output within the pressure range of 10 Pa–1 kPa pressure range under flat configuration and bending configuration of the device as shown schematically in the inset. (f) The voltage output from the device under repeated bending and releasing motions as schematically shown in the inset. (g) The voltage output from the nanogenerator under repeated twisting and releasing motion as shown schematically in the inset. (h) Output voltage and power variation across a range of load resistance of 5 k $\Omega$ –10 M $\Omega$ . The inset shows operated 54 LEDs directly connected to BONG (Video S1). (i) The charging performance of the commercial capacitors with the schematic of the used circuit in the inset. (j) The output power comparison of the BONG with the previously developed PENG and TENGs.

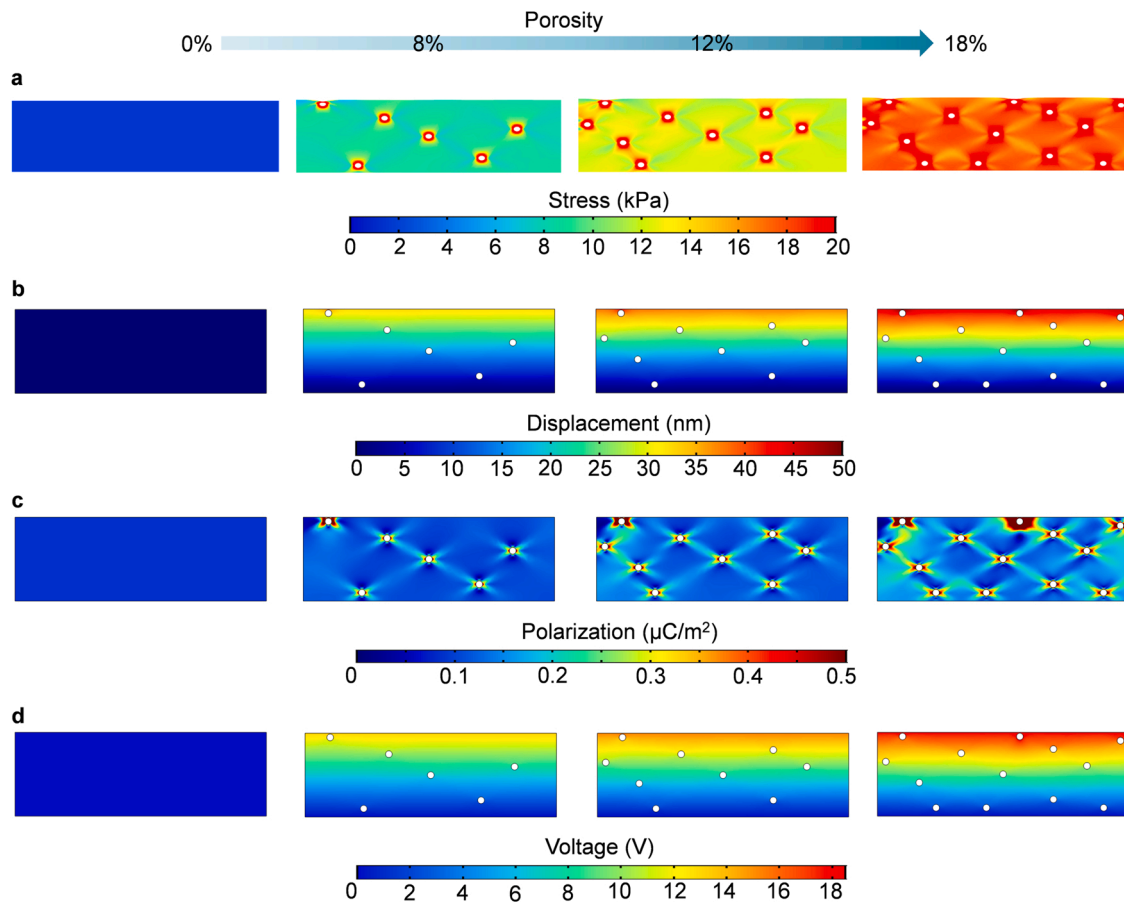
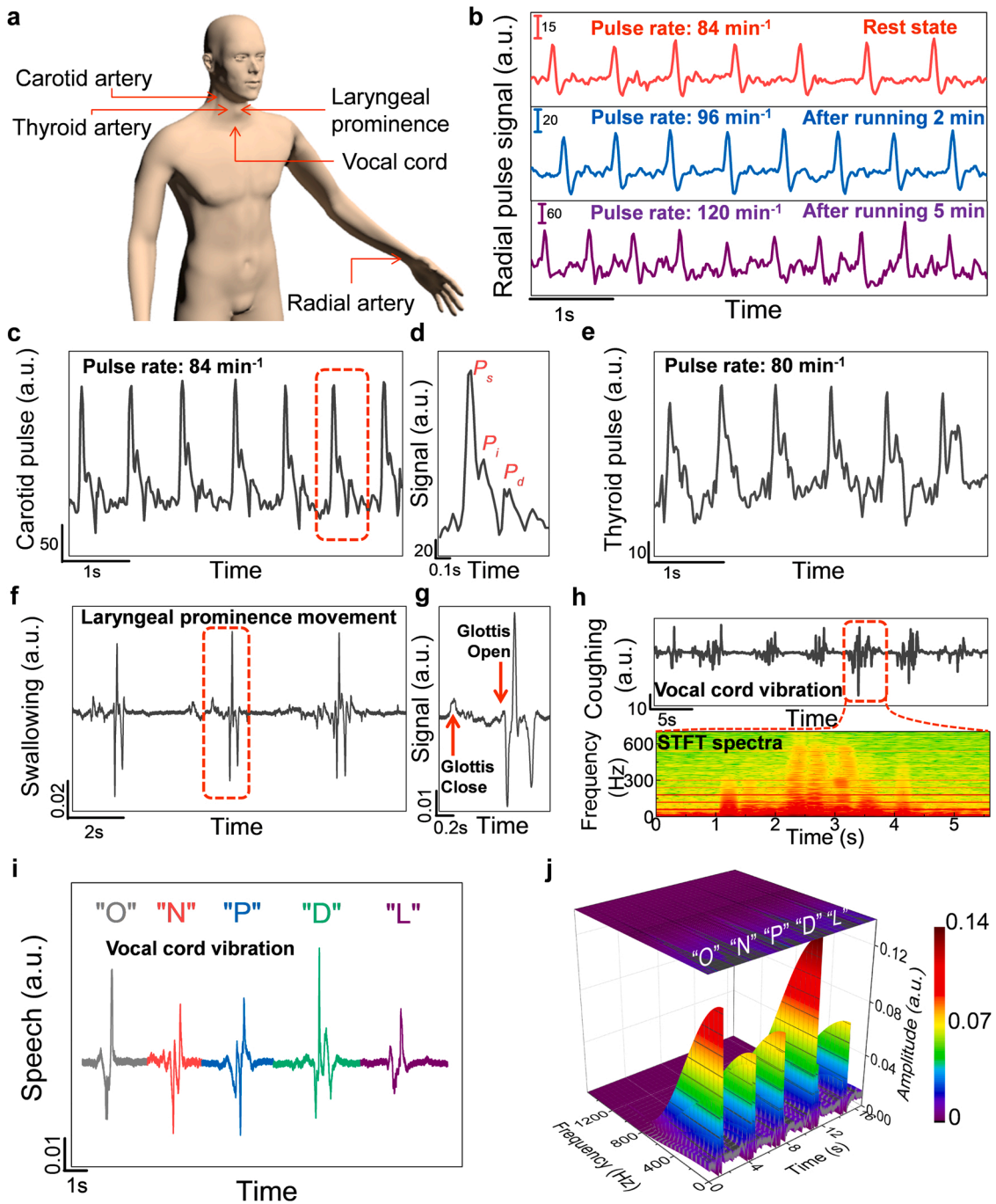


Fig. 6. Finite element based theoretical simulation. (a) The applied stress distribution, (b) the displacement distribution, (c) stress induced polarization distribution and (d) generated voltage distribution within the bio-organic films of different porosity as mentioned in the top portion.

(Fig. 6a). On the other hand, no such effect was observed in the Neat PVDF of 0% porosity. Consequently, the displacement of the porous PVDF films was increased with increasing porosity and of course larger than that Neat PVDF (Fig. 6b). Owing to the higher displacement/compressibility for PVDF-BP-1.0 film, the positive and negative current output (which is proportional to the input strain) for pressing and releasing stress respectively were similar (Fig. 5c) which was not the case for other PVDF-BP films. This higher displacement functionality with stress-concentration effect synergistically enhanced the stress induced polarization which was also found to be confined to the porous microstructures (Fig. 6c). Thus, the polarization was higher for PVDF of higher porosity. With this enhanced polarization, the PVDF with 18% porosity (experimentally, PVDF-BP-1.0) generated highest output voltage of 18 V under 15 kPa of pressure which was consistent with our experimental results ( $V_{oc} \sim 14$  V) (Fig. 6d). In obvious manner, the environmental bacteria engineered porous structure PVDF generated higher output voltage than that of non-porous Neat PVDF film.

With the superior sensitivity of the PVDF-BP-1.0 film based BONG, the device was implemented towards real-time healthcare monitoring sensor by attaching to the several body-parts of human body as shown in Fig. 7a. For example, upon attaching to the human wrist, the device can sense the radial artery pulse wave under different physical conditions. The device can detect the heart beat pulse rate of  $84 \text{ min}^{-1}$  which was increased to  $96 \text{ min}^{-1}$  and  $120 \text{ min}^{-1}$  when the device was attached to the wrist after exercising (running) for 2 and 5 min respectively (Fig. 7b). The radial artery pulse wave characteristic was composed of four systolic waves, such as, A-wave (initially positive), B-wave (early negative), C-wave (re-increasing), D-wave (late re-decreasing), and one diastolic wave, which was E-wave (positive) [33]. The important parameters to indicate the cardiovascular dysfunction are represented by

the ratio of peak heights such as E- and D- waves to A- wave (i.e.,  $P_{A/E}$ , and  $D/A$ , respectively) and the time delay ( $\tau_{EA}$ ) between the A- and E-wave. In this case, the parameters are continuously decreasing with increasing heart rate (i.e. from calm state to exercise conditions), such as at calm state  $P_{A/E} \sim 16$ ;  $D/A \sim -0.1$ ;  $\tau_{EA} \sim 0.58$ , after 2 min exercise  $P_{A/E} \sim 7.8$ ;  $D/A \sim -0.03$ ;  $\tau_{EA} \sim 0.54$  and after 5 min exercise  $P_{A/E} \sim 3.9$ ;  $D/A \sim -0.02$ ;  $\tau_{EA} \sim 0.33$ , which represented the diastolic dysfunction with increasing exercise, leading to the symptoms of heart failure. Therefore, our device can successfully discriminate the different physical activities. In addition, our developed BONG based sensor was capable to detect the carotid artery pulse wave when mounted to the neck of the volunteer (Fig. 7c). In this case, the device shows the same pulse rate ( $84 \text{ min}^{-1}$ ) as measured by radial artery pulse wave, thus representing high fidelity towards healthcare monitoring. A single pulse in Fig. 7d shows the main characteristic feature of pulse pressure wave consisting of main wave ( $P_s$ ) followed by predicrotic wave ( $P_i$ ) in systolic phase and the dicrotic wave ( $P_d$ ) in diastolic phase [33]. An artery augmentation index (AI) of 44% was extracted from the measured carotid pulse wave. The AI is an important cardiologic parameter generally used in clinical treatments which represents the elasticity of the human blood vessels and calculated as,  $AI = \frac{P_i}{P_s} \times 100\%$  [27]. The extracted AI value indicated a healthy young man and consistent with previously measured data [34]. Furthermore, upon mounting to the skin beneath the collarbone, the sensor can precisely detect the thyroid artery pulse wave (Fig. 7e). The characteristic waves of pulse pressure shape was similar to the carotid artery pulse wave and detected the pulse rate ( $\sim 80 \text{ min}^{-1}$ ) and AI value ( $\sim 49\%$ ) were almost consistent with the measured values from carotid pulse wave. Furthermore, by fastening the device to the throat, the motion of the laryngeal prominence (the



**Fig. 7.** Clinical applications of the BONG. (a) Schematic representing the healthcare monitoring positions of a human body used in our study. (b) Radial artery pulse measurement under rest and running physical activities. (c) Carotid artery pulse measurement with (d) an enlarge signal of one cycle. (e) Thyroid artery pulse signal measurement. (f) Laryngeal prominence movement signals with (g) one cycle signal showing glottis open and closing response. (h) Repeated coughing action signals (upper panel) with STFT of one signal (lower panel). (i) Vocal cord vibration signal during speaking different words of 'O', 'N', 'P', 'D', 'L' and (j) their 3-D STFT spectrogram.

Adam's apple) of a healthy young man was observed during the swallowing of saliva action repeatedly (Fig. 7f) via identifying the glottis opening and closing processes (Fig. 7g). Therefore, the device might be useful in a breathing monitor for the early detection of sudden infant death syndrome (SIDS) in sleeping infants, alerting parents to any potential problems [35]. Furthermore, the device has shown high fidelity in sensing the vocal cord vibration during repeated coughing actions (upper panel of Fig. 7h). The processed data by short-time Fourier transform (STFT) spectrogram (lower panel of Fig. 7h) evidenced that the frequency band spectrum of coughing sound covers the frequency

range up to 700 Hz which is in the same frequency characteristics of healthy young people coughing sound [36]. Therefore, the sensor could be used in diagnosis patient's damaged vocal cords, chronic obstructive pulmonary disease (COPD) such as, asthma, chronic bronchitis etc. by assessing frequency band of coughing action and even for early intervention of COVID-19 [2,37]. In order to analyze the damaged vocal cords, another potential method is to noninvasively monitor the epidermis as well as muscle movement deformation around the throat during phonation. We attached the sensor as a speech pattern recognition system, firmly to the human speaker's neck. Interestingly, when

different words (such as 'O', 'N', 'P', 'D', 'L') were spoken by the volunteer, the device was also capable to detect the vocal cord vibration synchronous to the speaking words and generated the electrical signal (Fig. 7i). In this case, the sensor mimics the vocal cord deformation in order to generate vibrotactile output signal waveform. The time-dependent position and amplitude of signal waveforms and corresponding STFT processed 3D-spectrograms agree with acoustic profile of each alphabet (Fig. 7j). It is evident that the maximum amplitude of all words is almost within the frequency range of 0–800 Hz (i.e., within the limit of vocal cord vibration frequency) [2]. Therefore, the developed sensor has the potential to develop vibrotactile hearing aids, aiding in speech rehabilitation training.

### 3. Conclusion

In summary, we have demonstrated the concept and a set of design rules to establish a bio-piezoelectric platform having good biocompatibility and piezoelectricity via integrating the biologically active bacteria and organic PVDF polymer. The bacterial protein engineered the microstructure of PVDF to develop porous bio-organic film and also interacted with the polymer chain to enhance the electroactive phase content and crystallinity. With appropriate content of bacterial protein, much improved piezoelectric co-efficient ( $d_{33} \sim -42.7$  pC/N) and figure of merit ( $FoM_p \sim 18.8 \times 10^{-12}$  Pa<sup>-1</sup>) were achieved in the bio-organic film which eventually benefited towards power generation ( $\sim 640$  mW/m<sup>2</sup>) that outperformed the previously developed piezoelectric and even triboelectric nanogenerators. This impressive bio-organic film based nanogenerator was not only demonstrated to be useful in powering consumer electronics but also implemented in the direction of real-time physiological signal detection based clinical applications. Deployed as piezoelectric energy harvester, our rationally designed bacterial protein engineered bio-organic film open a new avenue for next generation sustainable and autonomous biomedical systems with minimal invasiveness.

## 4. Experimental section

### 4.1. Isolation and purification of BKH2 bacterial protein (BP)

A noble thermophilic and anaerobic bacterial strain BKH2 (GenBank accession no.: KP231522) was used from our laboratory stock, collected from the soil of the hot spring of temperature 65 °C at Bakreshwar, West Bengal, India [16]. This bacterium secretes some extra cellular proteins in its growth medium which was isolated from cultured medium (6–7 days old), concentrated through lyophilization and purified through double-step purification by Sephadex G-100 column chromatographic technique [38]. Using this technique, some fractions (1 ml each) were collected and the protein content in the fraction was observed by measuring the optical densities at 280 nm on UV-Visible spectrophotometer. Therefore, in protein purification curve, a single major peak was noted while plotting the optical density value of protein content fractions with fraction numbers which confirm the presence of protein in the collected fractions (Fig. S9).

### 4.2. Materials and film preparation

The purified bioremediase-like protein [16] used in this experiment where 6 wt% (w/v) PVDF-DMF solution were prepared by dissolving PVDF (Sigma-Aldrich, USA,  $M_w = 275,000$ ) in N, N-dimethyl formamide (DMF, Merck, India). Three different concentrations of bacterial protein (BP) (such as 0.25, 0.5 and 1 wt%) were added with 10 ml of PVDF-DMF solutions. Using solution casting procedure, the films were deposited on clean glass substrates and subsequently dried at 60 °C for 6 h. Free-standing flexible films were prepared with labeling of "Neat PVDF" (where BP was not present) and PVDF-BP-0.25, PVDF-BP-0.50 and PVDF-BP-1.0 where 0.25 wt%, 0.50 wt% and 1.0 wt% of BP were added

into PVDF-DMF solutions respectively.

### 4.3. In-vitro biocompatibility study

In order to study the biocompatible nature of the bacterial protein mixed PVDF films, a green method was intended such as growth of *Escherichia coli* (*E. coli*) bacterium in the presence of the films. *E. coli* is the mostly common nonpathogenic bacterium. It can be cultured easily with short duration at ambient temperature and in a cost-effective manner. Luria Broth (LB) is the most commonly used growth medium for *E. coli* as it promotes fast growth [39]. Within the prepared LB liquid media (25 ml using standard method) ca. 10 µl of pre overnight *E. coli* culture was transferred. Then, Neat PVDF and PVDF-BP films were placed into the media and incubate overnight at 37 °C under continuous shaking. After 24 h, the optical density of the *E. coli* bacterium was measured using UV-Vis spectrophotometer that confirms the biocompatibility feature of BP mixed PVDF films and the bio-organic nanogenerator.

In order to conduct bio-compatibility test in solid media, LB agar solid media was also prepared using standard method [38]. In this method the LB media containing agar (1.5%) was poured into two petri dishes and allowed to get solidified. Then the Neat PVDF, PVDF-BP films and bio-organic nanogenerator were attached on the two different agar media plates and 100 µl ( $10^6$  bacterial cell/ml) of pre-grown *E. coli* culture was spread on both the agar plates containing the films and left at room temperature for 15 min. The petri agar plates were kept for incubation at 37 °C for 24 h. After the stipulated time period, the culture plates were collected for further characterizations. The films were separated very slowly from the culture media and prepared for FESEM and immunofluorescence microscopy images.

### 4.4. Sample preparation for FESEM and immunofluorescence microscopy measurement

After separation of Neat PVDF and PVDF-BP films from liquid LB medium and solid LB agar plates, they were placed on glass slide for air drying. Then, the dried films were employed for FESEM measurement. The immunofluorescence microscopy images of the films were captured after stained by Ethidium Bromide (EtBr) (red color) as a result, *E. coli* bacteria were observed as red color object under microscope.

### 4.5. Nanogenerator fabrication

In order to fabricate the bio-organic piezoelectric nanogenerator, metal-insulator-metal (MIM) structure was used where, conducting carbon films as top and bottom electrodes (of size: 20 × 15 mm) were attached on both sides of the dielectric bio-organic PVDF films. The electrical output leads were joined to each of the carbon electrodes. Finally, the electrode-PVDF electrode stack was encapsulated within Polydimethylsiloxane (PDMS) (Sylgard 184, Dow Corning Corp., USA) based elastomer for enhancing the robustness and to contribute compact structure to the fabricated device. The PDMS was prepared by mixing base and curing agents in the ratio of 10:1 and placing the resulting material in vacuum desiccators to eliminate air bubbles followed by heating at 60 °C for 3 h. The total thickness of the nanogenerator was 200 µm.

### 4.6. Nanogenerator performance characterization

To study the output performance of nanogenerator, human finger was imparted vertically. The vertically applied pressure was calculated according to previous literature [12–14, 21, 30, 31]. A digital storage oscilloscope (Agilent DSO3102A) and pico-ammeter (Keithley 6485) was used to measure the output voltage and current respectively.

#### 4.7. Material characterization

The detail surface morphological studies of films were performed by Field Emission Scanning Electron Microscopy (FESEM, FEI, INSPECT F50) and under the acceleration voltage of 10 kV. The structural compositions of bacterial protein doped PVDF films were extensively investigated using Fourier transform infrared spectroscopy in Attenuated Total Reflection (A529-P/QMIRacle-ATR-unit (Pike), TENSOR II, Bruker) mode. Additionally, to study the thermal properties of the bio-organic films, Differential Scanning Calorimeter (DSC) was carried out on a Perkin Elmer, STA-8000 instrument in liquid N<sub>2</sub> environment. Additionally, tensile strength of the films was also measured by a universal testing machine (Tinius Olsen H50KS) at a strain rate of 1 mm/min. The polarization (P) versus electric field (E) hysteresis loops were obtained from the ferroelectric testing system (P-E, PLC100V, Radiant Technology Precision) connected to a high voltage interface, employing bipolar triangular electric field (E) along the thickness direction at room temperature. The dielectric properties were measured using precision impedance analyzer (Wayne Kerr, 6500B). Finite element method based theoretical simulation was performed using COMSOL multiphysics software (version 5.5).

#### Associated Content

##### Supporting Information

The [supporting information](#) file consists of porosity calculation method (Note S1), finite element based calculation method (Note S2), the in-vitro biocompatibility test of PVDF-BP-1.0 film, cross-sectional FE-SEM of Neat PVDF and PVDF-BP films, the FT-IR spectra in the frequency region of 930 – 780 cm<sup>-1</sup> (Fig. S3), 3500–3000 cm<sup>-1</sup> (Fig. S5), 3075–2925 cm<sup>-1</sup> (Fig. S6), resonating structure of amino acid (Fig. S4), magnitude of electrostrictive coefficients (Fig. S7), output electrical energy per cycle from the BONG (Fig. S8), protein purification curve (Fig. S9), mechano-sensitivity comparison list (Table S1), output voltage, current, power output comparison list (Table S2), capacitor charging performances comparison list (Table S3), energy conversion efficiency comparison list (Table S4) of the BONG with the reported literature. Video S1 shows direct demonstration of powering 54 LEDs by direct connection to the developed BONG.

#### CRedit authorship contribution statement

**SKG, CG and DM** planned the entire work. **SKG and CG** prepared the composite samples and fabricated the device. **SKG, CG and KR** tested the device performances. **KR** assisted the sample preparation and critical analysis of the spectroscopic data. **SKG** analyzed the device performance related data. The biocompatibility and bacteria related work is supervised by **BDC** and the work is performed by **CG**. The NG related major part of article is written by **SKG**. Finally the entire manuscript is checked by all authors and approved for submissions.

#### Declaration of Competing Interest

The authors declare the following financial interests/personal relationships which may be considered as potential competing interests: Dipankar Mandal reports financial support was provided by Institute of Nano Science and Technology. Dipankar Mandal reports a relationship with Institute of Nano Science and Technology that includes: employment. Dipankar Mandal has patent pending to Assignee.

#### Acknowledgements

This work was financially supported by a grant from the Science and Engineering Research Board (EEQ/2018/001130), Government of India. C.G. acknowledges grant from DST Women Scientist Scheme A

(SR/WOS-A/PM-43/2018), Government of India. The Biophysics Laboratory of Department of Physics, Jadavpur University, India are gratefully acknowledged. Authors acknowledge DST, Govt. of India (FIST-II programme). K.R. is grateful to DST-INSPIRE fellowship (IF160559), India for financial support.

#### Appendix A. Supporting information

Supplementary data associated with this article can be found in the online version at [doi:10.1016/j.nanoen.2021.106843](https://doi.org/10.1016/j.nanoen.2021.106843).

#### References

- [1] A. Midilli, I. Dincer, M. Ay, Green energy strategies for sustainable development, *Energy Policy* 34 (2006) 3623–3633.
- [2] S.K. Ghosh, D. Mandal, Envisioned strategy for an early intervention in virus-suspected patients through non-invasive piezo- and pyro-electric-based wearable sensors, *J. Mater. Chem. A* 9 (2021) 1887–1909.
- [3] S.K. Ghosh, T.K. Sinha, M. Xie, C.R. Bowen, S. Garain, B. Mahanty, K. Roy, K. Henkel, D. Schmeißer, J.K. Kim, D. Mandal, Temperature-pressure hybrid sensing all-organic stretchable energy harvester, *ACS Appl. Electron. Mater.* 3 (2021) 248–259.
- [4] S.K. Ghosh, D. Mandal, Sustainable energy generation from piezoelectric biomaterial for noninvasive physiological signal monitoring, *ACS Sustain. Chem. Eng.* 5 (2017) 8836–8843.
- [5] S. Azimi, A. Golabchi, A. Nekookar, S. Rabbani, M.H. Amiri, K. Asadi, M. M. Abolhasani, Self-powered cardiac pacemaker by piezoelectric polymer nanogenerator implant, *Nano Energy* 83 (2021), 105781.
- [6] M. Pruvost, W.J. Smit, C. Monteux, P. Poulin, A. Colin, *npj Flex. Electron.* 3 (2019) 7.
- [7] P. Martins, A.C. Lopes, S. Lanceros-Mendez, Electroactive phases of poly(vinylidene fluoride): determination, processing and applications, *Prog. Polym. Sci.* 39 (2014) 683–706.
- [8] D. Mandal, K.J. Kim, J.S. Lee, Simple synthesis of palladium nanoparticles,  $\beta$ -phase formation, and the control of chain and dipole orientations in palladium-doped poly(vinylidene fluoride) thin films, *Langmuir* 28 (2012) 10310–10317.
- [9] V. Gupta, A. Babu, S.K. Ghosh, Z. Mallick, H.K. Mishra, D. Saini, Dipankar Mandal, *Appl. Phys. Lett.* 119 (2021) 000000, <https://doi.org/10.1063/5.0071625>.
- [10] N. Soin, D. Boyer, K. Prashanthi, S. Sharma, A.A. Narasimulu, J. Luo, T.H. Shah, E. Siores, T. Thundat, Exclusive self-aligned  $\beta$ -phase PVDF films with abnormal piezoelectric coefficient prepared via phase inversion, *Chem. Commun.* 51 (2015) 8257–8260.
- [11] S. Maji, P.K. Sarkar, L. Aggarwal, S.K. Ghosh, D. Mandal, G. Sheet, S. Acharya, Self-oriented  $\beta$ -crystalline phase in the polyvinylidene fluoride ferroelectric and piezo-sensitive ultrathin Langmuir-Schaefer film, *Phys. Chem. Chem. Phys.* 17 (2015) 8159–8165.
- [12] S.K. Ghosh, A. Biswas, S. Sen, C. Das, K. Henkel, D. Schmeißer, D. Mandal, Yb<sup>3+</sup>-assisted self-polarized PVDF based ferroelectric nanogenerator: a facile strategy of highly efficient mechanical energy harvester fabrication, *Nano Energy* 30 (2016) 621–629.
- [13] S.K. Ghosh, T.K. Sinha, B. Mahanty, S. Jana, D. Mandal, Porous polymer composite membrane based nanogenerator: a realization of self-powered wireless green energy source for smart electronics applications, *J. Appl. Phys.* 120 (2016), 174501.
- [14] S.K. Ghosh, T.K. Sinha, B. Mahanty, D. Mandal, Self-poled efficient flexible “ferroelectric” nanogenerator: a new class of piezoelectric energy harvester, *Energy Technol.* 3 (2015) 1190–1197.
- [15] J.J. Hug, D. Krug, R. Müller, Bacteria as genetically programmable producers of bioactive natural products, *Nat. Rev. Chem.* 4 (2020) 172–193.
- [16] M. Sarkar, N. Alam, B. Chaudhuri, B. Chattopadhyay, S. Mandal, Development of an improved E. coli bacterial strain for green and sustainable concrete technology, *RSC Adv.* 5 (2015) 32175–32182.
- [17] J. Black, *Biological Performance of Materials: Fundamentals of Biocompatibility*, CRC Press, 2005.
- [18] B.J. Lawrence, S.V. Madhally, Cell colonization in degradable 3D porous matrices, *Cell Adhes. Migr.* 2 (2008) 9–16.
- [19] S.K. Ghosh, D. Mandal, Synergistically enhanced piezoelectric output in highly aligned 1D polymer nanofibers integrated all-fiber nanogenerator for wearable nano-tactile sensor, *Nano Energy* 53 (2018) 245–257.
- [20] S.K. Ghosh, M.M. Alam, D. Mandal, The in situ formation of platinum nanoparticles and their catalytic role in electroactive phase formation in poly(vinylidene fluoride): a simple preparation of multifunctional poly(vinylidene fluoride) films doped with platinum nanoparticles, *RSC Adv.* 4 (2014) 41886–41894.
- [21] S.K. Ghosh, D. Mandal, Efficient natural piezoelectric nanogenerator: Electricity generation from fish swim bladder, *Nano Energy* 28 (2016) 356–365.
- [22] A. Tamang, S.K. Ghosh, S. Garain, M.M. Alam, Jr Haeberle, K. Henkel, D. Schmeißer, D. Mandal, DNA-assisted  $\beta$ -phase nucleation and alignment of molecular dipoles in PVDF film: a realization of self-poled bioinspired flexible polymer nanogenerator for portable electronic devices, *ACS Appl. Mater. Interfaces* 7 (2015) 16143–16147.

- [23] M.H. Chiu, E.J. Prenner, Differential scanning calorimetry: an invaluable tool for a detailed thermodynamic characterization of macromolecules and their interactions, *J. Pharm. Bioallied Sci.* 3 (2011) 39–59.
- [24] M. Gu, J. Zhang, X. Wang, W. Ma, Crystallization behavior of PVDF in PVDF-DMP system via thermally induced phase separation, *J. Appl. Polym. Sci.* 102 (2006) 3714–3719.
- [25] L. Zhu, Exploring strategies for high dielectric constant and low loss polymer dielectrics, *J. Phys. Chem. Lett.* 5 (2014) 3677–3687.
- [26] I. Kim, H. Roh, J. Yu, N. Jayababu, D. Kim, Boron nitride nanotube-based contact electrification-assisted piezoelectric nanogenerator as a kinematic sensor for detecting the flexion–extension motion of a robot finger, *ACS Energy Lett.* 5 (2020) 1577–1585.
- [27] A. Petritz, E. Karner-Petritz, T. Uemura, P. Schäffner, T. Araki, B. Stadlober, T. Sekitani, Imperceptible energy harvesting device and biomedical sensor based on ultraflexible ferroelectric transducers and organic diodes, *Nat. Commun.* 12 (2021) 2399.
- [28] J. Luo, Z. Wang, L. Xu, A.C. Wang, K. Han, T. Jiang, Q. Lai, Y. Bai, W. Tang, F. R. Fan, Z.L. Wang, Flexible and durable wood-based triboelectric nanogenerators for self-powered sensing in athletic big data analytics, *Nat. Commun.* 10 (2019) 5147.
- [29] J. Sun, X. Pu, M. Liu, A. Yu, C. Du, J. Zhai, W. Hu, Z.L. Wang, Self-healable, stretchable, transparent triboelectric nanogenerators as soft power sources, *ACS Nano* 12 (2018) 6147–6155.
- [30] B. Mahanty, S.K. Ghosh, S. Jana, Z. Mallick, S. Sarkar, D. Mandal, ZnO nanoparticle confined stress amplified all-fiber piezoelectric nanogenerator for self-powered healthcare monitoring, *Sustain. Energy Fuels* 5 (2021) 4389–4400, <https://doi.org/10.1039/D1SE00444A>.
- [31] K. Roy, S. Jana, S.K. Ghosh, B. Mahanty, Z. Mallick, S. Sarkar, C. Sinha, D. Mandal, Three-dimensional MOF-assisted self-polarized ferroelectret: an effective autoperpowered remote healthcare monitoring approach, *Langmuir* 36 (2020) 11477–11489.
- [32] Y. Park, Y.-E. Shin, J. Park, Y. Lee, M.P. Kim, Y.-R. Kim, S. Na, S.K. Ghosh, H. Ko, Ferroelectric multilayer nanocomposites with polarization and stress concentration structures for enhanced triboelectric performances, *ACS Nano* 14 (2020) 7101–7110.
- [33] S.K. Ghosh, J. Park, S. Na, M.P. Kim, H. Ko, A fully biodegradable ferroelectric skin sensor from edible porcine skin gelatine, *Adv. Sci.* 8 (2021), 2005010.
- [34] S. Munir, B. Jiang, A. Guilcher, S. Brett, S. Redwood, M. Marber, P. Chowienzyk, Exercise reduces arterial pressure augmentation through vasodilation of muscular arteries in humans, *Am. J. Physiol. Heart Circ. Physiol.* 294 (2008) H1645–H1650.
- [35] P.J. Fleming, R. Gilbert, Y. Azaz, P.J. Berry, P.T. Rudd, A. Stewart, E. Hall, Interaction between bedding and sleeping position in the sudden infant death syndrome: a population based case-control study, *Br. Med. J.* 301 (1990) 85–89.
- [36] S.K. Ghosh, P. Adhikary, S. Jana, A. Biswas, V. Sencadas, S.D. Gupta, B. Tudu, D. Mandal, Electrospun gelatin nanofiber based self-powered bio-e-skin for health care monitoring, *Nano Energy* 36 (2017) 166–175.
- [37] A.H. Morice, *Eur. Respir. J.* 24 (2004) 481–492.
- [38] M. Biswas, S. Majumdar, T. Chowdhury, B. Chattopadhyay, S. Mandal, U. Halder, S. Yamasaki, Bioremediase a unique protein from a novel bacterium BKH1, ushering a new hope in concrete technology, *Enzyme Microb. Technol.* 46 (2010) 581–587.
- [39] J.M. Willey, L. Sherwood, C.J. Woolverton, *Prescott's Microbiology*, McGraw-Hill, New York, 2011.



**Miss Chetana Ghosal** is pursuing Ph.D. from Department of Physics, Jadavpur University, India. She received her B.Sc. and M.Sc. degree in Physics from Vidyasagar University. She conducted her Ph.D. under Women Scientists Scheme-A (SR/WOSA/PM-43/2018), DST, Government of India. Her research interest includes bio-organic energy harvester and eco-friendly Piezoelectric Nanogenerator. She also worked on hot spring Bacteria and Nanoparticles based heavy metal removal procedure with polymer based bio-filter fabrication and waste water treatment.



**Dr. Sujoy Kumar Ghosh** is Marie Skłodowska-Curie Individual Fellow and currently working at Laboratorio NEST, Istituto Nanoscienze-CNR, Pisa, Italy. He was former Post-Doctoral Research Associate in UNIST, South Korea. He has completed his Ph.D. from Department of Physics, Jadavpur University, India. His research direction focused on experimental and simulation based materials physics. Specifically, piezo-, pyro-, ferro-, magento- and tribo-electric energy harvesting device design and their applications towards implantable medical devices are the *leitmotifs* of his research.



**Kritish Roy** is a DST-INSPIRE fellow, currently working for Ph.D. degree in Jadavpur University, Kolkata, India. His profound background is Chemistry. He has completed B.Sc. and M. Sc. from Jadavpur University in the year of 2013 and 2015 respectively. He is currently working on materials development and device fabrication for wearable sensors, actuators and energy harvesters.



**Prof. Brajadulal Chattopadhyay** was born in 13th January 1962 and he is currently working as a professor in the Department of Physics, Jadavpur University, India. Prof. Chattopadhyay received his Master (1987) and Ph.D. (1994) degrees from the University of Calcutta, India and worked at Bose Institute, India and Technical University of Delft, Netherlands. His scientific field lies mainly in the field of Bio-concrete development by using hot spring anaerobic bacteria to enhance the strength and durability of concrete structures. He is engaged in this area since 2001 and published numerous articles. He is also working in the field of Diabetes, Nicotine toxicity and Nano-biotechnology. He has already supervised several Ph.D. students and hold National and International patents.



**Dr. Dipankar Mandal** received his Ph.D. in 2008 from BTU Cottbus (currently known as BTU Cottbus-Senftenburg), Germany. Prior to that, he obtained his M.Tech. in Materials Science and Eng. (2004) and M.Sc. in Physics (2002) from IIT Kharagpur, India and Jadavpur University, Kolkata, India, respectively. He is currently working as a Scientist in the Institute of Nanoscience and Technology (INST), Mohali, India. He was an Assistant Professor in the Department of Physics, Jadavpur University, Kolkata, India from 2008 to 2017. His research interests include the synthesis of advanced multifunctional materials, flexible electronics, piezo-, tribo-, pyro-, ferro- and flexo-electric materials, organic photovoltaics, and electro-spinning systems for the development of new-generation nanofiber fabrication, 3D printing, smart textiles, and non-invasive bio-sensors for healthcare monitoring, and designing mechanical and thermal energy harvesters for self-powered devices and IoTs.



# Protein Promoted $\beta$ -phase Nucleation in Poly (vinylidene fluoride) for Energy Harvesting Applications

Chetana Ghosal<sup>1,a)</sup>, Sujoy Kumar Ghosh<sup>2,b)</sup>, Dipankar Mandal<sup>3,c)</sup>,  
Brajadulal Chattopadhyay<sup>1,d)</sup>

<sup>1</sup>Department of Physics, Jadavpur University, Kolkata 700032, India

<sup>2</sup>Organic Nano-Piezoelectric Device Laboratory (ONPDL), Department of Physics, Jadavpur University, Kolkata 700032, India

<sup>3</sup>Institute of Nano Science and Technology, Phase-10, Sector-64, Mohali, 160062, India.

Corresponding author: <sup>a)</sup>chetanaphys18@gmail.com, <sup>b)</sup>skghosh@research.jdvu.ac.in, <sup>c)</sup>dmandal@inst.ac.in, <sup>d)</sup>dbc\_physics@yahoo.co.in

**Abstract:** In this work, poly (vinylidene fluoride)/protein composite films are prepared which is free standing and flexible. Nucleation of electroactive  $\beta$ -phase in poly (vinylidene fluoride) (PVDF) and consecutive surface morphological changes with different weight percentage of protein is systematically investigated. Finally, the PVDF/protein composite film is used to make a mechanical energy harvesting device. The flexible device produces 2.5 V open-circuit voltage under repeated hand punching. Thus, the device can be used for self-powered consumer electronics in near future.

## INTRODUCTION

PVDF,  $(\text{CH}_2\text{-CF}_2)_n$  and its copolymers are classified as good dielectric materials and exhibits electroactive response, including piezo-, pyro- and ferro-electric effects<sup>1-4</sup>. Due to electroactive properties, PVDF promises wide range of applications such as in biomedicine, energy generation, storage, sensors and actuators, separator in power cell, proton exchange membranes, smart scaffolds, and many others<sup>3,4</sup>. Most of these applications are based on the electroactive phases in PVDF. It is a semi crystalline polymer consisting of at least four different crystalline polymorphs ( $\alpha$ ,  $\beta$ ,  $\gamma$ , and  $\delta$  phases)<sup>3-6</sup>. The most common polymorph designated as an electrically inactive non-polar phase, whereas others are electrically active polar phases. The  $\delta$  phase is transformed from the  $\alpha$ -phase by employing a high electrical field. However, of all polymorphs, the all-trans (TTTT) pseudohexagonal  $\beta$  phase exhibits the largest spontaneous polarization<sup>3-6</sup>. The presence of the  $\beta$  phase in PVDF shows superior ferro-, piezo-, and pyro-electricity in comparison to those of  $\gamma$  and  $\delta$  phases, whereas due to not early saturation of polarization in  $\gamma$  phase (TTTG), it can be utilized in high energy density storage applications<sup>1,3</sup>. Therefore, many attempts have been made to induce the electroactive  $\beta$  phase in PVDF by various methods such as mechanical stretching, casting from solution, application of high pressure, spin coating, addition of metal salts, formation of a nanocomposite, blending with polymers consisting of carbonyl groups, polarization via an applied field, and electrospinning<sup>3,5,6</sup>. In this work, a facile strategy has been attempted where one bacterial surface protein (Bioremediase like) was used as a nucleating agent for  $\beta$ -phase in PVDF. The prepared PVDF/protein free standing film consists of as high as 63 % electroactive phases. In addition, effect of protein on morphological changes of PVDF was systematically investigated with different concentration of protein doped PVDF films. Finally, a flexible mechanical energy harvesting device was fabricated which can produce 2.5 V open-circuit voltage under repeated hand-punching.

## EXPERIMENTAL SECTION

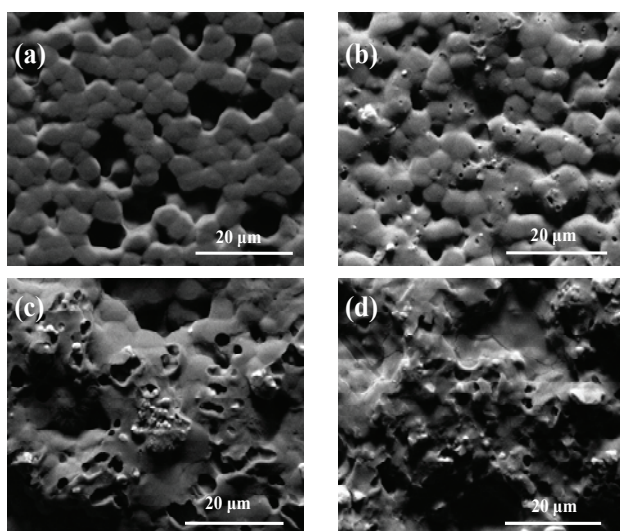
**Experimental Methodology:** Crude Bioremediase like protein was isolated from the cultured medium of BKH2 bacteria and prepared as a dust form through lyophilization<sup>7</sup>. PVDF solutions (6 wt% (w/v)) were prepared by

dissolving PVDF (Sigma-Aldrich, USA,  $M_w = 275000$ ) in N,N-dimethyl formamide (DMF, Merck, India). Several wt % of Crude Protein such as, 2, 4 and 7 wt% were added in to PVDF solutions. The films were deposited through a solution-casting process on clean glass substrates. The as-cast films were subsequently dried at 60°C for 12 h and free-standing flexible film was prepared. A reference film was prepared for comparison which was termed as Neat PVDF.

**Characterization:** Surface morphologies were studied by FESEM (FE-SEM, FEI, INSPECT F 50). The Fourier transform infrared spectroscopy (FTIR) (TENSOR II, Bruker) was performed with 4  $\text{cm}^{-1}$  spectral resolution and 16 number of scan. The device was prepared by simply pasting conducting copper (Cu) tape as electrodes on both sides of the films. The output voltage was recorded using National Instruments (NI) DAQ board (USB 6000) via online interface with PC with sampling rate 1000/sec.

## RESULTS AND DISCUSSIONS

**Surface morphology:** The surface morphology of Neat PVDF and Protein PVDF composite films were examined through FESEM images depicted in Fig. 1. Fig. 1(a) represents the FESEM image of Neat PVDF film and Fig. 1(b),(c),(d) represents FESEM images of Protein doped PVDF films at different concentration of Protein such as, 2, 4 and 7 wt% respectively. From FESEM images, it is evident that Neat PVDF possesses smooth surface morphology. On the other hand, layer of protein is very prominent on the surface of the protein-PVDF composite films. Additionally, with increasing concentration of protein additive in PVDF, agglomeration of protein was observed. Thus, FESEM image reveal that the protein distributed more uniformly in 2 wt % protein doped PVDF film as compare to the other higher concentrations.

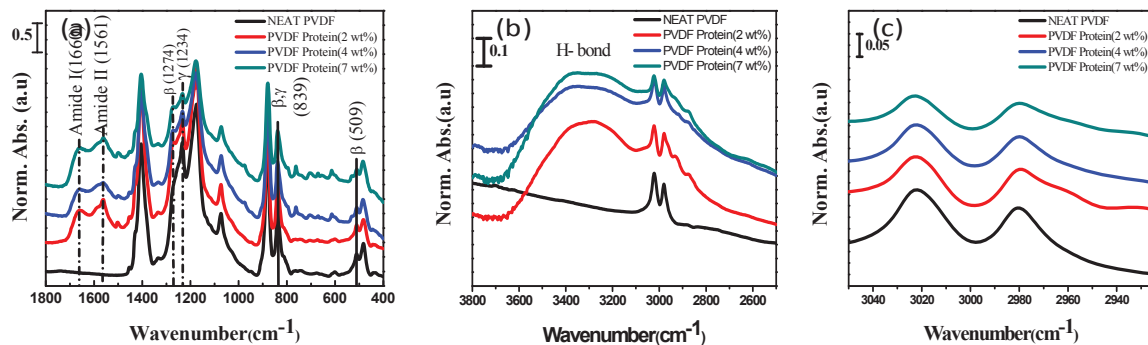


**FIGURE 1.** FESEM image of (a) Neat PVDF film (b) Protein doped PVDF film with 2 wt% concentration (c) 4 wt% Protein doped PVDF film (d) 7 wt% Protein doped PVDF film

**Electroactive phases quantification:** The FTIR spectra of Neat PVDF as well as protein PVDF composite films at different concentrations are shown in Fig. 2 and corresponding vibrational bands are labeled as per the presence of crystalline phases. The FTIR spectra of our films clearly shows the nucleation of the polar  $\beta$ -phase in the protein-PVDF composite films, as evident from the appearance of the intense vibrational band at 1274  $\text{cm}^{-1}$ , which is not present in the Neat PVDF film.

Protein doped PVDF films illustrate another additional intense peak arise at 1234  $\text{cm}^{-1}$  are due to the nucleation of the  $\gamma$ -phase. The semi polar  $\gamma$ -phase at 1234  $\text{cm}^{-1}$ , present in both the Neat PVDF and the protein-PVDF composite films. The peaks at 509 and 839  $\text{cm}^{-1}$  also indicate the  $\beta$ -phase formation in the protein-PVDF composite film. Even though the peak 839  $\text{cm}^{-1}$  presents in both Neat PVDF and protein-PVDF composite films but the absorption intensity increases in the case of protein-PVDF composite films. The absorbance is normalized at 1072  $\text{cm}^{-1}$  band as it has a linear dependence with the film thickness regardless of the crystalline modification. The absorption intensity at 839  $\text{cm}^{-1}$  band which is strongly appear in protein doped PVDF films, can be assigned to

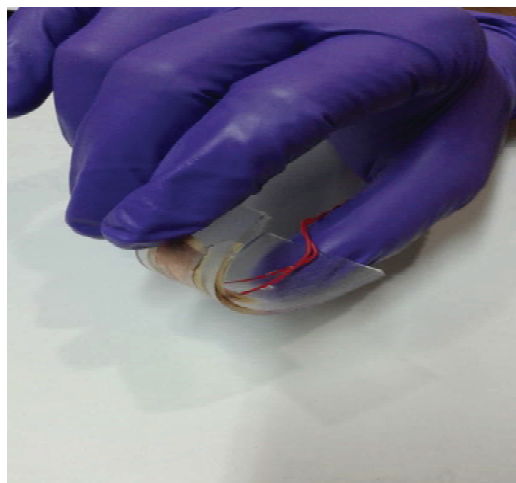
quantify the relative proportion of electro active phases ( $F_{EA}$ ) attributing to both  $\beta$  and  $\gamma$ - phases. The  $F_{EA}$  is related with the equation (1) as follows,



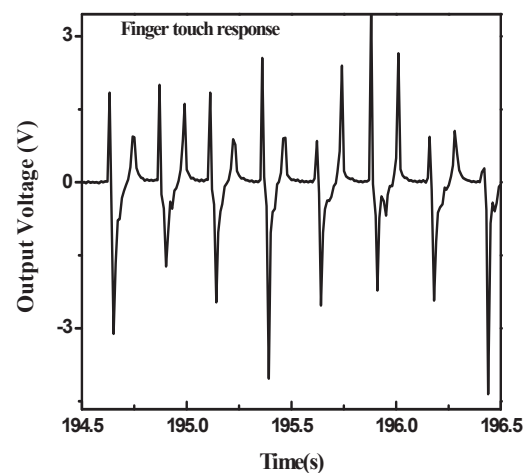
**FIGURE 2.** FT-IR spectra of Neat PVDF and Protein doped PVDF films of different concentration in (a) 1800-400  $\text{cm}^{-1}$  frequency region (b) 2500-3800  $\text{cm}^{-1}$  frequency region (c) 3050-2925  $\text{cm}^{-1}$  Frequency region.

$$F_{EA} = \frac{I_{EA}}{\left(\frac{K_{839}}{K_{764}}\right)I_{764} + I_{EA}} \times 100 \quad (1)$$

Where,  $I_{764}$  and  $I_{EA}$  are the absorbance intensity at 764 and 841  $\text{cm}^{-1}$  respectively,  $K_{764}$  and  $K_{839}$   $\text{cm}^{-1}$  are the absorption co-efficient at the respective wave numbers. Using the equation (1), it has been shown that there are a noticeable presence of electroactive phases *i.e.*, 63% for 2 wt%, 52% for 4 wt% and 51% for 7 wt% in the protein-PVDF composite films. Thus, it is manifested that protein doped PVDF films comprising of large amount of electroactive phase, highly suitable for piezo-electric based sensor, actuators and also for vibration based energy harvesters. These results emphasize on the fact that protein plays a significant catalytic role for nucleating the piezo-electric  $\beta$ -phase and subsequent stabilization. In FTIR spectrum [fig .2(a)], there exists two important intense peak at 1660  $\text{cm}^{-1}$  and at 1561  $\text{cm}^{-1}$  in protein-PVDF composite films, which indicates Amide-I and Amide-II band of



(a)



(b)

**FIGURE 3.** (a) Flexible mechanical energy harvesting device and (b) open-circuit output voltage under hand punching.

protein. However, these bands are absent in Neat PVDF film. The catalytic role of protein can be interpreted by the surface charge (of protein) and dipoles (of PVDF) interaction model. At the higher frequency region of the FTIR

spectra, a small amount of frequency shifting of the  $-\text{CH}_2$  asymmetric ( $\nu_{\text{as}}$ ) and symmetric ( $\nu_{\text{s}}$ ) stretching vibrational modes are observed (Fig.2c) in protein doped PVDF films, is the indication of the interfacial interaction causes from the surface charge of the protein ( $\sigma_{\text{eff}}^-$ ) and  $\text{CH}_2$  dipoles ( $\sigma_{\text{eff}}^+$ ) of PVDF. A broad peak appears in the  $3500\text{--}3000\text{ cm}^{-1}$  region within the FTIR spectrum [Fig.2(b)] of the protein-PVDF composite films, signifying that H-bond formation has occurred. The H-bond formation could be crucial for the orientation of the  $-\text{CH}_2$  and  $-\text{CF}_2$  dipoles, leading to the self-poled  $\beta$ -phase formation that has an importance for spontaneous Piezoelectricity generation.

**Device performance:** The performance of the as fabricated flexible device (Figure 3a) has been investigated under repeated hand punching. The generated open-circuit peak output voltage from the device was 2.5 V (Figure 3b). In addition, positive and negative peaks were generated regarding consecutive pressing and releasing the device respectively. Therefore, the device could have enormous potential in self-powered electronics in near future.

## CONCLUSIONS

In conclusion, the nucleation of electro active  $\beta$ -phase are performed with the Protein composite PVDF solution and flexible protein-PVDF films are prepared using a simple solvent casting technique. We use a eco-friendly biomaterial as a agent for the  $\beta$ -phase generation and for the preparation of the film which has a great importance for sustainable environment. Using this film we fabricated a energy harvester which can produce electrical energy by human touch. The generated energy can be used from self-powered bio-medical engineering to portable electronic gadgets in near future.

## ACKNOWLEDGEMENTS

The experimental supports received from Organic Nano-Piezoelectric Device Laboratory (SERB/1759/2014-15 under EMEQ scheme), and Biophysics Laboratory of Department of Physics, Jadavpur University are gratefully acknowledged. Authors acknowledge DST, Govt. of India (FIST-II programme) and for awarding INSPIRE fellowship (IF130865) to S.K.G.

## REFERENCES

1. A. J. Lovinger, *Science*, 1983, 220, 1115–1121.
2. K. Müller, D. Mandal, K. Henkel, I. Paloumpa and D. Schmeisser, *Appl. Phys. Lett.*, 2008, 93, 112901.
3. P. Martins, A. C. Lopes and S. Lanceros-Mendez, *Prog. Polym. Sci.*, 2014, 39, 683–706.
4. S. K. Ghosh, M. M. Alam, D. Mandal, *RSC Adv.* 4, 41886–41894 (2014).
5. A. Tamang, S. K. Ghosh, S. Garain, M. M. Alam, J. Haeberle, K. Henkel, D. Schmeisser, and D. Mandal. *ACS Appl. Mater. Interfaces* 2015, 7, 16143–16147
6. S. K. Ghosh, A. Biswas, S. Sen, C. Das, K. Henkel, D. Schmeisser, D. Mandal, *Nano Energy* 30, 621–629 (2016).
7. M. Sarkar, N. Alam, B. Chaudhuri, B. Chattopadhyay, S. Manda. *RSC Advances*. 2015, 5, 32175-32182

# Root Extracts (*Gymnadenia orchidis* Lindl) Facilitated Rapid Synthesis of Fluorescent Silver Nanoparticles (Ag-NPs) for Various Biological Applications

Shilpi Show, Chetana Ghosal, Brajadulal Chattopadhyay\*

Department of Physics, Jadavpur University, Kolkata, India

Email: \*bdc\_physics@yahoo.co.in

**How to cite this paper:** Show, S., Ghosal, C. and Chattopadhyay, B. (2017) Root Extracts (*Gymnadenia orchidis* Lindl) Facilitated Rapid Synthesis of Fluorescent Silver Nanoparticles (Ag-NPs) for Various Biological Applications. *Journal of Biomaterials and Nanobiotechnology*, 8, 109-124.

<http://dx.doi.org/10.4236/jbnb.2017.81008>

**Received:** December 7, 2016

**Accepted:** January 19, 2017

**Published:** January 22, 2017

Copyright © 2017 by authors and Scientific Research Publishing Inc.

This work is licensed under the Creative Commons Attribution International License (CC BY 4.0).

<http://creativecommons.org/licenses/by/4.0/>



Open Access

## Abstract

One pot rapid and green bio-synthesis of stable fluorescent silver nanoparticles (Ag-NPs) from silver nitrate solution using root extract of *Gymnadenia orchidis* Lindlat at ambient temperature is demonstrated productively. Surface Plasmon resonance of the synthesized Ag-NPs was shown to occur at 439 nm and two sharp fluorescence peaks at 610 and 780 nm were observed. FTIR study publicized the presence of chemically functional groups in the root extract surrounding the Ag-NPs, acting as stabilizers. XRD and FESEM analysis revealed that Ag-NPs were face centred cubic structure being spherical in shape with an average particle size of  $28 \pm 2$  nm ( $n = 100$ ). The stability of Ag-NPs in neutral pH environment was confirmed by Zeta Potential ( $\zeta$ ) behaviour. The Ag-NPs showed superior antioxidant activity. The notable photo-catalytic activity of biosynthesized Ag-NPs attributed to the existence of some proteins, responsible for degradation of methylene blue dye. Furthermore, Ag-NPs were found to exhibit a significant antibacterial effect against gram positive *Staphylococcus aureus* (*S. aureus*) bacteria.

## Keywords

Green Synthesis, *Gymnadenia orchidis* Lindl, Silver Nanoparticles, DPPH, Photo-Catalytic, Antibacterial

## 1. Introduction

Nanotechnology is a promising growing field in the area of interdisciplinary research work, having specialization as well as applications in biotechnology. The formation of silver nanomaterial or nanoparticles (NPs) is widely examined by different chemical and physical methodologies, but the tool involved in synthesis of NPs in a consistent

way is an important characteristic of nanotechnology [1]. Green synthesis of NPs of novel metals, such as Ag, Au, Pd, Pt, etc., as well as metal & nonmetal oxides such as silica nanoparticles (SiO<sub>2</sub>-NPs), alumina, zirconia, titanium, etc., using biological entities like plant extracts, bacteria, fungi, etc., shows considerable interest of research in last couple of years [2] [3]. The use of plant extracts in green synthesis of metal NPs shows its potential over microorganism because of easy to scale up, rapid, eco-friendly and cost effectiveness [2]. The Ag-NPs are being the most investigated nanomaterial because of its potential applications in various fields, including food, cosmetics, medicine, etc., and also realized as the new generation antimicrobial and antioxidant agents. Some recent reports dealt with the use of plants or parts of plants extract as good bio-reducing agent or in green-synthesis of the Ag-NPs have been well established, a few examples are *Memecylon umbellatum* [2], *Hevea brasiliensis* [4], *Volvariella volvacea* [5], *Stevia rebaudiana* [6], *Trachyspermum ammi*, *Papaver somniferum* [7], *Syzygium aromaticum* [8], *Dillenia indica* [9], *Piper pedicellatum* C.DC [10], *Solanum lycopersicum* [11] and *Prosopis farcta* [12].

*Gymnadenia orchidis* Lindl, a Himalayan endemic medicinal orchid is found in Hindu Kush Himalaya range. Its occurrence is sub-alpine and alpine zones from 2800 - 4200 metre above from the sea level (IUCN, 2004). Other than Nepal Himalayas, it is found in the same altitudinal ranges of India, Pakistan, Bhutan and China also. This plant was identified by the Botanical Survey of India, as the *Gymnadenia orchidis* Lindl of the orchidaceous family (Accession No.: 0046 dated 26.09.2014. V. No. SHRC-5/02/2012-Tech.-195). The powder root of this plant when mixed with water, forms a thick "Salep" which is traditionally used by the local people to get some relief against diabetes.

To the best of our knowledge, there has been no report where phytochemicals of *Gymnadenia orchidis* Lindl were utilized as bio-reducing agents in production of Ag-NPs. In the present study, we have demonstrated an easy green approach for the formation of Ag-NPs using root extract of *Gymnadenia orchidis* Lindl. The as-prepared Ag-NPs were categorized by several tools like UV-Vis spectroscopy, fluorescence spectrophotometer, X-ray diffractometer (XRD), Field Emission Scanning Electron Microscope (FESEM-EDAX), Fourier Transform Infrared Spectroscopy (FTIR), Thermal Gravimetric Analysis (TGA) and Zeta Potential from Dynamic Light Scattering (DLS). The antioxidant activity by DPPH assay of biosynthesized Ag-NPs was studied and compared with natural antioxidant activity of ascorbic acid. The photo-catalytic activity of Ag-NPs against methylene blue (MB) dye was also demonstrated. The antibacterial effect of the biosynthesized Ag-NPs against *Staphylococcus aureus* (*S. aureus*) was confirmed as well. The present protocol implies the room temperature (RT), cost efficient, facile and one-pot green synthesis of Ag-NPs and its possible applicability in different fields such as biomedical, water purification method [13], dye removal [14], etc.

## 2. Materials and Methods

### 2.1. Materials

All chemical used in the present study are of high purity. The analytical grade silver nitrate (AgNO<sub>3</sub>) was purchased from Sigma-Aldrich and Methylene Blue (MB), 1,1-di-

phenyl-2-picrylhydrazyl (DPPH) and Methanol ( $\text{CH}_3\text{OH}$ ) were obtained from Merck, Germany. All chemicals were used without further purifications. *Gymnadenia orchidis* Lindl plant roots were collected from local area of Nepal Himalayas (Darjeeling, West Bengal, India). Throughout the experiment, deionised (DI) water was used whenever necessary.

## 2.2. Preparation of Plant Root Extract

The root (inset of **Figure 1(a)**) of *Gymnadenia orchidis* Lindl was collected from the area of Nepal Himalayas (Darjeeling, West Bengal, India) and washed thoroughly with DI-water several times to remove unwanted entities from it. Afterwards, 5 g of root slices was pasted homogeneously using mortar and pestle. Then, the pasted root was added to 100 ml DI-water and boiled for 10 min followed by filtration through filter paper having diameter of  $0.02\ \mu\text{m}$ .



**Figure 1.** The photograph of (a) *Gymnadenia orchidis* Lindl plant, (b) *Gymnadenia orchidis* Lindlroots extract treated  $\text{AgNO}_3$  solution.

### 2.3. Biosynthesis of Ag-NPs

Aqueous silver nitrate ( $\text{AgNO}_3$ ) solution (0.1 mM) was prepared as precursor for the synthesis of Ag-NPs. 10 ml of *Gymnadenia orchidis* Lindl roots extract was added to 90 ml of precursor solution and kept at ambient temperature for 1 h to reduce the  $\text{Ag}^+$  ions. The colour of the reaction mixture turned colourless to dark brown solution [15] within 1 h due to the formation of Ag-NPs (Figure 1(b)). *Gymnadenia orchidis* Lindl roots extract might have some bio-reduction agents responsible for changing the colour of the reaction mixture.

### 2.4. Characterization of Synthesised Ag-NPs

Several tools were used to exemplify the final yields. The optical characterizations of Ag-NPs suspended in aqueous environment were performed with UV-Vis spectrophotometer (UV-3101PC, Shimadzu) and fluorescence spectrophotometer (Thermo scientific multiskan GO, SpectraMax M5 molecular device). The excitation wavelength ( $\lambda_{\text{exc}}$ ) to study the fluorescence characteristic of Ag-NPs was chosen at 390 nm. XRD measurements was carried out on a Bruker, D8 Advance, X-ray diffractometer, operated at a voltage of 40 kV and a current of 40 mA with Cu  $K_\alpha$  radiation ( $\lambda = 1.54 \text{ \AA}$ ). The surface morphology and composition of the bio-synthesized Ag-NPs were investigated by Field Emission Scanning Electron Microscopy (FE-SEM, FEI INSPECT F50) equipped with Energy dispersive spectrometer (EDAX, Bruker System). Fourier Transform Infrared Spectroscopy (FTIR-8700, Shimadzu) was employed to identify the types of the functional groups present in the Ag-NPs. The Ag-NPs powder was dried and crushed with KBr (1 wt%) to form pellet for receiving of FT-IR spectrum with a resolution of  $4 \text{ cm}^{-1}$ . The thermal stability of Ag-NPs was observed by determining the weight loss of the sample against elevated temperature in TGA/SDTA 851 °Mettler Toledo thermal analyzer system. The synthesized Ag-NPs powder was disseminated in deionized water and the Zeta potential was estimated using DLS (Zeta Sizer, Nano ZS 90, Malvern) equipment. Each experiment was repeated several times ( $n \geq 3$ ) to get the average data.

### 2.5. Antioxidant Activity

The antioxidant activity of green synthesized Ag-NPs was determined by using the DPPH free radical scavenging assay as described by Molyneux *et al.* [16]. In particulars, 1.0 g of DPPH was dissolved in 100 ml methanol. 3.0 ml of test sample (either containing Ag-NPs or ascorbic acid) was mixed to 3.0 ml of DPPH containing methanol and incubated for 30 min at RT. Four different concentrations of test sample were used for the study. The absorbance of the reaction mixture was noted at 517 nm using spectrophotometer. Ascorbic acid (a known innate antioxidant) was used as standard. The radical scavenging activity of Ag-NPs was measured by the percentage of inhibition of DPPH mixture discolouration using the following equation below:

$$\% \text{ of inhibition} = \frac{A_{\text{Blank}} - A_{\text{Sample}}}{A_{\text{Blank}}} \times 100$$

where,  $A_{\text{Blank}}$  and  $A_{\text{Sample}}$  are the values of absorbance (Optical density) of the standard



reaction mixture and the test mixture (standard reaction mixture containing Ag-NPs or ascorbic acid) respectively.

## 2.6. Photo-Catalytic Activity

Typically, 10  $\mu\text{M}$  MB dye solution was prepared as stock solution for the photo-catalytic activity of synthesized Ag-NPs. About 10 mg of freeze dried Ag-NPs was added to a 40 ml of MB dye solution in 100 ml glass beaker. Only MB dye solution (without Ag-NPs) was taken for reference. The absorbance of the mixture was noted after thoroughly mixing the reaction solution by magnetic stirrer. At different time intervals, aliquots of 2 - 3 ml suspension of the reaction mixture were filtered and used to estimate the photo-catalytic degradation of MB dye solution in presence of biosynthesized Ag-NPs. The change in absorbance spectrum due to the presence of Ag-NPs was consequently measured using UV-Vis spectrophotometer under UV light irradiation. Concentration of MB dye during degradation was calculated by the absorbance value at 663 nm. Percentage of degradation of MB dye in presence of Ag-NPs was calculated by using the following formula:

$$\% \text{ of Decolourization} = \frac{(C_0 - C)}{C_0} \times 100$$

where  $C_0$  is the initial concentration of MB dye solution and  $C$  is the concentration of dye solution in presence of Ag-NPs in different time intervals.

## 2.7. Antibacterial Activity

The antibacterial activity of biosynthesized Ag-NPs was examined by observing the zone of inhibition against the growth of a gram positive bacterium *S. aureus*. Luria-Broth (LB) medium containing agar (2%) was poured into Petridisc and allowed over night to get solidified. To the agar plate, 100  $\mu\text{l}$  of pre grown *S. aureus* bacterial cells ( $1 \times 10^8$  CFU/ml) were spread on it and left at room temperature for at least 15 min. On the agar bed, 4 wells (7 mm of diameter) were made using the cork borer. One well was filled with 50  $\mu\text{l}$  sterile DI-water and the rest of three wells were filled with 50  $\mu\text{l}$  of different concentration Ag-NPs solutions (25  $\mu\text{g}/\text{ml}$ , 50  $\mu\text{g}/\text{ml}$  and 100  $\mu\text{g}/\text{ml}$ ). Then the Petri plate was kept for incubation for 24 h at 37°C. After the stipulated time period, the zone of inhibition produced at the different wells was observed. Two replicates were maintained for each concentration and the mean diameter value was expressed in millimetres.

## 2.8. Statistical Analysis

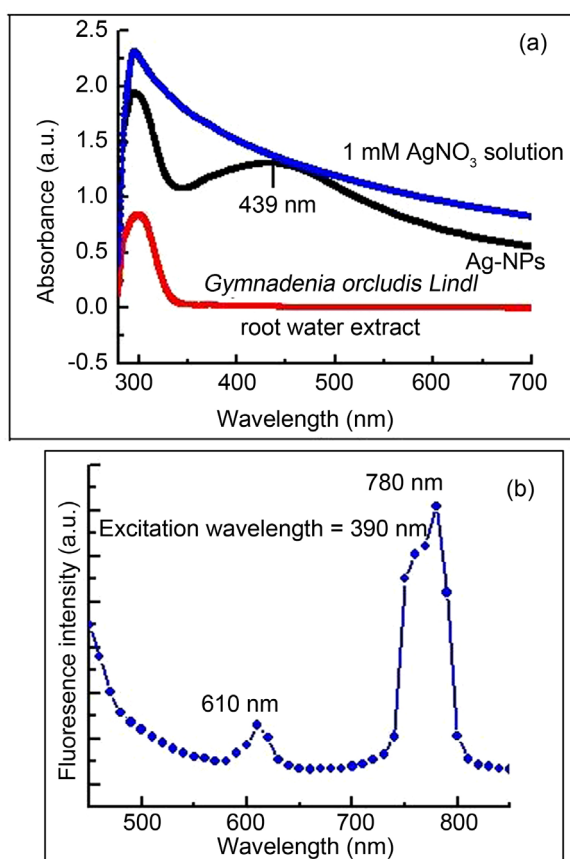
For each experimental set up, all the prepared samples were tested repeatedly. Each experiment was repeated at least three times. Data were presented as an average data with the S.D. where ever is possible.

# 3. Results and Discussion

## 3.1. Optical Properties

The development of the Ag-NPs was observed visually as the colour of the reaction

mixture turned from a colour less to a dark brown solution [15] within 1h as illustrated in **Figure 1(b)**. **Figure 2** are presents the UV-Vis spectraevolution of the  $\text{AgNO}_3$  solution (1 mM), *Gymnadenia orchidis* Lindl roots water extract, the root extract mixed  $\text{AgNO}_3$  solution (after 1 h) recorded at room temperature. No absorption peak was observed in  $\text{AgNO}_3$  solution and *Gymnadenia orchidis* Lindl roots water extract whereas in case of the root extract mixed  $\text{AgNO}_3$  solution, a broad visible absorption band ranging from 350 to 550 nm was observed. The wavelength corresponds to Surface Plasmon resonance (SPR) of as-prepared Ag-NPs, centered at ( $\lambda_{\text{max}}$ ) 439 nm (**Figure 2(a)**). Ag-NPs showed very interesting optical properties directly correlated with localised SPR having morphological dependence of the NPs. In conclusion no blue or red-shift phenomenon of the absorption band of Ag-NPs was observed. This may indicate that no alteration of the size and shape (*i.e.*, stable) of the Ag-NPs occur during incubation of bio-reduction process [17]. The room temperature fluorescence spectrum of the prepared Ag-NPs when excited at 390 nm is shown in **Figure 2(b)**. Two sharp visible peaks at 610 nm (orange) and 780 nm (red) were observed. These emission peaks were due to the local field enhancement via coupling to the transverse and longitudinal SPR [18].



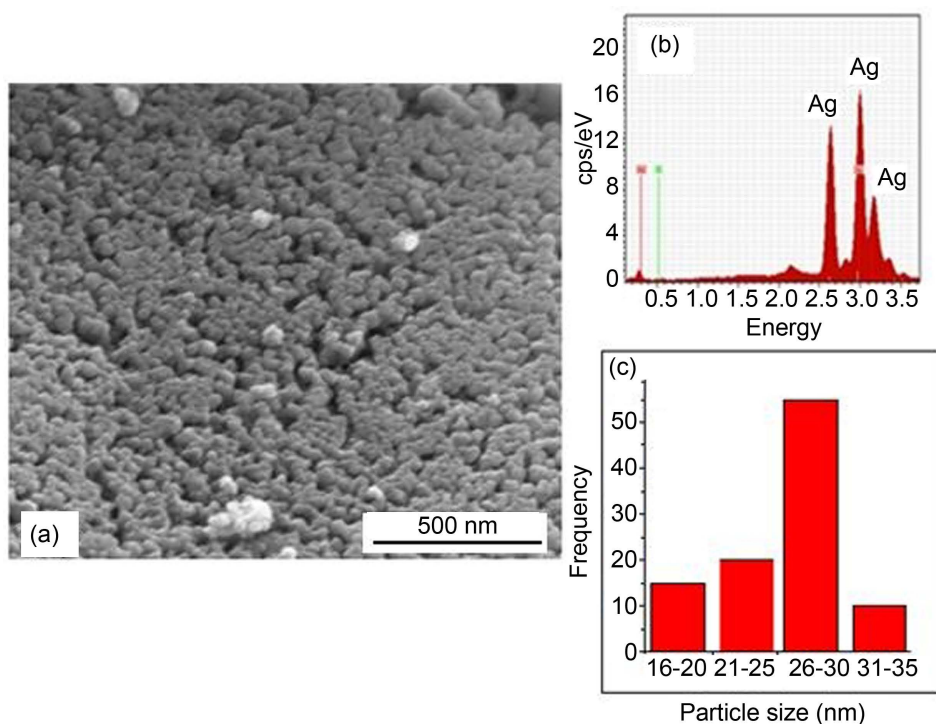
**Figure 2.** Spectroscopic analysis of the biosynthesized Ag-NPs dispersed in aqueous environment indicating (a) Absorbance spectrum and (b) Emission spectrum. The experimental Setup was repeated thrice and no significant errors were noted.

### 3.2. Morphological and Chemical Composition of Ag-NPs

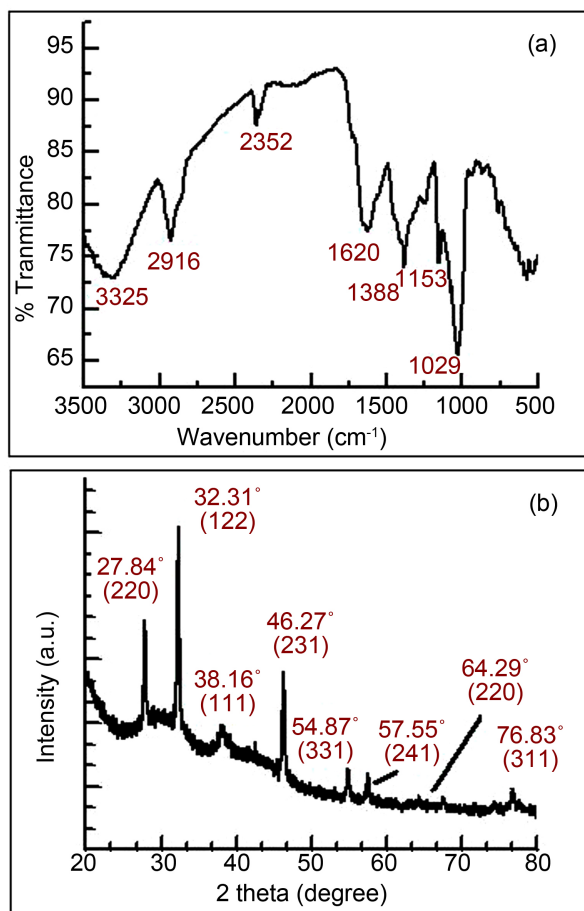
**Figure 3** indicates the FE-SEM image and EDAX spectra (inset of **Figure 3(a)**) of Ag-NPs formed by the interaction between *Gymnadenia orchidis* Lindl roots extract and AgNO<sub>3</sub> solution. FE-SEM image confirmed the Ag-NPs were quite uniform spherical in shape and polydisperse in nature. Few larger particles of Ag-NPs were appeared in the FE-SEM image which was due to NPs aggregation during synthesis process. This could lead to the variation in size of the particles. The histogram of the particle size distribution is shown in **Figure 3(b)**. This illustrates that the maximum average particle is around  $28 \pm 2$  nm ( $n = 100$ ). The EDAX analysis shown in the inset of **Figure 3** reveals the strong signal at 3 keV due to metallic nature of NPs [19].

### 3.3. FTIR and XRD Studies

FTIR spectrum (**Figure 4(a)**) was performed to confirm the chemically functional groups surrounded the Ag-NPs. It shows that the peak at  $3325\text{ cm}^{-1}$  corresponds to water and O-H vibrational frequency. The small peak at  $2916\text{ cm}^{-1}$  is characteristics of aldehydic C-H stretching vibration. The peaks at  $2352\text{ cm}^{-1}$  and  $1620\text{ cm}^{-1}$  represents the asymmetric stretching of C-H and carbonyl specific absorption (C=C) or amide I respectively. The peak at  $1388\text{ cm}^{-1}$  corresponds of aromatic amine and nitro groups or amide II due to the N=O bending vibrations. Peaks at  $1153\text{ cm}^{-1}$  and  $1029\text{ cm}^{-1}$  confirm the presence of C=O and C-OH stretching vibrations. FTIR study has confirmed that the carbonyl group from amino acid residue and peptide of proteins (amide I) both has the stronger ability to bind metals. It signifies that the protein may be responsible



**Figure 3.** (a) FE-SEM image (Magnification: 200,000 $\times$ ) (b) EDAX spectrum and (c) Histogram showing the particle size distribution ( $n = 100$ ) of Ag-NPs formed by the interaction of *Gymnadenia orchidis* Lindl roots extract and AgNO<sub>3</sub> solution.



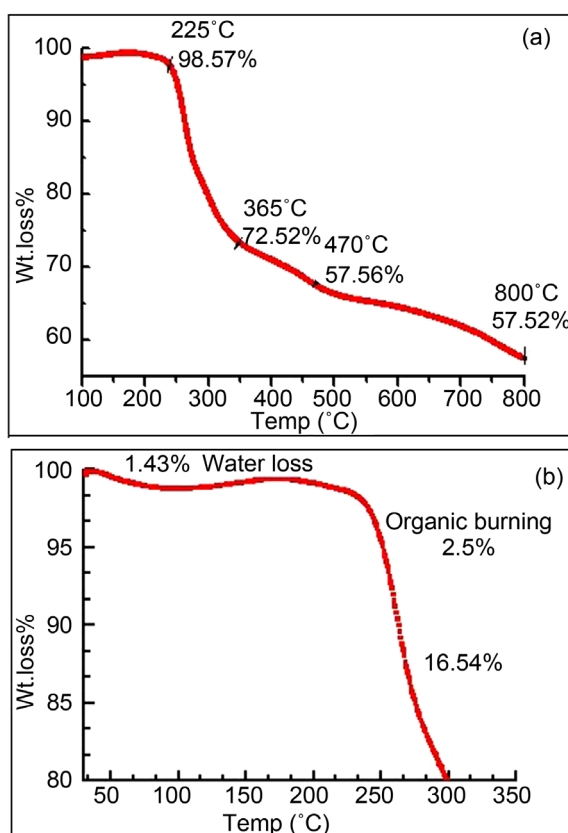
**Figure 4.** (a) FTIR spectrum and (b) XRD pattern of the green synthesized Ag-NPs. The experimental Setup was repeated thrice and no significant errors were noted.

for forming a surface layer on the metallic Ag-NPs that helps in stabilization of Ag-NPs.

The XRD pattern (**Figure 4(b)**) of biosynthesized Ag-NPs shows the peaks at  $2\theta = 38.2^\circ$ ,  $64.3^\circ$  and  $76.8^\circ$  correspond to the diffraction due to (111), (220) and (311) planes respectively. It confirmed the crystalline face centred cubic structure [JCPDS, File No: 40738] of Ag-NPs. Apart from above three peaks several peaks were also observed. The unassigned diffraction peaks could be due to the crystallization of bio-organic phase that occurred on the surface of the biosynthesized Ag-NPs. The size of the synthesized Ag-NPs was calculated from X-ray line broadening using the Debye-Scherrer formula given as  $D = 0.9\lambda/\beta \cos\theta$ , where  $D$  was the average size of crystalline ( $\text{\AA}$ ),  $\lambda$  was the X-ray wavelength used ( $\text{\AA}$ ) in measurement,  $\beta$  the angular line width at half maximum intensity and  $\theta$  the Bragg's angle (degrees). For (122) reflection plane the size of the Ag-NPs was calculated to be around 30 nm which was in good agreement with the data obtained from FE-SEM analysis.

### 3.4. Thermal Properties of Ag-NPs

**Figure 5(a)** indicates thermal properties of biosynthesized Ag-NPs measured from



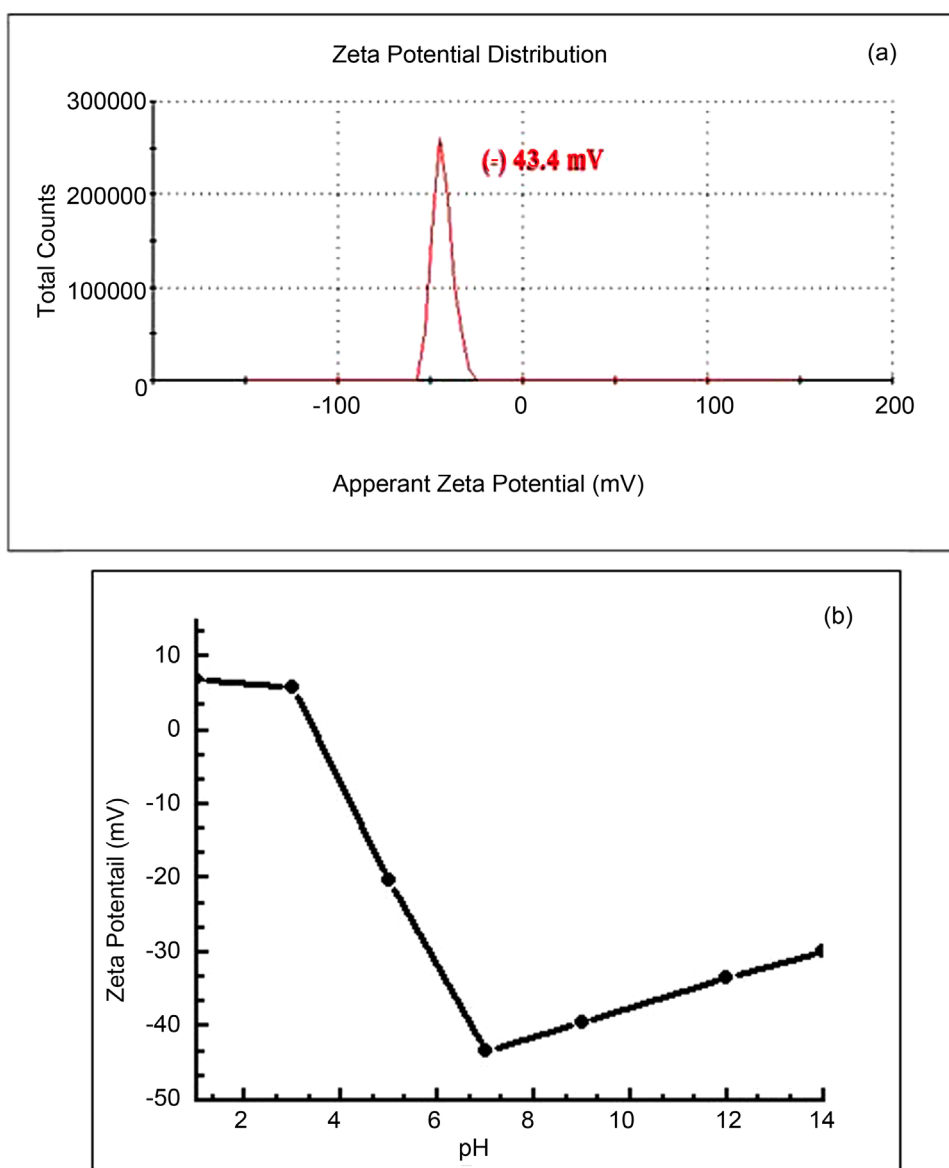
**Figure 5.** (a) The TGA graph of the green synthesized Ag-NPs up to 800°C, (b) Enlarged TGA curve of powder Ag-NPs up to 300°C. The experimental Setup was repeated thrice and no significant errors were noted.

room temperature (30°C) to 800°C using TGA. A ceramic ( $\text{Al}_2\text{O}_3$ ) crucible was used for heating and measurements were carried out in  $\text{N}_2$  atmosphere at the heating rate of 10°C/min. TGA curve of powder Ag-NPs is more precisely shown in **Figure 5(b)** (up to 300°C). It was found from TGA curve that dominant weight loss of the Ag-NPs occurred in the temperature range between 225°C to 300°C. There was almost 1.43% weight loss below 225°C due to loss of water molecules present in biosynthesized Ag-NPs. Above 225°C, there was 2.45% weight loss due to the burning of the organic constituents. In conclusions, TGA graph of biosynthesized Ag-NPs showed that the effective loss of weight (20.31%) occurred up to 300°C temperature. Also, there was a steady weight loss occurred up to 800°C temperature. The total weight loss up to 800°C for Ag-NPs (**Figure 5(a)**) was about 42.48%. The observed behaviour is most likely as a consequence of the surface desorption of phytochemicals surrounded in NPs. Thus, plant roots extract-stabilized Ag-NPs are accepted to be fabricated of molecules conscientious for the diminution of metal ions and stabilizing the particles in the mixture solution. The melting and boiling temperatures of smaller particles were observed less compare to the larger particles as explained by Kasthuri *et al.* [20].

### 3.5. Stability of Ag-NPs

The Zeta potential ( $\zeta$ ) of the biosynthesized Ag-NPs was found to be (–) 43.4 mV in

neutral pH background (Figure 6(a)). It concludes that Ag-NP<sub>s</sub> are very stable. The large negative  $\zeta$  value could be due to the capping of polyphenolic constituents present in the roots extract [21]. The negative nature of  $\zeta$  prevented Ag-NPs from the agglomeration and made it good dispersion stability. The pH dependence of  $\zeta$  value of biosynthesized Ag-NPs in aqueous environment is shown in (Figure 6(b)). Aqueous Ag-NPs suspension exhibited good stability  $\zeta(-)$  43.4 mV at neutral pH whereas the same exhibited moderate stability between the pH ranges of 7 - 14. The magnitude of  $\zeta(-29.9$  mV) at pH 14 signified to a less stable NPs suspension compare to neutral medium. This report also suggested that smaller Ag-NPs were present at low pH (<5), since the less stability would be expected for small particles because of increased surface free energy [22].



**Figure 6.** (a) Zeta Potential ( $\zeta$ ) curve of synthesized Ag-NPs in neutral pH environment and (b) pH dependence of  $\zeta$  value of biosynthesized Ag-NPs in aqueous environment. The experimental setup was repeated thrice and the average with Standard Error of Zeta potential was presented.

### 3.6. Antioxidant Activity of Ag-NPs

The anti-oxidative effect of green synthesized Ag-NPs on DPPH is thought to be due to their hydrogen donating capability [23]. As DPPH is a familiar as lipophilic radical, this readily accepts electron from the antioxidant materials and converts its colour from violet to yellow. At 517 nm, the absorbance of the DPPH solution (*i.e.* the blank) was 0.501. The reduction in absorbance of DPPH at 517 nm caused by the samples (Ag-NPs or ascorbic acid) was measured in triplicate after 10 min interval. The tested samples (Ag-NPs or ascorbic acid) showed very good activity when calculated using equation [1] and compared with the standard used (Table 1). There was a decrease in absorption at 517 nm signifying that the roots extract and Ag-NPs had hydrogen donating ability. From the above analysis, the samples (Ag-NPs or ascorbic acid) showed a concentration dependent radical scavenging capacity. This observation was further corroborated by calculating percentage inhibition for all the test samples (Ag-NPs or ascorbic acid). It was pragmatic that biosynthesized Ag-NPs exhibited moderate activity as free radical scavenger compared to the control. At 0.002 mg/ml concentration as-prepared Ag-NPs showed maximum antioxidant activity. The antioxidant activity of Ag-NPs using *Gymnadenia orchidis* Lindl roots extract may be due to the presence of some active phytochemical compounds in the plant roots.

### 3.7. Photo-Catalytic Activity of Ag-NPs

Photo-catalytic activity of green synthesized Ag-NPs on degradation of MB dye is demonstrated successfully (Figure 7(a)). The degradation of MB dye was carried out in the presence of Ag-NPs at different time interval in visible region under UV light irradiation. Firstly, the absorption peaks of MB dye solution at 663 nm were decreased regularly with the increase of the exposure time which indicates the photo-catalytic degradation of MB dye under UV light irradiation. The percentage of degradation efficiency of biosynthesized Ag-NPs was calculated using Equation (2) and tabulated in Table 2. Within 120 min the MB dye was degraded by 57.1% which concluded the fact that biosynthesized Ag-NPs were effective photo catalyst within small exposure time. The notable photo catalytic activity of biosynthesized Ag-NPs was mainly because of the presence of some facade proteins that surrounded the Ag-NPs [24]. Table 2 indicates the change of % of decolorization of MB dye with the exposure time of UV light irradiation, in presence of biosynthesized Ag-NPs. Figure 7(b) indicates the normalize

**Table 1.** Antioxidant activity study of as prepared Ag-NPs by DPPH assay.

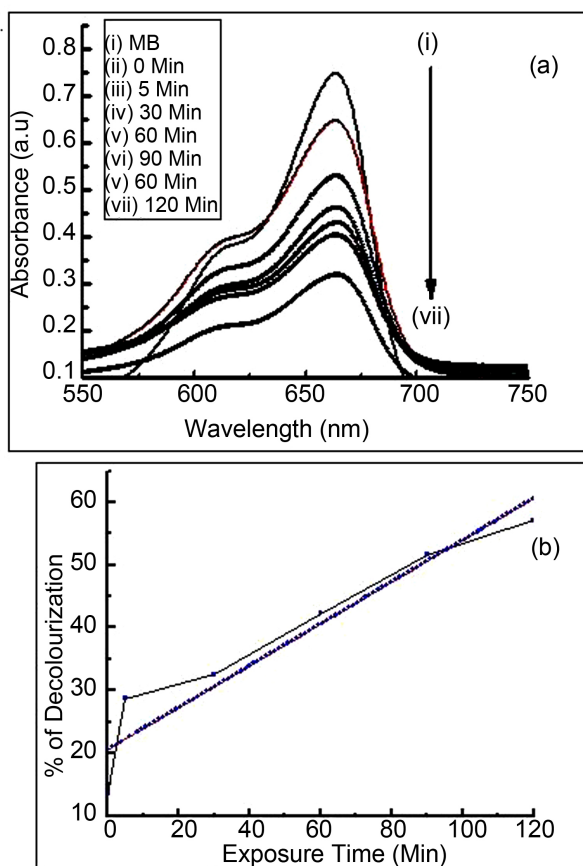
Concentration (mg/mL) Ag-NPs	Absorbance of reaction mixture with % inhibition	Ascorbic Acid	Absorbance of reaction mixture with % inhibition
0.001	0.398 ± 0.04	20.56 ± 0.2	79.04 ± 0.1
0.002	0.321 ± 0.03	35.93 ± 0.1	80.44 ± 0.2
0.003	0.348 ± 0.01	30.54 ± 0.4	76.65 ± 0.2
0.005	0.390 ± 0.04	22.16 ± 0.2	78.84 ± 0.4

Absorbance value from scavenging effect of standard control on DPPH at 517 nm was 0.501 ± 0.04.

**Table 2.** Photo-catalytic activity study of Ag-NPs.

Exposure time (in Mins)	Amount of degradation of MB dye (in %)
0	13.5
5	28.7
30	32.5
60	42.3
90	51.6
120	57.1

Absorbance values of 10 μM MB dye solution react with Ag-NPs at 663 nm was  $C_0 = 0.7472$ .



**Figure 7.** (a) Photocatalytic measurement of MB dye solution treated with the biosynthesized Ag-NPs. (b) Percentage of decomposition of MB dyes when treated with biosynthesized Ag-NPs at different functional time intervals. The blue dotted line is the mean curve of the experimental data. The experimental Setup was repeated thrice and no significant errors were noted.

graph of the data as stated in **Table 2**.

### 3.8. Antibacterial Activity of Ag-NPs

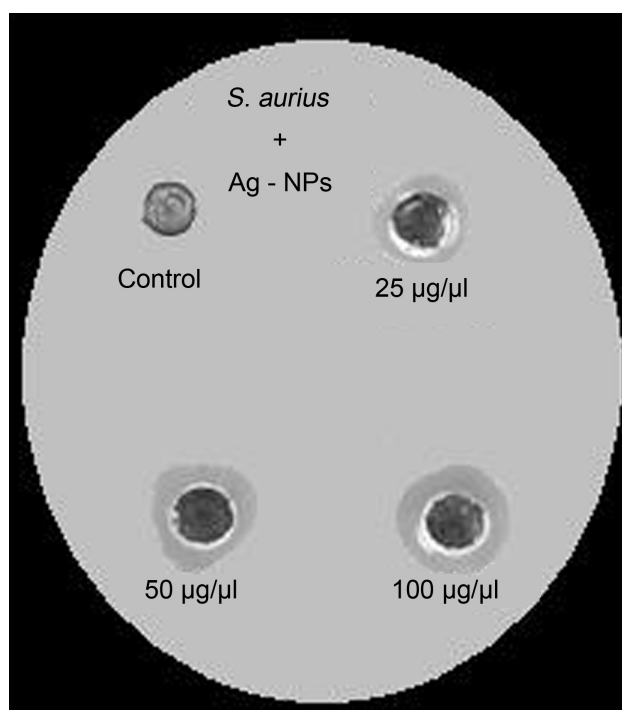
The diameters of the inhibition zones were measured against gram positive *S. aureus* bacterial growth. The experimental setup was repeated thrice and the average diameter



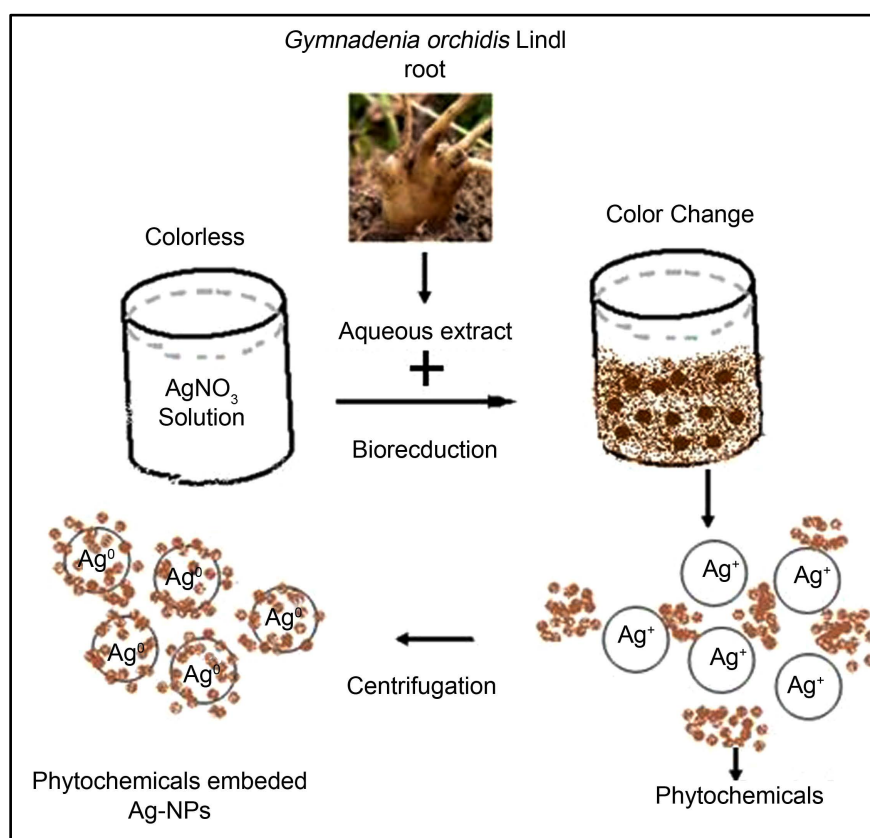
of inhibition was given with standard error. Three different concentrations of biosynthesized Ag-NPs solutions viz., 25  $\mu\text{g/ml}$ , 50  $\mu\text{g/ml}$  and 100  $\mu\text{g/ml}$  were used and the corresponding diameters of inhibition zones were determined as  $(15 \pm 0.1)$ ,  $(16 \pm 0.3)$  and  $(18 \pm 0.2)$  mm respectively (**Figure 8**). As the concentration of Ag-NPs increased the inhibition zone of bacterial growth was also increased. This result concludes that the biosynthesized Ag-NPs possesses prominent antibacterial activity against *S. aureus* bacteria. It was earlier reported that the antibacterial effect of Ag-NPs was caused by the interaction of membrane of bacterial cell wall and Ag-NPs, hence ensuing in amplified bacterial membrane permeability and as a result, death of the bacteria [25].

### 3.9. Probable Pathway of Ag-NPs Formation

It was observed that the aqueous extract of powder root of *Gymnadenia orchidis* Lindl contains some polyphenols, proteins, terpenoids and carbohydrates etc. (data communicated). The probable pathway involved for the green synthesis of Ag-NPs may be explained by the presence of nitrate reductive protein (FTIR data) or polyphenols (Zeta potential value) in the root extract of *Gymnadenia orchidis* Lindl. It is assumed that the biosynthesis of Ag-NPs by *Gymnadenia orchidis* Lindl roots extract follows a similar bio-reduction pathway as shown in **Figure 9**. The protein present in the roots extract was seen capping on the surface of Ag-NPs. This was confirmed by FTIR spectra (**Figure 4(a)**) that clearly revealed the amide I and amide II bands at 1620 and 1388  $\text{cm}^{-1}$  respectively. The peak at 1388  $\text{cm}^{-1}$  confirmed also the presence of aromatic amine and nitro groups.



**Figure 8.** Antibacterial activity of the green synthesized Ag-NPs against *S. aureus* strain. The experimental setup was repeated thrice and the average with Standard Error of diameters of the inhibition zone was presented.



**Figure 9.** The probable pathway of Ag-NPs formation by the interaction of *Gymnadenia orchidis* Lindlroots extract and AgNO<sub>3</sub> solution.

#### 4. Conclusion

The green synthesis of Ag-NPs by the roots extract of *Gymnadenia orchidis* Lindl is a simplistic, rapid, ecological and low price technique at ambient temperature. This is a significant development for the formation of Ag-NPs as it allows better organization over their nanostructures. The presence of some phytochemicals like terpenoids, proteins and polyphenols in *Gymnadenia orchidis* Lindlroots extract may act as bio-reducer in the diminution process of Ag<sup>+</sup> to Ag<sup>0</sup> and thus to Ag-NPs. This study would provide a suitable utilization of the *Gymnadenia orchidis* Lindl as a hopeful agent in many biological applications. The photo-catalytic efficiency against MB dye molecules in short time exposure may be useful in technique involved for water purification systems and dye effluent treatment. The as-prepared Ag-NPs exhibit noticeably and considerably antibacterial cause that may be applicable as a prospective outcome for assorted biomedical entities.

#### Conflict of Interests

The authors declare that there is no conflict of interests regarding the publication of this paper.

#### Acknowledgements

The work was performed by the authors own support. The experimental facilities ob-

tained from Biophysical Laboratory of Physics Department of Jadavpur University are gratefully acknowledged.

## References

- [1] Natarajan, K., Selvaraj, S. and Ramachandramurthy, V. (2010) Microbial Production of Silver Nanoparticles. *Digest Journal of Nanomaterials and Biostructures*, **5**, 135-140.
- [2] Arunachalam, K.D., Annamalai, S.K. and Hari, S. (2013) One-Step Green Synthesis and Characterization of Leaf Extract-Mediated Biocompatible Silver and Gold Nanoparticles from *Memecylon umbellatum*. *International Journal of Nanomedicine*, **8**, 1307-1315. <https://doi.org/10.2147/IJN.S36670>
- [3] Show, S., Tamang, A., Chowdhury, T., Mandal, D. and Chattopadhyay, B.D. (2015) Bacterial (BKH1) Assisted Silica Nanoparticles from Silica Rich Substrates: A Facile and Green Approach for Biotechnological Applications. *Colloids and Surfaces B: Biointerfaces*, **126**, 245-250. <https://doi.org/10.1016/j.colsurfb.2014.12.039>
- [4] Guidelli, E.J., Ramos, A.P., Zaniquelli, M.E.D. and Baffa, O. (2011) Green Synthesis of Colloidal Silver Nanoparticles Using Natural Rubber Latex Extracted from *Hevea brasiliensis*. *Spectrochimica Acta Part A: Molecular and Biomolecular Spectroscopy*, **82**, 140-145. <https://doi.org/10.1016/j.saa.2011.07.024>
- [5] Philip, D. (2009) Biosynthesis of Au, Ag and Au-Ag Nanoparticles Using Edible Mushroom Extract. *Spectrochimica Acta Part A: Molecular and Biomolecular Spectroscopy*, **73**, 374-381. <https://doi.org/10.1016/j.saa.2009.02.037>
- [6] Yilmaz, M., Turkdemir, H., Kilic, M.A., Bayram, E., Cicek, A. and Mete, A. (2011) Biosynthesis of Silver Nanoparticles Using Leaves of *Stevia rebaudiana*. *Materials Chemistry and Physics*, **130**, 1195-1202. <https://doi.org/10.1016/j.matchemphys.2011.08.068>
- [7] Vijayaraghavan, K., Nalini, S.P.K., Prakash, N.U. and Madhankumar, D. (2012) One Step Green Synthesis of Silver Nano/Microparticles Using Extracts of *Trachyspermum ammi* and *Papaver somniferum*. *Colloids and Surfaces B: Biointerfaces*, **94**, 114-117. <https://doi.org/10.1016/j.colsurfb.2012.01.026>
- [8] Vijayaraghavan, K., Nalini, S.P.K., Prakash, N.U. and Madhankumar, D. (2012) Biomimetic Synthesis of Silver Nanoparticles by Aqueous Extract of *Syzygium aromaticum*. *Materials Letters*, **75**, 33-35. <https://doi.org/10.1016/j.matlet.2012.01.083>
- [9] Singh, S., Saikia, J.P. and Buragohain, A.K. (2013) A Novel "Green" Synthesis of Colloidal Silver Nanoparticles (SNP) using *Dillenia indica* Fruit Extract. *Colloids and Surfaces B: Biointerfaces*, **102**, 83-85. <https://doi.org/10.1016/j.colsurfb.2012.08.012>
- [10] Tamulya, C., Hazarika, M., Borah, S.C., Das, M.R. and Boruah, M.P. (2013) *In Situ* Biosynthesis of Ag, Au and Bimetallic Nanoparticles Using *Piper pedicellatum* C.DC: Green Chemistry Approach. *Colloids and Surfaces B: Biointerfaces*, **102**, 627-634. <https://doi.org/10.1016/j.colsurfb.2012.09.007>
- [11] Umadevi, M., Bindhu, M.R. and Sathe, V.A. (2013) A Novel Synthesis of Malic Acid Capped Silver Nanoparticles Using *Solanum lycopersicum*s Fruit Extract. *Journal of Materials Science & Technology*, **29**, 317-322. <https://doi.org/10.1016/j.jmst.2013.02.002>
- [12] Miri, A., Sarani, M., Bazaz, M.R. and Darroudi, M. (2015) Plant-Mediated Biosynthesis of Silver Nanoparticles Using *Prosopis farcta* Extract and Its Antibacterial Properties. *Spectrochimica Acta Part A*, **141**, 287-291. <https://doi.org/10.1016/j.saa.2015.01.024>
- [13] Savage, N. and Mamadou, S.D. (2005) Nanomaterials and Water Purification: Opportunities and Challenges. *Journal of Nanoparticle Research*, **7**, 331-342. <https://doi.org/10.1007/s11051-005-7523-5>
- [14] Yolaa, M.L., Erenb, T., Atar, N. and Wang, S. (2014) Adsorptive and Photocatalytic Removal of Reactive Dyes by Silver Nanoparticle-Colemanite Ore Waste. *Chemical Engineering*

- Journal*, **242**, 333-340. <https://doi.org/10.1016/j.cej.2013.12.086>
- [15] Noginov, M.A., Zhu, G., Bahoura, M., Adegoke, J., Small, C. and Ritzo, B.A. (2007) The Effect of Gain and Absorption on Surface Plasmons in Metal Nanoparticles. *Applied Physics B*, **86**, 455-460. <https://doi.org/10.1007/s00340-006-2401-0>
- [16] Tripathi, R.M., Kumar, A., Shrivastav, P., Singh, B. and Shrivastav, R. (2013) Catalytic Activity of Biogenic Silver Nanoparticles Synthesized by *Ficus panda* Leaf Extract. *Journal of Molecular Catalysis B: Enzymatic*, **96**, 75-80. <https://doi.org/10.1016/j.molcatb.2013.06.018>
- [17] Molyneux, P. (2004) The Use of the Stable Free Radical Diphenylpicrylhydrazyl (DPPH) for Estimating Antioxidant Activity. *Journal of Science and Technology*, **26**, 211-219.
- [18] Gengan, R.M., Anand, K., Phulukdaree, A. and Chuturgoon, A. (2013) A549 Lung Cell Line Activity of Biosynthesized Silver Nanoparticles Using *Albizia adianthifolia* Leaf. *Colloids and Surfaces B: Biointerfaces*, **105**, 87-91. <https://doi.org/10.1016/j.colsurfb.2012.12.044>
- [19] Mulvaney, P. (1996) Surface Plasmon Spectroscopy of Nanosized Metal Particles. *Langmuir*, **12**, 788-800. <https://doi.org/10.1021/la9502711>
- [20] Kasthuri, J., Kathiravan, K. and Rajendiran, N. (2009) Phyllanthin-Assisted Biosynthesis of Silver and Gold Nanoparticles: A Novel Biological Approach. *Journal of Nanoparticle Research*, **11**, 1075-1085. <https://doi.org/10.1007/s11051-008-9494-9>
- [21] Sathishkumar, M., Sneha, K., Won, S.W., Cho, C.W., Kimand, S. and Yun, Y.S. (2009) *Cinnamon zeylanicum* Bark Extract and Powder Mediated Green Synthesis of Nano-Crystalline Silver Particles and Its Bactericidal Activity. *Colloids and Surfaces B: Biointerfaces*, **73**, 332-338. <https://doi.org/10.1016/j.colsurfb.2009.06.005>
- [22] Pandey, S., Mewada, A., Thakur, M., Shinde, S., Shah, R., Oza, G. and Sharon, M. (2013) Rapid Biosynthesis of Silver Nanoparticles by Exploiting the Reducing Potential of *Trapabispinosa* Peel Extract. *Journal of Nanoscience*, **10**, 516357-516373.
- [23] Pettibone, J.B., Elzey, S. and Grassian, V.H. (2008) An Integrated Approach toward Understanding the Environmental Fate, Transport, Toxicity and Health Hazards of Nanomaterials. In: Grassian, V.H., Ed., *Nanoscience and Nanotechnology: Environmental and Health Impacts*, Wiley, Hoboken, 47-50. <https://doi.org/10.1002/9780470396612.ch3>
- [24] Baumann, J., Wurn, G. and Bruchlausen, F.V. (1979) Prostaglandin, Synthetase Inhibiting  $O_2^-$  Radical Scavenging Properties of Some Flavonoids and Related Phenolic Compounds. *Arc Pharmacol*, **307**, R1-R77.
- [25] Jain, N., Bhargava, A. and Panwar, J. (2013) Enhanced Photocatalytic Degradation of Methylene Blue Using Biologically Synthesized "Protein-Capped" ZnO Nanoparticles. *The Chemical Engineering Journal*, **13**, 01563-01568.



**Submit or recommend next manuscript to SCIRP and we will provide best service for you:**

Accepting pre-submission inquiries through Email, Facebook, LinkedIn, Twitter, etc.

A wide selection of journals (inclusive of 9 subjects, more than 200 journals)

Providing 24-hour high-quality service

User-friendly online submission system

Fair and swift peer-review system

Efficient typesetting and proofreading procedure

Display of the result of downloads and visits, as well as the number of cited articles

Maximum dissemination of your research work

Submit your manuscript at: <http://papersubmission.scirp.org/>

Or contact [jbnb@scirp.org](mailto:jbnb@scirp.org)

# A MICROBIAL PROTEIN-ASSISTED SILICA BALL COMPRISING OF SILICA-NANOPARTICLES WITH PLAUSIBLE OPTICAL PROPERTIES FOR MULTIPLE APPLICATIONS

Research

AUTHOR: Brajadul Chattopadhyay

August 2017

Shilpi Show<sup>1</sup>, Krishna Chattopadhyay<sup>2</sup>, Chetana Ghosal<sup>1</sup>, Brajadul Chattopadhyay<sup>1\*</sup>

<sup>1</sup>Department of Physics, Jadavpur University, Kolkata 700032, India

<sup>2</sup>Department of Chemistry, Jadavpur University, Kolkata 700032, India

## CORRESPONDENCE AUTHOR

Brajadul Chattopadhyay  
Department of Physics, Jadavpur University  
Raja S.C. Mallick Road, Kolkata-700032  
India  
Email: bdc\_physics@yahoo.co.in  
Phone: +91-9433343917  
Fax: +91-33-24138917

## CONFLICTS OF INTEREST

There are no conflicts of interest for any of the authors.

Received Date: 30<sup>th</sup> June 2017

Accepted Date: 09<sup>th</sup> July 2017

Published Date: 08<sup>th</sup> Aug 2017

Copy rights: © This is an Open access article distributed under the terms of Creative Commons Attribution 4.0 International License.

## ABSTRACT

**Background:** Production of mesoporous silica nanoparticles and its conceivable applications in the fields of chromatography, surface polishing, catalysis and drug delivery etc. has gained momentum recently. We demonstrate here an efficient methodology for the amicable synthesis of silica balls consisting of mesoporous silica nanoparticles (SiO<sub>2</sub>-NPs) by using a secretory protein (bioremediase). The protein was isolated from a thermophilic non-pathogenic bacterium BKH1 (GenBank Accession No. FJ177512).

**Methods:** Silica ball was formed at ambient temperature by mixing the dissolved bacterial protein dropwise to an organic precursor tetra-ethyl-orthosilicate (TEOS) solution at neutral pH environment. Surface morphology and compositional studies of prepared silica ball were carried out by using High-Resolution Transmission Electron Microscope (HRTEM) and Field Emission Scanning Electron Microscope equipped with Energy Dispersive X-ray Analyzer (FESEM-EDX). Fourier Transform Infrared Spectroscopy (FTIR) and X-ray diffraction (XRD) studies were further carried out for auxiliary characterization to determine the nature of SiO<sub>2</sub>-NPs. Stability of the as prepared SiO<sub>2</sub>-NPs was determined by noting the Zeta potential ( $\zeta$ ). The dye degradation activity of the silica balls was noted against different dyes.

**Results:** Silica ball thus formed consisted of silica nanoparticles whose average dimensions were  $20 \pm 10$  nm ( $n = 100$ ). The size of the silica ball and also the sizes of the constituents' nanoparticles depend on the protein concentration in the reaction mixture. The result of zeta potential implied the moderate stability of SiO<sub>2</sub>-NPs at neutral pH environment. The SiO<sub>2</sub>-NPs showed green fluorescence emission which might have feasibly applications in the field of biomedical imaging. The decolourizing effect of silica ball on various dyes is a cost effective phenomenon as it can be used repeatedly.

**Conclusion:** The protein-assisted silica balls preparation has a special consequence as it is an environmentally benign, lucrative and one pot synthesis approach which could be used repeatedly for various biomedical and chromatographic packing purposes.

**KEYWORDS:** Bioremediase protein, Nanoparticles, Silica ball, Tetraethyl orthosilicate,

## INTRODUCTION

There is an immense compact of interest in the field of nanoscale particles like mesoporous silica and its conceivable applications in the different fields like chromatographic, surface polishing, catalysis, medical implants, and drug delivery etc. [1-3]. Silica nanoparticles (SiO<sub>2</sub>-NPs) have fascinated considerable attention from researchers due to their enormous potential applications. First, the band gap of a-SiO<sub>2</sub> is very large which means that vacuum ultraviolet excitation is needed for optical experiments. Second, the fact that the material is amorphous allows for a wide variety, and greater number, of atomic-scale defects than would be accommodated by the ordered structure of a crystal. As a result, many of the optical and electronic properties of a-SiO<sub>2</sub> are dominated by these defects which have, therefore, been the focus of much of the research on this material. The defects may be extremely important, by the way, in both electronic and optical applications of a-SiO<sub>2</sub>. Defects in thermal oxides on Si devices, especially if charged, can influence carrier mobility near the surface as well as the threshold of field-effect transistors. Defects in optical fibres may limit the ultimate optical attenuation either by absorption or scattering.

Properties like biocompatibility, low toxicity, and scalable accessibility have fuelled studies that extent its reasonable applications from cell differentiation to drug or Si-RNA delivery systems and imagenology [4-7]. However, conventional methods for the production of SiO<sub>2</sub>-NPs follow a self assembly mechanism where physical, chemical as well as structural properties of the nanoparticle (NPs) are controlled by both reactant ratios and investigational conditions [8-10]. Anderson et al. (1998) and others synthesized NPs using both charged and neutral templates and showed that the addition of co-solvent produced more spherical particles [11, 12].

Present efforts are focused on the search for new biological synthetic routes for SiO<sub>2</sub>-NPs formation involving lower costs and a less ecological impact while also maintaining both reproducibility and biocompatibility. This work recommends a single step, rapid, convenient green technique for the formation of amorphous, along with thermally and chemically stable silica balls consisting of SiO<sub>2</sub>-NPs with controlled size using a microbial secretory bacterial protein (bioremediase), which can be used in cost effective manner in various purposes. Moreover, we have explored the characteristics of the final product with a view of the possible nanobiotechnological and optoelectronics applications, wherein properties such as size, dispersion, surface charge of the SiO<sub>2</sub>-NPs are essential.

## MATERIALS AND METHOD

The bacterial strain BKH1 (Gen Bank accession number FJ177512) was obtained from the Biophysics Laboratory, Department of Physics, Jadavpur University [13]. The analytical grade TEOS was purchased from the Merck, USA. All other fine chemicals were purchased from Spectro Chem. Pvt. Ltd. India.

### Isolation and purification of the bioremediase Protein

Bioremediase protein (UniProt Knowledgebase Accession Number P86277) is secreted by the bacterium BKH1 in the growth medium while growing in the medium. The protein was purified from 6 to 7 days old bacterial culture medium similarly as described by Biswas et al. [13]. Double step purification through Sephadex G-100 column chromatographic technique was employed to purify the enzyme. Biosilicification assay was done to ensure the silica leaching activity of the purified protein as described earlier [13].

### Bio-production of SiO<sub>2</sub>-NPs

For the biosynthesis of silica ball consisting of SiO<sub>2</sub>-NPs, 100 µg purified bioremediase bacterial protein (1 µg/10 µl deionized water) was added drop wise in a 1 ml organic silica rich substrate (TEOS, 0.1 mol/L) solution in a 5 ml plastic vial and kept at ambient temperature for 24 h at pH neutral condition. Same experiment was performed by taking different concentrations of the protein (25, 50 and 150 µg respectively) separately. After adding the protein, spherical ball like structure was formed within the reaction mixture. The bio-transformed reaction commodities were collected using a long for-shape. Afterwards, the product was subsequently washed twice with ethanol-deionized (DI) water solution and dried at 65 °C temperature in vacuum desiccators for 24 h. Finally, some of the dried balls were crushed by mortar pestle to get fine powder for further auxiliary characterizations.

### Optical and Electron Microscopic Characterizations

The morphology of silica ball was studied by FESEM. The as-prepared silica ball was crushed into fine powder by using mortar-pestle. The SiO<sub>2</sub>-NPs powder sample was dispersed in DI-water and the optical characterizations were performed with UV-Vis spectrophotometer (UV-3101PC, Shimadzu) and fluorescence spectrophotometer (LS 50B, Perkin Elmer). The 280 nm was used as excitation wavelength ( $\lambda_{exc}$ ). A pinch of SiO<sub>2</sub>-NPs

powder sample was taken, coated with gold for the surface morphology images and compositional studies of the SiO<sub>2</sub>-NPs were examined further in Field Emission Scanning Electron Microscopy (FE-SEM, FEI INSPECT F50, The Netherlands) equipped with Energy dispersive spectrometer (EDX, Bruker System) using QUANTAX ESPIRIT 1.9 software. The morphological study of as-prepared SiO<sub>2</sub>-NPs was also performed by using a High Resolution Transmission Electron Microscopy (HR-TEM, JEOL JEM 2100, Japan). Samples for the TEM were prepared by drop casting the isolated and re-suspended solution on carbon coated copper grids.

### Zeta Potential

The synthesized SiO<sub>2</sub>-NPs powder was dispersed in Milli-Q water and the particles size as well as zeta potential experiment was characterized through DLS (Zeta Sizer, Nano ZS 90, Malvern) experiment.

### X-ray Diffraction

XRD measurements of as-prepared powder SiO<sub>2</sub>-NPs sample was carried out on a Bruker, D8 Advance, X-ray diffractometre instrument operated at a voltage of 40 kV and a current of 40 mA with Cu-K<sub>α</sub> radiation.

### FTIR and Raman Spectra Analysis

FTIR was used to identify the chemical and functional groups involves in SiO<sub>2</sub>-NPs. The prepared SiO<sub>2</sub>-NPs powder was dried and crushed with KBr (1% wt), pelleted and the FTIR spectra were recorded on a FTIR-8700, Shimadzu one instrument at a resolution of 4 cm<sup>-1</sup>. The Raman spectroscopy for the as-prepared SiO<sub>2</sub>-NPs was carried out using Laser Raman spectrometer (alpha 300, Witec, Germany) with the excitation wavelength of 532 nm and 20 mW output power for the irradiation time of 5 seconds.

### Thermo-gravimetric Weight-loss Analysis (TGA)

The thermal stability of SiO<sub>2</sub>-NPs was observed by determining the weight loss of the sample against elevated temperature in TGA/SDTA 851 °Mettler Toledo thermal analyzer system.

### Photo-catalytic Activity of SiO<sub>2</sub>-NPs for Decolourization of Dyes

The photo-catalytic of the as prepared silica balls containing SiO<sub>2</sub>-NPs was tested for decomposing various dyes (Methylene blue, Methyl orange and Bromophenol blue). The silica ball was immersed in a 100 ml solution of a dye (10 μM) and incubated for several minutes at room temperature. The optical density of the dye solution was checked at different intervals (5 min) at respective absorption maximum of the corresponding dye. Percentage of decolourization of the dye was determined and plotted in the graph. The same silica balls were repeatedly used for decolourization of different dyes. After each degradation reaction, the silica balls were washed repeatedly with deionized water: acetone (1:1 v/v) and then air dried for next experimental purposes.

### Statistical analysis

For each experiment prepared sample was tested repeatedly to confirm the obtained results.

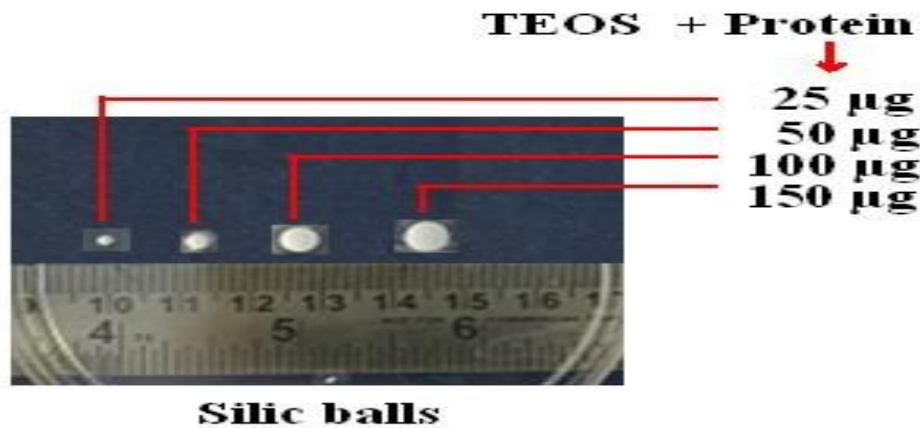
## RESULTS AND DISCUSSION

### Morphological and Compositional Characterization of SiO<sub>2</sub>-NPs

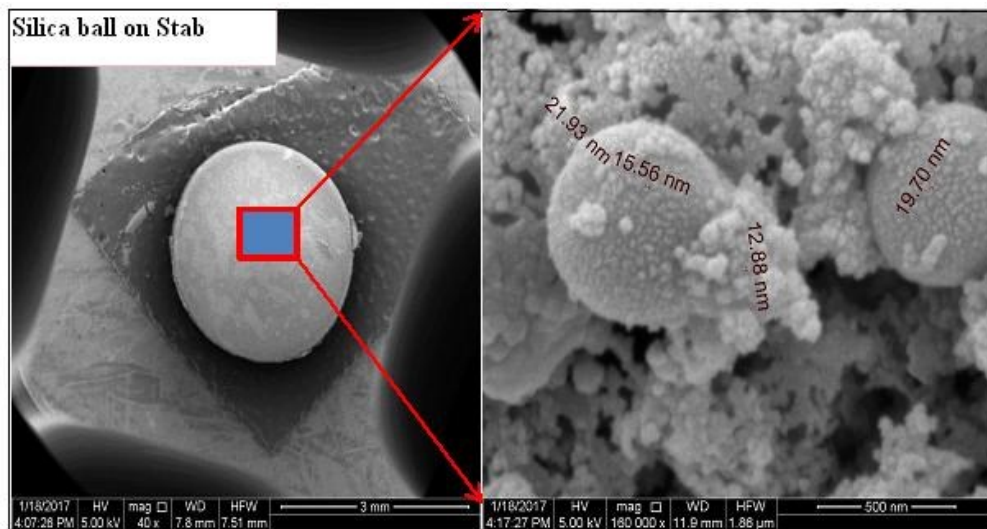
Formation of silica balls by using bioremediase protein is shown in the Fig. 1. The size of the ball depends on the protein concentration as observed visually. The FESEM image of the silica ball surface showed that the ball consisted of mostly silica nanoparticles along with some silica nano-ball of bigger sizes (Fig. 2).

The formation of silica ball consisting of silica nanoparticles was observed by the FE-SEM image (Fig. 3A), TEM image (Fig. 3B) and confirmed by EDX analysis (inset of Fig. 3A). The results suggested that SiO<sub>2</sub>-NPs assembled to form silica ball due to the interaction of bioremediase protein and TEOS solution. It similarly confirmed the successful synthesis of Si-NPs using bioremediase protein from TEOS as an organic precursor [14]. The synthesized Si-NPs were quite regular in shape and consistently dispersed as observed in both FE-SEM and TEM images. The average size of synthesized SiO<sub>2</sub>-NPs was measured as 20 ± 10 nm (n = 100) when analyzed from both FE-SEM and TEM images. EDX analysis (Inset of Fig. 3) of the specimen indicated the two strong evidence peaks of Silicon (Si) and Oxygen (O<sub>2</sub>) that confirmed that powder form of sample consisted of Silicon (Si) and Oxygen (O<sub>2</sub>) with atomic wt. 33.33% and 66.67% respectively which corroborated to the previous result [15]. TEM image also suggested the amorphous nature of the as prepared SiO<sub>2</sub>-NPs.

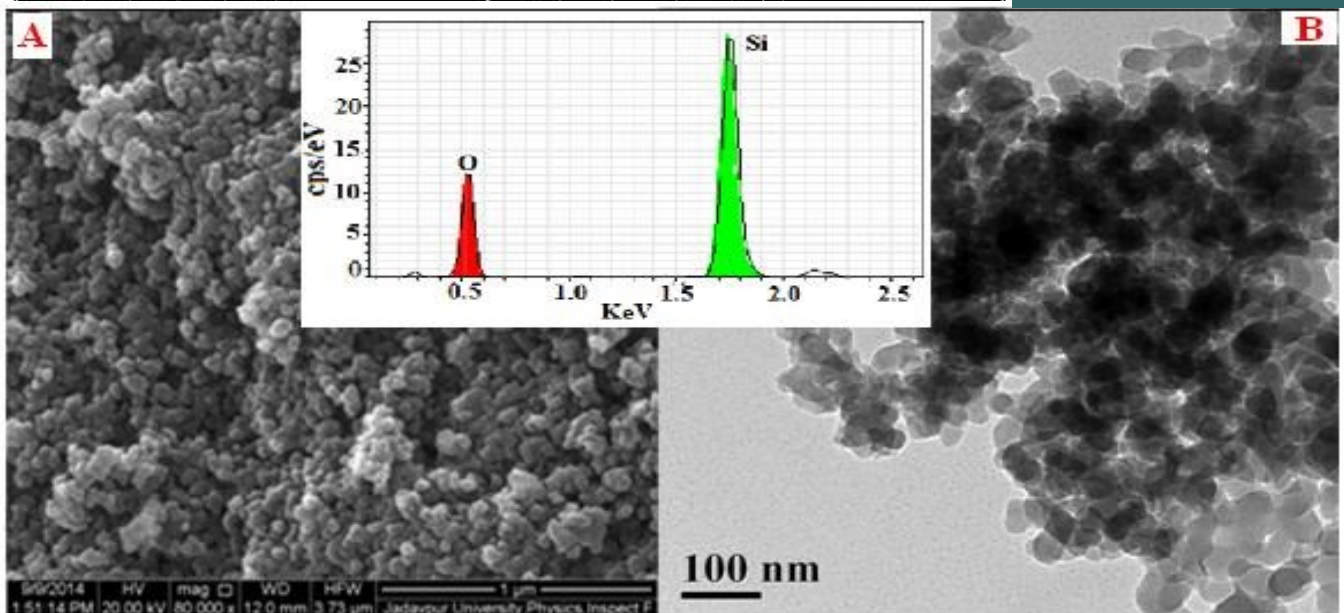




**Fig. 1:** Photographic images of silica balls formed by the interaction of different concentrations of bacterial protein with TEOS at neutral pH.

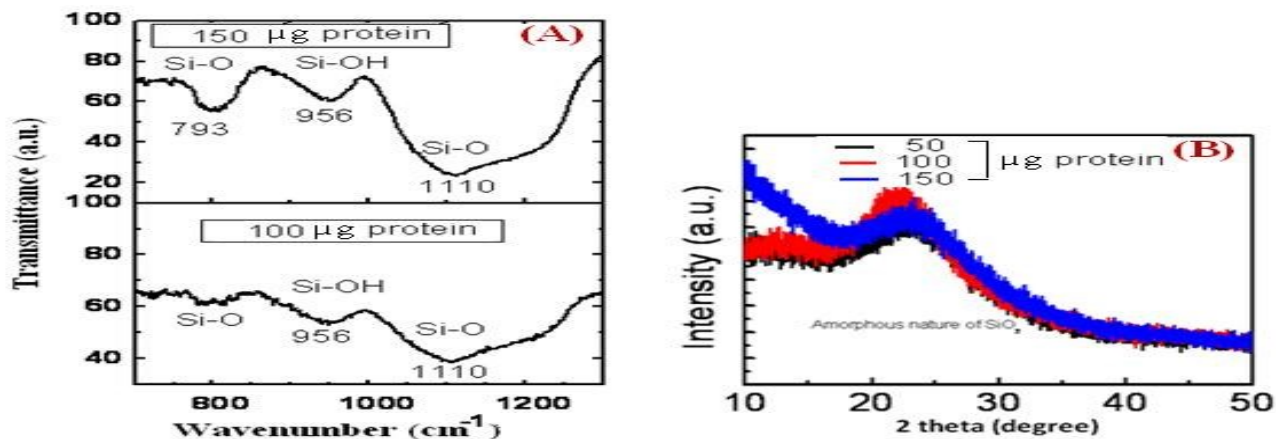


**Fig. 2:** FE-SEM image of silica ball and its constituents  $\text{SiO}_2$ -NPs formed by the Interaction of bacterial protein with TEOS at neutral pH.



**Fig. 3:** (A) FE-SEM image of constituents  $\text{SiO}_2$ -NPs obtained from silica ball. (B) TEM image of constituents  $\text{SiO}_2$ -NPs obtained from silica ball. Inset of the Fig. 3 shows the composition analysis by EDX of constituents  $\text{SiO}_2$ -NPs obtained from silica ball.

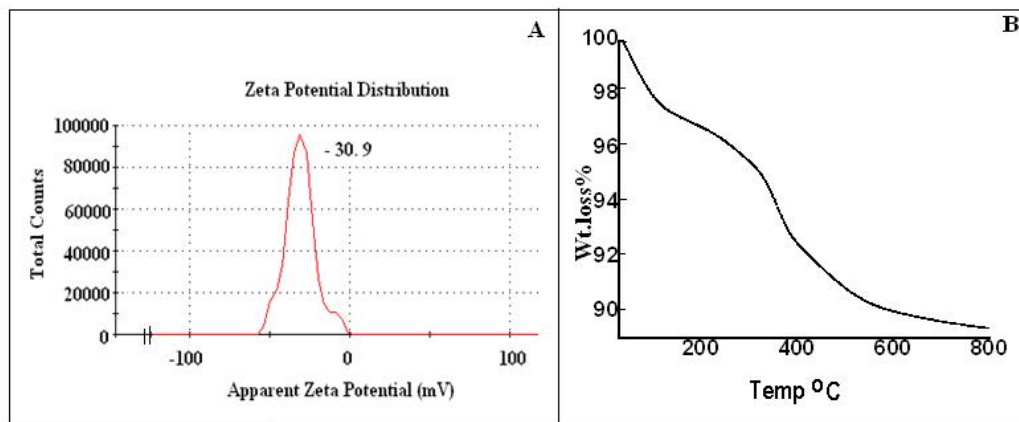
The possible vibrational bands shown at  $1097\text{ cm}^{-1}$  ( $\nu_{\text{as}}$ : Si-O) and  $790\text{ cm}^{-1}$  ( $\nu_{\text{s}}$ : Si-O) were the two strong evidence of the formation of  $\text{SiO}_2$ -NPs. The absorption bands appeared between  $800$  and  $1269\text{ cm}^{-1}$  had been ascribed as a superimposition of assorted  $\text{SiO}_2$  peaks, Si-OH bonding and residual organic groups [14]. The amorphous nature of prepared  $\text{SiO}_2$ -NPs was confirmed from the XRD observation (Fig. 4B), as there is no sharp crystalline diffraction peak [15, 16]. The broadness of XRD graph might be due to the small size as well as infectivity of inner configuration of the particles [16, 17].



**Fig. 4:** (A) FT-IR spectra of constituents  $\text{SiO}_2$ -NPs obtained from silica ball when reaction mixture contained  $150\text{ }\mu\text{g}$  proteins (upper panel) and  $100\text{ }\mu\text{g}$  proteins (lower panel) respectively. (B) XRD pattern of the as prepared  $\text{SiO}_2$ -NPs obtained from silica balls at different concentration of proteins used.

### Stability of $\text{SiO}_2$ -NPs

The Zeta potential ( $\zeta$ ) of the  $\text{SiO}_2$ -NPs was found to be  $(-)$   $30.9\text{ mV}$  (Fig. 5A) in balanced pH surroundings.  $\text{SiO}_2$ -NPs were stable in nature and bounded with negative type of surface charges as it is the typical characteristic of  $\text{SiO}_2$ -NPs. The nature of Zeta potential was negative which further suggested the good dispersion stability property as well as preventing the sample from further agglomeration. Fig. 5B indicated conventional thermal properties of biosynthesized  $\text{SiO}_2$ -NPs measured from room temperature ( $30\text{ }^\circ\text{C}$ ) to a very high temperature ( $800\text{ }^\circ\text{C}$ ) by using TGA method. TGA is mainly used for characterizing the structural properties as well as for confirmation of the thermal stability of the materials. A ceramic ( $\text{Al}_2\text{O}_3$ ) crucible was used for heating and measurements were carried out in  $\text{N}_2$  atmosphere at the heating rate of  $10\text{ }^\circ\text{C}/\text{min}$ . It is known that all the water molecules of the surfactant are removed when temperature is raised nearly equal to  $130\text{ }^\circ\text{C}$  [18]. There was practically no change in mass of the  $\text{SiO}_2$ -NPs within the temperature range of  $500$  to  $800\text{ }^\circ\text{C}$  which implied that the as-prepared  $\text{SiO}_2$ -NPs could be used in chromatographic packing for its stability at higher temperature.



**Fig. 5:**(A) Zeta Potential ( $\zeta$ ) curve of synthesized  $\text{SiO}_2$ -NPs in neutral environment. (B) Thermogravimetric analysis of weight-loss curves for  $\text{SiO}_2$ -NPs.

Fig. 5A represents the UV-Vis absorption spectra of SiO<sub>2</sub>-NPs when well dispersed in DI-water. It observes a small absorption peak centered at about 360 nm. The estimated band gap ( $E_g$ ) of SiO<sub>2</sub>-NPs was found to be 3.4 eV which was similar to the previous data [15, 16]. The room temperature fluorescence spectra of as-prepared SiO<sub>2</sub>-NPs are shown in Fig. 5B. A broad emission observed at UV-region, which is composed of a sharp peak centered at 440 nm. The sharp visible (blue) emission peak may be due to the electron-hole recombination of the self-trapped exciton (STE). This peak is slightly blue shifted because of the smaller-sized SiO<sub>2</sub>-NPs as evident from the TEM image (Fig. 3B). The mechanism involved in blue band is an oxide associated process either from the oxide itself or from infectivity within structure of the oxide. However, sometimes the blue band could be resultant of a non-stoichiometric suboxide, SiO<sub>x</sub> ( $x < 2$ ), having value of band gap smaller than that of SiO<sub>2</sub>. The appropriate justification for blue band formation from deficiency of non-bridging oxygen hole centre, or from infectivity of the oxide itself is now more eye-catching. SiO<sub>2</sub>-NPs can be utilized in a range of biomedical applications like killing of unwanted bacteria with UV irradiation and use as an optical probe as well as optoelectronic devices for various medical diagnoses by using the visible emission.

### Raman Spectra Analysis

Fig. 7 illustrates room temperature Raman spectra of synthesized SiO<sub>2</sub>-NPs in a wavelength range of 4050–50 cm<sup>-1</sup>. The Raman spectra of the prepared materials similarly confirmed the typical nature of SiO<sub>2</sub>-NPs. In details, the major peak at 410 cm<sup>-1</sup> was the main characteristic peak of SiO<sub>2</sub>-NPs. It is due to mainly coming from the bending mode of oxygen in n-membered rings ( $n > 4$ ) and it was well known as R line. Peak appears at 818 cm<sup>-1</sup> was the involvement of Silica network optical mode as well; vibrational mode due to (OH) - group with admiration to Si contributed the peaks at 980 cm<sup>-1</sup>. The typical symmetric stretching peak at ~490 (D1) have been attributed to the bulk infectivity in fourfold and threefold ring like structure of SiO<sub>2</sub> tetrahedral atom [19 - 22]. Subsequently, Raman studies of SiO<sub>2</sub>-NPs have been established the surface-related optical properties as well. However, Raman peak amplitude of SiO<sub>2</sub>-NPs scientifically depends on the specific surface areas as similar to previous literature [23].

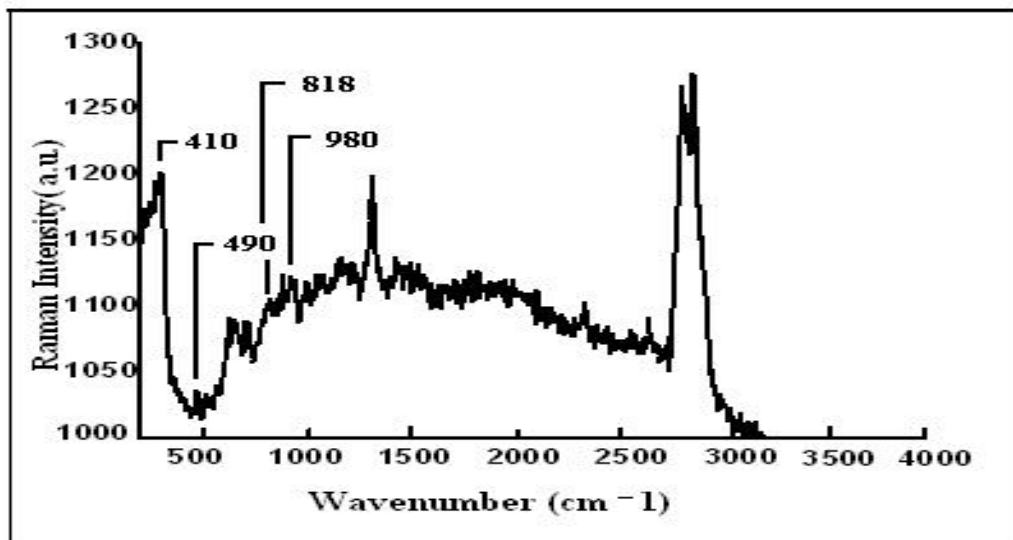
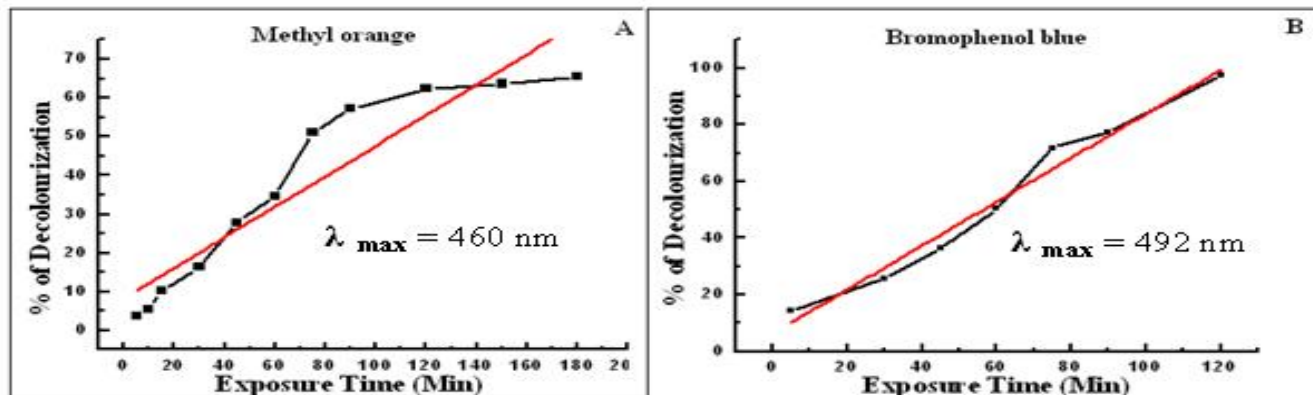


Fig. 7: Raman spectra analysis for synthesized SiO<sub>2</sub>-NPs obtained from silica ball when 150 μg proteins used in the reaction mixture.

### Decolourizing Effect of Silica ball

The photo-catalytic activity of the prepared silica ball consisting of SiO<sub>2</sub>-NPs was successfully demonstrated (Fig. 8). The degradation of Methyl orange (Fig. 8A), Bromophenol blue (Fig. 8B) and Methylene blue (data not supplied) dyes was carried out in the presence of silica ball at different time intervals in the visible region. It was observed that the absorption maxima of Methyl orange (460 nm), Bromophenol blue (492) and Methylene blue (663 nm) were decreased regularly with the incubation time indicating the photo-catalytic degradation those dyes due to the action of the silica balls. The percentage of degradation efficiency of biosynthesized silica balls was determined and plotted in the Fig. 8. Almost 100% degradation of Bromophenol blue and 70 to 80% degradation of Methylene blue and Methyl orange dyes were noted in presence of silica ball. The lesser degradation of the last two dyes might be due to deposition of the Bromophenol blue dye on the surface of silica ball which was used first and thus less exposed surface of SiO<sub>2</sub>-NPs was available for those two dyes. The repeated use of the biosynthesized silica balls suggested that it could

be an effective photo-catalyst for water purification system and dye effluent treatment.



**Fig. 8:** Dye degradation activities of silica ball where (A) Methyl orange and (B) Bromophenol blue dyes were used as substrate.

## CONCLUSIONS

A microbial protein assisted silica ball consisting SiO<sub>2</sub>-NPs using an Organic (TEOS) silica precursor is effectively established. The constituent particles of the as-prepared samples are systematically characterized using different tools like UV-Vis, Fluorescence, HR-TEM, FE-SEM, XRD, TGA and FTIR spectra. Fluorescence data shows a broad emission in visible region. This result suggests its further utilization in various biomedical applications as an optical probe for medical diagnosis. The value of Zeta potential ( $\zeta$ ) of the SiO<sub>2</sub>-NPs indicates the immovability of SiO<sub>2</sub>-NPs in dispersed neutral medium, preventing it from the further agglomeration. The formation of silica balls via an effortless biocompatible protein assisted methodology shows its potential and notable optical properties for direct use in various fields.

## Author's contributions

Shilpi Show: She did the all experimental work and substantially contributed to conception, acquisition of data and analysis of data.

Krishna Chattopadhyay: She involved in drafting the manuscript and revising it critically for important intellectual content.

Chetana Ghosal: She took part in dyes degradation work and substantially contributed to acquisition and analysis of data

Brajadulal Chattopadhyay: He made the substantial contributions to conception and designs the experimental procedures for acquisition of data and interpretation of data. He was also involved in drafting the manuscript and revising it critically for important intellectual content.

## Acknowledgments

The experimental facilities obtained from Biophysical Laboratory of Physics Department of Jadavpur University are gratefully acknowledged.

## Funding/Financial Disclosure

The work was performed under the supervision of Professor Brajadulal Chattopadhyay and there was no financial support obtained for the work. Only support from Biophysics Laboratory from its own research facilities involved in the work.

## REFERENCES

- [1] Huo, Q., Feng, J., Schuth, F., Stucky, G. D. (1997). Preparation of Hard Mesoporous Silica Spheres. *Chemistry of Material*, 9(1): 14 – 17.
- [2] Ozin, G. A. (1992). Nanochemistry: Synthesis in diminishing dimensions. *Advance Materials*, 4: 612 – 649.
- [3] Gunter. B., Gru'n, M., Unger K. K., Matsumoto, A., Kazuo, T. (1998). Tailored syntheses of nanostructured silicas: Control of particle morphology, particle size and pore size. *Supramolecular Science*, 5: 253– 259.
- [4] Bao, X., Wei, X., Wang, Y., Jiang, H., Yu, D., Hu, M. (2014). Effect of Silica-Based Nanomaterials and Their Derivate with PEGylation on Cementoblasts. *Annals of Biomedical Engineering*, 42 (8): 1781 – 1789.

- [5] Kell, A. J., Barnes, M. L., Slater, K., Lavigne, C. (2012). Functionalised silica nanoparticles stable in serum-containing medium efficiently deliver siRNA targeting HIV-1 co-receptor CXCR4 in mammalian cells. *International Journal of Nano and Biomaterials* 2, 4(3-4): 223 – 242.
- [6] Liu, X., Qian, H., Ji, Y., Li, Z., Shao, Y., Hu, Y., Tong, G. X., Li, L., Guo, W., Guo, H. (2012). Mesoporous silica-coated NaYF<sub>4</sub> nanocrystals: facile synthesis, in vitro bioimaging and photodynamic therapy of cancer cells. *RSC Advances*, 2(32): 12263 – 12268.
- [7] Natarajan, S. K., Selvaraj, S. (2014). Mesoporous silica nanoparticles: Importance of surface modifications and its role in drug delivery. *RSC Advances*, 4: 14328 – 14334.
- [8] Monnier, A., Schu<sup>th</sup>, F., Huo, Q., Kumar, D., Margolese, D., Maxwell, R. S., Stucky, G. D., Krishnamurthy, M., Petroff, P., Firouzi, A., Janicke, M., Chmelka, B. F. (1993). Cooperative formation of inorganic-organic interfaces in the synthesis of silicate mesostructures. *Science*, 261: 1299 – 1303.
- [9] Firouzi, A., Kumar, D., Bull, L. M., Besier, T., Sieger, P., Huo, Q., Walker, S. A., Zasadzinski, J. A., Glincka, C., Nicol, J., Margolese, D., Stucky, G. D., Chmelka, B. F. (1995). Cooperative organization of inorganic-surfactant and biomimetic assemblies. *Science*, 267: 1138 – 1143.
- [10] Huo, Q., Margolese, D. I., Ciesla, U., Demuth, D. G., Feng, P., Gier, T. E., Sieger, P., Firouzi, A., Chmelka, B. F.; Schu<sup>th</sup>, F. Stucky, G. D. (1994). Organization of Organic Molecules with Inorganic Molecular Species into Nanocomposite Biphase Arrays. *Chemistry of Materials*, 6: 1176 – 1191.
- [11] Anderson, M. T., Martin, J. E., Odinek, J. G., Newcomer, P. P. (1998). Surfactant-Templated Silica Mesophases Formed in Water: Cosolvent Mixture. *Chemistry of Materials*, 10: 311.
- [12] Gru<sup>n</sup>, M., Unger, K. K., Matsumoto A., Tsutsumi, K. (1999). Novel pathways for the preparation of mesoporous MCM-41 materials: control of porosity and morphology. *Microporous and Mesoporous Materials*, 27: 207 – 216.
- [13] Biswas, M., Majumdar, S., Chowdhury, T., Chattopadhyay, B.D., Mandal, S., Halder, U., Yamasaki, S. (2010). Bioremediase a unique protein from a novel bacterium BKH1, ushering a new hope in concrete technology. *Enzyme and Microbial Technology*, 46: 581 – 587.
- [14] Chowdhury, T., Sarkar, M., Chaudhuri, B., Chattopadhyay, B.D., Halder, U.C. (2015). Participatory role of zinc in structural and functional characterization of bioremediase: a unique thermostable microbial silica leaching protein. *Journal of Biological Inorganic Chemistry*, 20(5): 791 – 803.
- [15] Show, S., Tamang, A., Chowdhury, T., Mandal, D., Chattopadhyay, B.D. (2015). Bacterial (BKH1) Assisted Silica Nanoparticles from Silica Rich Substrates: A Facile and Green approach for biotechnological applications. *Colloids and Surfaces B: Biointerfaces*, 126: 245 – 250.
- [16] Show, S., Chattopadhyay, B.D. (2016). Protein Mediated Silica Particles with pH Controlled Porosity and Morphology. *Advances in Microbiology*, 6: 986 – 998.
- [17] Wei, Z., Yan, P., Feng, W., Dai, J., Wang, Q., Xia, T. (2006). Microstructural characterization of Ni nanoparticles prepared by anodic arc plasma. *Materials Characterization*, 57(3): 176 – 181.
- [18] Unger, K.K. (1979). Porous Silica. *Journal of Chromatography Library*, 16: 237-242.
- [19] Umari, P., Pasquarello, A. (2003). First-principles analysis of the Raman spectrum of vitreous silica: comparison with the vibrational density of states, *Journal of Physics: Condensed Matter*, 15(16): S1547 – S1552.
- [20] Ane<sup>da</sup>, A., Carbonaro, C.M., Clemente, F., Corpino, R., Ricci, P. C. (2003). Raman Investigation of Surface OH-Species in Porous Silica. *Journal of Physical Chemistry B*, 107 (49): 13661 – 13664.
- [21] Ane<sup>da</sup>, A., Carbonaro, C.M., Clemente, F., Corda, L., Corpino, R., Ricci, P.C. (2003). Surface hydroxyls in porous silica: a Raman spectroscopy study, *Materials Science and Engineering: C*, 23 (6-8): 1069 – 1072.
- [22] Galeener, F.L. (1982). Planar rings in vitreous silica, *Journal of Non-Crystalline Solids*, 49(1-3): 53 – 62.
- [23] Alessi, A., Agnello, S., Buscarino, G., Gelardi, F.M. (2013). Structural properties of core and surface of silica nanoparticles investigated by Raman spectroscopy. *Journal of Raman Spectroscopy*, 44(6): 810 – 816.

## Contact Us:

### SIFT DESK

Deerpark Dr, #75, Fullerton, CA, 92831, United States.

E-mail: [helpdesk@siftdesk.org](mailto:helpdesk@siftdesk.org)

Visit us on the web at: [www.siftdesk.org](http://www.siftdesk.org)